

## Middlesex University Research Repository:

an open access repository of  
Middlesex University research

<http://eprints.mdx.ac.uk>

Rossek, Sacha J, 1995.  
Direct optical control of a microwave phase shifter using GaAs field-effect transistors.  
Available from Middlesex University's Research Repository.

---

### Copyright:

Middlesex University Research Repository makes the University's research available electronically.

Copyright and moral rights to this thesis/research project are retained by the author and/or other copyright owners. The work is supplied on the understanding that any use for commercial gain is strictly forbidden. A copy may be downloaded for personal, non-commercial, research or study without prior permission and without charge. Any use of the thesis/research project for private study or research must be properly acknowledged with reference to the work's full bibliographic details.

This thesis/research project may not be reproduced in any format or medium, or extensive quotations taken from it, or its content changed in any way, without first obtaining permission in writing from the copyright holder(s).

If you believe that any material held in the repository infringes copyright law, please contact the Repository Team at Middlesex University via the following email address:  
[eprints@mdx.ac.uk](mailto:eprints@mdx.ac.uk)

The item will be removed from the repository while any claim is being investigated.

# Direct Optical Control of a Microwave Phase Shifter Using GaAs Field-Effect Transistors

Sacha J. Rossek

*Communications Research Group  
School of Electronic Engineering  
Faculty of Technology  
Middlesex University*

September 1995

A thesis submitted to Middlesex University in partial fulfilment of the  
requirements for the degree of Doctor of Philosophy

To my late grandfathers  
Anthony Rossek (1917–1994)  
and Benjamin Challenger (1907–1977).

# Abstract

## Direct Optical Control of a Microwave Phase Shifter Using GaAs Field-Effect Transistors

*Sacha J. Rossek*

THE design and analysis of a novel optical-to-microwave transducer based upon direct optical control of microwave gallium arsenide (GaAs) field-effect transistor (FET) switches is the subject of this thesis. The switch is activated by illuminating the gate depletion region of the FET device with laser light having a photon energy and wavelength appropriate to the generation of free carriers (electron-hole pairs) within GaAs. The effects of light on the DC and microwave properties of the GaAs FET are explored and analyzed to permit the characterization of the switching performance and transient response of a reflective microwave switch. The switch is novel in that it utilizes direct optical control, whereby the optically controlled GaAs FET is directly in the path of the microwave signal and therefore relies on optically-induced variations in the microwave characteristics of the switch. This contrasts with previous forms of optically controlled switches which rely on indirect methods with the optical stimulus inducing variations in the DC characteristics of the GaAs FET, such that there is no direct interaction between the optically illuminated GaAs FET and the microwave signal. Measured and simulated results relating to the switching performance and transient response of the direct optically controlled microwave switch have been obtained and published as a result of this work. For the first time, good agreement is achieved between the measured and simulated results for the rise and fall times associated with the transient response of the gate photovoltaic effect in optically controlled GaAs FET switches. This confirms that the GaAs FET, when used as an optically controlled microwave switch, has a transient response of the order of several micro-seconds. An enhanced model of the GaAs FET switch has been developed, which represents a more versatile approach and leads to improved accuracy in predicting switching performance. This approach has been shown to be valid for both optical and electrical control of the GaAs FET. This approach can be used to model GaAs FET switches in discrete

or packaged forms and predicts accurately the occurrence of resonances which may degrade the switch performance in both switching states. A novel method for tuning these resonances out of the switch operating band has been developed and published. This allows the switch to be configured to operate over the frequency range 1 to 20 GHz. The agreement between the models and measured data has been shown to hold for two very different GaAs FET structures.

The results of the direct optically controlled microwave GaAs FET switch have been used as the basis for the design of a novel direct optically controlled microwave phase shifter circuit. Measured and simulated results are in good agreement and verify that the performance of the optically controlled phase shifter is comparable with previously published results for electrically controlled versions of the phase shifter. The 10 GHz phase shifter was optically controlled over a 1 GHz frequency range and exhibited a mid-band insertion loss of 0.15 dB.

The outcome of the work provides the basis for directly controlling the phase of a microwave signal using the output of an optical sensor, with the GaAs FET acting as an optical-to-microwave transducer through a monolithic interface.

# Contents

<b>Dedications</b>	<b>i</b>
<b>Abstract</b>	<b>ii</b>
<b>Acknowledgements</b>	<b>xiv</b>
<b>Glossary</b>	<b>xv</b>
<b>Physical Constants</b>	<b>xx</b>
<b>Acronyms</b>	<b>xxi</b>
<b>1 Introduction</b>	<b>1</b>
<b>2 Literature Review</b>	<b>7</b>
2.1 Introduction . . . . .	7
2.2 Optically Controlled Microwave GaAs FET's . . . . .	9
2.2.1 Static Optical Response of Microwave GaAs FET's . . . . .	11
2.2.2 Dynamic Optical Response of Microwave GaAs FET's . . . . .	21
2.3 Optically Controlled GaAs FET Devices . . . . .	32
2.3.1 Optically Controlled Amplification . . . . .	32
2.3.2 Optical Injection-Locking and Frequency Tuning of Oscillators .	34
2.3.3 Optically Controlled Phase Shifting . . . . .	35
2.3.4 Optically Controlled Mixing . . . . .	35
2.3.5 Optically Controlled Switching . . . . .	36
2.3.6 Optical Detection . . . . .	37
2.4 GaAs FET-Based Switches . . . . .	38
2.5 GaAs FET-Based Phase Shifters . . . . .	42
2.6 MMIC and OMMIC Technology . . . . .	43
<b>3 Static Photo-Effects in Microwave GaAs FET's</b>	<b>54</b>
3.1 Introduction . . . . .	54
3.2 Optical Control of GaAs FET's . . . . .	56

3.3	Photoconductive Effects . . . . .	59
3.4	Photovoltaic Effects . . . . .	60
3.4.1	Barrier Interface Photovoltaic Effect . . . . .	60
3.4.2	Gate Depletion Photovoltaic Effect . . . . .	61
3.5	Predominant Photo-Effect in Microwave FET's . . . . .	63
3.6	Evaluation of the Gate Photo-Effect . . . . .	66
3.7	GaAs FET Static Electrical Parameters . . . . .	67
3.7.1	Pinch-Off Voltage . . . . .	67
3.7.2	Gate Schottky Junction Ideality Factor . . . . .	68
3.7.3	Gate Schottky Junction Reverse Saturation Current . . . . .	69
3.7.4	Gate Schottky Junction Built-In Potential . . . . .	69
3.8	GaAs FET Static Optical Parameters . . . . .	69
3.8.1	Optically Illuminated GaAs FET Area . . . . .	69
3.8.2	Optical Power Reflectivity . . . . .	70
3.8.3	Photon Flux Density . . . . .	71
<b>4</b>	<b>Dynamic Photo-Effects in Microwave GaAs FET's</b>	<b>73</b>
4.1	Introduction . . . . .	73
4.2	Dynamic Photovoltaic Effects . . . . .	74
4.2.1	Barrier Interface Photovoltaic Effect . . . . .	74
4.2.2	Gate Depletion Photovoltaic Effect . . . . .	74
4.3	GaAs FET Transient Response . . . . .	75
4.3.1	Gate Junction Capacitance . . . . .	76
<b>5</b>	<b>Microwave Switching With GaAs FET's</b>	<b>78</b>
5.1	Introduction . . . . .	78
5.2	Hybrid II GaAs FET Model . . . . .	80
5.3	'On' State GaAs FET Switch Model . . . . .	80
5.3.1	Series Channel Resistance . . . . .	81
5.3.2	Drain and Source Resistances . . . . .	82
5.4	'Off' State GaAs FET Switch Model . . . . .	83
5.4.1	Electrode Capacitance . . . . .	83
5.4.2	Drain-to-Source Resistance . . . . .	85
5.4.3	Gate Depletion Region Capacitance . . . . .	85
5.4.4	Charging Resistances . . . . .	85
5.5	Modelling of Hybrid GaAs FET Switches . . . . .	85
5.5.1	Package Model . . . . .	86
5.5.2	Gate Resistance . . . . .	86

<b>6</b>	<b>Optical Switching of Microwave GaAs FET's</b>	<b>89</b>
6.1	Introduction . . . . .	89
6.2	Hybrid GaAs FET Switch Design . . . . .	90
6.2.1	Drain Circuit . . . . .	91
6.2.2	Source Circuit . . . . .	92
6.2.3	Gate Circuit . . . . .	93
6.2.4	Bias Circuit . . . . .	94
6.3	Optically Controlled Switch State Modelling . . . . .	94
6.3.1	Static Optical Control . . . . .	95
6.3.2	Switch State . . . . .	96
6.4	GaAs FET Switch State Results . . . . .	98
6.4.1	Optically 'On' State . . . . .	99
6.4.2	'Off' state . . . . .	101
<b>7</b>	<b>Transient Response of Optically Controlled GaAs FET's</b>	<b>105</b>
7.1	Introduction . . . . .	105
7.2	Transient Response Under Optical Control . . . . .	106
7.2.1	Transient Response Measurement . . . . .	106
7.2.2	Transient Response Modelling . . . . .	107
7.3	Optical Transient Response Results . . . . .	108
<b>8</b>	<b>Microwave GaAs FET Phase Shifters</b>	<b>113</b>
8.1	Introduction . . . . .	113
8.2	Reflective Type Phase Shifters . . . . .	114
8.2.1	Hybrid Coupled Phase Shifter . . . . .	115
8.2.2	Switched-Line Phase Shifter . . . . .	115
8.2.3	Loaded-Line Phase Shifter . . . . .	116
8.3	Loaded-Line Phase Shifter Design . . . . .	117
8.3.1	Analysis . . . . .	117
8.3.2	Shunt Loaded-Line Configurations . . . . .	117
8.4	Large Phase Shifts In Loaded-Line Elements . . . . .	119
8.4.1	Three-Stage Phase Shifter . . . . .	119
8.4.2	Four-Stage Phase Shifter . . . . .	120
<b>9</b>	<b>Phase Shifting Using Optically Switched FET's</b>	<b>122</b>
9.1	Introduction . . . . .	122
9.2	Optically Controlled Phase Shifter Design . . . . .	123
9.2.1	GaAs FET Switch State Impedance . . . . .	124
9.2.2	Impedance Transformation Networks . . . . .	125
9.3	Phase Shifter Modelling . . . . .	126

9.4	Optically Controlled Phase Shifter Results . . . . .	127
9.4.1	Optically controlled 30° Phase Shifter . . . . .	129
9.4.2	Optically controlled 45° Phase Shifter . . . . .	129
<b>10</b>	<b>Inter-Electrode Capacitance and Frequency Tuning in GaAs FET's</b>	<b>132</b>
10.1	Introduction . . . . .	132
10.2	Inter-Electrode Capacitance Evaluation . . . . .	133
10.2.1	Current Methods . . . . .	134
10.2.2	Coplanar Stripline Methods . . . . .	135
10.3	Inter-Electrode Capacitance Simulation . . . . .	136
10.3.1	3-D Field Simulation Methods . . . . .	136
10.3.2	Field Simulation Boundaries . . . . .	137
10.3.3	Parameter Evaluation . . . . .	139
10.3.4	Experimental GaAs FET Geometries . . . . .	139
10.4	Inter-Electrode Capacitance Results . . . . .	140
10.5	Frequency Tuning in GaAs FET Switches . . . . .	140
10.5.1	Simulation of GaAs FET Switch Resonances . . . . .	141
10.5.2	GaAs FET Switch Sensitivity Analysis . . . . .	142
10.5.3	Tuning Methods and Results . . . . .	142
10.6	Broadband GaAs FET Switch Operation . . . . .	143
<b>11</b>	<b>Monolithic Circuit Considerations</b>	<b>148</b>
11.1	Introduction . . . . .	148
11.2	Inductive Tuning Element . . . . .	149
11.2.1	Cascode Analysis With Resistive Feedback . . . . .	151
11.2.2	Cascode Analysis With GaAs FET Feedback . . . . .	153
11.3	Monolithic Active Inductor Design . . . . .	155
11.3.1	Monolithic Active Inductance . . . . .	155
11.3.2	Monolithic Active Inductance Variation . . . . .	155
11.4	Active Inductor Performance . . . . .	156
11.4.1	Improved Active Inductor Modelling . . . . .	157
11.4.2	Comparison of Active Inductance Results . . . . .	159
<b>12</b>	<b>Discussion of Results</b>	<b>164</b>
12.1	Introduction . . . . .	164
12.2	Discussion of Results . . . . .	164
12.2.1	Switch State Performance [12.1, 12.2] . . . . .	165
12.2.2	Switch Transient Response [12.2] . . . . .	166
12.2.3	GaAs FET Inter-electrode Capacitance [12.3] . . . . .	166
12.2.4	GaAs FET Resonances and Tuning [12.3] . . . . .	167

12.2.5	Phase Shifter Performance [12.1]	167
12.2.6	Monolithic Active Inductor	167
<b>13</b>	<b>Conclusions</b>	<b>170</b>
<b>14</b>	<b>Recommendations for Further Research</b>	<b>172</b>
14.1	Recommendations for Further Research	172
14.1.1	Experimental Work	172
14.1.2	Theoretical/Simulation Work	174
14.2	Phase shifter Applications	175
14.2.1	Electro-Optic Microwave Sensor	175
14.2.2	Phased-Array Radar	177
<b>A</b>	<b>Pascal Computer Programs</b>	<b>181</b>
A.1	Microstrip Open-End Correction	181
A.2	Asymmetric Tee-Junction Compensation	182
A.3	Impedance Step Compensation	183
A.4	Optical Reflectivity	184
A.5	Switch Impedance Transformation	185
A.6	Phase Shifter Design	187
A.7	GaAs FET Active Inductor	191
<b>B</b>	<b>Design Expressions</b>	<b>194</b>
B.1	Gate Depletion Region Photocurrent	194
B.2	Optical Reflectivity	196
B.3	Gate Depletion Region Lateral Extension	198
B.4	Phase Shifter Matching Stub	199

# List of Figures

1.1	Conceptual diagram of an optically controlled radio sensor network. (a) Distributed wireless sensor network. (b) Integrated opto-microwave transducer. . . . .	3
2.1	Schematic of an OMMIC-based phased-array antenna system incorporating optoelectronic microwave signal generation, distribution and detection [2.4]. . . . .	9
2.2	A microwave fibre-optic subsystem for personal radio communications [2.2]. . . . .	37
3.1	Schematic cross-section of a basic microwave GaAs MESFET. . . . .	56
3.2	Plan view schematic of two typical microwave MESFET gate structures, illustrating the difference in compatibility with an optical beam spot. (a) Interdigitated (multi-finger) gate. (b) $\Pi$ -gate. . . . .	57
3.3	Optical absorption coefficient as a function of wavelength for gallium arsenide at 300 K. . . . .	58
3.4	Photoconductive effects within MESFET's, illustrating the process of intrinsic (band-to-band) photo-excitation and its occurrence within the basic FET structure. . . . .	59
3.5	Static equivalent circuit of the channel-to-substrate interface while under optical illumination. . . . .	60
3.6	Internal photovoltaic effect, demonstrating the change in the interface barrier height between the channel and substrate (arrows show current flow). (a) Without illumination. (b) With illumination. . . . .	61
3.7	Band-to-band photo-excitation of an electron-hole pair in a metal semiconductor (Schottky) junction. (a) Within the depletion region. (b) Within the semiconductor region. . . . .	62
3.8	External photovoltaic effect within the gate depletion region, created by the large external gate resistance (arrows show current flow). (a) Without illumination. (b) With illumination. . . . .	64
3.9	Static equivalent circuit of the gate Schottky junction while under optical illumination. . . . .	65

3.10	Apparatus used in the static and dynamic optical and electrical measurements. . . . .	67
3.11	Forward current-voltage characteristics of the gate Schottky junction of the ATF-10136 with $V_{DS} = 0V$ . . . . .	68
3.12	Cross-sectional view of a GaAs FET, indicating the areas of optical absorption created by the lateral extensions of the gate depletion region. . . . .	70
4.1	Dynamic equivalent circuit of the channel-to-substrate interface while under optical illumination. . . . .	75
4.2	Dynamic equivalent circuit of the gate Schottky junction while under optical illumination. . . . .	75
5.1	Basic hybrid $\Pi$ lumped equivalent circuit model of a GaAs FET (small-signal amplifier mode). . . . .	81
5.2	Approximate lumped equivalent circuit of a GaAs FET switch in the 'on' state, indicating the physical origins of the lumped circuit elements. . . . .	81
5.3	Approximate lumped equivalent circuit of a GaAs FET switch in the 'off' state, indicating the physical origins of the lumped circuit elements. . . . .	84
5.4	Approximate lumped equivalent circuit package model for the range of Hewlett Packard GaAs FET's [5.7]. . . . .	86
6.1	Microstrip circuit layout for direct optically controlled microwave switch. . . . .	91
6.2	Micro-X package layout for the Hewlett Packard range of GaAs FET's. (a) Plan view. (b) Cross-sectional View. . . . .	92
6.3	Schematic representation of the optically controlled reflective microwave GaAs FET switch in shunt configuration. . . . .	92
6.4	Two-section microstrip bias-tee arrangement (dimensions in $\mu m$ ). . . . .	95
6.5	Gate Schottky junction equivalent circuit while under continuous optical illumination. . . . .	96
6.6	Simulation layout generated within MDS for determining the switch characteristics of both FET structures in the 'on' state. . . . .	98
6.7	Simulation layout generated within MDS for determining the switch characteristics of both FET structures in the 'off' state. . . . .	99
6.8	Measured ( $\square$ ) and simulated ( $\times$ ) return loss for the optically 'on' state of the GaAs FET switch. (a) ATF-10136. (b) ATF-13136. . . . .	100
6.9	Measured ( $\square$ ) and simulated ( $\times$ ) phase for the optically 'on' state of the GaAs FET switch. (a) ATF-10136. (b) ATF-13136. . . . .	101
6.10	Measured ( $\square$ ) and simulated ( $\times$ ) return loss for the 'off' state of the GaAs FET switch. (a) ATF-10136. (b) ATF-13136. . . . .	102
6.11	Measured ( $\square$ ) and simulated ( $\times$ ) phase for the 'off' state of the GaAs FET switch. (a) ATF-10136. (b) ATF-13136. . . . .	103

7.1	Microstrip circuit layout of the transient response measurement for the direct optically controlled microwave switch. . . . .	107
7.2	Simulation layout generated within MDS for determining the switch transient response of both FET structures. . . . .	109
7.3	Measured ( $\square$ ) and simulated ( $\times$ ) transient response for optical FET switch circuit including oscilloscope probe. (a) ATF-10136. (b) ATF-13136. . . . .	111
8.1	Schematic representation of two ideal phase shifter configurations. (a) Reflection type. (b) Transmission type. . . . .	114
8.2	Schematic representation of a hybrid coupled phase shifter. . . . .	115
8.3	Schematic representation of a switched-line phase shifter. . . . .	116
8.4	Schematic representation of a shunt loaded-line phase shifter. . . . .	116
8.5	Impedance transformation in loaded-line phase shifters. (a) Shunt stub mounting. (b) Tandem stub mounting. . . . .	118
8.6	Schematic representation of a three stage loaded-line phase shifter. . . . .	119
8.7	Schematic representation of a four-stage loaded-line phase shifter. . . . .	120
9.1	Measured ( $\square$ ) and simulated ( $\times$ ) Smith chart plots of ATF-10136 GaAs FET switch for optically ‘on’ state. . . . .	124
9.2	Measured ( $\square$ ) and simulated ( $\times$ ) Smith chart plots of ATF-10136 GaAs FET switch for ‘Off’ state. . . . .	125
9.3	Schematic of impedance transformation network for optically controlled loaded-line phase shifter. . . . .	126
9.4	MDS simulation and optimization layout for direct optically controlled loaded-line phase shifter. . . . .	127
9.5	Microstrip circuit layout for direct optically controlled loaded-line phase shifters. . . . .	128
9.6	Measured ( $\square$ ) and simulated ( $\times$ ) response for the optically controlled 30° loaded-line phase shifter. (a) Differential insertion loss. (b) Differential phase shift. . . . .	129
9.7	Measured ( $\square$ ) and simulated ( $\times$ ) response for the optically controlled 45° loaded-line phase shifter. (a) Differential insertion loss. (b) Differential phase shift. . . . .	130
10.1	Geometric configuration used to determine the drain-to-source capacitance (a) CPS Geometry. (b) Electric (—) and magnetic(- -) field distribution. . . . .	134
10.2	HFSS simulation layout for GaAs FET illustrating bounding box. . . . .	138
10.3	SEM photographs of the two different gate structures. (a) ATF-10136 interdigitated gate. (b) ATF-13136 T-type gate. . . . .	144

10.4	HFSS electric field contour plots for drain and source metallization layers per cell (all dimensions in $\mu\text{m}$ ). (a) ATF-10136 GaAs FET. (b) ATF-13136 GaAs FET. . . . .	145
10.5	'On' state ( $\square, *$ ) and 'off' state ( $\odot, \nabla$ ) resonance frequency variation with open-circuit gate stub length. . . . .	146
11.1	Circuit diagram of active inductor cascode GaAs FET arrangement with parallel feedback resistor. . . . .	150
11.2	Circuit diagram of active inductor cascode GaAs FET arrangement with GaAs FET feedback element. . . . .	150
11.3	Simplified AC lumped equivalent circuit of the active inductor configuration with feedback resistor. . . . .	152
11.4	Simplified AC lumped equivalent circuit of the active inductor configuration with common-gate GaAs FET feedback. . . . .	154
11.5	MDS simulation schematic of simplified active inductor. . . . .	157
11.6	MDS simulation schematics for GaAs FET active inductor (a) GaAs FET model schematic. (b) Active inductor schematic. . . . .	160
11.7	Simulated Smith chart plot of ATF-10136 GaAs FET-based active inductor switch. . . . .	161
11.8	MDS simulation of inductive ( $\square$ ) and capacitive ( $\odot$ ) properties of the GaAs FET active tuning element. . . . .	162
11.9	MDS simulation of resistive properties of the GaAs FET active tuning element. . . . .	162
14.1	Measured performance of ATF-35576 pseudomorphic HEMT switch in 'off' state ( $\square$ ) and optically 'on' state ( $\odot$ ). (a) Return loss. (b) Phase change upon reflection. . . . .	178
14.2	Schematic cross-section of ribbon cable structure, showing typical dimensions for optical fibre communication applications. . . . .	179
14.3	Schematic cross-section of the typical layout of a MMIC-based electro-optic microwave sensor interface. . . . .	179
B.1	Simplified schematic cross-section of a microwave GaAs MESFET. . . .	195
B.2	Optical reflection from the surface passivation layer of a GaAs FET. . .	197
B.3	Simplified schematic cross-section of a microwave GaAs MESFET. . . .	198
B.4	Schematic of stub impedance matching network for optically controlled loaded-line phase shifter. . . . .	200

# List of Tables

2.1	Chronicle of the principal developments in the optical control of microwave GaAs FET's. . . . .	10
2.2	Chronicle of the principal developments into optically controlled GaAs FET applications. . . . .	33
2.3	Chronicle of the principal developments into GaAs FET switching. . . . .	38
2.4	Performance parameters for experimental SPST and SPDT GaAs FET switches [2.89]. . . . .	41
6.1	Values for intrinsic GaAs FET switch equivalent circuit elements. . . . .	97
6.2	Circuit element values for FET package model [6.4]. . . . .	98
7.1	Rise and fall times associated with the gate photovoltaic effect in the FET switch. . . . .	110
9.1	Experimentally obtained switch data for ATF-10136 GaAs FET. . . . .	124
10.1	Principal device dimensions used to model the GaAs FET inter-electrode capacitance. . . . .	140
10.2	Principal parameters used to evaluate the GaAs FET inter-electrode capacitance. . . . .	141
10.3	Open-circuit gate stub length required for determining switch frequency operation. . . . .	143
11.1	Equivalent circuit element values for ATF-10136 GaAs FET model [11.3].	158

# Acknowledgements

I AM grateful to my director of studies, Mr. C.E. Free, for his encouragement, guidance and valuable suggestions during technical discussions which led to the development of this thesis. I wish to thank my second supervisor, Prof. J. Butcher, for his feedback on the progress of my research work and his comments on the draft thesis. Also my head of school, Prof. G.F. Goldspink, for his advice during appraisals of my work.

The efforts of the following members of staff at Middlesex University are appreciated; Mr. B. Tang for providing technical support for the simulation packages used in this investigation, Mr. R. Gledhill for his maintenance of  $\text{\LaTeX} 2_{\epsilon}$  used in the preparation of this thesis, Mr. P. Kershaw for providing SEM pictures of the FET devices, Mr. K. Bone for the use of microstrip etching facilities, Mr. L. Miraziz for his help with artwork production, Messrs. K.E. Pitt and M. Scott for their assistance with some initial work on wire bonding.

I would like to acknowledge staff at Middlesex University and Bristol Babcock Limited involved in the Teaching Company Scheme which provided some financial support for this project.

I am thankful to my family and friends who have shown an interest in my work and always provided moral support.

# Glossary

Symbol	Description	Unit
$A^*$	Modified Richardson constant	$\text{Am}^{-2}\text{K}^{-2}$
$A_G$	Gate area	$\text{m}^2$
$A_i$	Effective illuminated area	$\text{m}^2$
$B_{qi}$	Loaded-line susceptance (multiple-bit)	S
$B_{si}$	Loaded-line susceptance (single-bit)	S
$C_{ds}$	'Off' state drain-to-source capacitance	F
	Drain-to-source capacitance in GaAs FET model	F
$C_{gd}$	'Off' state gate-to-drain capacitance	F
	Gate-to-drain capacitance in GaAs FET model	F
$C_{gs}$	'Off' state gate-to-source capacitance	F
	Gate-to-source capacitance in GaAs FET model	F
$C_{dsp}$	Drain-to-source package coupling capacitance	F
$C_{gdp}$	Gate-to-drain package coupling capacitance	F
$C_{gsp}$	Gate-to-source package coupling capacitance	F
$C_g$	Gate capacitance	F
$C_p$	Oscilloscope probe capacitance	F
$C_{sub}$	Interface barrier capacitance	F
$\bar{C}$	Capacitance per unit length	$\text{Fm}^{-1}$
$E_c$	Electron energy at conduction band edge	J
$E_f$	Fermi energy	J
$E_g$	Semiconductor band-gap	J
$E_v$	Electron energy at valance band edge	J
$E_{ph}$	Photon energy	J
$I_D$	Gate Schottky junction current	A
$I_{DS}$	Drain-to-source current	A
$I_{GS}$	Gate-to-source current	A
$I_S$	Gate Schottky junction reverse saturation current	A
$I_{pc}$	Photoconductive channel current	A
$I_{ph}$	Short-circuit gate photocurrent	A

Symbol	Description	Unit
$I_{phi}$	Channel-to-substrate photocurrent	A
$J_S$	Gate Schottky junction reverse saturation current density	$\text{Am}^{-2}$
$J_{depi}$	Gate depletion region photocurrent density	$\text{Am}^{-2}$
$J_{ph}$	Short-circuit gate photocurrent density	$\text{Am}^{-2}$
$L_{DS}$	Drain-to-source inter-electrode spacing	m
$L_{GS}$	Gate-to-source inter-electrode spacing	m
$L_{GD}$	Gate-to-drain inter-electrode spacing	m
$L_D$	Drain electrode length	m
$L_G$	Gate electrode length	m
$L_S$	Source electrode length	m
$L_d$	Drain bond wire inductance	H
$L_g$	Gate bond wire inductance	H
$L_s$	Source bond wire inductance	H
$L_i$	Illuminated lateral extension of gate depletion region	m
$L_p$	Hole diffusion length	m
$N$	Channel doping density	$\text{m}^{-3}$
$N_G$	Refractive index of gallium arsenide	
$N_S$	Refractive index of silicon nitride	
$N_{ph}$	Number of photons per unit volume	$\text{m}^{-3}$
$P_{opt}$	Incident optical power per unit area	$\text{Wm}^{-2}$
$Q_g$	Charge associated with gate capacitance	C
$R$	Optical power reflectivity	
$R_G$	Gate bias resistance	$\Omega$
$R_c$	Channel resistance in GaAs FET model	$\Omega$
$R_{ch}$	'On' state active channel resistance	$\Omega$
$R_{co}$	'On' state contact resistance	$\Omega$
$R_d$	'On' state drain resistance	$\Omega$
	Drain contact resistance in GaAs FET model	$\Omega$
$R_s$	'On' state source resistance	$\Omega$
	Source contact resistance in GaAs FET model	$\Omega$
$R_{dc}$	'Off' state drain charging resistance	$\Omega$
$R_{sc}$	'Off' state source charging resistance	$\Omega$
$R_{ds}$	'Off' state drain-to-source resistance	$\Omega$
	Drain-to-source resistance in GaAs FET model	$\Omega$
$R_{ext}$	Active inductor feedback resistance	$\Omega$
$R_g$	Gate contact resistance	$\Omega$
$R_{gd}$	'On' state gate-to-drain resistance	$\Omega$

Symbol	Description	Unit
$R_{gs}$	'On' state gate-to-source resistance	$\Omega$
$R_i$	Input resistance	$\Omega$
$R_{on}$	'On' state resistance	$\Omega$
$R_{osc}$	Oscilloscope resistance	$\Omega$
$R_p$	Oscilloscope probe resistance	$\Omega$
$R_{sub}$	Substrate resistance	$\Omega$
$T$	Absolute temperature	K
$T_d$	Drain package transmission line model	
$T_g$	Gate package transmission line model	
$T_s$	Source package transmission line model	
$T_{12}$	Reverse transmission at air/Si <sub>3</sub> N <sub>4</sub> boundary	
$T_{21}$	Forward transmission at air/Si <sub>3</sub> N <sub>4</sub> boundary	
$V_{DS}$	Drain-to-source voltage	V
$V_{GG}$	Gate reverse bias voltage	V
$V_{GS}$	Gate-to-source voltage	V
$V_{GSi}$	Illuminated gate-to-source voltage	V
$V_L$	Laser diode bias voltage	V
$V_P$	Terminal pinch-off voltage	V
$V_{oc}$	Open-circuit gate voltage under illumination	V
$V_{ph}$	Gate depletion region photovoltage	V
$V_{phi}$	Channel-to-substrate depletion region photovoltage	V
$W_G$	Gate periphery	m
$X_{swi}$	Switch state reactance	$\Omega$
$Y_0$	Transmission line characteristic admittance	S
$Y_{in}$	Input admittance of active inductor	S
$Y_m$	Main loaded-line admittance	S
$Y_{si}$	Loaded-line admittance	S
$Z_0$	Transmission line characteristic impedance	$\Omega$
$Z_{in}$	Input impedance of active inductor	$\Omega$
$Z_m$	Main loaded-line impedance	$\Omega$
$Z_{oc}$	Open-circuit stub impedance	$\Omega$
$Z_p$	Oscilloscope probe impedance	$\Omega$
$Z_s$	Transformation stub impedance	$\Omega$
$Z_{swi}$	Switch state impedance	$\Omega$
$a$	Thickness of recessed GaAs epitaxial layer	m
$a_e$	Thickness of unrecessed GaAs epitaxial layer	m
$c$	Velocity of light in a vacuum	ms <sup>-1</sup>

Symbol	Description	Unit
$c_p$	Circuit parameter	
$c_r$	Circuit response	
$f$	Frequency	Hz
$f_T$	FET current gain cut-off frequency	Hz
$f_r$	Switch resonance frequency	GHz
$g_m$	Microwave transconductance	S
$g_p$	Electron-hole pair generation rate	$\text{m}^{-3}\text{s}^{-1}$
$h$	Planck's constant	Js
	Microstrip substrate height	m
$i_{ext}$	Feedback current of active inductor	A
$i_{in}$	Input current of active inductor	A
$k$	Boltzmann's constant	$\text{JK}^{-1}$
$k_{ds}$	Drain-to-source elliptic integral argument	
$k_{ds1}$	Drain-to-source elliptic integral argument	
$l_g$	Open-circuit gate stub length	mm
$l_{oc}$	Open-circuit correction length	m
$l_{pas}$	Thickness of silicon nitride passivation layer	m
$n$	Ideality factor	
$q$	Electronic charge	C
$p$	Hole density	$\text{m}^{-3}$
$r$	Amplitude reflection coefficient	
$t$	Microstrip line thickness	m
	Time	s
$t_p$	Probe time constant	s
$v_c$	Controlling voltage in GaAs FET model	V
$v_{ext}$	Feedback voltage of active inductor	V
$v_{gs}$	Gate-to-source voltage	V
$v_{in}$	Input voltage of active inductor	V
$w$	Width of gate depletion region	m
	Microstrip line width	m
$w_n$	Width of undepleted channel region	m
$\Delta c_p$	Change in circuit parameter	
$\Delta c_r$	Change in circuit response	
$\Delta n$	Light generated excess electron density	$\text{m}^{-3}$
$\Delta p$	Light generated excess hole density	$\text{m}^{-3}$
$\Delta\phi$	Phase shift	degrees
$\Gamma$	Total optical reflection coefficient	

Symbol	Description	Unit
$\Gamma_1$	Optical reflection at air/Si <sub>3</sub> N <sub>4</sub> boundary	
$\Gamma_2$	Optical reflection at Si <sub>3</sub> N <sub>4</sub> /air boundary	
$\Gamma_3$	Optical reflection at Si <sub>3</sub> N <sub>4</sub> /GaAs boundary	
$\Phi_0$	Surface photon flux density	m <sup>-2</sup> s <sup>-1</sup>
$\alpha$	Optical absorption coefficient	m <sup>-1</sup>
$\beta$	Phase propagation constant	radm <sup>-1</sup>
$\epsilon_0$	Permittivity in a vacuum	Fm <sup>-1</sup>
$\epsilon_{eff}$	Effective relative permittivity	
$\epsilon_r$	Relative permittivity	
$\lambda$	Wavelength of incident light	m
$\lambda_c$	Cut-off wavelength of incident light	m
$\lambda_s$	Microstrip wavelength	m
$\mu_0$	Low-field drift mobility	m <sup>2</sup> s <sup>-1</sup> V <sup>-1</sup>
$\nu_p$	Phase velocity	ms <sup>-1</sup>
$\nu_{sat}$	Saturation velocity	ms <sup>-1</sup>
$\omega$	Angular frequency	rads <sup>-1</sup>
$\phi_B$	Built-in potential of a Schottky-barrier junction	V
$\rho$	Reflection coefficient	
$\rho_c$	Specific contact resistance	$\Omega$ m
$\theta_0$	Electrical length of 50 $\Omega$ line	degrees
$\theta_S$	Electrical length of silicon nitride passivation layer	degrees
$\theta_m$	Electrical length of main loaded-line	degrees
$\theta_{oc}$	Electrical length of open-circuit stub	degrees
$\theta_s$	Electrical length of transformation stub	degrees
$\tau_m$	Transconductance phase delay	s
$\tau_n$	Electron lifetime	s
$\tau_p$	Hole lifetime	s

# Physical Constants

Quantity	Symbol	Value
Angstrom unit	Å	1 Å = $10^{-10}$ m
Modified Richardson constant	$A^*$	8.2 $\text{Acm}^{-2}\text{K}^{-2}$
Boltzmann constant	$k$	$1.38066 \times 10^{-23}$ $\text{JK}^{-1}$
Electronic charge	$q$	$1.60218 \times 10^{-19}$ C
Electron volt	eV	1 eV = $1.60218 \times 10^{-19}$ J
Permittivity in vacuum	$\epsilon_0$	$8.85418 \times 10^{-12}$ $\text{Fm}^{-1}$
Relative permittivity in GaAs	$\epsilon_r$	13.1
Planck's constant	$h$	$6.62617 \times 10^{-34}$ Js
Velocity of light in a vacuum	$c$	$2.99792 \times 10^8$ $\text{ms}^{-1}$
Low-field drift mobility in GaAs	$\mu_0$	2500 $\text{cm}^2\text{s}^{-1}\text{V}^{-1}$

# Acronyms

Abbreviation	Definition
CG	Common-gate
CPS	Coplanar stripline
CPW	Coplanar waveguide
DH	Double heterostructure
DPST	Double pole, single throw
DPDT	Double pole, double throw
EM	Electro-magnetic
FET	Field-effect transistor
HBT	Hetero-junction bipolar transistor
HEMT	High electron mobility transistor
HFSS	High-frequency structure simulator (HP 85180A)
MAG	Maximum available gain
MDS	Microwave and RF design systems (HP 85150B)
MESFET	Metal-semiconductor field-effect transistor
MIC	Microwave integrated circuit
MMIC	Monolithic microwave integrated circuit
NEP	Noise equivalent power
OEIC	Optoelectronic integrated circuit
OMMIC	Optical microwave monolithic integrated circuit
OPFET	Optical field-effect transistor
PBT	Permeable base transistor
PHEMT	Pseudomorphic high electron mobility transistor
SEM	Scanning electron microscope
SPST	Single pole, single throw
SPDT	Single pole, double throw
TEM	Transverse electro-magnetic
2-DEG	Two-dimensional electron gas
3-D	Three-dimensional

# Chapter 1

## Introduction

OVER the past decade major advances have been made in the fabrication of monolithic microwave integrated circuits (MMIC's), permitting a variety of microwave circuits and sub-systems to be implemented in a monolithic format. Concurrently, there has been a considerable amount of progress in the development of optical systems based upon optoelectronic devices such as laser diodes, photo-detectors and modulators. In their development, MMIC's and monolithic optical components were considered as two separate disciplines. However, due to advances in the fabrication of microwave and photonic devices and since both technologies use identical materials and processes based upon gallium arsenide (GaAs) and are therefore compatible, there is considerable current interest in their interaction. The integration of microwave and optical devices as optical microwave monolithic integrated circuits (OMMIC's) is imminent and will inevitably have its greatest impact on the communications industry, where the demand for highly integrated, high performance and reliable systems becomes ever greater.

Various investigations, particularly in the early 1980's [1.1–1.6], demonstrated that the direct optical control of microwave signals was feasible and that a number of useful microwave circuit functions could be achieved using this principle. These included oscillator tuning, oscillator locking and the gain control of amplifiers, primarily for the use in optical transmission in phased-array radar systems [1.7–1.10]. These circuits rely on GaAs metal-semiconductor field-effect transistors (MESFET's)<sup>†</sup> as the principal element for optically controlling the microwave signals, due to their widespread use in MMIC's. The main incentives for developing these types of circuit were to achieve isolation from the control signal, a faster response time and to permit a greater degree of circuit integration than had hitherto been possible.

In many industrial processes there is a need to monitor such quantities as displacement, temperature, flow rate, liquid level and chemical composition. Ideally, the measurement technique should be reliable, robust, corrosion resistant, intrinsically safe and free from external interference. An increasing number of these requirements are

---

<sup>†</sup>In this thesis the term FET is used when referring to microwave MESFET's.

being met by using optical techniques, with optical fibre sensors providing distinct advantages over their electrical counterparts. In addition to the individual sensing element, many industrial sensing environments require a distributed sensor network, whereby information from a number of remote sensors is relayed to a central control unit. Two techniques currently exist for conveying the sensor information to a central control unit. The first consists of a hard-wired link whereby a physical connection exists between each sensor and the central control unit. In some cases such a system is not practical or cost-effective due to the difficulty of routing large amounts of cable. A second technique, which overcomes the problems associated with the hard-wired link, uses wireless telemetry techniques to convey the information. In such a system each sensor is connected via a radio link to a central control unit, therefore removing the cost associated with the cabling and its distribution. At present, such radio sensors combine a conventional electrical sensor with a microwave transmitter, with the output from the sensor modulating the microwave carrier signal. Currently none of these radio sensors has been combined with optical sensors, although one might expect that this could be achieved by simply converting the optical information to an electrical equivalent and using this to control the modulation stages of a microwave transceiver. This is feasible with current optical sensors, which invariably convert the optically sensed data to an electrical equivalent prior to the signal processing stages. In terms of the radio sensor application, the optical-to-electrical conversion stage is unnecessary and is actually a drawback in terms of the overall circuit complexity, cost and performance. Therefore, in this investigation a novel technique for achieving direct optical control of a microwave transceiver is examined, where the optical signal directly controls a function within a microwave transceiver. This was to be achieved through the development of a novel direct optically controlled microwave switch, forming the basis of an optically controlled microwave phase modulator. In addition, it was intended that this device would permit the integration of the optical and microwave circuit functions such that a single chip or ‘drop-in’ sensor could be developed, making such a device versatile in its sensing application. To permit such a level of integration, it is necessary for the optical-to-microwave devices to employ direct optical control as opposed to the indirect methods of optical control [1.9, 1.11–1.13] that have previously been considered in the literature. A conceptual block diagram of the optically controlled microwave transceiver applied within a radio sensor network is depicted in Figure 1.1.

The main body of this work addresses itself to the characterization of microwave GaAs FET switches under direct optical control, as well as conventional electrical control. A review of the literature is included in Chapter 2 and addresses current methods of achieving general optical control in GaAs FET’s, electrical control in GaAs FET switches and electrical control in phase shifters. The static photo-effects in microwave GaAs FET’s are considered in Chapter 3 with a particular bias towards photovoltaic

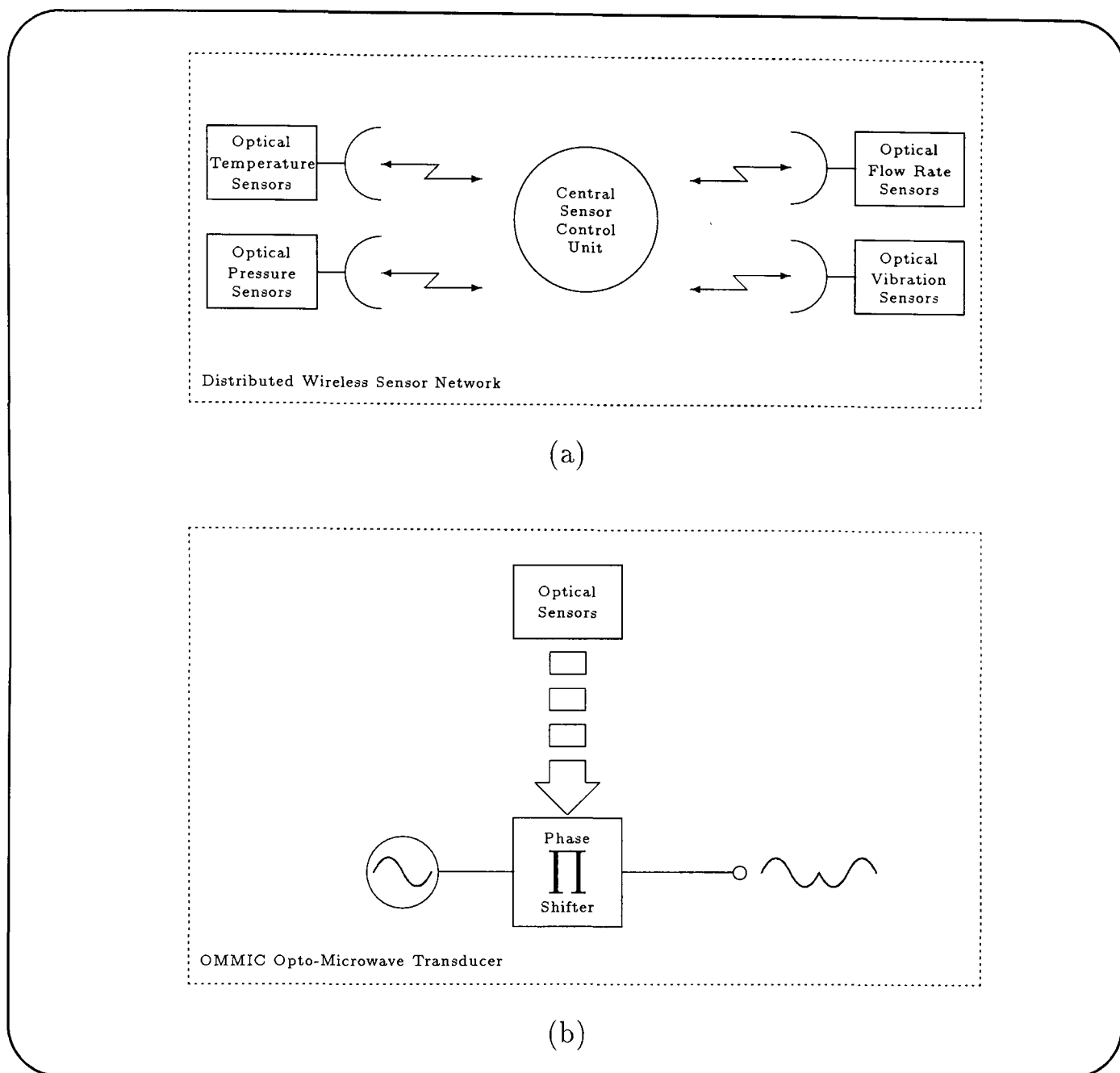


**Figure 1.1:** Conceptual diagram of an optically controlled radio sensor network. (a) Distributed wireless sensor network. (b) Integrated opto-microwave transducer.

effects associated with the gate depletion region of the FET [1.14]. In addition, Chapter 3 includes experimental results relating to the verification of previous work on the gate depletion region photovoltaic effect. The GaAs FET responsivity to switched and modulated optical stimuli is considered in Chapter 4, along with some recent developments in the modelling of the dynamic optical response of GaAs FET's.

The preceding chapters provide a foundation upon which the novel aspects of this investigation are based. The analytical work begins with the design and modelling of a reflective microwave GaAs FET switch, described in Chapter 5, and this is combined with the optically controlled GaAs FET concepts of Chapter 3 in the realization of an optically controlled microwave switch. The operation of a novel microwave reflective GaAs FET switch subjected to static optical control is discussed in Chapter 6. Simulated and measured results for the switching characteristics of the direct optically controlled GaAs FET switch [1.15] are presented in Chapter 6. This work is extended

in Chapter 7 to permit the modelling of the transient response of the optically controlled switch [1.16], enabling a comparison between measured and simulated results for the GaAs FET under switched optical control. The experimental and modelling steps presented in Chapters 6 and 7 are applied to GaAs FET switches incorporating two very different gate structures, under both optical and conventional electrical control [1.16].

Using the results for the optically controlled microwave GaAs FET switch, a direct optically controlled microwave phase shifter is described in Chapter 9, based upon the well-established theory for electrically controlled diode phase shifters examined in Chapter 8. In addition, Chapter 9 presents simulated and experimental results for a single-bit  $30^\circ$  loaded-line phase shifter with both direct optical and conventional electrical control of the GaAs FET switching element [1.15].

In considering the simulation of the GaAs FET microwave switch, it was found that previously published models were inadequate in predicting the microwave performance of the switch in either state. Thus Chapter 10 includes modified models to predict accurately the microwave switching characteristics of the GaAs FET and in particular, describes a new method for evaluating the inter-electrode capacitance of the FET using 3-dimensional field simulation software [1.17]. Furthermore, the improved model for the GaAs FET microwave switch enables the occurrences of resonances in either, or both, switching states to be predicted accurately, resulting in a switch that can be configured to operate over the frequency range 1 to 20 GHz [1.17].

The circuits described in this thesis establish the principle of direct optical control of a microwave GaAs FET switch and phase shifter using hybrid circuits and commercially available packaged GaAs FET's. However, a design strategy was chosen so that there could be a straightforward extension to monolithic layouts if required, and this is discussed in Chapter 11. The thesis is concluded in Chapter 13, with a survey of the theoretical and experimental results presented in Chapter 12. Suggestions for future work and a discussion of the potential integration of the optical sensor with the microwave circuits described is considered in Chapter 14.

# References

- [1.1] C. Baack, G. Elze, and G. Walf, "GaAs M.E.S.F.E.T.: A high-speed optical detector," *Electron. Lett.*, vol. 13, p. 193, Mar. 1977.
- [1.2] J. C. Gammel and J. M. Ballantyne, "The OPFET: A new high speed optical detector," in *Proc. IEDM Tech. Dig.*, pp. 120–123, 1978.
- [1.3] J. J. Pan, "GaAs MESFET for high-speed optical detection," in *Proc. 22nd SPIE Int. Tech. Symp.*, vol. 150 of *Laser & Fiber Optics Communications*, (Monterey, CA), pp. 175–184, 1978.
- [1.4] J. Graffeuil, P. Rossel, and H. Martinot, "Light-induced effects in GaAs F.E.T.s," *Electron. Lett.*, vol. 15, pp. 439–441, July 1979.
- [1.5] A. A. de Salles, "Optical control of GaAs MESFET's," *IEEE Trans. on Microwave Theory & Tech.*, vol. MTT-31, pp. 812–820, Oct. 1983.
- [1.6] P. R. Herczfeld, A. S. Daryoush, A. Rosen, P. Stabile, and V. M. Contarino, "Optically controlled microwave devices and circuits," *RCA Review*, vol. 46, pp. 528–551, Dec. 1985.
- [1.7] A. A. A. de Salles, *Optical control of microwave field effect transistors*. Ph.D. thesis, Univ. of London, 1982.
- [1.8] R. N. Simons and K. B. Bhasin, "Analysis of optically controlled microwave/millimeter-wave device structures," *IEEE Trans. Microwave Theory Tech.*, vol. MTT-34, pp. 1346–1355, Dec. 1986.
- [1.9] P. R. Herczfeld, A. Paoletta, A. Daryoush, W. Jemison, and A. Rosen, "Optical phase and gain control of a GaAs MMIC transmit-receive module," in *Proc. Eur. Microwave Conf.*, (Stockholm), pp. 831–836, Sept. 1988.
- [1.10] A. Paoletta and P. R. Herczfeld, "Optical control of a GaAs MMIC transmit/receive module," in *Proc. IEEE MTT-S Int. Microwave Symp. Dig.*, pp. 959–962, May 1988.
- [1.11] A. Paoletta and P. R. Herczfeld, "Optical gain control of a GaAs MMIC distributed amplifier," *Microwave Optical Tech. Lett.*, vol. 1, pp. 13–16, Mar. 1988.

- 
- [1.12] W. D. Jemison, T. Berceli, A. Paoella, P. R. Herczfeld, D. Kasemset. and A. W. Jacomb-Hood, "Optical control of a digital phase shifter," in *Proc. IEEE MTT-S Int. Microwave Symp. Dig.*, pp. 233–236, 1990.
- [1.13] A. Paoella, A. Madjar, P. R. Herczfeld, and D. Sturzebecher, "Optically controlled GaAs MMIC switch using a MESFET as an optical detector," in *Proc. IEEE MTT-S Int. Microwave Symp. Dig.*, pp. 941–944, 1990.
- [1.14] S. J. Rossek and C. E. Free, "Optical control of microwave signals using GaAs FETs," *IEE Electron. Commun. Eng. J.*, vol. 6, pp. 21–30, Feb. 1994.
- [1.15] S. J. Rossek and C. E. Free, "Optically controlled microwave switching and phase shifting using GaAs FET's," *IEEE Microwave Guided Wave Lett.*, vol. 5, pp. 81–83, Mar. 1995.
- [1.16] S. J. Rossek and C. E. Free, "The transient response and switching performance of direct optically controlled microwave GaAs FET's." Submitted for Publication to IEEE Trans. on MTT.
- [1.17] S. J. Rossek and C. E. Free, "Methods for accurately evaluating interelectrode capacitance and frequency tuning range in microwave GaAs FET switches," *Electron. Lett.*, vol. 31, pp. 764–765, Apr. 1995.

# Chapter 2

## Literature Review

### Contents

---

<b>2.1</b>	<b>Introduction . . . . .</b>	<b>7</b>
<b>2.2</b>	<b>Optically Controlled Microwave GaAs FET's . . . . .</b>	<b>9</b>
2.2.1	Static Optical Response of Microwave GaAs FET's . . . . .	11
2.2.2	Dynamic Optical Response of Microwave GaAs FET's . . . . .	21
<b>2.3</b>	<b>Optically Controlled GaAs FET Devices . . . . .</b>	<b>32</b>
2.3.1	Optically Controlled Amplification . . . . .	32
2.3.2	Optical Injection-Locking and Frequency Tuning of Oscillators	34
2.3.3	Optically Controlled Phase Shifting . . . . .	35
2.3.4	Optically Controlled Mixing . . . . .	35
2.3.5	Optically Controlled Switching . . . . .	36
2.3.6	Optical Detection . . . . .	37
<b>2.4</b>	<b>GaAs FET-Based Switches . . . . .</b>	<b>38</b>
<b>2.5</b>	<b>GaAs FET-Based Phase Shifters . . . . .</b>	<b>42</b>
<b>2.6</b>	<b>MMIC and OMMIC Technology . . . . .</b>	<b>43</b>

---

### 2.1 Introduction

THE amalgamation of monolithic optical and microwave devices as OMMIC's has been an active area of research for almost two decades and had even been envisaged prior to the commercial availability of MMIC technology. Despite research efforts, the delay in the availability of a commercial OMMIC process probably stems from the distinction that existed between the semiconductor device physicist and microwave design engineer. It was not until the mid-1980's that these two traditionally separate

disciplines began to merge as academic and commercial establishments experienced increased accessibility to foundry processes and bridged the interdisciplinary gap between the concepts of optics and microwaves. These research efforts have led, for example, to the monolithic integration of laser diodes and photodetectors with microwave GaAs FET's [2.1] and the development of microwave fibre optic links [2.2,2.3]. This merging has its roots in the development of phased-array radar systems and indeed this has been the main incentive for research into optical and microwave interactions over the past 18 years. There are many situations, both military and commercial, where it is necessary to be able quickly to manipulate a microwave radar beam. Typical phased-arrays may contain hundreds or even thousands of radiating elements in order to produce a controllable and well-defined pencil beam. Difficulties can arise both in the control of the phases of the currents feeding these elements and in the distribution of signals to the various elements. Optical techniques can be used to mitigate these difficulties.

The large number of radiating elements in a phased-array dictates that the beam-forming networks which introduce the digital control signals should be small, light-weight and immune from electrical interference. Since the radiating elements can be implemented effectively with MMIC technology, the microwave signals can be controlled easily through optical fibre/MMIC monolithic interfaces. The distribution of microwave signals to the elements may also present problems due to size and interference between closely spaced feed lines. A conventional waveguide feed distribution system would be far too cumbersome a solution and coaxial cables, although they offer a lighter and more flexible solution, do not yield the precise transmission phase properties and low loss which are essential for this application. Thus the use of an optical-fibre distribution system, in which an optical signal is modulated by the microwave signal, not only meets the requirements of the beam-forming networks, but also allows both the microwave and control signals to be transmitted using a single optical network. The technique of signal distribution in phased-array radars is illustrated in Figure 2.1 [2.4].

The focus of current research efforts into OMMIC phased-array radar systems has been a consequence of the present industrial MMIC programme being orientated towards military applications with very specific, short term goals. As pointed out by Herczfeld [2.5], changes in the engineering world demand that a broader approach needs to be taken to the development of optical and microwave interactions, to provide more flexible programmes which will serve consumer applications. The innovative application of optical and microwave interactions in the development of a distributed sensor system, as considered in this present research, has not been addressed in the literature and represents the first move towards commercial OMMIC-based systems. Despite this potential commercial application, it has been established that the novel optical-to-microwave transducer that forms the basis of the transceiver section of the opto-microwave sensor developed during this investigation, has distinct similarities to

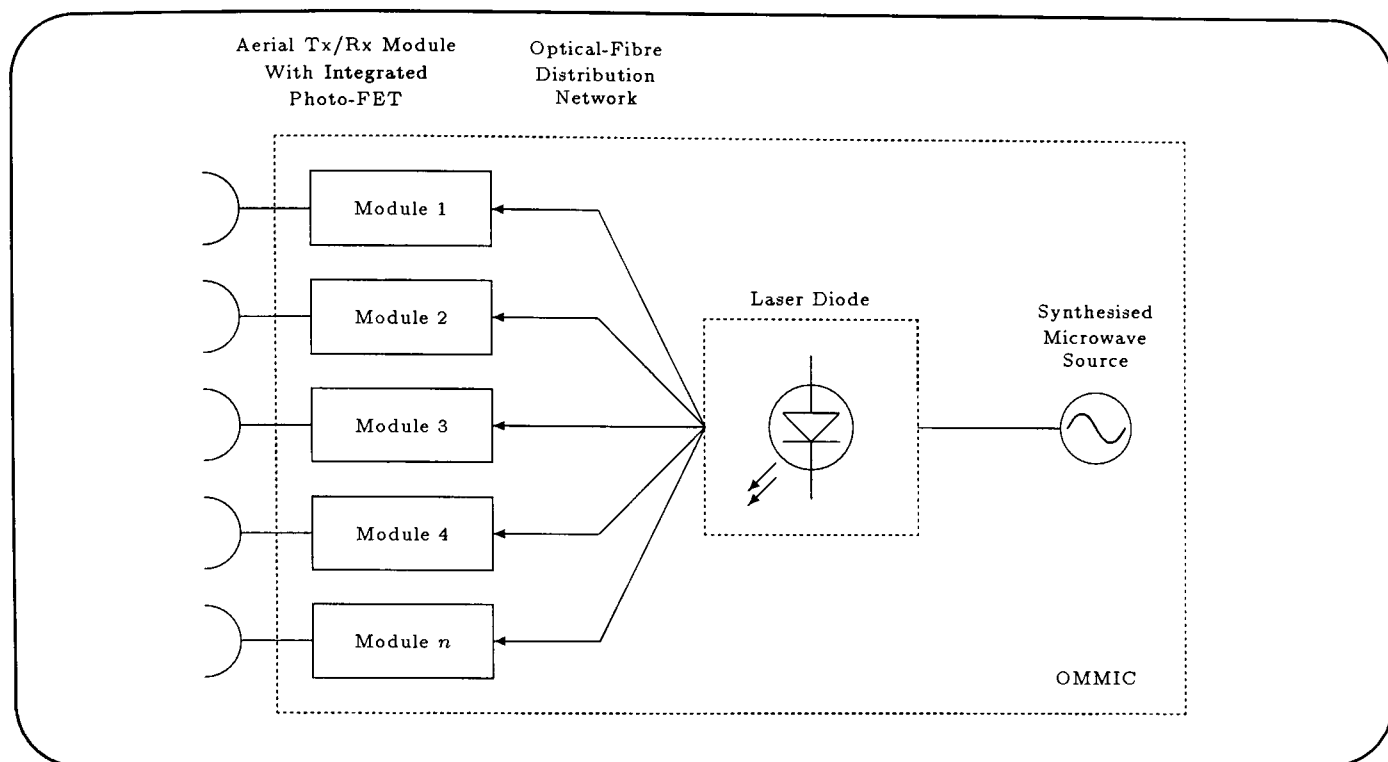


**Figure 2.1:** Schematic of an OMMIC-based phased-array antenna system incorporating optoelectronic microwave signal generation, distribution and detection [2.4].

the optically controlled gain and phase requirements of the transceiver of a phased-array radar system.

During this investigation a number of areas of the literature were identified and reviewed in order to assess the state-of-the-art technology available with monolithic optical and microwave circuits. Thus, this literature review has been divided into the following subject areas:

- Optically controlled microwave GaAs FET's
- Optically controlled GaAs FET Devices
- GaAs FET-based switches
- GaAs FET-based phase shifters
- MMIC and OMMIC technology

## 2.2 Optically Controlled Microwave GaAs FET's

The sensitivity to light of low-frequency transistors was recognized at an early stage and such opto-transistors lend themselves to a variety of general optoelectronic applications. In contrast, the observation of optically-induced effects in microwave transistors was first published in the literature by Baack *et al.* [2.6] in 1977, almost a decade after the establishment of the FET as a suitable transistor for use at microwave frequencies. Since then, research and development into the interaction between photonics and

microwaves has intensified, with the notable outcomes summarized chronologically in Table 2.1.

Optical Interactions in Microwave GaAs FET's		
Dates	Principal Outcomes	Principal References
⇒ 1980	<ul style="list-style-type: none"> <li>• initial observations of optical control in microwave GaAs FET's</li> <li>• measurement of static &amp; dynamic photo-response</li> <li>• controversy over predominant photo-effect</li> </ul>	[2.6–2.12]
1981 ⇒ 1985	<ul style="list-style-type: none"> <li>• theoretical and experimental study of static gate (external) photovoltaic effect</li> <li>• theoretical study of dynamic photo-effects</li> <li>• establishment of predominant static &amp; dynamic photo-effects</li> </ul>	[2.13–2.17]
1986 ⇒ 1990	<ul style="list-style-type: none"> <li>• observation of optical control in microwave HEMT's</li> <li>• observation of photo-avalanche effects</li> <li>• theoretical and experimental study of trapping effects in opto-FET's</li> <li>• review of optical control in microwave semiconductors</li> </ul>	[2.18–2.23]
1991 ⇒ 1995	<ul style="list-style-type: none"> <li>• theoretical and experimental study of photo-effects in HEMT's</li> <li>• theoretical and experimental study of the GaAs FET under continuous, sinusoidal and switched optical illumination</li> </ul>	[2.24–2.30]

**Table 2.1:** Chronicle of the principal developments in the optical control of microwave GaAs FET's.

The optical control of microwave devices for OMMIC applications has tended to be focussed upon optically controlled FET's, due to their widespread application in MMIC's. The use of conventional styles of photodetection, such as *p-i-n* and avalanche photodiodes, has been integrated within MMIC technology, but requires additional fabrication stages and therefore detracts from the compatibility benefits of commercially available monolithic microwave and optical technologies. In particular, the optical con-

trol of metal-semiconductor field-effect transistors (MESFET's) has been the subject of the majority of current publications to date. Although, the improved microwave performance and increasing commercial availability of high electron mobility transistors (HEMT's) and heterojunction bipolar transistors (HBT's) has led to some more recent publications dedicated to the optical responsivity of these devices. Investigations relating to optical control in microwave transistors can be classified broadly into those relating to the static and dynamic optical response.

### 2.2.1 Static Optical Response of Microwave GaAs FET's

The static optical response of GaAs FET's refers to the DC and microwave (i.e.  $S$ -parameter) properties under continuous (static) optical illumination. Since the microwave and DC parameters are related, results presented in the literature often refer to both optically-induced DC and microwave parameter variations.

Optically-induced variations in the  $S$ -parameter performance of a microwave GaAs FET were first observed and measured by Pan [2.7] using  $1\ \mu\text{m}$  gate length MESFET's, in common-gate and common-source arrangements used to provide optical detection. Pan measured the magnitude of the  $S_{21}$ -parameter for the common-gate configuration over the frequency range 1 to 2 GHz. An approximate 15 dB increase in the magnitude of the  $S_{21}$ -parameter was reported at mid-band when the FET was illuminated by an incandescent light source. For the common-source configuration, Pan also measured the complete set of  $S$ -parameters over the frequency range 20 to 1300 MHz and for two different drain and gate bias conditions, with the magnitude of  $S_{21}$  showing the greatest variation between dark and illuminated states. The  $S_{21}$ -parameter measurements were extended to cover the frequency range 7 to 10.5 GHz, under incandescent and infra-red illumination. With incandescent illumination the FET showed an approximately 2.5 dB increase in the magnitude of  $S_{21}$  at mid-band, compared with the infra-red illumination, while the phase of  $S_{21}$  showed little variation between dark and illuminated conditions with either light source. Pan suggested that the observed changes in the illuminated GaAs FET's were due to photoconductivity changes in the source-to-gate and drain-to-gate regions, and depletion layer width variation with light intensity. Variations in the device  $S$ -parameters under different illumination were explained by considering the optically-induced variations in the intrinsic elements of the standard small-signal lumped equivalent circuit model for the GaAs FET.

Optically-induced DC variations were reported first by Graffeuil *et al.* [2.8], who illuminated a  $1\ \mu\text{m}$  gate length GaAs FET with a 5 mW light-emitting diode (LED). They observed changes in the FET pinch-off voltage which were attributed to electron-hole generation in the illuminated space-charge layer beneath the gate (i.e. gate depletion region). This change in the pinch-off voltage was then used to establish the variation in the transconductance of the GaAs MESFET under illumination. By comparing

measured and computed values, they established that a 10% variation of transconductance and a 25% variation of drain current was possible for a light intensity variation as low as 0.2 mW. For a 10% variation in the gate-to-source and drain-to-source capacitances of the MESFET they deduced that a light intensity variation of greater than 2 mW was needed. They concluded that the photo-effects observed in their GaAs FET's were photovoltaic phenomena.

Edwards [2.9] measured the change in the drain current-voltage characteristics of an illuminated microwave GaAs FET structure, with and without a gate electrode. The removal of the gate electrode eliminated the effect of the gate Schottky barrier and this was used to demonstrate photovoltaic effects occurring between the substrate and the *n*-type epitaxial channel regions. The devices were illuminated by the focussed output from a helium-neon (HeNe) laser and by floodlight from the internal illumination of a microscope. With a resistance of 47  $\Omega$  at the gate of the FET, a photosensitivity of approximately 1300  $\text{AW}^{-1}$  was measured. The photocurrent gain was found to be slightly higher with the gate of the FET open or negatively biased. The use of the two-terminal FET, rather than a normal gated FET, had the advantage that more light was able to reach the active channel and channel-to-substrate interface regions because of the absence of the gate metal. By increasing the light intensity from 0.01 to 100  $\mu\text{W}$  the variation in the substrate voltage and drain current (backgating effect) was measured. From this, Edwards showed that for low light levels the substrate photovoltage exhibited a logarithmic increase with light intensity.

The most significant study of the 1980's into the static optical response of microwave GaAs MESFET's was made by de Salles and Forrest [2.31], who carried out an experimental and theoretical characterization of the photo-response of the MESFET. This work investigated the photo-response variation as a function of light intensity and bias conditions, with an emphasis on the gate depletion region photovoltaic effect. De Salles [2.13] derived an expression for the short-circuit gate photocurrent density in the MESFET given by

$$J_{ph} = q(1 - R)\Phi_0 \left[ \frac{\alpha^3 L_p^2 w_n e^{-\alpha w}}{\alpha^2 L_p^2 - 1} + \alpha w \right] \quad (2.1)$$

where  $R$  is the surface optical reflectivity,  $q$  the electronic charge,  $\Phi_0$  the photon flux density at the surface,  $\alpha$  the optical absorption coefficient,  $L_p$  the minority-carrier (hole) diffusion length,  $w_n$  the width of the undepleted channel region and  $w$  the width of the gate depletion region. The combination of the photocurrent and a large resistance ( $\geq 50 \text{ k}\Omega$ ), placed at the gate of the FET, generated a large photovoltaic effect which de Salles [2.13, 2.32] approximated to an open-circuit photovoltage given by

$$V_{oc} = \frac{nkT}{q} \ln \frac{J_{ph}}{J_S} \quad (2.2)$$

where  $n$  is the ideality factor,  $k$  Boltzmann's constant and  $J_S$  the reverse saturation current density of the gate Schottky barrier junction. By illuminating a 0.5  $\mu\text{m}$

gate length MESFET with a 2 mW variable output from a double-heterostructure GaAs/GaAlAs laser diode focussed to a 50  $\mu\text{m}$  spot diameter, de Salles measured the following responses.

- Current-voltage characteristics for the Schottky barrier gate junction at various light intensity levels.
- Drain current-voltage characteristics of the FET with a fixed light level, under various reverse gate bias conditions and with a gate bias resistances of 1 k $\Omega$  and 1 M $\Omega$ .
- Schottky barrier photovoltage under various light levels, gate reverse bias conditions and with a gate bias resistance of 1 M $\Omega$ .

From these results de Salles was able to obtain very good agreement between the measured and calculated DC photo-responses of the FET due to the gate depletion region photovoltaic effect. Furthermore, by including a large gate bias resistance ( $\geq 50$  k $\Omega$ ) de Salles showed that the photo-response at the gate of the FET could be likened to controlling the gate of the FET electrically. Using the photocurrent expression to predict the change in gate voltage due to the gate depletion region photovoltaic effect, de Salles was able to estimate the  $S$ -parameter variations under optical control over the frequency range 2 to 8 GHz. These results showed very close agreement with measured values. The parasitic resistances associated with the FET equivalent model showed a decrease of about 10% in the illuminated state due to photoconductive effects. A major variation in the  $S_{21}$ -parameter was observed under illumination when the gate resistance was changed from 1 k $\Omega$  to 1 M $\Omega$ , due to the gate depletion region photovoltaic effect. No significant variations were observed in the rest of the  $S$ -parameters under similar conditions, although the transconductance and gate-to-source capacitance showed an increase of 10 to 20% with illumination. De Salles [2.13] also performed a preliminary study of the backgating effect due to optically-induced substrate current.

By assuming the gate metallization of the MESFET to be semi-transparent to light Chaturvedi *et al.* [2.33] calculated the gate depletion region photovoltage as

$$V_{ph} = \frac{kT}{q} \ln \left( \frac{p + \Delta p}{p} \right) \quad (2.3)$$

where  $\Delta p$  is the light-generated excess hole concentration and  $p$  is the equilibrium hole concentration in the active layer. The light-generated excess hole concentration was obtained from

$$\Delta p = \frac{\tau_p}{a} \left[ \frac{P_{opt} \lambda}{hc} \right] (1 - e^{-\alpha a}) \quad (2.4)$$

where  $\tau_p$  is the minority carrier lifetime,  $\lambda$  the wavelength of the incident light,  $h$  Planck's constant,  $P_{opt}$  the incident optical power per unit area and  $a$  the thickness of the active layer. From these expressions they were able to calculate the change in the drain current under illumination, although no experimental verification was presented.

The gain, drain current and  $S$ -parameter variations over the frequency range 3 to 8 GHz were measured by Mizuno [2.14], for a 0.5  $\mu\text{m}$  gate length MESFET at various light intensity levels using a fibre-coupled semiconductor laser operating at a wavelength of 829 nm. Over this frequency range the gain of the MESFET was controlled optically by increasing the light intensity from 0.01 to 0.14 mW, and electrically by decreasing the gate reverse bias, to give an approximate 20 dB change in gain. Mizuno described the optically-induced gate voltage variations as being similar to controlling the FET electrically and showed that the  $S$ -parameters varied in a similar manner under optical and electrical control.

Using a 1.3  $\mu\text{m}$  gate length MESFET illuminated by an injection laser operating at a wavelength of 827 nm, Gautier *et al.* [2.15] measured the variation in the  $S$ -parameters over the frequency range 2 to 8 GHz for various gate bias conditions and under two different light levels of 0.3 and 2 mW. They measured also variations in the DC transconductance and reverse gate current of the MESFET and attributed these changes to the photovoltaic effect within the gate Schottky junction and the photoconductive effect occurring in the active region of the channel. These results showed good agreement when compared with a unidimensional model that described the light effects on the DC transconductance of the FET.

Analytical determinations of the drain current-voltage characteristics for a GaAs MESFET, InP MESFET,  $\text{Al}_{0.3}\text{Ga}_{0.7}\text{As}/\text{GaAs}$  HEMT and GaAs permeable base transistor (PBT) under optical illumination were made by Simons and Bhasin [2.18]. By calculating the optically-induced voltage at the gate of these devices, based upon the expression given by Chaturvedi *et al.* [2.33], they observed that the  $\text{Al}_{0.3}\text{Ga}_{0.7}\text{As}/\text{GaAs}$  HEMT had the highest photosensitivity, followed by the GaAs PBT and GaAs MESFET, with the InP MESFET having the lowest photo-response. The optical gain of a normally-off MESFET was found to be a maximum if the gate bias was such that the MESFET was in the pinch-off condition. This result agreed with the previous findings of de Salles [2.13, 2.32], Mizuno [2.14] and Gautier *et al.* [2.15]. Variations in the small-signal parameters such as channel conductance, gate-to-source capacitance and transconductance were computed and compared with experimental values obtained by Sun *et al.* [2.34] and Gautier *et al.* [2.15]. In this work they considered a 1  $\mu\text{m}$  gate length GaAs MESFET with a indium tin oxide (ITO) gate metallization, transparent to visible light, illuminated by an optical power density of  $1 \text{ mWcm}^{-2}$  at a wavelength of 0.87  $\mu\text{m}$ . They calculated that the channel conductance increased by about 15% under illumination. Some discrepancies occurred between the measured and computed

results for the DC transconductance and gate-to-source capacitance but these were attributed to the simplicity of the analytical model used in their computations.

Experimental results for the optically-induced gate voltage, the increase in the drain current, the RF gain and the change in the  $S$ -parameters of a  $0.5 \mu\text{m}$   $\pi$ -gate AlGaAs/GaAs HEMT and  $0.3 \mu\text{m}$   $\pi$ -gate GaAs MESFET under optical illumination were presented by Simons [2.19]. The current-voltage characteristics of the Schottky barrier gate junction of both devices, illuminated by a laser diode with an output power of 1.5 to 1.7 mW and wavelength of  $0.83 \mu\text{m}$ , showed that the HEMT device generated a light-induced voltage at the gate of 0.57 V while the MESFET produced a voltage of just 0.24 V. These results verified previous theoretical studies by Simons and Bhasin [2.18] of the AlGaAs/GaAs HEMT and were the first results relating specifically to the gate depletion region photovoltaic effect with no external gate bias resistance. From the drain current-voltage characteristics under illumination, the GaAs MESFET showed a larger optically-induced drain current than did the AlGaAs/GaAs HEMT device and this observation was attributed to the larger gate-to-source and gate-to-drain spacings in the MESFET increasing the coupling efficiency between the incident radiation and the active layer. The measured DC transconductance was shown to be insensitive to optical illumination, with a maximum change of less than 2 mS in the illuminated state. Measured  $S$ -parameters, over the frequency range 45 MHz to 26.5 GHz, showed that  $S_{11}$ ,  $S_{22}$  and  $S_{12}$  were affected by optical illumination and that these effects were more pronounced when the devices were biased close to pinch-off. The optically-induced changes in these  $S$ -parameters were shown to be due to increases in the gate and source capacitances and decreases in the drain-to-gate feedback capacitance, gate charging resistance and the channel resistance, associated with a simplified model for the devices under optical illumination. The simplified model under optical illumination was based upon the GaAs MESFET model published by Minasian [2.35]. An increase of 0.5 to 2.0 dB in the magnitude of the  $S_{21}$ -parameter was observed for reverse gate bias levels of -0.5 and -0.95 V, respectively, although the phase showed no change under optical illumination. Using the HEMT as an optical detector, a responsivity of  $3.53 \text{ AW}^{-1}$  and a quantum efficiency of greater than 500% were recorded.

Photo-multiplication effects were demonstrated by Madjar *et al.* [2.20], when illuminating a  $0.5 \mu\text{m}$  gate length GaAs MESFET operated close to the avalanche breakdown voltage of the gate-drain Schottky barrier. For a drain voltage of 0.0 to 8.0 V and with the gate biased at pinch-off, they measured the drain current response of the FET when illuminated by a quartz-halogen lamp with an optical output power of  $45 \mu\text{W}$  and a wavelength of  $0.8 \mu\text{m}$ . This showed that a more pronounced increase in drain current for the illuminated state over that for unilluminated (dark) conditions occurred as the gate-drain junction approached the critical field for avalanche breakdown. Under these conditions, the photo-induced carriers are in a very high electric field environ-

ment and therefore highly energetic. These excess carriers cause secondary emissions by collisions with the crystal atoms, thereby leading to multiplication of the current, with the observed phenomenon being an optically-induced avalanche effect. The photo-multiplication factor for the MESFET was measured at approximately 12.33. When used as a photodetector the photo-multiplication can enhance the optical response of the device. However, caution is required to avoid premature avalanche breakdown. They also evaluated the effect of the silicon dioxide/silicon nitride ( $\text{SiO}_2/\text{Si}_3\text{N}_4$ ) surface passivation on the coupling efficiency of the incident light beam and estimated the reflection coefficient to be  $\frac{1}{3}$ , which is consistent with the poor coupling observed by other investigators.

A study of the DC optical response of a  $0.5 \mu\text{m}$   $\text{Al}_{0.3}\text{Ga}_{0.7}\text{As}/\text{GaAs}$  HEMT was presented by de Salles and Romero [2.24]. This followed a similar pattern to de Salles' earlier investigation of GaAs MESFET's [2.32]. They compared calculated and experimental results for the drain current-voltage characteristics of the HEMT incorporating photoconductive and photovoltaic effects. The photoconductive effect was associated with photon absorption only in the GaAs layer of the HEMT which resulted in an increase in the electron concentration in the 2-dimensional gas (2-DEG) channel. This effect was dominant when the incident photon energy was equal to or greater than the GaAs band-gap but smaller than the AlGaAs band-gap, with the electron concentration in the 2-DEG channel due to illumination estimated as

$$\Delta n = \frac{\tau_n}{a} \left[ \frac{P_{opt}\lambda}{hc} \right] (1 - e^{-\alpha a}) \quad (2.5)$$

where  $\tau_n$  is the electron lifetime and  $a$  the thickness of the GaAs layer. An approximate 5 mA increase in the drain current of the HEMT was observed due to the photoconductive effect under three different gate bias conditions, which was in very close agreement with calculated results. The HEMT was illuminated by a HeNe laser source with an incident optical power of 0.2 mW and a wavelength of 632.8 nm, focussed to a  $50 \mu\text{m}$  diameter spot. The photovoltaic effect occurred as a result of photons absorbed in the AlGaAs layer and only when a high bias resistor was present at the gate of the HEMT. For this to take place, the photon energy of the incident light had to be equal to or greater than the AlGaAs band-gap. The use of a large gate resistor ( $1.2 \text{ M}\Omega$ ) meant that the change in the drain current could be estimated in an almost identical manner to that used previously by de Salles to model the gate depletion region photovoltaic effect in MESFET's [2.13, 2.32]. The drain current-voltage characteristics for the photovoltaic effect was measured with  $1.2 \text{ M}\Omega$ ,  $100 \text{ k}\Omega$  and  $0 \Omega$  gate resistors and under three different gate bias conditions. These showed good agreement with calculated results obtained from the the expressions of Chaturvedi *et al.* [2.33]. As with the MESFET, the maximum photovoltaic effect was obtained when the HEMT was biased close to its pinch-off condition and with the inclusion of the  $1.2 \text{ M}\Omega$  gate resistance. Using a simplified small-signal model for the HEMT and standard expressions

for some of the small-signal parameters of this model, they estimated the change in the transconductance, gate-to-source capacitance and drain-to-source resistance of the HEMT under both photo-effects. Under the photoconductive effect, no changes were predicted in the transconductance and gate-to-source capacitance, although the drain-to-source resistance was expected to be reduced by the optical illumination. Based upon this they predicted that there would be a negligible change in the  $S_{11}$ ,  $S_{12}$  and  $S_{21}$  parameters and a reasonable variation in  $S_{22}$  under photoconductive effects. Under photovoltaic control they anticipated an increase in both the gate-to-source capacitance and transconductance as a result of optically-induced gate voltage variations.

The wavelength dependence of the photo-response of a HEMT was measured by Romero *et al.* [2.36]. They established that photoconductive effects dominated the optical response at a wavelength of  $0.85 \mu\text{m}$ , and that at  $0.633 \mu\text{m}$  the photovoltaic effect prevails. They explained the occurrence of these photo-effects in HEMT's in a similar way to de Salles and Romero [2.24].

An analytical model for an ion-implanted GaAs opto-FET (OPFET) was developed by Pal and Chattopadhyay [2.37] by considering photovoltaic effects in the gate Schottky barrier junction of a FET. They considered optical radiation through a transparent or semi-transparent gate of the FET, which resulted in the following photo-effects:

- electron-hole pairs in the gate depletion region due to photon absorption, thus modifying the channel current and gate leakage current,
- photo-generated forward bias created by a photovoltage across the metal semiconductor gate junction.

By considering a gradual channel approximation for the charge distribution due to ion-implantation, photo-generation in the channel of the FET and charge loss due to recombination effects, they established an expression for the drain-to-source current of the OPFET. From this they evaluated threshold voltage and drain current variations with and without photovoltaic and recombination effects by considering different levels of implant dose, optical photon flux density and trap centre density.

Lo and Lee [2.25] performed a two-dimensional theoretical study using numerical analysis to verify the occurrence of photovoltaic effects in the channel-to-substrate interface of GaAs MESFET's. Two GaAs MESFET structures were simulated, both with  $0.5 \mu\text{m}$  gate lengths and identical gate-to-source and gate-to-drain spacings, but with one of the MESFET's a  $1 \mu\text{m}$  buffer layer separating the  $n$ -type channel and semi-insulating substrate was also included. The gate, source and drain contact metallizations were considered opaque to light and a two-region mobility model was used to define the field-dependent mobility of electrons in GaAs. They began by considering the drain current-voltage characteristics of the MESFET with a photon flux of

$10^{20} \text{ cm}^{-2}\text{s}^{-1}$  which corresponded to a output power of 2 mW focused to a  $50 \mu\text{m}$  diameter spot. They considered depth profiles for electron concentration, hole concentration and conduction band edge along the centre of the gate with and without illumination and a depth profile of electron concentration along the centre of the regions between the source and the gate with and without illumination. From these results they concluded that the change of gate depletion region width and the photo-generated free-carriers in the gate depletion junction were negligible and made no significant contribution to the increase in drain current under illumination. They suggested that the photovoltaic effect occurring at the channel-to-substrate interface was responsible for the photo-induced drain current. This was consistent with the experimental results reported by Edwards [2.9]. In addition, they evaluated the reverse gate current-voltage characteristics due to illumination and established an open-circuit photovoltage which was in close agreement with the measurements of de Salles [2.32]. They showed that a change in the built-in voltage of the depletion region under illumination, as had been suggested by Graffeuil *et al.* [2.8], was not possible for the optical power available from a semiconductor laser diode. The two MESFET structures with and without the buffer layer were compared under illumination by determination of the drain current-voltage characteristics. These results showed that the photo-induced drain current was greater for the unbuffered device. This was attributed to the fact that the depletion width on the channel side due to the forming of the channel-to-substrate interface space-charge region and the depletion width change due to illumination were reduced by the  $n$ -type buffer layer. However, the photovoltaic effect was still strong enough to cause a substantial increase in the drain current under illumination.

The most significant study in the early 1990's of the static photo-response of GaAs MESFET's was made by Madjar *et al.* [2.26]. They developed a comprehensive model for the illuminated GaAs MESFET based upon the transport equations for the device. This enabled the dependence of the photo-response on bias conditions, the wavelength and intensity of the optical source and the particulars of the device structure to be accurately modelled. The complete model incorporated the following features:

- the device could be operated in any desirable biasing mode (active or beyond pinch-off),
- the intensity and wavelength of the optical source were accounted for explicitly,
- the analysis was based on basic principles, components of the optically-induced current derived from the differential equations governing the charge carrier transport,
- the photovoltaic effect in the channel-to-substrate interface was fully characterized for the first time.

Their model broke down the photo-response into a number of photoconductive and photovoltaic effects occurring within specific regions of the GaAs FET. By considering the excess electron and hole distributions in the channel, they developed an approximate expression for the photoconductive current under illumination. This showed that the photoconductive current decreased with increasing gate bias, was independent of the drain bias and intensified with increasing optical power density. Since the width of the channel was small ( $\sim 0.1 \mu\text{m}$ ), the photoconductive current was in the submicro-amp range and was neglected for typical optical power densities. The optical leakage current via the substrate due to photons absorbed between the drain and source bonding pads was also derived. This leakage current could be minimized by having the source and drain bonding pads far apart and not facing each other. Since the effective illuminated area associated with the leakage current was small, the leakage current was assumed to be negligible. The photovoltaic effect in the channel-to-substrate interface was evaluated by considering the change in the potential barrier at this interface. They termed this effect the *internal* photovoltaic effect, and showed that it was independent of biasing conditions. By using a standard Newton-Raphson approach they were able to solve for the internal photovoltage under low and high level illumination conditions. These expressions indicated that the internal photovoltaic effect could be optimized by:

- increasing the optical intensity level,
- choosing an optical wavelength appropriate to the thickness of the GaAs active layer,
- increasing the channel-to-substrate interface barrier by reducing the semi-insulating substrate concentration and increasing its thickness.

They identified two optically-induced currents associated with the internal photovoltaic effect. The first concerned an increase in the drain current as a result of a decrease in the channel-to-substrate interface barrier, which in turn extended the active channel region. Their approximate expression for the drain photocurrent was based upon the preliminary analysis by de Salles [2.13, 2.32]. For a uniformly doped active layer, this photocurrent could be optimized by applying zero bias to the gate of the MESFET. This photocurrent was shown to be typically in the milli-amp range. The second photocurrent, arising from the reduction in the channel-to-substrate interface barrier, was associated with an increase in the substrate current. This increase in substrate current was accounted for by considering a phototransistor model, from which an analytical expression was developed for the increase in substrate current due to illumination. Based upon this, the substrate current was shown to be small compared with the drain photocurrent and would only become predominant over the drain

photocurrent when the MESFET was operated in the pinch-off condition. Finally, they characterized the photovoltaic effect in the gate depletion region and identified this as the *external* photovoltaic effect. They derived an expression for the short-circuit gate photocurrent which followed the approach of de Salles [2.13]. Although this photocurrent was shown to be in the micro-amp range, the inclusion of a large resistance at the gate of the MESFET was shown to generate a large photovoltage. Expressions were developed for the gate photovoltage under low and high levels of optical illumination. In addition, the optical reflections due to surface passivation layers, which had been estimated in previous investigations, were accounted for by considering multiple reflections due to the differing refractive indices of the surface passivation and GaAs layers. By considering the change in the drain current of the MESFET under illumination, they showed that in the absence of a large resistance at the gate the internal photovoltaic effect was the dominant photo-effect. However, the inclusion of the large gate resistor made the external photovoltaic effect predominant. Measurements were performed on a  $1\ \mu\text{m}$  gate length MESFET illuminated by a semiconductor laser with a variable output power ( $2\ \mu\text{W}$  to  $3.5\ \text{mW}$ ) and wavelength (500 to 850 nm). These results related to the complete and individual photo-response dependences with optical and bias conditions and showed very good agreement with those obtained from their analytical analysis. For the internal photovoltaic effect, their measurements showed that an approximate change of 0.7 V for the photovoltage was achieved by varying the optical power output from the laser source. The drain photocurrent variation with optical power was measured with  $1\ \text{M}\Omega$  and  $0\ \Omega$  gate bias resistances, and showed very good agreement with their calculated values.

A numerical analysis of an ion-implanted GaAs OPFET was presented by Chakrabarti *et al.* [2.38]. They obtained drain current-voltage characteristics under dark and illuminated conditions, based upon analytical expressions obtained by solving numerically the one-dimensional Poisson equation for the OPFET structure. Their theoretical analysis accounted for the following basic factors:

- reflection of the incident radiation from the gate metallization as well as the metal-GaAs interface,
- forward voltage developed across the Schottky barrier due to the gate depletion region photovoltaic effect,
- dependence of the gate depletion edge depths on the channel voltage,
- modulation of the width of the gate region by incident radiation.

In their analysis they assumed the external gate bias resistance to be very high so that the photovoltaic effect in the gate depletion region became the dominant factor in determining the characteristics of the OPFET under illumination. This gave them

also justification to ignore the photovoltaic effect in the channel-to-substrate barrier. They considered that by using a suitable gate metallization thickness, about 90% of the incident light could be transmitted to the GaAs layer. As in the previous investigations, a gradual channel approximation was used to evaluate the drain current for a 1  $\mu\text{m}$  gate length FET. They concluded that for a high gate bias resistance, the optical radiation controlled the saturation drain current by changing the channel conductance rather than its conductivity, as had been suggested by Mishra *et al.* [2.39].

### 2.2.2 Dynamic Optical Response of Microwave GaAs FET's

The dynamic optical response of microwave GaAs FET's refers to the high-speed photo-response of the device while under switched or modulated optical illumination. Primarily, this is concerned with the optical stimulus being modulated in amplitude by a microwave or radio frequency (RF) signal, or by a high-speed digital signal.

The first observations and measurements of the optical control of microwave GaAs FET's were associated with the dynamic optical response of the FET. This investigation by Baack *et al.* [2.6] measured the pulse height, 10 to 90% rise time and half width time for the voltage at the output of a 1  $\mu\text{m}$  gate length MESFET illuminated by the focussed output of a pulsed semiconductor laser operating at a wavelength of 910 nm. The MESFET was found to give the best response when the gate was biased beyond the pinch-off condition. The pulsed results were compared with those of an avalanche photodiode (APD), biased at 80 V to give the fastest pulse response. The measured rise time for the MESFET was 46 ps, which compared favourably with the 74 ps value for the APD. They concluded that the GaAs MESFET had a low quantum efficiency at the laser wavelength of 910 nm, due to the long penetration depth, and suggested that operation at 850 nm would improve the quantum efficiency and the pulse response.

The first observations of optically controlled switching were made by Yen and Barnoski [2.40], who observed optically controlled switching in silicon bipolar junction transistor (BJT) oscillators. The optical stimulus was provided by superimposing an RF signal on a DC bias and then modulating a GaAlAs laser diode which had an output power of 0.3 mW. The silicon BJT oscillator was designed to operate at 1.85 GHz with the transistor bias voltage set slightly below the threshold for oscillation. When the oscillator was illuminated by the laser source, the DC illumination switched the transistor 'on' and the RF illumination phase-locked the oscillator output. They attributed the turning-on of the transistor to an optically-induced increase in the transistor base current which was measured to be approximately 10  $\mu\text{A}$ . They suggested also that the transistor oscillator would experience output voltage amplitude and frequency variations under illumination due to modification of the transistor base resistance and collector barrier capacitance by the additional optically-generated carriers.

The high-speed detection characteristics of a 1 and 2  $\mu\text{m}$  gate length GaAs MES-

FET illuminated by the focussed output of a mode-locked laser and a HeNe laser respectively, were measured by Gammel and Ballantyne [2.10]. In the first case they measured the dynamic photo-response of the MESFET to a 15 ps optical pulse under various gate bias conditions. These results showed that the photo-response had a fast rise time. This was followed by a slow fall which became more pronounced with large drain currents (i.e. smaller gate voltages). The fall time was of the order of 45 ps and the photoconductive device gain was estimated to be 1.3 and 2 for drain currents of 2 mA and 40 mA respectively. The peak pulse output voltage was found to increase linearly with input optical power level. In their explanation of the dynamic optical response of the MESFET, they discounted photovoltage amplification at the gate (i.e. photodiode effect) and optical modulation of the gate depletion region width as the responsible mechanisms. Instead, they concluded that their data were consistent only with a photoconductive mechanism and interpreted the long fall time in the optical pulse response of the MESFET as the consequence of carriers excited outside the high-field region having to drift and diffuse into this region before being collected. Finally, they compared some performance parameters of the OPFET with those of a high-quality photodiode and showed that the OPFET had better high frequency performance, lower contact resistance, no shunt capacitance and a larger photoconductive gain. Based upon these performance advantages, they proposed an integrated waveguide and OPFET structure whereby a glass waveguide running over or under the gate electrode would provide a monolithic optical interface to the optically sensitive regions of the MESFET.

The dynamic photo-response of a 1  $\mu\text{m}$  gate length GaAs MESFET was measured by Sugeta and Mizushima [2.11]. The device was illuminated by the focussed output from a GaAlAs double heterostructure (DH) laser which had a wavelength of 0.82  $\mu\text{m}$  and was directly modulated by pulses of 100 ps duration and 2 GHz repetition rate. With approximately 50  $\Omega$  resistance present at both the gate and drain of the FET, they measured the rise and fall times of the gate and drain voltages to be about 100 ps, although it was recognized that these results were limited by the response of the measuring probe. They suggested that the photo-response of the MESFET was due to the sweep-out effect of photo-generated carriers in the depletion layer as in the case of a photodiode, and substantiated their theory by measuring the gate photocurrent response. From this they estimated that the MESFET had an external quantum efficiency of about 15%. By measuring the drain photocurrent response they showed that the ratio of the drain to gate photocurrents was given by  $(1 + g_m R_G)$ , where  $g_m$  is the GaAs FET microwave transconductance and  $R_G$  the gate bias resistance. This suggested that the photo-response mechanism was a combination of the photodiode action in the depletion layer and the FET amplification action. They concluded that the contribution of the photoconductive modulation in the channel of the GaAs MESFET,

as described by Gammel and Ballantyne [2.10], was quite small.

Subsequently Gammel and Ballantyne [2.12] measured the variation in signal power with laser spot position at the drain of an illuminated  $2\ \mu\text{m}$  gate length MES-FET operated in the active and pinch-off regions. The illumination was obtained from a HeNe laser with a  $1.1\ \mu\text{m}$  spot diameter. In the active bias mode, the gate current was found to be a factor of 10 smaller than that necessary to explain the observed drain current, suggesting that substantial modulation of the channel conductivity was taking place. They explained the discrepancy between the photo-response mechanism described in their earlier investigation [2.10] and that given by Sugeta and Mizushima [2.11] to be due to the different optical wavelengths used in the two investigations. This meant that in their work reported in both [2.10] and [2.12], the shorter wavelength light resulted in an absorption depth less than the GaAs active layer thickness. This, combined with the accurate focussing of the light beam into the high-field region of the FET, meant that the efficiency of the photoconductivity modulation was high. They suggested that the longer wavelengths used in the investigation by Sugeta and Mizushima [2.11] resulted in very little of the light being absorbed in the high-field region and they concluded that nearly all of the photo-generated carriers must have been created in the substrate or in portions of the active layer outside the high-field region of the FET.

In response to the comments by Gammel and Ballantyne [2.12] on the predominant photo-mechanism in their GaAs FET's, Sugeta and Mizushima [2.41] explained that they were unable still to observe any photoconductive modulation effect in their GaAs MESFET devices. However, they made no comment on using a shorter wavelength illumination in order to observe the photoconductive effect, as had been proposed by Gammel and Ballantyne [2.12].

The optical detection properties of the GaAs FET for optical modulation frequencies up to 750 MHz were investigated by MacDonald [2.42]. Two types of FET were studied. One was an experimental device with the gate connected directly to the grounded source and the second was a commercially available FET. MacDonald began by measuring the static current-voltage characteristics for both FET's, from which he estimated the DC photo-responsivity to be  $56\ \text{AW}^{-1}$  for the experimental device and over  $1200\ \text{AW}^{-1}$  for the commercial FET. The AC photo-responsivity of the commercial FET was measured under various drain bias conditions, by illuminating the FET with the modulated output of a semiconductor laser which emitted an average power of  $14\ \mu\text{W}$  at a wavelength of 816 nm. For bias voltages from 0.4 to 4.0 V he showed that the AC photo-responsivity was approximately proportional to the inverse square root of the laser modulation frequency, and that the photo-responsivity rose approximately exponentially with bias voltage. At a laser modulation frequency of 100 MHz, the AC photo-responsivity of the commercial FET was more than  $6\ \text{AW}^{-1}$  and rose to

100  $\text{AW}^{-1}$  at 1 MHz. He measured also the noise equivalent power (NEP) for the commercial FET, and found it to be less than  $10^{-12} \text{ WHz}^{-\frac{1}{2}}$  up to 100 MHz. The rise in the NEP at high frequencies was attributed to the loss in photo-response with increasing frequency. Finally, he compared the response of the FET photo-detector with that of a commercial APD, using an optical PCM signal at  $5 \text{ Mbs}^{-1}$ . With the FET biased at 3.0 V and the APD at 140 V, he measured the noise levels to be approximately the same for both photo-detectors. However, the FET produced a larger signal by a factor of 10.

The controversy surrounding the mode of operation of the GaAs MESFET under modulated optical illumination prompted an investigation by Forrest *et al.* [2.16], in which they identified the relative roles of the photoconductive and photovoltaic effects. They began by considering the individual effects of the photoconductive and photovoltaic mechanisms in a typical microwave GaAs MESFET structure and established analytical expressions for the photocurrent dependence on optical modulation frequency. They explained that, between the drain and source electrodes, a photoconductive current could flow provided a drain-to-source potential existed to extract the photo-generated carriers. Their photoconductive current expression implied a slow response resulting from carrier trapping, and, for typical FET parameters, yielded a photoconductive gain of greater than 1000. Photovoltaic effects were said to occur in the depletion regions associated with the gate Schottky barrier junction and the interface between the active channel, buffer and substrate layers. These photovoltaic effects were shown to exercise a control over the drain current through the control of the depletion regions on either side of the channel. The authors presented an equivalent circuit for the gate depletion region photovoltaic effect, based upon small-signal FET parameters, and established three time constants associated with this effect. The photovoltaic effect at the channel-to-buffer interface was shown to be of little relevance to the high-frequency response of the MESFET photo-detector. This resulted from the long time constant due to the high capacitance associated with this thin depletion zone of large surface area. Using typical microwave GaAs MESFET parameters they established roll-off frequencies of 1.6 MHz for the photoconductive effect and 6.4 and 53 GHz for the photovoltaic effect. They showed further that, by incorporating a large gate resistance, the photovoltaic responsivity could be made as large as that associated with the photoconductive effect, but this large resistance incurred severe frequency roll-off constraints due to the time constant associated with the combination of gate resistance and gate-to-source capacitance. They predicted a photovoltaic gain of 3, which yielded a photo-responsivity of several  $\text{AW}^{-1}$ . This prediction showed good agreement with measurements obtained from illuminating a  $0.5 \mu\text{m}$  gate length GaAs MESFET with laser light modulated at 2.8 GHz. Finally, they proposed that the photo-response of the MESFET could be improved by providing a buried gate arrangement.

The photo-sensitivity of the GaAs FET to optical and electron-beam ( $e$ -beam) stimulation at various modulation frequencies up to 1.3 GHz was studied by Noad *et al.* [2.17]. The use of  $e$ -beam stimulation allowed the FET photo-sensitivity to be mapped at resolutions of tens of nanometres compared with an optical resolution limited to 2 to 3  $\mu\text{m}$ . It allowed also the penetration depth and hence the location of  $e$ -beam generated carriers to be varied. The optical stimulation allowed the photo-sensitivity to be evaluated over a wide range of frequencies by intensity-modulating a laser diode. Since both stimulation methods involve the same primary mechanism of electron-hole pair generation, Noad *et al.* combined these techniques to study the mechanisms involved in FET photo-sensitivity. They used packaged 1  $\mu\text{m}$  gate length GaAs FET's with the device lids removed. The  $e$ -beam stimulation was used to evaluate the photo-sensitivity for modulation frequencies from 0 to 100 kHz and the optical output from a GaAlAs/GaAs DH laser diode operating at wavelengths of 783 and 890 nm provided frequency-response data from 500 kHz to 1.3 GHz. They were able to establish the photo-response mechanisms by measuring the variation in the gate and drain current response with  $e$ -beam position, FET bias conditions, optical wavelength and modulation frequency. From these results they proposed that the high-frequency photo-response of the MESFET at 1 GHz was dominated by photoconductive effects, in which photo-generated carriers within the active layer are collected in the drain-source circuit. Furthermore, they noted another photo-effect at high modulation frequencies which could not have been photoconductive. The photoconductive effect was shown to yield a moderate gain of about 2. At low-frequencies they attributed the photo-response to phototransistor action caused by both the Schottky gate as well as by the photovoltage induced at the channel-to-substrate interface. This photovoltaic effect was shown to yield a large gain ( $\sim 1000$ ) and dominated the photo-response at frequencies of 200 to 300 MHz. They concluded that the ultimate high-frequency cut-off of the FET as an optical detector would be limited only by transit-time effects, making the device useful for frequencies as high as 50 GHz.

A theoretical and experimental analysis of the relative effects of device geometry, hole traps in the channel and backgating on the dynamic photo-response of the GaAs MESFET was performed by Papaionannou and Forrest [2.21]. Based upon the expression presented in the earlier analysis of Forrest *et al.* [2.16] and assuming trap-free conditions, they calculated a photoconductive cut-off frequency of 440 MHz. In this calculation, surface recombination effects on the carrier lifetime were neglected, due to the fact that carriers are forced to travel far from the surface by the space-charge region under the gate. To investigate the effects of deep traps, they measured the photo-responsivity of a 0.5  $\mu\text{m}$  gate length GaAs MESFET illuminated by a GaAlAs laser operating at a wavelength of 850 nm. These results were obtained over the frequency range 250 kHz to 2.6 GHz by direct modulation of the laser. Their measurements veri-

fied the contribution of traps up to about 150 MHz, with the non-uniform decay in the responsivity being a result of many traps and the transition from one trapping mechanism to the next. They identified three trap level contributions with cut-off frequencies of 4, 12 and 75 MHz, although only one of these could be identified from hole trap level tables. The responsivity from 150 to 400 MHz was due to the trap-free lifetime which was in close agreement with the predicted limit of 440 MHz. Above 600 MHz the response was attributed to amplification of the photovoltage generated across the gate load, with a cut-off frequency of 1.5 GHz. They also analyzed the backgating effect (i.e. variation in drain current when a bias is applied to the substrate) as a result of the photovoltaic effect occurring at the channel-to-buffer interface. By measuring the photovoltage between the drain and substrate contacts, they established that the channel substrate responsivity was almost constant up to 100 Hz. From 100 Hz to 2 kHz the response began to decrease with a cut-off at 2 kHz, which was attributed to the  $RC$  time constant of the channel-to-substrate junction and was in close agreement with their theoretical value.

Using the expressions developed by Shur and Eastman [2.43] and Shur [2.44], Simons and Bhasin [2.18] evaluated theoretically the switching time and power-delay product of a GaAs MESFET with and without illumination, as a function of device active layer thickness and gate dissipation power. These calculations indicated that as a result of the optically-induced gate voltage, an improvement in the switching time and a lowering of the switching energy occurred. They suggested also that the MESFET could be used as an optically controlled microwave switch and calculated that the switch would have an insertion loss of 0.5 dB and an isolation greater than 25 dB at 10 GHz.

Singh and Pal [2.45] performed a theoretical analysis of the switching characteristics of a silicon MESFET under optical control, making use of the expressions developed by Takada *et al.* [2.46], to model the capacitive regions of the GaAs MESFET and the GaAs FET RF switch model analyzed by Gopinath and Rankin [2.47]. They modified the capacitance expressions developed in [2.46] to include the effects of photo-generation in the gate depletion region and in the active channel region. Their theoretical calculations for a 1  $\mu\text{m}$  gate length silicon MESFET established that with increasing optical flux the gate-to-source capacitance decreased under depletion mode and increased under enhancement mode operation. The drain-to-source resistance associated with the low-impedance state of the switch model was evaluated from the drain current expression under illumination, developed in their earlier work [2.48]. This resistance was found to decrease with increasing optical flux. They concluded by showing that the  $RC$  time constant, associated with the drain-to-source resistance and gate-to-source and gate-to-drain capacitance combination, increased with increasing photon flux.

Darling and Uyemura [2.22] measured the DC optical gain and illuminated large-signal characteristics of a 3  $\mu\text{m}$  gate length GaAs MESFET when optically gated with a HeNe laser source emitting at a wavelength of 632.8 nm. The dependence of the optical gains on the applied electrical bias, and optical intensity, position and spot size was measured and related to theory in order to establish the dominant DC gain mechanisms. By sweeping the focussed output from the laser across the FET, they established that the inter-electrode regions were most sensitive to the light. This was attributed to the non-transparent nature of the metallization regions, typically no thinner than 3000  $\text{\AA}$ . This agreed with their theoretical analysis, which showed that no significant optical transmission occurred through a gold metallization thicker than 500  $\text{\AA}$ . In addition, their measurements showed that increasing the drain-to-source voltage resulted in a significant increase in the sensitivity of the gate-to-drain inter-electrode region, and this was attributed to the propagation of the gate depletion region beyond the gate metal at saturated drain currents. By measuring the drain photocurrent response variation with drain-to-source bias, gate-to-source bias and optical power level, they were able to establish which photo-mechanisms were dominant in the GaAs MESFET. They established that for low optical power levels ( $\lesssim 40 \mu\text{W}$ ), the drain response gave photocurrent gains of 5 to 10, which could be adequately accounted for by photoconductivity of the channel and substrate alone. This agreed also with results obtained from a transit-time photoconductivity model. However, at higher optical power levels, the drain response increased to give photocurrent gains of 50 to 70, which were greater than a saturating photoconductive current could produce. Their measurements suggested that a photovoltaic effect was now dominant, involving an effective shift in the pinch-off voltage (i.e. backgating effect). Since this photovoltaic mechanism was associated with a large  $RC$  time constant of the substrate, they anticipated that its response would roll-off quickly with frequency. They concluded that the roll-off points associated with trapping effects [2.16, 2.21] and photovoltaic gate biasing through a large external gate resistor [2.13, 2.32], meant that the gain-bandwidth product of the GaAs FET would largely be determined by transit-time photoconductivity alone.

By modifying their earlier theoretical analysis of the optically controlled switching characteristics of silicon MESFET's [2.45], Singh and Pal [2.49] evaluated the optical influence on the RF switching parameters of a GaAs MESFET. This involved the inclusion of surface recombination via deep traps at or close to the surface, which had been found by Mishra *et al.* [2.39] to be of significance in GaAs MESFET's. Surface recombination was found to reduce slightly the optically-induced effects on the gate-to-source capacitance and, at a fixed optical flux density, the drain-to-source resistance increased with increasing surface trap density.

Using modulated laser light over the frequency range 10 MHz to 10 GHz, Paoletta *et al.* [2.50] compared the dynamic photo-responses of two conventional GaAs-MMIC

MESFET's with that of a *p-i-n* photodiode. Their measurements showed the MESFET devices to have a significantly larger response ( $\sim 10$  dB) than the photodiode at lower frequencies, due to its internal gain. In the absence of an external gate bias resistor, the gain was attributed to the photovoltaic effect at the channel-to-substrate interface. The photo-response crossover frequencies between the photodiode and the two MESFET's were 250 MHz and 1 GHz respectively. The difference in frequency response between the two MESFET's was attributed to differences in the optical coupling efficiencies of the two devices. It was concluded that the cut-off frequency associated with the channel-to-substrate photovoltaic effect could be improved by tailoring the doping profile at the barrier, without causing any adverse affect on the microwave characteristics of the MMIC. This, combined with an improvement in optical coupling was expected to increase the frequency response up to 10 GHz so that it would equal or better that of the photodiode.

An in-depth study of the static and dynamic photo-responses of the GaAs MESFET was performed by Paoletta [2.27]. He evaluated, theoretically and experimentally, the various photocurrents and photovoltages in the GaAs MESFET as functions of optical input parameters (wavelength, intensity and modulation frequency), input gate voltage, gate resistance and device characteristics.

A brief literature review of the applications of optically controlled microwave GaAs FET's under static and dynamic illumination was presented by Madjar *et al.* [2.51]. They presented also a summary of their earlier work [2.26] on the static optical response of the GaAs FET, and used the static photo-effects they had established as the basis for describing the practical implications of using modulated optical illumination. They proposed the following dynamic limitations on the photo-response in microwave FET's as a consequence of either small-signal sinusoidal or square-wave modulation of the optical stimulus:

- a very small time constant (pico-second range) associated with the gate current photo-response, due to the gate capacitance and load resistance,
- a small time constant (nano-second range) associated with the photoconductive current; this was based upon a channel time constant of 100 to 500 times that of the recombination process in GaAs, with a recombination lifetime of 3 to 5 ns in GaAs,
- a cut-off frequency of several MHz for low optical powers and 200 to 500 MHz for large optical powers, associated with the internal photovoltaic effect; this was based upon the  $RC$  time constant associated with the channel-to-substrate barrier, with the junction resistance showing a nonlinear decrease and the junction capacitance a nonlinear increase with increasing optical power. This was verified by illuminating a commercial GaAs MESFET and these results showed further

that the frequency response had a roll-off of less than 20 dB/decade, which was attributed to deep level traps in GaAs, as shown previously by Papaionannou and Forrest [2.21],

- an  $RC$  time constant of around  $1 \mu\text{s}$  associated with the external photovoltaic effect, due to the large gate bias resistance ( $\geq 100 \text{ k}\Omega$ ) and small gate capacitance ( $\lesssim 1 \text{ pF}$ ) combination.

They concluded that the photovoltaic effects had a large but slow response, making their effects very small at microwave frequencies but useful for switching applications with typical response times in the micro-second range. This meant that, at microwave frequencies, the photo-response of the MESFET would be small.

The variation in the dynamic photo-response of the GaAs MESFET as a function of optical power over a light modulating frequency range of 300 kHz to 3 GHz was investigated by Paoletta *et al.* [2.52]. A laser diode provided a maximum optical output power of 2.3 mW at a wavelength of 840 nm, with the light modulating signal power maintained at 0.5 mW. Experimental results revealed a square-law relationship between the FET photo-response (i.e. microwave power) and the optical power, down to 0.3 mW of optical power. Below this, the ratio of optical power and microwave power no longer followed a square-law behaviour. The 3 dB bandwidth was shown to be approximately constant at 50 MHz down to an optical power of 0.6 mW, with a value of 35 MHz at 0.3 mW and 5 MHz at  $36 \mu\text{W}$ . Since no external gate bias resistance was included during their measurements, the internal photovoltaic effect was considered to be the dominant photo-mechanism. For substrate resistances below  $1 \text{ M}\Omega$ , they expressed the gain-bandwidth product associated with the internal photovoltaic effect as the ratio of the microwave transconductance to the channel-to-substrate barrier capacitance.

Madjar *et al.* [2.28, 2.53] developed a model for the external and internal photovoltaic effects in MESFET's under pulsed optical control. These models were largely based upon their earlier analysis of the static photo-response of the MESFET [2.26]. To model the influence of the internal photovoltaic effect under pulsed optical illumination, they used an equivalent circuit for the channel-to-substrate barrier. This comprised the optically-induced barrier current source shunted by a diode, the substrate resistance and the barrier capacitance. The equivalent circuit for the gate Schottky junction, used to represent the influence of the external photovoltaic effect, consisted of the optically-induced short-circuit gate photocurrent source shunted by a combination of Schottky diode, gate capacitance and the gate bias network. The gate bias network included the gate bias voltage source and large gate resistance. From these models they derived nonlinear differential equations to represent the dependence of the photovoltages on the optical signal parameters (intensity, wavelength and pulse duration), gate bias voltage, gate resistance and device parameters. Using these expressions they simulated the optical pulse response of the MESFET by using numerical methods (Runge-Kutta

techniques). From their analytical models and typical MESFET and optical signal parameters, they predicted that the internal photovoltaic effect would have a fall time of about  $2 \mu\text{s}$  and a rise time of  $0.1 \mu\text{s}$ , with the rise time decreasing with increasing optical power. For the external photovoltaic effect, the rise and fall times were in the submicro-second range with a  $1 \text{ M}\Omega$  gate bias resistance, although the drain photocurrent was a factor of approximately 10 greater than that for the internal photovoltaic effect. They measured the photo-response of a  $1 \mu\text{m}$  gate length MESFET illuminated by a 20 to  $30 \mu\text{s}$  light pulse from a laser diode emitting at a wavelength of 850 nm. Their experimental results verified the general trend in the variation of the MESFET photo-response under pulsed optical control, although the measured and simulated results were obtained for different gate loading and optical pulse conditions.

An analytical model for the switching characteristics of optically controlled GaAs MESFET's was presented by Chakrabarti *et al.* [2.54]. They considered the variation in the drain current-voltage characteristics, drain-to-source and internal gate-to-source capacitances, drain-to-source resistance, transconductance, input  $RC$  time constant and cut-off frequency under illumination. Furthermore, the variation of these parameters with gate length and channel doping concentration was numerically evaluated under dark and illuminated conditions. In their model it was assumed that the gate metal was semitransparent to the incident light and that a large resistance was present at the gate of the MESFET. Their evaluation of the drain current-voltage characteristics in the dark and illuminated states followed a similar approach to their earlier work [2.38], except that the channel was assumed to be uniformly doped. They followed a similar approach to that of Takada *et al.* [2.46] and Singh and Pal [2.49] to evaluate the small-signal lumped equivalent circuit elements of the MESFET under dark and illuminated conditions, except that the change in the minority carrier lifetime under illumination was accounted for explicitly. The expressions they derived were used to determine theoretically the variation in the parameters of a  $1 \mu\text{m}$  gate length MESFET under illumination. They calculated that for a minority carrier lifetime of  $10^{-8}$  s under dark conditions, a value of  $3.93 \times 10^{-11}$  s for the minority carrier lifetime was obtained with an incident optical power density of  $5 \text{ Wm}^{-2}$ . For the same optical power density of  $5 \text{ Wm}^{-2}$ , their calculations showed that illumination increased the drain-to-source and internal gate-to-source capacitances, transconductance and cut-off frequency by approximately 20, 10, 15 and 5%, respectively. The  $RC$  time constant, defined in terms of gate-to-source capacitance and transconductance, decreased under illumination by approximately 3%.

A model was developed by Paoletta *et al.* [2.29] for the GaAs MESFET under modulated illumination at radio and microwave frequencies. The modelling techniques used and experimental results presented were based largely upon the earlier works of Paoletta [2.27] and Madjar *et al.* [2.26]. They modified the photocurrent expressions

developed by Madjar *et al.* [2.26] to include optical illumination composed of a static component, due to a DC bias applied to the light source, and a dynamic component, due to a sinusoidal signal applied to the light source. Using an equivalent circuit for the channel-to-substrate barrier, which comprised the optically-induced barrier current source shunted by a diode, the substrate resistance and the barrier capacitance, they evaluated an expression for the light-frequency dependent internal photovoltage. They developed also an expression for the light-frequency dependent external photovoltage based upon a model for the gate Schottky junction which comprised the optically-induced short-circuit gate photocurrent source shunted by a Schottky diode, gate capacitance and the gate bias network. The gate bias network included the gate bias voltage source and large gate resistance. They determined also the low-frequency gain, and the gain-bandwidth products associated with both the internal and external photovoltaic effects, based upon the work of Paoella [2.27]. From their theoretical analysis, they predicted that at low light modulating frequencies the photo-response would be 'flat', and that, with the presence of a large gate bias resistance, the frequency spectrum would roll-off at several MHz. Without the gate resistance the internal photovoltaic effect was predicted to dominate, yielding a flat response extending above 100 MHz, and with a roll-off of 20 dB/decade beyond the cut-off frequency. For frequencies in the microwave range, the contribution of the photocurrent, generated as a result of the internal photovoltaic effect, was expected to level-off as it reached a similar magnitude to those of the gate and photoconductive currents. The gate and photoconductive currents were calculated to roll-off at approximately 20 to 30 GHz, although the photo-response would be small, with the photoconductive current being negligible and the gate photocurrent being in the micro-amp range. They established that the frequency response was a function of optical power and gate bias by illuminating a 1  $\mu\text{m}$  gate length MESFET. The laser source emitted at a wavelength of 850 nm with a maximum output power of 3.5 mW, and was modulated over the frequency range 300 kHz to 3 GHz. Their measurements showed that, for the internal photovoltaic effect, the low frequency gain decreased and 3 dB bandwidth increased with increasing optical power. A comparison of the calculated and measured frequency photo-responses showed that the measured 3 dB bandwidth ( $\sim 100$  MHz) for the internal photovoltaic effect gave good agreement with theory, but that the theoretical model did not predict accurately the roll-off. This was attributed to deep trap levels not included in their model. Finally, they showed that, by increasing the gate reverse bias from 0 to -2 V, the 3 dB bandwidth of the external photovoltaic effect could be increased from 7 to 70 MHz.

## 2.3 Optically Controlled GaAs FET Devices

The use of optically controlled microwave GaAs FET's over the past 18 years has been directed towards phased-array radar applications. The devices can be classified into the following areas in accordance with the particular signal distribution and beam-formation requirements of such radar systems:

- Optically controlled amplification
- Optical injection-locking and frequency tuning of oscillators
- Optically controlled phase shifting
- Optically controlled mixing
- Optically controlled switching
- Optical detection

A number of these applications have been reviewed over the last decade. The notable outcomes are summarized chronologically in Table 2.2.

### 2.3.1 Optically Controlled Amplification

To achieve active beam formation in phased-array radar systems, it is necessary to control accurately the signal gain and phase through each transmit and receive element. It was this requirement that prompted a number of investigations into optically controlling the gain of microwave GaAs FET amplifiers. This was achieved first by de Salles and Forrest [2.57] and de Salles [2.13,2.32], wherein a common-source MESFET amplifier was designed using standard low-power techniques and was controlled optically by directly focusing light onto the sensitive regions of the FET. By incorporating a large resistor (100 k $\Omega$ ) in the gate bias network, they used the photovoltaic effect in the gate depletion region to control optically the gate-to-source voltage and therefore the gain of the FET, in a manner identical to electrically controlling the gain of the FET via the gate-to-source voltage. They were able to achieve gain increases in excess of 20 dB at 2.8 GHz with a few micro-watts of optical power when the FET was biased close to the pinch-off condition. The rate at which the gain could be changed was stated to be limited by the time constant associated with the gate resistor and gate-to-source capacitance combination. This was estimated to be approximately 50 ns.

Based upon the optically controlled FET amplifier configuration investigated by de Salles [2.13], Berceci and Chapman [2.66] performed a theoretical analysis to show that optical illumination could be used to give a significant improvement in both the amplifier linearity and intermodulation distortion. This was achieved by optimal adjustment

Optically Controlled GaAs FET Applications		
Dates	Principal Outcomes	Principal References
⇒ 1980	<ul style="list-style-type: none"> <li>• optical injection-locking &amp; frequency tuning in GaAs FET oscillators</li> <li>• optical switching in microwave GaAs FET oscillators</li> </ul>	[2.40, 2.55]
1981 ⇒ 1985	<ul style="list-style-type: none"> <li>• theoretical and experimental study of optical-injection locking</li> <li>• study of optically controlled amplification in GaAs FET's</li> </ul>	[2.13, 2.32, 2.34, 2.56, 2.57]
1986 ⇒ 1990	<ul style="list-style-type: none"> <li>• optically controlled phased-array module</li> <li>• optical phase control in microwave GaAs FET oscillators</li> <li>• indirect optically controlled switching of GaAs FET's</li> <li>• optically controlled mixing in microwave GaAs FET's</li> <li>• indirect optically controlled phase shifting using GaAs FET's</li> </ul>	[2.58–2.63]
1991 ⇒ 1995	<ul style="list-style-type: none"> <li>• use of HEMT and HBT devices in optically controlled applications</li> <li>• mobile radio systems using GaAs FET photo-detectors</li> </ul>	[2.2, 2.24, 2.50, 2.64, 2.65]

**Table 2.2:** Chronicle of the principal developments into optically controlled GaAs FET applications.

of the light intensity and by proper termination of the optically-induced current at the gate of the FET.

Direct optical control of the gain in a HEMT-based amplifier, without the inclusion of the large gate resistor, was achieved by Simons [2.19]. This resulted in a gain increase of 2 dB at 13.25 GHz. For a MESFET-based amplifier, the optically-induced increase in gain was only 1.2 dB at 9 GHz. In each case no change in the phase was observed, and the gain increase was found to be greatest when the devices were biased close to pinch-off. Subsequently the MESFET was cascaded with a distributed amplifier and a 3 dB increase in gain over the frequency range 2 to 18 GHz was achieved by illuminating the MESFET with 1.5 mW of optical power.

An approximate 15 dB increase in gain over the frequency range 5 to 8 GHz

was achieved by Paoella *et al.* [2.58, 2.67] by indirect optical control of an MMIC distributed amplifier. An MMIC-compatible low-frequency GaAs FET was used as an optical detector, with the optically-induced output voltage from the FET being amplified in an MMIC operational amplifier and then used to control electrically the gain of the distributed amplifier.

De Salles and Romero [2.24] measured a 31 dB optically-induced increase in gain at 4.7 GHz for a HEMT-based amplifier with a 1.2 M $\Omega$  gate resistance and with the HEMT biased close to pinch-off.

Madjar *et al.* [2.68] proposed that the compressive nature of the photovoltaic effects, established in their earlier investigation [2.26] into the photo-response of GaAs MESFET's, could be used as the basis to achieving RF logarithmic amplification. They suggested that a logarithmic response could be obtained from the output of a microwave GaAs FET amplifier where the gain is controlled from the output of a laser diode modulated by the RF input signal. The operation of the RF logarithmic amplifier was verified by measuring the constant, modulated and pulsed illumination response of the MESFET, which showed that the drain current pulse amplitude was a logarithmic function of the optical power and that the gain was a decreasing function of the optical power for a fixed voltage sinusoidal light modulating signal.

### 2.3.2 Optical Injection-Locking and Frequency Tuning of Oscillators

Optical injection-locking and tuning have been investigated as a means of replacing conventional electrical injection-locking in phased-array radar systems in order to achieve synchronization (phase-locking) of remotely located microwave sources. Also, Moncrief [2.55] has suggested that the optical tuning in microwave GaAs FET's can be used to replace varactor diodes in Electronic Warfare (EW) applications.

Optical injection-locking was observed first by Yen and Barnoski [2.40] in a silicon BJT oscillator. It was shown to be possible not only at the fundamental frequencies but also at various subharmonics. Since then, a number of researchers have investigated direct optical injection-locking and tuning of microwave GaAs MESFET oscillators [2.13, 2.31, 2.32, 2.34, 2.50, 2.56, 2.57, 2.69–2.71]. The optically-induced frequency changes have been explained generally by optically-induced variations in the device capacitances as a result of photoconductive and photovoltaic effects, occurring within specific regions of the FET. Typically, optical tuning ranges of 10% and optical injection-locking ranges of tens of mega-Hertz have been achieved, primarily at X-band.

Sun *et al.* [2.34] have found that common-source FET oscillators are 5 times more optically frequency sensitive than common-drain configurations. Loriou *et al.* [2.56] have demonstrated optically controlled frequency modulation up to 2 MHz in mi-

crowave GaAs MESFET oscillators. Blanchflower and Seeds [2.60] demonstrated frequency and phase control in a GaAs MESFET oscillator by incorporating the optically injection-locked oscillator in a phase-locked loop. They achieved a tuning range of 8 MHz and a locking range of 1.2 MHz. Esman *et al.* [2.61] have reported the direct optical phase control of a 7.2 GHz microwave FET oscillator. The relative phase between the oscillator and the optically injection-locked signal was adjusted by optically tuning the oscillator frequency to yield a locking bandwidth of 2.6 MHz, phase tuning of 0 to 187° and optical tuning of 125 MHz.

Optical injection-locking and tuning has been reported more recently in HEMT-based oscillators [2.24, 2.36, 2.64, 2.72–2.74] and HBT-based oscillators [2.65, 2.75, 2.76].

### 2.3.3 Optically Controlled Phase Shifting

Optically controlled phase shifting required for beam-steering in phased-array radar systems has been reported in the literature only by using indirect optical techniques.

Herczfeld *et al.* [2.59] extended the earlier work on indirect optical gain control by Paoletta *et al.* [2.58, 2.67] to permit indirect optical control of both gain and phase. They combined their distributed amplifier arrangement, used to provide indirect optical gain control, with a conventional MMIC phase shifter to provide phase control. The electrical control signal to the phase shifter was derived from a low-frequency MESFET configured as a photo-detector. This resulted in the indirect optical control of the phase over 45° by increasing the optical power level from 0 to 51  $\mu\text{W}$ .

In a similar fashion to Herczfeld *et al.* [2.59], Jemison *et al.* [2.62] achieved indirect optical control of a digital MMIC phase shifter. They used a low-frequency MESFET as an optical detector and converted the optically-induced voltage at the output of the MESFET to a digital equivalent which was used to control the state of a phase shifter. They achieved 360° total phase shift by increasing the optical power from 0 to 310  $\mu\text{W}$ .

### 2.3.4 Optically Controlled Mixing

The technique of optically controlled microwave mixing in which the local oscillator is modulated on to an optical carrier and applied directly to the transistor mixing element can offer significant advantages in terms of receiver front-end performance. This arrangement reduces the number of front-end components and thereby reduces the cost and improves the signal-to-noise performance. A single low-noise FET connected in this configuration will provide both the mixing function and some RF gain. One situation where the use of such a mixer technique has been postulated is that of wideband distribution from satellite ground stations in a cable television system, where optical fibres are used to carry the signals from inaccessible receiving locations to signal processing centres [2.77]. In these circumstances, exploiting direct interac-

tion of optical and microwave signals would maintain the signal quality and low loss performance offered by the optical fibres.

Using a 0.25  $\mu\text{m}$  gate length microwave GaAs FET incorporated in appropriate feedback and impedance-matching circuitry, Rauscher *et al.* [2.63] performed the functions of photo-detection, harmonic generation, mixing and local oscillator generation for down-conversion in an optical-to-microwave link receiver. The optically controlled mixer was shown to operate for light modulating frequencies up to 89 GHz.

Simons and Bhasin [2.19] performed preliminary experiments on the use of a Al-GaAs/GaAs HEMT as a optical-to-microwave mixer. They directly modulated light from a laser diode at a frequency of 6 GHz, and this was used to illuminate the HEMT while a microwave signal at 9 GHz was coupled electrically to the gate terminal. They observed an intermediate frequency (IF) signal of 3 GHz at the drain of the HEMT but made no further measurements on the mixer performance.

Recently, Paoletta *et al.* [2.78] have demonstrated optically controlled mixing using the nonlinearities associated with the internal photovoltaic effect in GaAs FET's. Their experimental results showed that, for optical modulation frequencies below 700 MHz, the mixer exhibited a lower noise figure than that of a *p-i-n* detector/Schottky diode mixer combination.

### 2.3.5 Optically Controlled Switching

In advanced phased-array radar systems, where MMIC digital phase shifters provide beam-steering and multiple beam formation capabilities, FET switching elements are often required. In the case of digital command data being distributed via optical fibre techniques, an optically controlling switching element would be desirable. So far in the literature, investigations of optically controlled switching have either involved indirect forms of optical switching or direct forms involving non-standard MMIC elements.

Indirect optical control of a commercial GaAs MMIC switch has been reported by Paoletta *et al.* [2.79]. They used a pinched-off GaAs MESFET as an optical detector to convert an optically pulsed signal to an equivalent electrical pulse which was subsequently amplified and applied to the electrical control input of an MMIC switch. The switch was tested with an optical pulse of 0.1 mW and duration 1  $\mu\text{s}$  to give an isolation of 20 dB and an insertion loss of 1.5 dB at a frequency of 10 GHz.

A MESFET-compatible GaAs optoelectronic switch which relied on a photoconductive effect between two ohmic contacts separated by the buffer layer of the device was fabricated by Riesz *et al.* [2.80]. Measurements on this device showed an 'off'-to-'on' resistance ratio of about 500, with the switching speed limited by carrier lifetime in the buffer layer which was estimated to be between 600 ps and 1 ns. The microwave performance of their switch was not tested.

A gate-less FET-based optoelectronic switch, which required no electrical bias,

was fabricated by Freeman *et al.* [2.81]. For 1 mW of optical power, they measured their switch to have an isolation of greater than 20 dB and an insertion loss of about 3 dB at a frequency of 10 GHz. The switching time at 4 GHz was limited to about 1.5  $\mu$ s due to capacitive effects.

### 2.3.6 Optical Detection

Microwave HEMT devices have been used as photo-detectors in microwave fibre-optic systems for personal radio communications. These systems rely on a large number of radio base stations to provide sufficient signal coverage over a specified area, and it is therefore important that these base stations are compact and implemented using a cost effective technology. Such a system is an ideal candidate for the implementation of an MMIC-compatible optical technology where a microwave HEMT device, used as a photo-detector, provides the interface between the optically integrated waveguides, modulators and laser diodes, and the MMIC radio transceiver. The concept for such a system is illustrated in Figure 2.2 [2.2].

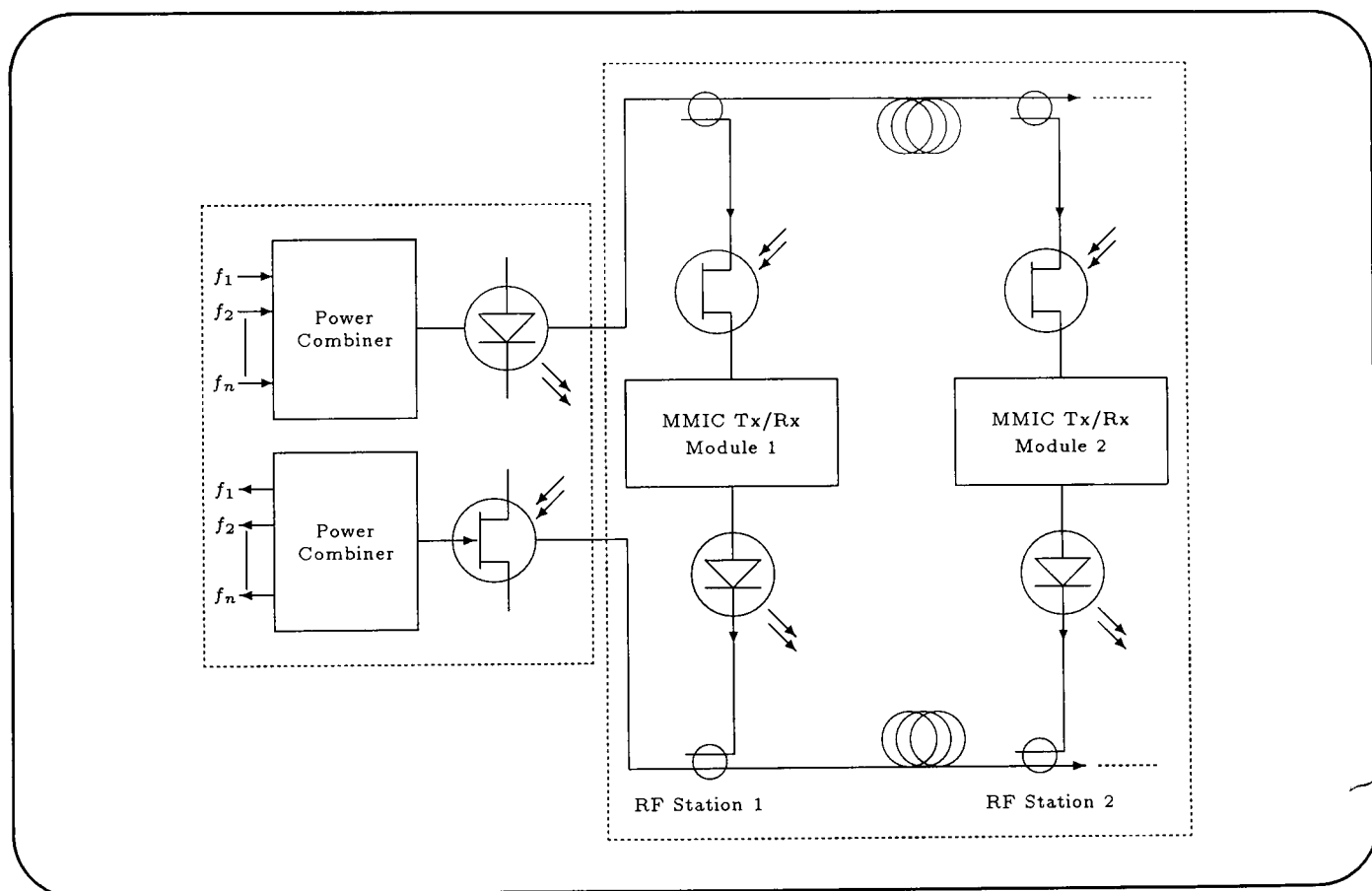


**Figure 2.2:** A microwave fibre-optic subsystem for personal radio communications [2.2].

Ogawa *et al.* [2.2] and Banda *et al.* [2.82] have performed preliminary investigations of such a communication link and have shown that the use of the HEMT in place of a *p-i-n* diode as the photo-detector offers an improved optical DC responsivity and lower link insertion loss at low microwave frequencies, due to the HEMT's internal gain. However, the *p-i-n* diode does offer a flatter response at the higher microwave

frequencies ( $\gtrsim 15$  GHz), and bit error rate measurements showed the HEMT-based link to have a substantially higher noise floor.

## 2.4 GaAs FET-Based Switches

In the early 1980's, the difficulty of implementing conventional *p-i-n* switching diodes within a standard MMIC process was recognized and this led to the development of MMIC switches based upon GaAs FET's. The evolution of the GaAs FET switch is summarized in Table 2.3.

Electrically Controlled GaAs FET Switches		
Dates	Principal Outcomes	Principal References
$\Rightarrow$ 1980	<ul style="list-style-type: none"> <li>• experimental study on hybrid SPST and SP8T GaAs FET switches</li> <li>• use of lumped inductive tuning for bandwidth improvement</li> </ul>	[2.83, 2.84]
1981 $\Rightarrow$ 1985	<ul style="list-style-type: none"> <li>• development of 'on' &amp; 'off' state MMIC GaAs FET switch models</li> <li>• use of integrated inductive tuning for bandwidth improvement</li> <li>• development of dual-gate GaAs FET switches</li> <li>• switch performance enhancements using multiple GaAs FET configurations</li> </ul>	[2.85–2.90]
1986 $\Rightarrow$ 1990	<ul style="list-style-type: none"> <li>• development of custom MMIC GaAs FET switch models</li> <li>• broadband measurements on GaAs FET switches</li> </ul>	[2.91–2.96]
1991 $\Rightarrow$ 1995	<ul style="list-style-type: none"> <li>• MMIC GaAs FET switch models</li> </ul>	[2.97]

**Table 2.3:** Chronicle of the principal developments into GaAs FET switching.

The use of the GaAs FET as a microwave switch was reported first by Liechti [2.83]. By switching the drain supply voltage, he achieved an insertion gain of 10 dB in the switch 'on' state and 20 dB insertion loss in the 'off' state. The combination led to a net isolation of 30 dB.

Gaspari and Yee [2.84] identified five possible configurations for the GaAs FET to operate as a single-pole, single-throw (SPST) microwave switch. They performed measurements on a number of GaAs FET's with gate lengths of 1 and 2  $\mu\text{m}$ , connected

in a series switch configuration. With no drain bias applied and by switching the gate voltage between zero bias and pinch-off, they achieved insertion losses of 3 dB and 13 dB in the ‘on’ and ‘off’ states respectively, at a frequency of 4 GHz. Although the switch had an inherently broadband response, they sacrificed bandwidth and insertion loss in the ‘on’ state to improve the isolation of the switch by resonating the estimated values for the equivalent gate-to-source and gate-to-drain capacitance of the switch in the ‘off’ state with a parallel wire inductance. This improved the isolation of the switch from about 8 dB to 34 dB at 4.5 GHz, with the switch having a bandwidth of about 500 MHz. They combined 16 GaAs FET switch elements to develop a SP8T switch for satellite switched-time division multiple access (SS-TDMA) spacecraft applications. With the inclusion of the inductive tuning the switch matrix exhibited an insertion loss of 8 to 10 dB in the ‘on’ state and a isolation of greater than 50 dB over a 500 MHz bandwidth centered at 4 GHz. The switching speed of the module was measured as 1 ns and was limited by the switch driver circuit.

The first comparisons of insertion loss performance for series and shunt mounted GaAs FET switch configurations were performed by McLevige and Sokolov [2.85] using a simplified model for the ‘on’ and ‘off’ states of a specific FET. From their simplified model which consisted of a resistor and capacitor connected in parallel, they established from estimated values for the capacitance and resistance in both states that an ‘on’ state insertion loss of 0.7 dB and an ‘off’ state tuned isolation of 28.5 dB resulted for a series-connected bidirectional SPDT GaAs FET switch at 10 GHz. In their experimental GaAs FET work they achieved reactive tuning by including a monolithically fabricated inductor, placed in parallel with the drain-to-source region of the FET. They measured an ‘on’ state insertion loss of 0.7 dB and an ‘off’ state isolation of 28 dB at 10.2 GHz, which were in very good agreement with their modelled results. The switch had a bandwidth of about 600 MHz, which was limited by the reactive tuning in the ‘off’ state and could be increased to about 900 MHz by using a FET with a smaller gate periphery, at the expense of an increased insertion loss. They concluded that their resonant FET switch would be useful for future MMIC applications.

Vorhaus *et al.* [2.86] investigated a GaAs dual gate FET (DGFET) as a microwave switch in which the drain of the DGFET was biased for normal maximum gain operation, with the microwave input signal applied to one of the gates and the bias at the other gate used to control the ‘on’ and ‘off’ states of the DGFET switch. Using 1  $\mu\text{m}$  gate length DGFET’s, they fabricated single-pole, single-throw (SPST), double-pole, double-throw (DPST) and single-pole, four-throw (SP4T) switches. For the SPST switch they measured a net isolation in excess of 30 dB at 10 GHz, while the magnitudes and phases of  $S_{11}$ ,  $S_{12}$  and  $S_{22}$  showed little variation in either switching state. The maximum available gain (MAG) was measured at 10 GHz, with values between 10 and 13 dB for the SPST switch and 8 and 11 dB for the DPST switch. They presented

also a model for the DGFET switches based upon the standard lumped equivalent circuit for the DGFET, and estimated the parameters of their model from measurements on their devices and using data from previous publications.

The most significant study of GaAs FET switches was performed by Ayasli [2.87] and Ayasli *et al.* [2.98]. They presented a comprehensive model for the GaAs FET switch. This model used two different lumped equivalent circuits to represent the various regions of the FET in the ‘on’ and ‘off’ states. They modified previously published expressions, which had been used in the evaluation of the lumped equivalent circuit parameters of a common-source GaAs FET, to account for the device properties under switched operation. They applied the model to a shunt connected FET switch, or reflective configuration, in which the microwave signal was applied to the drain of the FET with the source at RF ground. The drain and source were not biased in either switching state and the switch state was controlled solely by switching the gate between zero bias and pinch-off. The capacitance of the FET in the ‘off’ state was resonated in a similar manner to that described by McLevige and Sokolov [2.85], with the exception that now the inductance was a combination of the monolithic inductor across the drain-to-source contact and the inherent overlay inductance of the drain air-bridge interconnections present in the multi-gate fingered MESFET’s. They established also that the gate bias network had a significant influence on their equivalent circuit in the ‘off’ state, and therefore the gate bias network was configured to present a high impedance by using a two-section low-pass filter. Based upon the switch state equivalent circuits and typical parameters for their 1  $\mu\text{m}$  gate length MESFET switches, they calculated the ratio of the drain-to-source resistance in the ‘off’ and ‘on’ states to be 800 at 10 GHz, decreasing to 420 at 20 GHz. They estimated a theoretical switching speed of 0.3 ns from their model, which compared with a value of 1 ns obtained from measurement. It was suggested that, in their measurements of the switching speed, the gate bias network had an effect on the results and also that the bias network design could be optimized to achieve a switching speed that was closer to their theoretical predictions. Measurements on two of their resonated GaAs FET switches, combined to form an MMIC transmit/receive switch, indicated a minimum ‘on’ state insertion loss of 0.5 dB and a 1 dB insertion loss bandwidth of 8 to 12 GHz. They also used a number of their GaAs FET’s as switching elements in the design of an X-band four-bit MMIC phase shifter which incorporated two loaded-line and two switched-line phase shifters to give 16 discrete phase states between 0 and 360°.

Using a switch configuration almost identical to that of Ayasli [2.87], Sokolov *et al.* [2.88] developed a Ka-band one-bit 180° switched-line phase shifter. They used also a length of monolithic transmission line to resonate the pinch-off capacitance between the drain and source of the FET, and a high impedance at the gate terminal was provided by a bonding wire inductance. They performed measurements on the

GaAs FET switches at 30 GHz and established that the switch losses were due to resistive dissipation. Since the parasitic resistances of the FET were significant at their frequencies of interest, they used a self-aligned gate technique to fabricate the FET switch. This involved the inclusion of a low sheet resistance  $n^+$ -type implant on either side of the gate contact. This technique resulted in the ‘on’ state insertion loss being improved by more than 1 dB due to a reduction of 1.5 to 2 times in the open channel resistance.

Using a switch model similar to that proposed by Ayasli [2.87], together with the capacitance expressions developed by Takada *et al.* [2.46], Gopinath and Rankin [2.47] determine analytically the performance dependence of GaAs FET switches on various device parameters. In particular, they developed expressions for the switch quality factor and power handling capabilities, and used these to investigate their variation with active layer doping density and thickness, inter-electrode spacing, gate length and buffer layer thickness at a frequency of 10 GHz. These calculations showed that the switch quality factor could be improved by increasing the active layer doping density, decreasing the inter-electrode spacing and gate length, and increasing the thickness of the buffer layer. In their calculations, they omitted the ‘off’ state drain-to-source capacitance, due to its small value.

Fryklund and Walline [2.89] fabricated monolithic SPST and SPDT GaAs FET switches. The SPST switch was constructed from two shunt-connected FET’s and a single series FET, and the SPDT switch from two series-connected FET’s and one shunt FET. The insertion loss, VSWR and isolation were measured and are summarized in Table 2.4. They measured also a worst-case transition time of 3 ns for the SPST switch, which, when combined with an estimated 5 ns delay in the switch driver circuit, was projected to lead to a total switching speed of less than 10 ns.

Switch Type/Frequency	Switch Performance Parameters [2.89]		
	Insertion Loss dB	Isolation dB	VSWR
SPST/10 GHz	1.25	16	1.6
SPDT/6 GHz	1.25	30	1.9

**Table 2.4:** Performance parameters for experimental SPST and SPDT GaAs FET switches [2.89].

Using a reflective GaAs FET switch arrangement similar to that of Ayasli [2.87], Andricos *et al.* [2.90] used a seven-element *RLC* network to model their switches. The *RLC* elements were determined empirically for three different gate peripheries and an open-circuit condition was achieved at the gate of the FET by using a 5 k $\Omega$  resistor in

the gate bias circuit. The switches were incorporated into loaded-line and Lange-style phase shifters to provide a monolithic six-bit phase shifter operating over  $C$ -band.

The approximate switching  $Q$ -factor and figure-of-merit for series-mounted SPST discrete GaAs FET switches with differing gate lengths and peripheries were determined by Gutmann *et al.* [2.91] over the frequency range 50 MHz to 18 GHz. They used a similar model to that of Ayasli [2.87] to evaluate some of the switch performance parameters and, for the six FET devices tested, they found that the channel resistance in the ‘on’ state was lower for FET’s with large gate periphery, higher channel doping, shorter gate length and drain-to-source spacing, higher pinch-off voltage and with an  $n^+$ -type surface layer. They used also a 5 k $\Omega$  resistor to establish a high RF impedance at the gate of the FET. Then, for a total capacitance of 0.06 pF in the off-state, the switching figure-of-merit was calculated to be 435 GHz.

Measured and simulated  $S$ -parameter data over the frequency range 10 to 13.84 GHz for a shunt-mounted discrete GaAs FET switch were presented by Upadhyayula *et al.* [2.92]. Their model was based on that of Ayasli [2.87], but was extended to include lead inductances, gate resistance and capacitances in order to account for the drain not being at DC earth potential (i.e. floating). They used DC measurements on the FET to establish the resistive components of the equivalent circuit and computer optimization based on measured  $S$ -parameter data to evaluate the remaining element values.

Recently, Ehoud *et al.* [2.99] performed  $S$ -parameter measurements on a number of GaAs FET switches in series and shunt configurations over the frequency range 0.45 to 26.5 GHz. They used these results for each switch state to extract the equivalent circuit parameters used in the switch model. These equivalent circuit parameters were then linearly scaled to model devices with identical gate structures but differing gate peripheries.

Current developments in GaAs FET switching have tended to be focussed upon generating models which are specific to a particular MMIC foundry process [2.97].

## 2.5 GaAs FET-Based Phase Shifters

Investigations into MMIC-compatible switches were motivated primarily by the desire to achieve digitally controlled phase shifting and electrical control between transmit and receive sections in highly integrated phased-array radar systems.

Ayasli [2.87] and Ayasli *et al.* [2.98] used their GaAs FET switches in the development of a MMIC transmit/receive switch and a four-bit phase shifter. The phase shifter used two switched-line elements to provide 180° and 90° phase shifts, with each element requiring three electrically controlled switches. The remaining two-bits of the phase shifter were provided by two loaded-line elements to give 45° and 22.5° phase shifts.

with each element here requiring two electrically controlled switches. The complete phase shifter exhibited 16 discrete phase states between 0 and 360° with an insertion loss of  $5.1 \pm 0.6$  dB and a phase error of less than 10° for any bit, at a frequency of 10 GHz.

An MMIC single-bit 180° switched line phase shifter was developed by Sokolov *et al.* [2.88], based upon their self-aligned gate FET switches, to operate over the frequency range 27.5 to 30 GHz. Their phase shifter used four switching elements and yielded a 2.5 to 3 dB insertion loss and a maximum phase error of 10 to 20°.

An MMIC six-bit phase shifter was fabricated by Andricos *et al.* [2.90]. This incorporated two Lange coupler elements to achieve 90° and 180° phase shifts, and three loaded-line elements to produce 45°, 22.5° and 11.25° phase shifts. A final loaded-line element was designed to give a variable phase shift from 0 to 11°. Each bit of the phase shifter required two switching elements, with the variable bit providing a phase shift related to the applied gate bias voltage. The overall phase shifter had an insertion loss of  $8.7 \pm 1.2$  dB and a worst-case phase error of  $\pm 9^\circ$ , over the frequency range 5 to 6 GHz.

Upadhyayula *et al.* [2.92] fabricated an MMIC single-bit loaded-line phase shifter which used two switching elements and provided a phase shift of 22.5° over the frequency range 11 to 12.4 GHz.

## 2.6 MMIC and OMMIC Technology

Although the past decade has seen major advances in the fabrication of MMIC's and monolithic optical components, the bulk of this work has considered the microwave and optical aspects independently. Subsequently, this led to the development of very high-performance MMIC's and optical electronic integrated circuits (OEIC's) which are not mutually compatible. Such OEIC's achieve the total integration of photodiodes, lasers, FET's and amplifiers on GaAs through the use of non-standard device fabrication processes which are far from being compatible with commercially offered MMIC processes. Bhasin *et al.* [2.100] have developed an optically controlled MMIC phase shifter with an integrated *p-i-n* photodiode interface, but this was achieved only through the use of a modified MMIC fabrication process. Real compatibility can be achieved only through the use of a MMIC-compatible photo-detector, hence the interest here in the microwave GaAs FET. Some proof-of-concept demonstrations of the use of the FET as an monolithic MMIC-compatible interface have been reported by Herczfeld *et al.* [2.59] for phased-array radar applications, and by Ogawa *et al.* [2.2] and Banda *et al.* [2.82] for fibre-optic personal radio communication systems. Herczfeld *et al.* [2.59] provided indirect optical gain and phase control using completely MMIC-compatible components, although their indirect means of optical control does tend to

---

detract from the benefits of OMMIC's. Ogawa *et al.* [2.2] and Banda *et al.* [2.82] used a HEMT as a MMIC-compatible monolithic detector for a personal radio communication system. This provided the system with an improved gain but higher noise floor and indicates the potential for future OMMIC developments.

# References

- [2.1] M. Kuno, T. Sanada, M. M. H Nobuhara, T. Fujii, O. Wada, and T. Sakurai, "Four-channel AlGaAs/GaAs optoelectronic integrated transmitter array," *Appl. Phys. Lett.*, vol. 49, pp. 1575–1577, Dec. 1986.
- [2.2] H. Ogawa, D. Polifko, and S. Banda, "Millimeter-wave fiber optics systems for personal radio communication," *IEEE Trans. Microwave Theory Tech.*, vol. 40, pp. 2285–2293, Dec. 1992.
- [2.3] H. P. Hsu, M. de la Chapelle, and J. J. Gulick, "Fiber optic links for microwave signal transmission," in *Proc. SPIE Int. Tech. Symp.*, vol. 716 of *High Frequency Optical Communications*, pp. 69–75, 1986.
- [2.4] R. N. Simons, *Optical control of microwave devices*, ch. 7, pp. 165–166. Boston: Artech House, 1990.
- [2.5] P. Herczfeld, "Monolithic microwave-photonic integrated circuits: A possible follow-up to MIMIC," *Microwave J.*, pp. 64–78, Jan. 1992.
- [2.6] C. Baack, G. Elze, and G. Walf, "GaAs M.E.S.F.E.T.: A high-speed optical detector," *Electron. Lett.*, vol. 13, p. 193, Mar. 1977.
- [2.7] J. J. Pan, "GaAs MESFET for high-speed optical detection," in *Proc. 22nd SPIE Int. Tech. Symp.*, vol. 150 of *Laser & Fiber Optics Communications*, (Monterey, CA), pp. 175–184, 1978.
- [2.8] J. Graffeuil, P. Rossel, and H. Martinot, "Light-induced effects in GaAs F.E.T.s," *Electron. Lett.*, vol. 15, pp. 439–441, July 1979.
- [2.9] W. D. Edwards, "Two and three terminal gallium arsenide FET optical detectors," *IEEE Elect. Dev. Lett.*, vol. EDL-1, pp. 149–150, Aug. 1980.
- [2.10] J. C. Gammel and J. M. Ballantyne, "The OPFET: A new high speed optical detector," in *Proc. IEDM Tech. Dig.*, pp. 120–123, 1978.
- [2.11] T. Sugeta and Y. Mizushima, "High speed photoresponse mechanism of a GaAs-MESFET," *Japan. J. Appl. Phys.*, vol. 19, pp. L27–L29, Jan. 1980.

- [2.12] J. C. Gammel and J. M. Ballantyne, "Comments on High speed photoresponse mechanism of a GaAs-MESFET," *Japan. J. Appl. Phys.*, vol. 19, pp. L273–L275, May 1980.
- [2.13] A. A. A. de Salles, *Optical control of microwave field effect transistors*. Ph.D. thesis, Univ. of London, 1982.
- [2.14] H. Mizuno, "Microwave characteristics of an optically controlled GaAs MESFET," *IEEE Trans. Microwave Theory Tech.*, vol. MTT-31, pp. 596–599, July 1983.
- [2.15] J. L. Gautier, D. Pasquet, and P. Pouvil, "Optical effects on the static and dynamic characteristics of a GaAs MESFET," *IEEE Trans. Microwave Theory Tech.*, vol. MTT-33, pp. 819–822, Sept. 1985.
- [2.16] J. R. Forrest, F. P. Richards, and A. Perichon, "The microwave MESFET optical detector," in *Proc. IEEE IEDM Tech. Dig.*, (San Francisco), pp. 529–532, Nov. 1982.
- [2.17] J. P. Noad, E. H. Hara, R. H. Hum, and R. I. MacDonald, "FET photodetectors: A combined study using optical and electron-beam stimulation," *IEEE Trans. Electron Devices*, vol. ED-29, pp. 1792–1797, Nov. 1982.
- [2.18] R. N. Simons and K. B. Bhasin, "Analysis of optically controlled microwave/millimeter-wave device structures," *IEEE Trans. Microwave Theory Tech.*, vol. MTT-34, pp. 1346–1355, Dec. 1986.
- [2.19] R. N. Simons, "Microwave performance of an optically controlled AlGaAs/GaAs high electron mobility transistor and GaAs MESFET," *IEEE Trans. Microwave Theory Tech.*, vol. MTT-35, pp. 1444–1455, Dec. 1987.
- [2.20] A. Madjar, P. R. Herczfeld, and A. Paoletta, "Photoavalanche effects in a GaAs MESFET," *Microwave Optical Tech. Lett.*, vol. 3, pp. 60–62, Feb. 1990.
- [2.21] G. J. Papaionannou and J. R. Forrest, "On the photoresponse of GaAs MESFET's: Backgating and deep traps effect," *IEEE Trans. Electron Devices*, vol. ED-33, pp. 373–378, Mar. 1986.
- [2.22] R. B. Darling and J. P. Uyemura, "Optical gain and large-signal characteristics of illuminated GaAs MESFET's," *IEEE J. Quantum Electron.*, vol. QE-23, pp. 1160–1171, July 1987.
- [2.23] A. J. Seeds and A. A. A. de Salles, "Optical control of microwave semiconductor devices," *IEEE Trans. Microwave Theory Tech.*, vol. 38, pp. 577–585, May 1990.

- [2.24] A. A. de Salles and M. A. Romero, "Al<sub>0.3</sub>Ga<sub>0.7</sub>As/GaAs HEMT's under optical illumination," *IEEE Trans. Microwave Theory Tech.*, vol. 39, pp. 2010–2017, Dec. 1991.
- [2.25] S. H. Lo and C. P. Lee, "Numerical analysis of the photoeffects in GaAs MESFET's," *IEEE Trans. Electron Devices*, vol. 39, pp. 1564–1570, July 1992.
- [2.26] A. Madjar, P. R. Herczfeld, and A. Paoella, "Analytical model for optically generated currents in GaAs MESFETs," *IEEE Trans. Microwave Theory Tech.*, vol. 40, pp. 1681–1691, Aug. 1992.
- [2.27] A. Paoella, *The photoresponse of the GaAs MESFET*. Ph.D. Thesis, Drexel Univ., PA, USA, 1992.
- [2.28] A. Madjar, A. Paoella, and P. R. Herczfeld, "Modeling the optical switching of MESFET's considering the external and internal photovoltaic effects," *IEEE Trans. Microwave Theory Tech.*, vol. 42, pp. 62–67, Jan. 1994.
- [2.29] A. Paoella, A. Madjar, and P. R. Herczfeld, "Modeling the GaAs MESFET's response to modulated light at radio and microwave frequencies," *IEEE Trans. Microwave Theory Tech.*, vol. 42, pp. 1122–1130, July 1994.
- [2.30] M. A. Romero and P. R. Herczfeld, "Negative photoresponse in modulation doped field effect transistors (MODFET's): Theory and experiment," *IEEE Trans. Microwave Theory Tech.*, vol. 43, pp. 511–517, Mar. 1995.
- [2.31] J. R. Forrest and A. A. de Salles, "Optics control microwaves," *Microwave Syst. News*, pp. 112–122, June 1981.
- [2.32] A. A. de Salles, "Optical control of GaAs MESFET's," *IEEE Trans. on Microwave Theory & Tech.*, vol. MTT-31, pp. 812–820, Oct. 1983.
- [2.33] G. J. Chaturvedi, R. K. Purohit, and B. L. Sharma, "Optical effect on GaAs MESFETs," *Infrared Phys.*, vol. 23, no. 2, pp. 65–68, 1983.
- [2.34] H. J. Sun, R. J. Gutmann, and J. M. Borrego, "Photoeffects in common-source and common-drain microwave GaAs MESFET oscillators," *Solid-St. Electron.*, vol. 24, no. 10, pp. 935–940, 1981.
- [2.35] R. A. Minasian, "Simplified GaAs M.E.S.F.E.T. model to 10 GHz," *Electron. Lett.*, vol. 13, pp. 549–551, Sept. 1977.
- [2.36] M. A. Romero, A. Bangert, X. Zhang, and P. R. Herczfeld, "Wavelength dependence of the optical control of a HEMT oscillator," *Microwave Optical Tech. Lett.*, vol. 5, pp. 38–41, Jan. 1992.

- [2.37] B. B. Pal and S. N. Chattopadhyay, "GaAs OPFET characteristics considering the effect of gate depletion with modulation due to incident radiation," *IEEE Trans. Electron Devices*, vol. 39, pp. 1021–1027, May 1992.
- [2.38] P. Chakrabarti, N. L. Shrestha, S. Srivastava, and V. Khemka, "An improved model of ion-implanted GaAs OPFET," *IEEE Trans. Electron Devices*, vol. 39, pp. 2050–2059, Sept. 1992.
- [2.39] S. Mishra, V. K. Singh, and B. B. Pal, "Effect of radiation and surface recombination on the characteristics of an ion-implanted GaAs MESFET," *IEEE Trans. Electron Devices*, vol. 37, pp. 2–10, Jan. 1990.
- [2.40] H. W. Yen and M. K. Barnoski, "Optical injection locking and switching of transistor oscillators," *Appl. Phys. Lett.*, vol. 32, pp. 182–184, Feb. 1978.
- [2.41] T. Sugeta and Y. Mizushima, "Author's reply to Comments on high speed photoresponse mechanism of a GaAs-MESFET," *Japan. J. Appl. Phys.*, vol. 19, p. L275, May 1980.
- [2.42] R. I. MacDonald, "High gain optical detection with GaAs field effect transistors," *Appl. Opt.*, vol. 20, pp. 591–594, Feb. 1981.
- [2.43] M. S. Shur and L. F. Eastman, "Current-voltage characteristics, small-signal parameters, and switching times of GaAs FET's," *IEEE Trans. Electron Devices*, vol. ED-25, pp. 607–612, June 1978.
- [2.44] M. S. Shur, "Analytical model of GaAs MESFET's," *IEEE Trans. Electron Devices*, vol. ED-25, pp. 612–618, June 1978.
- [2.45] V. K. Singh and B. B. Pal, "Optically-controlled switching characteristics of silicon MESFETs," *Solid-St. Electron.*, vol. 30, no. 3, pp. 267–272, 1987.
- [2.46] T. Takada, K. Yokoyama, M. Ida, and T. Sudo, "A MESFET variable-capacitance model for GaAs integrated circuit simulation," *IEEE Trans. Microwave Theory Tech.*, vol. MTT-30, pp. 719–724, May 1982.
- [2.47] A. Gopinath and J. B. Rankin, "GaAs FET RF switches," *IEEE Trans. Electron Devices*, vol. ED-32, pp. 1272–1278, July 1985.
- [2.48] V. K. Singh, S. N. Chattopadhyay, and B. B. Pal, "Optically controlled characteristics in an ion-implanted silicon MESFET," *Solid-St. Electron.*, vol. 29, pp. 707–711, July 1986.
- [2.49] V. K. Singh and B. B. Pal, "Effect of optical radiation and surface recombination on the RF switching parameters of a GaAs MESFET," *IEE Proc.*, vol. 137, pp. 124–128, Apr. 1990.

- [2.50] A. Paoletta, P. R. Herczfeld, A. Madjar, and T. Higgins, "Optical response of the GaAs MESFET at microwave frequencies and applications," in *Proc. IEEE MTT-S Int. Microwave Symp. Dig.*, pp. 487–490, 1991.
- [2.51] A. Madjar, A. Paoletta, and P. R. Herczfeld, "Light interaction with GaAs MESFET and its applications—A review," *Microwave Optical Tech. Lett.*, vol. 6, pp. 22–27, Jan. 1993.
- [2.52] A. Paoletta, P. R. Herczfeld, and A. Madjar, "The effect of optical intensity on the photoresponse of the GaAs MESFET," *Microwave Optical Tech. Lett.*, vol. 6, pp. 38–42, Jan. 1993.
- [2.53] A. Rosen and F. Zutavern, eds., *High-power optically activated solid-state switches*, ch. 9, pp. 187–217. Boston: Artech House, 1994.
- [2.54] P. Chakrabarti, S. K. Shrestha, A. Srivastava, and D. Saxena, "Switching characteristics of an optically controlled GaAs-MESFET," *IEEE Trans. Microwave Theory Tech.*, vol. 42, pp. 365–375, Mar. 1994.
- [2.55] F. J. Moncrief, "LEDs replace varactors for tuning GaAs FETs," *Microwaves*, vol. 18, pp. 12–13, Jan. 1979.
- [2.56] B. Loriou, J. Guena, and J. F. Sautereau, "Optically frequency modulated GaAs MESFET oscillator," *Electron. Lett.*, vol. 17, pp. 901–902, Nov. 1981.
- [2.57] A. A. de Salles and J. R. Forrest, "Theory and experiment for the GaAs MESFET under optical illumination," in *Proc. 11th Eur. Microwave Conf.*, (Amsterdam), pp. 280–285, Sept. 1981.
- [2.58] A. Paoletta and P. R. Herczfeld, "Optical gain control of a GaAs MMIC distributed amplifier," *Microwave Optical Tech. Lett.*, vol. 1, pp. 13–16, Mar. 1988.
- [2.59] P. R. Herczfeld, A. Paoletta, A. Daryoush, W. Jemison, and A. Rosen, "Optical phase and gain control of a GaAs MMIC transmit-receive module," in *Proc. Eur. Microwave Conf.*, (Stockholm), pp. 831–836, Sept. 1988.
- [2.60] I. D. Blanchflower and A. J. Seeds, "Optical control of frequency and phase of GaAs MESFET oscillator," *Electron. Lett.*, vol. 25, pp. 359–360, Mar. 1989.
- [2.61] R. D. Esman, L. Goldberg, and J. F. Weller, "Optical phase control of an optically injection-locked FET microwave oscillator," *IEEE Trans. Microwave Theory Tech.*, vol. 37, pp. 1512–1518, Oct. 1989.
- [2.62] W. D. Jemison, T. Berceci, A. Paoletta, P. R. Herczfeld, D. Kasemset, and A. W. Jacomb-Hood, "Optical control of a digital phase shifter," in *Proc. IEEE MTT-S Int. Microwave Symp. Dig.*, pp. 233–236, 1990.

- [2.63] C. Rauscher, L. Goldberg, and A. M. Yurek, "GaAs FET demodulator and down-converter for optical-microwave links," *Electron. Lett.*, vol. 22, pp. 705–706, June 1986.
- [2.64] A. Bangert, J. Rosenzweig, A. Hülsmann, G. Kaufel, K. Köhler, and J. Schneider, "Optical control of pseudomorphic HEMT-based MMIC oscillators," *Microwave Optical Tech. Lett.*, vol. 6, pp. 36–38, Jan. 1993.
- [2.65] A. Bangert and T. Lauterbach, "Initial observations of optical injection locking of oscillators using heterojunction bipolar transistors," *Electron. Lett.*, vol. 28, pp. 621–623, Mar. 1992.
- [2.66] T. Berceci and A. Chapman, "Improved linearity of MESFET amplifiers with optical illumination," in *Proc. Eur. Microwave Conf.*, (Rome), pp. 814–819, Sept. 1987.
- [2.67] A. Paoella and P. R. Herczfeld, "Optical control of a GaAs MMIC transmit/receive module," in *Proc. IEEE MTT-S Int. Microwave Symp. Dig.*, pp. 959–962, May 1988.
- [2.68] A. Madjar, A. Paoella, and P. R. Herczfeld, "The compressive nature of optical detection in GaAs MESFETs and possible applications as an RF logarithmic amplifier," *IEEE Trans. Microwave Theory Tech.*, vol. 41, pp. 165–167, Jan. 1993.
- [2.69] A. A. de Salles and J. R. Forrest, "Initial observations of optical injection locking of GaAs metal semiconductor field effect transistor oscillators," *Appl. Phy. Lett.*, vol. 38, pp. 392–394, Mar. 1981.
- [2.70] A. A. A. de Salles, "An analysis of the optical injection locking of GaAs MESFET oscillators," in *Proc. SPIE Int. Tech. Symp.*, vol. 477 of *Optical Tech. for Microwave Appl.*, pp. 114–118, 1984.
- [2.71] A. Bangert and M. Ludwig, "A direct optical injection locked 8 GHz MMIC oscillator," in *Proc. IEEE MTT-S Int. Microwave Symp. Dig.*, pp. 499–502, 1991.
- [2.72] T. P. Higgins, "Direct optical subharmonically injection-locked MESFET oscillators," *Microwave Optical Tech. Lett.*, vol. 6, pp. 33–36, Jan. 1993.
- [2.73] D. Yang, P. K. Bhattacharya, and T. Brock, "Direct optical injection locking of monolithically integrated  $\text{In}_{0.53}\text{Ga}_{0.47}\text{As}/\text{In}_{0.52}\text{Al}_{0.48}\text{As}$  MODFET oscillators." *Electron. Lett.*, vol. 29, pp. 944–945, May 1993.

- [2.74] D. Yang, P. Bhattacharya, R. Lai, T. Brock, and A. Paoletta, "Optical control and injection locking of monolithically integrated  $\text{In}_{0.53}\text{Ga}_{0.47}\text{As}/\text{In}_{0.52}\text{Al}_{0.48}\text{As}$  MODFET oscillators," *IEEE Trans. Electron Devices*, vol. 42, pp. 31–37, Jan. 1995.
- [2.75] M. Karaküçük, W. Q. Li, P. N. Freeman, J. R. East, G. I. Haddad, and P. K. Bhattacharya, "A direct optically injection-locked 2.6GHz HBT oscillator," *Microwave Optical Tech. Lett.*, vol. 6, pp. 609–611, Aug. 1993.
- [2.76] P. N. Freeman, W. Li, M. Karaküçük, J. R. East, G. I. Haddad, and P. K. Bhattacharya, "Optically controlled microwave oscillators fabricated using GaAs/AlGaAs HBTs with transparent ITO emitter contacts," in *Proc. SPIE Int. Tech. Symp.*, vol. 2155, pp. 24–28, Jan. 1994.
- [2.77] G. Grimes, "Where microwave and optics meet," *Photonics Spectra*, vol. 23, pp. 101–110, May 1989.
- [2.78] A. Paoletta, S. Malone, , and T. B. P. R. Herczfeld, "MMIC compatible lightwave-microwave mixing technique," *IEEE Trans. Microwave Theory Tech.*, vol. 43, pp. 518–522, Mar. 1995.
- [2.79] A. Paoletta, A. Madjar, P. R. Herczfeld, and D. Sturzebecher, "Optically controlled GaAs MMIC switch using a MESFET as an optical detector," in *Proc. IEEE MTT-S Int. Microwave Symp. Dig.*, pp. 941–944, 1990.
- [2.80] F. Riesz, B. Szentpáli, P. Gottwald, and M. Németh-Salley, "A novel MESFET-compatible GaAs optoelectronic switch," *Microwave Optical Tech. Lett.*, vol. 5, pp. 112–114, Mar. 1992.
- [2.81] J. L. Freeman, S. Ray, D. L. West, and A. G. Thompson, "Optoelectronic devices for unbiased microwave switching," in *Proc. IEEE MTT-S Int. Microwave Symp. Dig.*, pp. 673–676, 1992.
- [2.82] S. Banda, E. Suematsu, and H. Ogawa, "Photoparametric amplifier/converter in lightwave communication systems," in *Proc. 23rd Eur. Microwave Conf.*, (Madrid), pp. 747–750, Sept. 1993.
- [2.83] C. A. Liechti, "Microwave field-effect transistors—1976," *IEEE Trans. Microwave Theory Tech.*, vol. MTT-24, pp. 279–300, June 1976.
- [2.84] R. A. Gaspari and H. H. Yee, "Microwave GaAs FET switching," in *Proc. IEEE MTT-S Int. Microwave Symp. Dig.*, pp. 58–60, 1978.
- [2.85] W. V. McLevige and V. Sokolov, "Resonating GaAs FET devices for microwave switching," *IEEE Trans. Electron Devices*, vol. ED-28, pp. 198–204, Feb. 1981.

- [2.86] J. L. Vorhaus, W. Fabian, P. B. Ng, and Y. Tajima, "Dual-gate GaAs FET switches," *IEEE Trans. Electron Devices*, vol. ED-28, pp. 204–211, Feb. 1981.
- [2.87] Y. Ayasli, "Microwave switching with GaAs FETs," *Microwave J.*, vol. 25, pp. 61–74, Nov. 1982.
- [2.88] V. Sokolov, J. J. Geddes, A. Contolatis, P. E. Bauhahn, and C. Chao, "A *K*-band GaAs monolithic phase shifter," *IEEE Trans. Microwave Theory Tech.*, vol. MTT-31, pp. 1077–1083, Dec. 1983.
- [2.89] D. Fryklund and R. Walline, "Low cost, low drain, high speed, wideband GaAs MMIC switches," *Microwave J.*, pp. 121–125, Dec. 1985.
- [2.90] C. Andricos, I. J. Bahl, and E. L. Griffin, "*C*-Band 6-bit GaAs monolithic phase shifter," *IEEE Trans. Microwave Theory Tech.*, vol. MTT-33, pp. 1591–1596, Dec. 1985.
- [2.91] R. J. Gutmann, D. Fryklund, and D. Menzer, "Characterization and design of GaAs MESFETs for broadband control applications," in *Proc. IEEE MTT-S Int. Microwave Symp. Dig.*, pp. 389–392, 1986.
- [2.92] L. C. Upadhyayula, R. L. Camisa, G. Taylor, S. N. Subbarao, and S. G. Liu, "Passive GaAs FET switch models and their application in phase shifters," in *Proc. IEEE MTT-S Int. Microwave Symp. Dig.*, pp. 903–906, 1987.
- [2.93] M. J. Schindler and A. Morris, "DC–40 GHz and 20–40 GHz MMIC SPDT switches," *IEEE Trans. Microwave Theory Tech.*, vol. 35, pp. 1486–1493, Dec. 1987.
- [2.94] M. J. Schindler, M. E. Miller, and K. M. Simon, "DC–20 GHz  $N \times M$  passive switches," *IEEE Trans. Microwave Theory Tech.*, vol. 36, pp. 1604–1613, Dec. 1988.
- [2.95] M. B. Shifrin, P. J. Katzin, and Y. Ayasli, "Monolithic FET structures for high-power control component applications," *IEEE Trans. Microwave Theory Tech.*, vol. 37, pp. 2134–2141, Dec. 1989.
- [2.96] P. Katzin, M. B. S. B. E. Bedard, and Y. Ayasli, "High-speed, 100+ RF switches using GaAs MMICs," *IEEE Trans. Microwave Theory Tech.*, vol. 40, pp. 1989–1996, Nov. 1992.
- [2.97] C. M. Buck, K. R. Williams, and R. Leblanc, "The development of MMIC switch FET models for the Philips microwave D07M foundry process," in *IEE Colloquium*, vol. Digest No: 1994/092 of *Modelling, Design and Application of MMIC's*, (London), pp. 9/1–9/6, 1994.

- 
- [2.98] Y. Ayasli, A. Platzker, J. Vorhaus, and L. D. Reynolds Jr., "A monolithic single-chip X-band four-bit phase shifter," *IEEE Trans. Microwave Theory Tech.*, vol. MTT-30, pp. 2201–2206, Dec. 1982.
- [2.99] A. Ehoud, L. P. Dunleavy, S. C. Lazar, and R. E. Branson, "Extraction techniques for FET switch modeling," *IEEE Trans. Microwave Theory Tech.*, vol. 43, pp. 1863–1868, Aug. 1995.
- [2.100] K. B. Bhasin, P. C. Claspy, M. A. Richard, R. R. Romanofsky, M. Benedett, G. Gustafson, and W. Walters, "Control of a GaAs monolithic Ka-band phase shifter using a high-speed optical interconnect," *IEEE Trans. Microwave Theory Tech.*, vol. 38, pp. 686–688, May 1990.

# Chapter 3

## Static Photo-Effects in Microwave GaAs FET's

### Contents

---

<b>3.1</b>	<b>Introduction . . . . .</b>	<b>54</b>
<b>3.2</b>	<b>Optical Control of GaAs FET's . . . . .</b>	<b>56</b>
<b>3.3</b>	<b>Photoconductive Effects . . . . .</b>	<b>59</b>
<b>3.4</b>	<b>Photovoltaic Effects . . . . .</b>	<b>60</b>
3.4.1	Barrier Interface Photovoltaic Effect . . . . .	60
3.4.2	Gate Depletion Photovoltaic Effect . . . . .	61
<b>3.5</b>	<b>Predominant Photo-Effect in Microwave FET's . . . . .</b>	<b>63</b>
<b>3.6</b>	<b>Evaluation of the Gate Photo-Effect . . . . .</b>	<b>66</b>
<b>3.7</b>	<b>GaAs FET Static Electrical Parameters . . . . .</b>	<b>67</b>
3.7.1	Pinch-Off Voltage . . . . .	67
3.7.2	Gate Schottky Junction Ideality Factor . . . . .	68
3.7.3	Gate Schottky Junction Reverse Saturation Current . . . . .	69
3.7.4	Gate Schottky Junction Built-In Potential . . . . .	69
<b>3.8</b>	<b>GaAs FET Static Optical Parameters . . . . .</b>	<b>69</b>
3.8.1	Optically Illuminated GaAs FET Area . . . . .	69
3.8.2	Optical Power Reflectivity . . . . .	70
3.8.3	Photon Flux Density . . . . .	71

---

### 3.1 Introduction

**S**TATIC photo-effects in microwave GaAs FET's have been examined by a number of investigators and experimental work has been carried out to exploit a variety

of microwave circuit functions, as outlined in the literature review of Chapter 2. Of particular significance is the work of de Salles [3.1, 3.2] and more recently Madjar *et al.* [3.3], who have both developed comprehensive models relating the device physics of the FET structure to its photo-responsivity. In this chapter the modelling of the GaAs FET under continuous (static) optical illumination was examined in order to establish optical control in the GaAs FET-based switches and phase shifters developed in this work. Furthermore, the static models for the illuminated GaAs FET were used as a basis for modelling the switched (dynamic) optical response of the GaAs FET-based switches.

Section 3.2 explains the fundamental principles underlying the electro-optic interaction in microwave GaAs FET's and this is elaborated upon in Sections 3.3 and 3.4 where particular photo-mechanisms are identified. Specifically, Section 3.3 describes the photoconductive effect in the active channel of the GaAs FET and Section 3.4 considers the photovoltaic effects occurring in the gate depletion region and barrier interface region of the GaAs FET. A photo-effect suitable for direct optical switching of the GaAs FET is described in Section 3.5 and experimentally assessed in Section 3.6. Finally, Sections 3.7 and 3.8 describe experimental and theoretical methods that were used in the determination of some of the important optical and electrical parameters required in subsequent chapters to evaluate the switching performance of the optically controlled GaAs FET.

The key points of this chapter are identified below.

- **Description and review of the following optically-induced mechanisms in microwave GaAs FET's under continuous optical illumination:**
  - photoconductive effect
  - barrier interface (internal) photovoltaic effect
  - gate depletion region (external) photovoltaic effect.
- **Description and identification of a predominant photo-effect for optically controlled GaAs FET switching.**
- **Test arrangement for evaluating the optical and microwave properties of the experimental GaAs FET's.**
- **Experimental and theoretical determination of the following static microwave and optical parameters associated with the experimental GaAs FET's:**
  - pinch-off voltage
  - ideality factor

- reverse saturation current
- gate Schottky barrier built-in potential
- illuminated GaAs FET area
- surface optical power reflectivity.

## 3.2 Optical Control of GaAs FET's

The fundamental principles underlying the electro-optic interaction can be examined, and the essential operation of a FET subject to static optical stimulus understood, by considering the basic FET structure, shown in Figure 3.1.

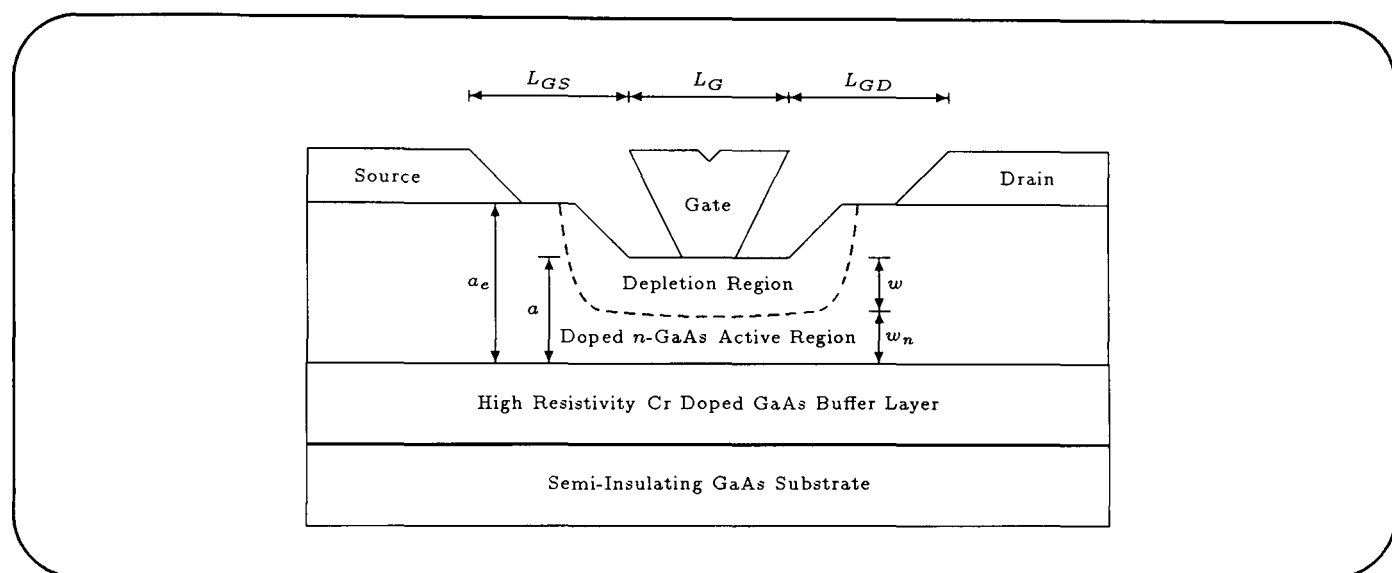


**Figure 3.1:** Schematic cross-section of a basic microwave GaAs MESFET.

For microwave applications at frequencies greater than a few giga-Hertz, and in particular for MMIC's, the GaAs FET has become the principal device for amplifying and switching signals. The structure of a microwave GaAs FET differs only slightly from that of the well known silicon Junction-FET (JFET). The principal differences lie in the fact that the gate electrode is constructed as a metal-semiconductor Schottky contact, as opposed to the conventional  $p^+ - n$  contact used in JFET's, and that the gate length (defined in the direction of current flow) must be very short ( $\lesssim 1 \mu\text{m}$ ). The shorter gate length results in a lower gate input capacitance,  $C_{gs}$ , and therefore increases the transistor's current gain cut-off frequency,  $f_T$ , as given by [3.4]

$$f_T = \frac{g_m}{2\pi C_{gs}} \quad (3.1)$$

where  $g_m$  is the intrinsic microwave transconductance. Furthermore, in the interest of keeping the gate resistance low and hence the microwave power gain high, the gate is fed through as many points as possible, yielding an interdigitated gate structure. This is important in terms of the optical responsivity of the FET since this effectively

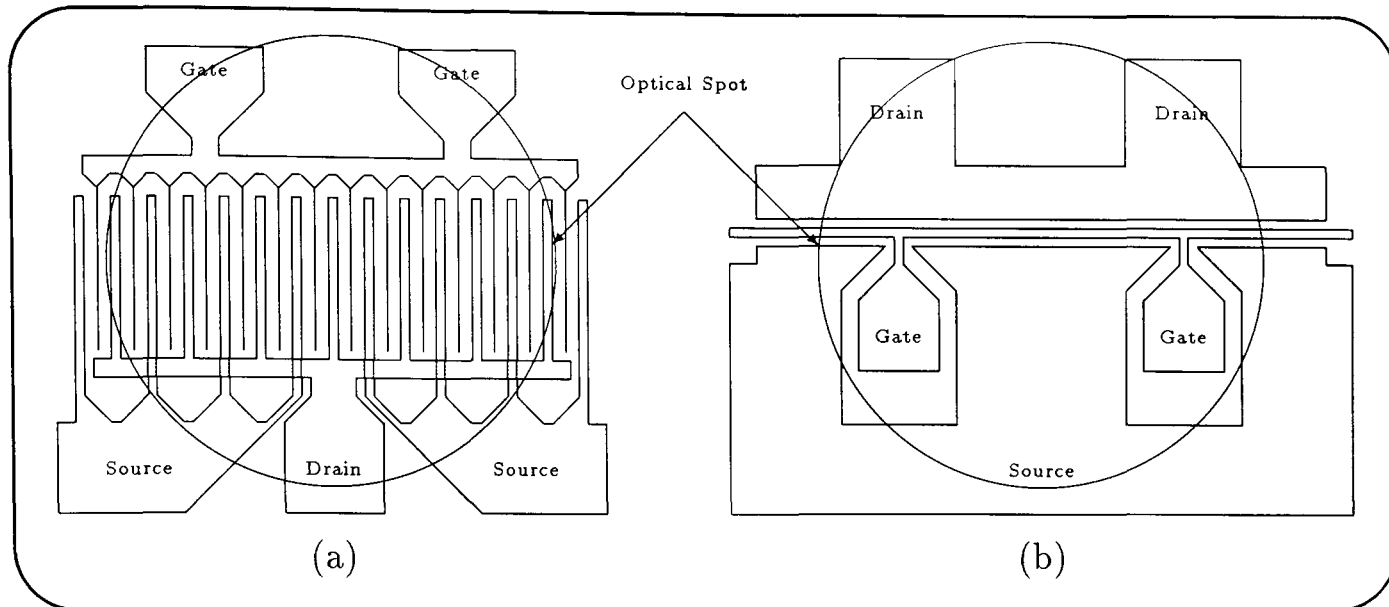


**Figure 3.2:** Plan view schematic of two typical microwave MESFET gate structures, illustrating the difference in compatibility with an optical beam spot. (a) Interdigitated (multi-finger) gate. (b)  $\Pi$ -gate.

increases the optical absorption area and reduces the incompatibility between the shape of the optical spot and the FET structure, as depicted in Figure 3.2.

The increased use of multiple gate fingers in modern microwave MESFET's has led to the gate width of the device being more commonly referred to as the gate periphery, defined as the product of the actual gate width of the MESFET and the number of gate fingers. In relation to the optical responsivity of the FET the following structural points are of interest.

1. The gate-to-source and gate-to-drain inter-electrode spacings,  $L_{GS}$  and  $L_{GD}$ , since these define the regions where optical absorption occurs.
2. The Schottky gate depletion region since this gives rise to a photovoltaic effect.
3. The interface between the high resistivity buffer layer and the  $n$ -type channel since the resultant interface barrier potential gives rise to a photovoltaic effect.

When the FET is illuminated, optical absorption can take place only within the gate-to-source and gate-to-drain inter-electrode spacings, since the thickness of the ohmic contact metallization ( $\gtrsim 0.3 \mu\text{m}$ ) prevents absorption elsewhere within the structure. The inter-electrode spacings expose the active regions of the FET such that photo-excitation of free-carriers (electron-hole pairs) can take place within the semiconductor material. This excitation can occur only when the illumination has a photon energy that is greater than, or equal to the band-gap of the semiconductor, the photon energy being related to the wavelength,  $\lambda$ , of the incident light by

$$E_{ph} = \frac{hc}{\lambda} \quad (3.2)$$

where  $h$  is Planck's constant and  $c$  the velocity of light in a vacuum. The choice of optical wavelength will be influenced further by the required optical absorption depth within the semiconductor material. In a semiconductor material, the photon flux density,  $\Phi(y)$ , decays exponentially with distance,  $y$ , into the material as given by

$$\Phi(y) = \Phi_0(1 - R)e^{-\alpha y} \quad (3.3)$$

where  $\alpha$  is the optical absorption coefficient of the semiconductor,  $R$  the Fresnel (optical) reflection coefficient and  $\Phi_0$  the incident photon flux density at the surface of the material (i.e. at  $y = 0$ ). The optical absorption depth ( $1/\alpha$ ) defines the depth at which the photon flux density has fallen to  $1/e$  of the surface value. The dependence of the optical absorption coefficient on optical wavelength for GaAs is shown in Figure 3.3 [3.5].

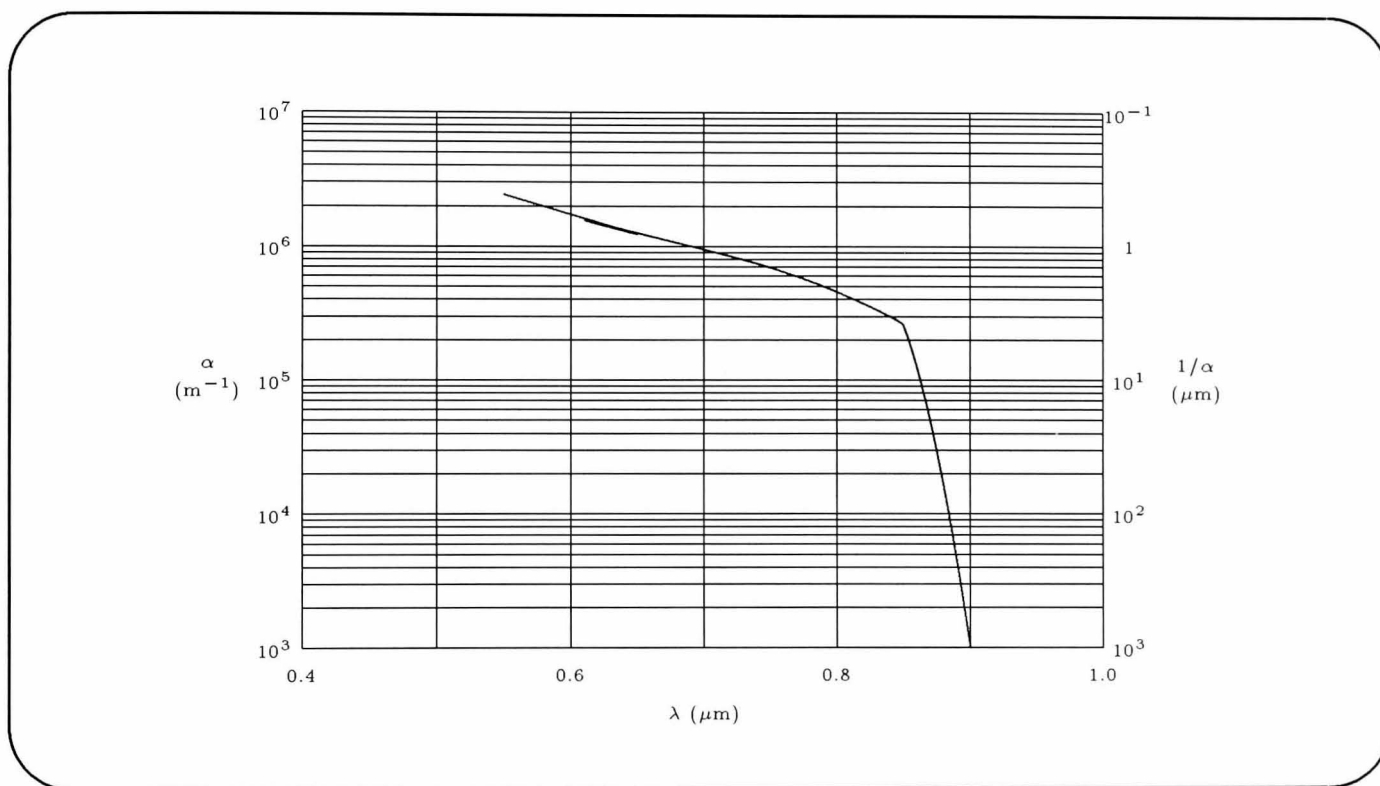


**Figure 3.3:** Optical absorption coefficient as a function of wavelength for gallium arsenide at 300 K.

This curve shows that a given semiconductor material is usable only over a limited wavelength range. The upper cut-off wavelength occurs when the incident photon energy at the surface of the material is insufficient to create an electron-hole pair. The upper cut-off wavelength,  $\lambda_c$ , is determined for a given material by

$$\lambda_c = \frac{hc}{E_g} \quad (3.4)$$

where  $E_g$  is the band-gap of the semiconductor. Thus, for GaAs with a band-gap of 1.42 eV, free carriers will be generated provided the wavelength of the incident light is less than approximately 875 nm, which can be obtained from standard laser diode and LED sources. The lower cut-off wavelength occurs because the absorption coefficient

value at shorter wavelengths is very large and the optical radiation is absorbed very near the surface of the semiconductor.

The photon absorption within the FET and the subsequent optically-induced changes in its RF and DC performance can be understood through consideration of both photoconductive and photovoltaic phenomena which occur within specific regions of the FET structure.

### 3.3 Photoconductive Effects

The absorption of photon energy within the active  $n$ -type channel of the FET structure generates excess carriers and increases the conductivity of this region, thus setting up a photoconductive current in addition to any drain current. Figure 3.4 illustrates the familiar photoconductive effect and its occurrence within the basic FET structure.

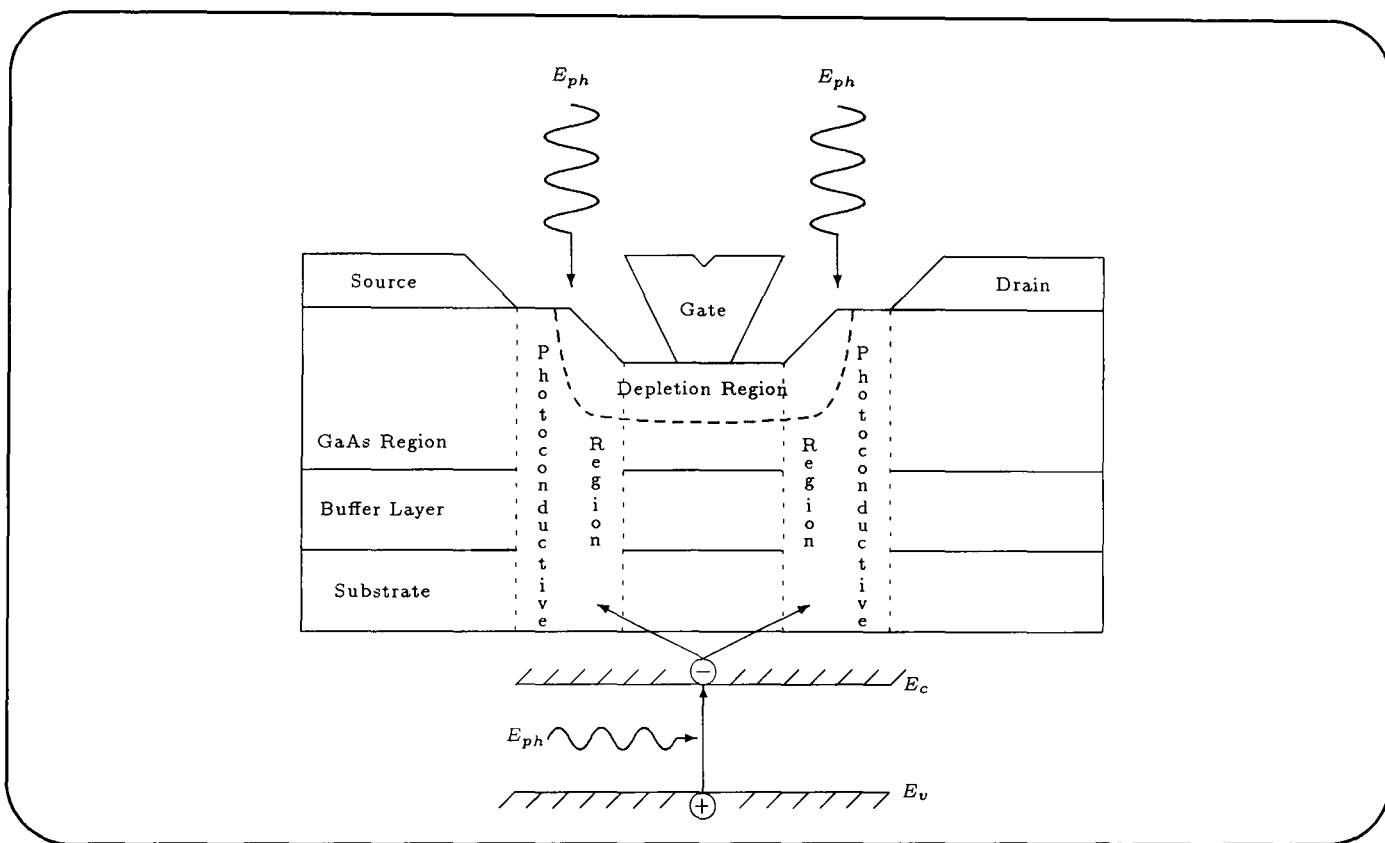


**Figure 3.4:** Photoconductive effects within MESFET's, illustrating the process of intrinsic (band-to-band) photo-excitation and its occurrence within the basic FET structure.

Due to the relatively large doping levels in the  $n$ -type epitaxial layer, typically greater than  $10^{17} \text{ cm}^{-3}$ , the distribution of the optically generated excess carriers in this region will be governed by minority carriers (i.e. holes). The photoconductive current can be evaluated by solving the transport equations governing the optically-induced excess hole concentration for the device under suitable boundary conditions, as shown by Madjar *et al.* [3.3].

## 3.4 Photovoltaic Effects

Two photovoltaic effects occurring in optically illuminated microwave FET's have been identified in the literature and these can be related to photon absorption within the Schottky gate depletion region and the channel-to-substrate barrier interface region.

### 3.4.1 Barrier Interface Photovoltaic Effect

Since a difference in doping levels exists between the  $n$ -type epitaxial layer and the semi-insulating substrate, electrons diffuse from the epitaxial layer to the substrate giving rise to a potential barrier or depletion region at their interface as occurs in  $p$ - $n$  junctions. When photon absorption occurs at this interface barrier, electron-hole pairs are generated within the depletion region, and the electric field associated with this region sweeps these carriers in opposite directions, in a manner similar to that of a photodiode. This establishes a photocurrent across the junction which can be quantified by consideration of the excess carrier density in this barrier region and the optically exposed areas of the FET, as shown by Madjar *et al.* [3.3]. Since the high-resistivity substrate is electrically in series with the junction, the above photocurrent generates a photovoltage which opposes the interface barrier potential and subsequently reduces the barrier height in the illuminated region of the FET. This effect has been termed the *internal* photovoltaic effect by Madjar *et al.* [3.3]. This photovoltage,  $V_{phi}$ , can be determined by modelling the illuminated channel-to-substrate junction as a photocurrent source,  $I_{phi}$ , a diode representing the rectifying junction and a resistor,  $R_{sub}$ , representing the substrate resistance, as shown in Figure 3.5.

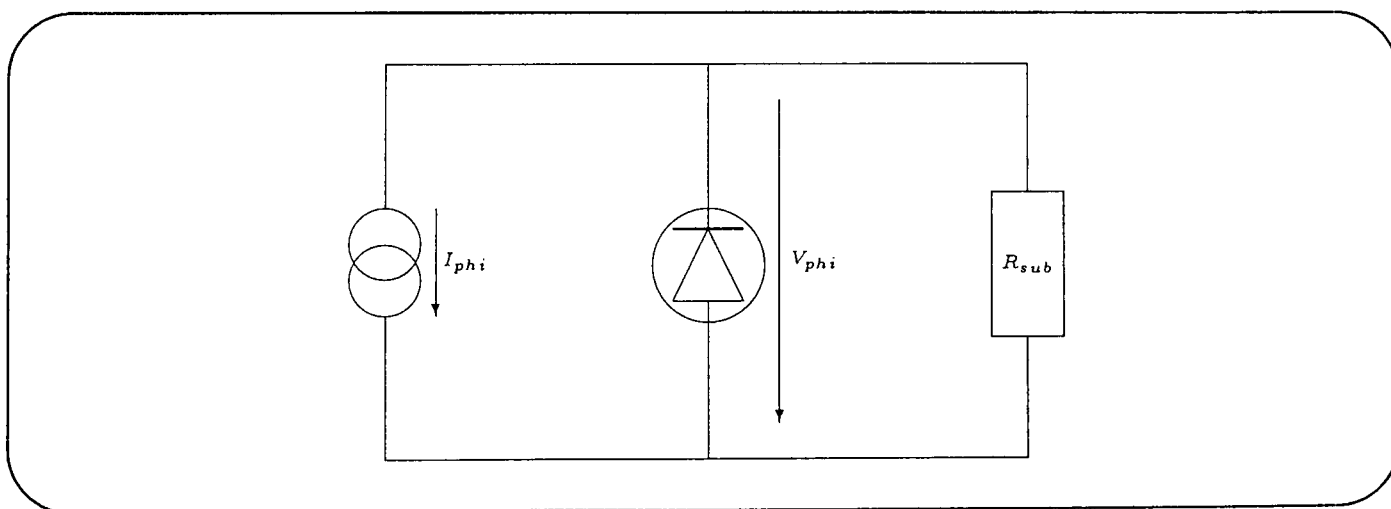


**Figure 3.5:** Static equivalent circuit of the channel-to-substrate interface while under optical illumination.

The reduction in the interface barrier height effectively extends the  $n$ -type channel in the illuminated regions, resulting in an increase in the drain current. Further it relaxes the restriction on electrons entering into the semi-insulating substrate, creating a larger substrate current, as illustrated in Figure 3.6.

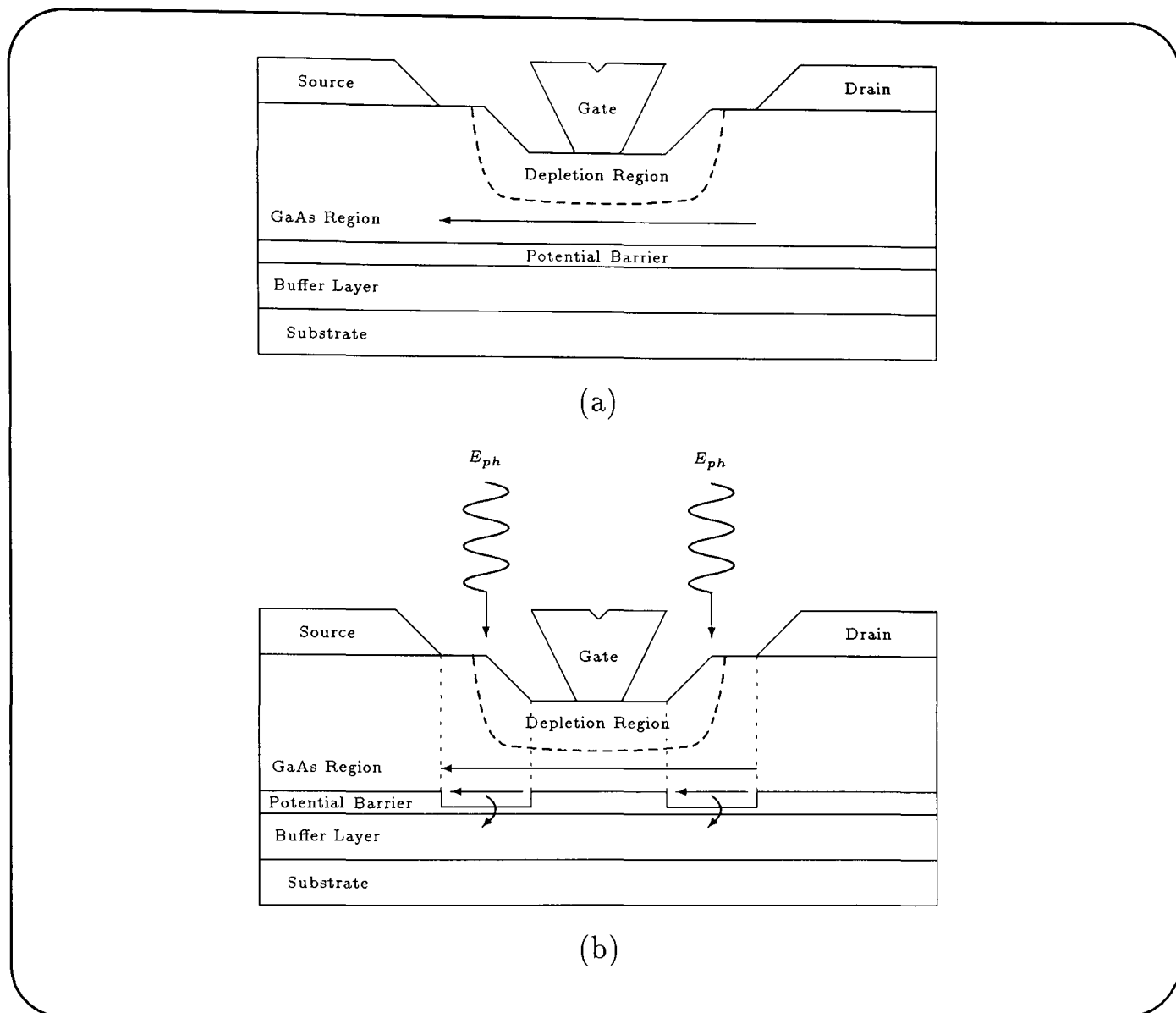


**Figure 3.6:** Internal photovoltaic effect, demonstrating the change in the interface barrier height between the channel and substrate (arrows show current flow). (a) Without illumination. (b) With illumination.

The sum of these two current components results in an optically-induced increase in the drain current which is commonly known as a backgating effect. In the microwave switch circuit described in this thesis, the backgating effect plays no significant role in achieving optically controlled switching.

### 3.4.2 Gate Depletion Photovoltaic Effect

The depletion region set up by an external reverse bias at the gate of a FET provides an additional area for photon absorption. When illuminated, this region acts in a manner almost identical to that of a Schottky photodiode. The high internal electric field associated with the Schottky gate junction causes electron-hole pairs generated by the photon absorption to separate, Figure 3.7(a). In addition, electron-hole pairs generated by photon absorption away from the depletion region (within the  $n$ -type epitaxial region) can contribute to the photo-effect by diffusing into the depletion region before recombination takes place, Figure 3.7(b). Only carriers generated within a minority

carrier diffusion length or so of the edge of the depletion region are likely to be able to do this.

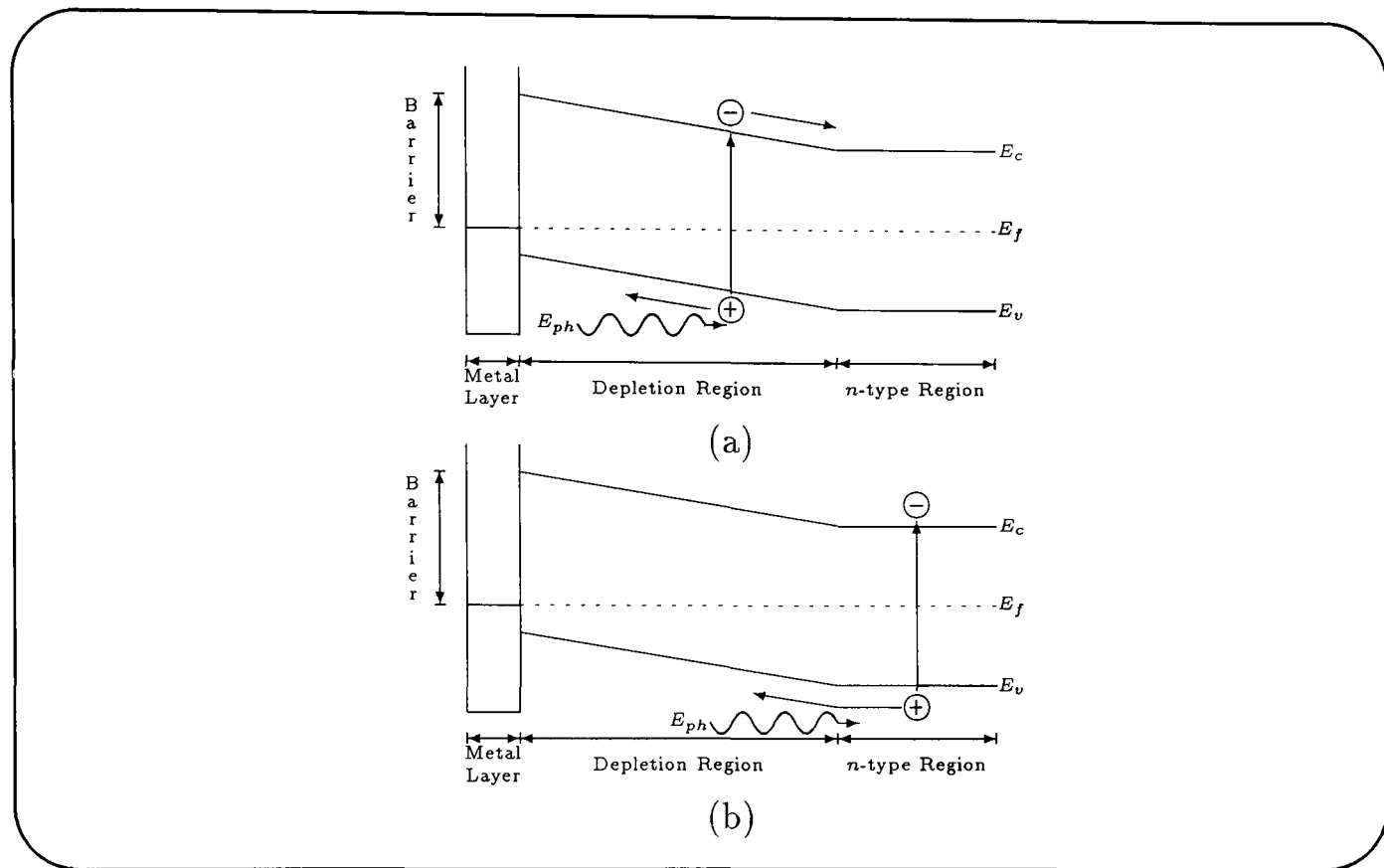


**Figure 3.7:** Band-to-band photo-excitation of an electron-hole pair in a metal semiconductor (Schottky) junction. (a) Within the depletion region. (b) Within the semiconductor region.

The gate short-circuit photocurrent generated by these processes thus consists of two components: that due to optically generated carriers from within the illuminated part of the gate depletion region, obtained by considering the rate of change of optically generated carriers over the gate depletion region depth, and that due to optically generated carriers from within the  $n$ -type channel diffusing into the gate depletion region, obtained by differentiating the optically generated carrier distribution at the interface between the gate depletion region and  $n$ -type channel. De Salles [3.1] developed a mathematical expression to represent these phenomena, and because of the significance of this expression in modelling the direct optical control achieved in the switch circuits described in this thesis, the origins of his expression are examined in more detail in Appendix B.1.

De Salles' expression was used subsequently by Madjar *et al.* [3.3] in the determination of a simplified expression for the photocurrent. They approximated the photocurrent to its pinched-off value, in which the carrier diffusion component could be ignored, such that the photocurrent,  $I_{ph}$ , due to an illuminated area,  $A_i$ , of the FET is given by

$$I_{ph} = q(1 - R)\Phi_0 A_i (1 - e^{-\alpha a}) \quad (3.5)$$

where  $a$  is the thickness of the recessed GaAs epitaxial layer. The above photocurrent will develop a corresponding photovoltage across any resistance shunting the gate of the FET. The resistance in question may be due to the microstrip circuit or the gate bias network. Madjar *et al.* [3.3] have termed this the *external* photovoltaic effect.

### 3.5 Predominant Photo-Effect in Microwave FET's

For typical microwave FET and optical parameters, the photoconductive effect generates a photocurrent in the submicro-amp range, due to the small width of the  $n$ -type channel, and can thus be neglected. The optically-induced gate current is typically in the micro-amp range and, as a result, generates a small photovoltage under normal FET biasing conditions. Since the photocurrent associated with the reduction in the channel-to-substrate interface barrier is in the milli-amp range, the interface barrier photovoltaic effect dominates the static optical response in microwave GaAs FET's under normal bias conditions, and can generate typically a backgate voltage of about 0.8 V. Although the optically-induced gate current is small, its effect can be made significant by loading the gate terminal of the FET with a large bias resistance, in which case the gate depletion region photovoltaic effect becomes predominant over the barrier interface photovoltaic effect, generating a photovoltage sufficiently large to overcome any reverse bias applied to the gate and hence forward bias the FET. The resulting optically-induced voltage, developed across the large gate bias resistor, is superimposed on any reverse gate bias that may be present. Since this photovoltage is equivalent to forward biasing the gate junction, the resultant gate-to-source voltage is reduced and subsequently the extension of the depletion region into the  $n$ -type channel is reduced, allowing a larger drain current to flow as shown in Figure 3.8.

From this the gate-to-source voltage in the illuminated state,  $V_{GSi}$  can be expressed as

$$V_{GSi} = V_{GG} + V_{ph} \quad (3.6)$$

where  $V_{GG}$  is the gate junction reverse bias and  $V_{ph}$  the photovoltage developed across the large gate bias resistance.

This effect is particularly attractive as the primary method for optical control in microwave applications, since the photo-induced variations in the DC and RF characteristics of the FET can be regarded as equivalent to controlling the FET via its gate-to-source voltage. Thus, since the modelling of the FET's DC and RF performance subject to particular reverse bias is well established, this model can be extended simply to predict the outcome of optically controlling the FET. Furthermore, many microwave signal control applications, such as the switching circuit described in the later chapters of this thesis, rely on the voltage at the gate of the FET as the principal controlling

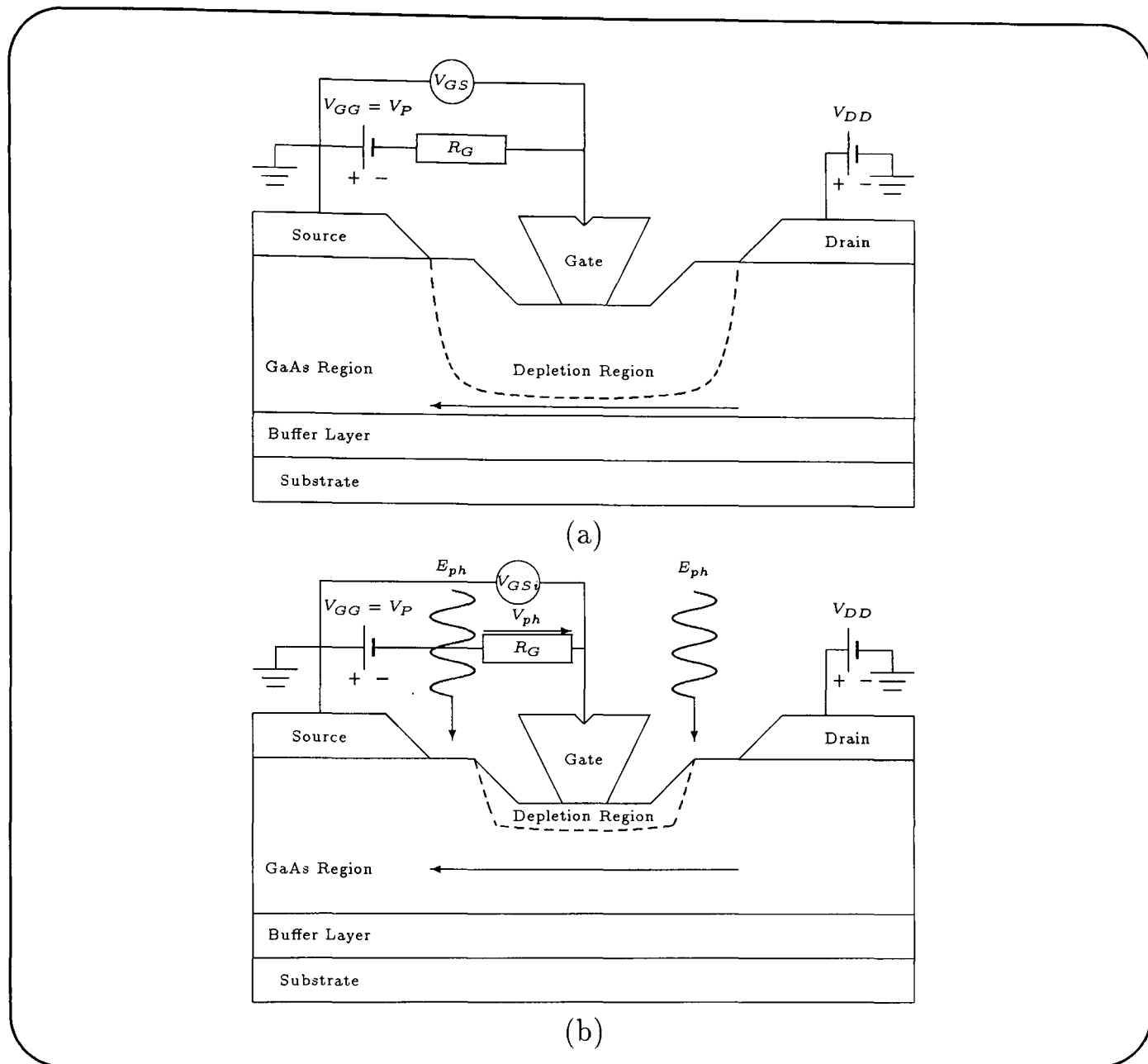


**Figure 3.8:** External photovoltaic effect within the gate depletion region, created by the large external gate resistance (arrows show current flow). (a) Without illumination. (b) With illumination.

mechanism. The foregoing discussion indicates that these functions can be achieved using optical techniques. This would enable the FET to be controlled solely by optical techniques or by a combination of DC and optical means such that a single gate FET effectively becomes a two terminal control device and, similarly, a dual gate MESFET a three terminal control device. The optically-induced change in the gate-to-source voltage can be quantified by modelling the illuminated gate Schottky junction.

This model comprises a current source, representing the gate short-circuit photocurrent,  $I_{ph}$ , shunted by the gate Schottky junction diode and the DC gate bias circuit, which incorporates the large gate bias resistance,  $R_G$ , as shown in Figure 3.9.

If a large resistor, typically greater than  $100\text{ k}\Omega$ , is placed in the gate bias circuit, and provided that a high level of illumination is incident on the FET, an effective open-circuit condition is created at the gate terminal. Under this condition de Salles [3.1] has shown that the resultant gate-to-source voltage, in the illuminated state,

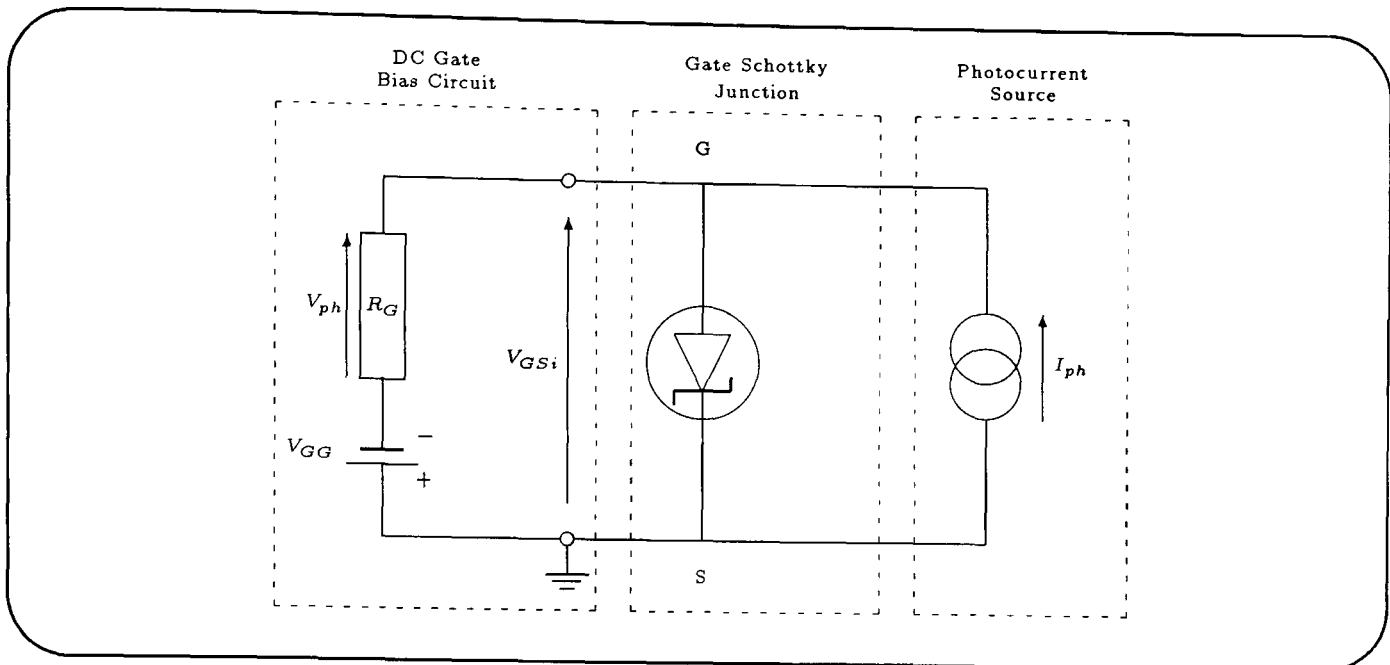


**Figure 3.9:** Static equivalent circuit of the gate Schottky junction while under optical illumination.

can be approximated by the standard open-circuit voltage expression for a Schottky photodiode, given by

$$V_{GSi} = \frac{nkT}{q} \ln \left( \frac{I_{ph}}{I_S} + 1 \right) \quad (3.7)$$

where  $T$  is the absolute temperature,  $q$  the electronic charge,  $k$  Boltzmann's constant and  $n$  and  $I_S$  are respectively the ideality factor and reverse saturation current associated with the Schottky junction. If a low level of illumination is incident on the FET, such that the gate photovoltage is insufficient to completely overcome the gate reverse bias therefore still leaving the FET reverse biased, then the Schottky diode current can be ignored, with the resultant illuminated gate-to-source voltage being given simply by

$$V_{GSi} = V_{GG} + I_{ph}R_G. \quad (3.8)$$

The fundamental limitation to optically controlling commercial microwave GaAs FET's utilized in the switching and phase shifting circuits described in this thesis, is that of poor optical coupling. This results from the limited exposed active areas that are available due to the very fine inter-electrode spacings, which are typically no greater than a few micro-metres. The problem of poor optical coupling is exaggerated further when the shape of the optical beam is considered in relation to the GaAs FET structure. In general, commercial microwave FET's have a long gate width, typically several hundred micro-metres. This, combined with the small inter-electrode spacings, makes the shape of the optically responsive FET regions incompatible with that of a circular beam which could be expected to emerge from an optical source or optical fibre. This problem of optical coupling was, to some extent, overcome in this investigation using two simple techniques to enable commercial FET's to be used under optical control on a standard optical source. The first technique was to choose an FET with

numerous gate fingers, so that the number of optically sensitive regions in the FET structure is increased. This constitutes an increase in the gate periphery and therefore, a direct increase in the gate photocurrent. In the second technique, the optical beam from the laser diode source was focused using a microscope objective. This raised the gate photocurrent by increasing the photon flux density. In the latter technique the optical beam spot was positioned correctly over the sensitive regions of the FET using a micro-positioning platform.

### 3.6 Evaluation of the Gate Photo-Effect

Due to the significance of the gate photovoltaic effect in the realization of the optically controlled switching element described in this thesis, some initial experimental work was carried out to evaluate the static optical and electrical parameters of the GaAs FET. The Hewlett Packard range of low-noise packaged GaAs FET's [3.6] was used in all the experimental work described herein. Initially, experiments were carried out on the ATF-10136 GaAs FET, and this work was extended subsequently to include the ATF-13136 GaAs FET which had a significantly different gate structure, verifying the models and techniques proposed in this thesis. As packaged FET's were used, the hermetically sealed lid had to be removed carefully to permit optical access to the active regions of the GaAs FET. All static optical measurements were made using a continuous wave InGaAlP visible laser diode module (VLM). This laser diode provided a peak optical output power of 5 mW at a wavelength of 670 nm. Thus, for the ATF-10136 FET with a channel depth of approximately  $0.1 \mu\text{m}$  and at a wavelength of 670 nm ( $\alpha \sim 10^6 \text{ m}^{-1}$ ), equation (3.3) predicts that approximately 10% of the incident optical power will be absorbed in the gate depletion region with the FET biased at pinch-off and assuming no surface reflections. Since this device was a class 3A laser product, laser eye protection goggles were worn throughout the experimental work. The laser diode module was mounted in a modified microscope platform. This allowed the optical beam spot to be focussed by a microscope objective, with the focal point adjusted through movement in the vertical plane ( $z$ -direction). The position of the optical beam spot in the horizontal plane ( $x$ - $y$  position) could also be manoeuvred accurately. This experimental arrangement is shown in Figure 3.10.

In order to evaluate a theoretical value for the short-circuit gate photocurrent a number of electrical and optical parameters associated with the GaAs FET need to be determined. Where possible these were obtained by experiment, since these parameters are invariably device dependent. From these parameters and equation (3.5) an approximate value for the static short-circuit gate photocurrent could be established.

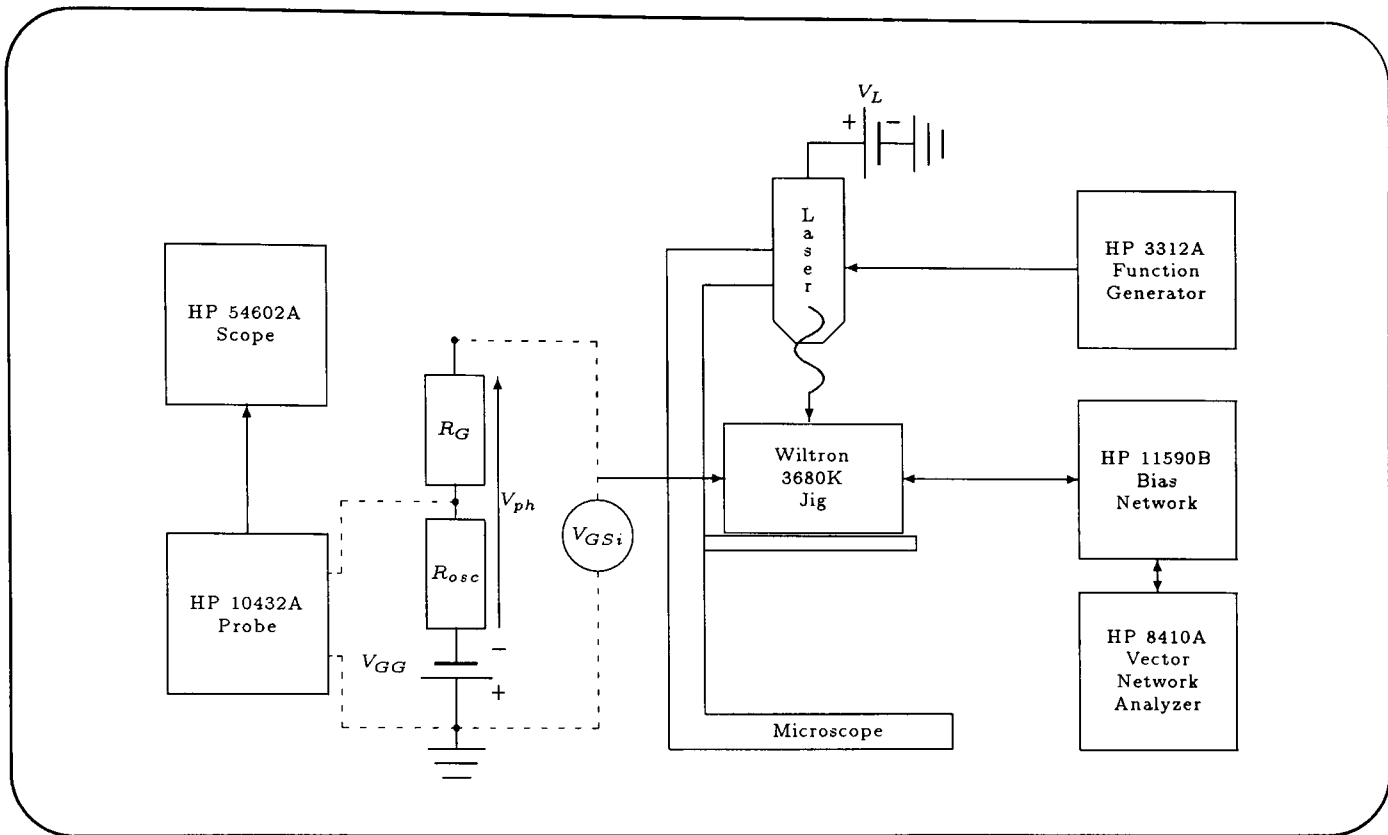


**Figure 3.10:** Apparatus used in the static and dynamic optical and electrical measurements.

## 3.7 GaAs FET Static Electrical Parameters

The required static electrical parameters of the GaAs FET include the following.

- Pinch-off Voltage,  $V_P$ .
- Gate Schottky junction ideality factor,  $n$ .
- Gate Schottky junction reverse saturation current,  $I_S$ .
- Gate Schottky junction built-in potential,  $\phi_B$ .

The pinch-off voltage quoted by the manufacturer can have a large variation from device to device, and since the remaining electrical parameters are not provided, all four parameters were determined approximately by experiment.

### 3.7.1 Pinch-Off Voltage

The pinch-off voltage,  $V_P^\dagger$ , was established experimentally by measuring the drain current and gate voltage characteristics of the GaAs FET in the manner described by Fukui [3.7]. This gave an approximate pinch-off voltage of -1.6 V, with the manufacturer quoting a typical value of -1.3 V and maximum and minimum values of -4.0 V and -0.5 V respectively for the ATF-10136 [3.6].

<sup>†</sup>In this thesis  $V_P$  is used to describe the terminal pinch-off voltage (i.e. the gate-to-source voltage required to bring about pinch-off).

### 3.7.2 Gate Schottky Junction Ideality Factor

The ideality factor,  $n$ , describes the departure from the ideal diode characteristics of the Schottky diode junction at the gate of the GaAs FET. Therefore, the current-voltage behaviour of the gate Schottky junction can be expressed as [3.5]

$$I_{GS} = I_S \left\{ \exp \left( \frac{qV_{GS}}{nkT} \right) - 1 \right\} \quad (3.9)$$

where  $I_{GS}$  and  $V_{GS}$  are the gate-to-source current and voltage respectively, when the source and drain are at DC earth potential. Re-arranging into a general straight-line form and assuming that the junction is forward biased, in which case  $I_{GS} \gg I_S$ , then

$$\ln I_{GS} \simeq \left( \frac{q}{nkT} \right) V_{GS} + \ln I_S. \quad (3.10)$$

Therefore a plot of  $\ln I_{GS}$  against  $V_{GS}$  should yield a straight line with the gradient given by  $q/nkT$ , enabling the ideality factor to be estimated as

$$n = \left( \frac{q}{kT} \right) \frac{dV_{GS}}{d(\ln I_{GS})}. \quad (3.11)$$

The forward current-voltage characteristics of the gate Schottky junction were measured for the ATF-10136 FET and these are plotted in Figure 3.11.

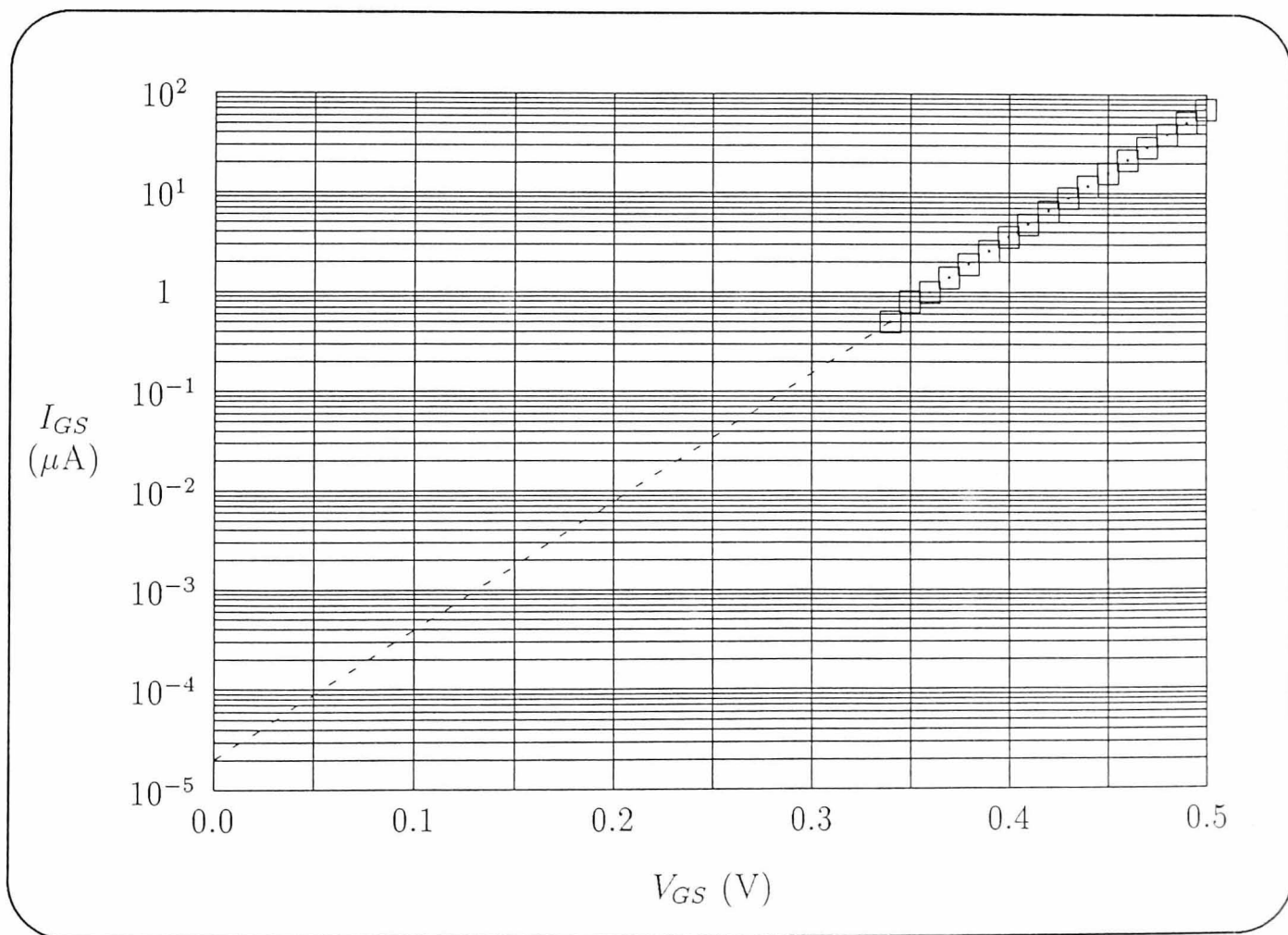


**Figure 3.11:** Forward current-voltage characteristics of the gate Schottky junction of the ATF-10136 with  $V_{DS} = 0V$ .

From this plot and for an absolute temperature of 298 K, the ideality factor was estimated to be 1.29, which is within the expected range of 1.1 to 1.3 [3.7].

### 3.7.3 Gate Schottky Junction Reverse Saturation Current

From equation (3.10) and Figure 3.11 it can be seen that the intercept with the vertical axis will give the value of  $\ln I_S$ . This was determined by extrapolation of the forward current-voltage characteristics to intercept the vertical axis and gave a reverse saturation current of approximately 20 pA.

### 3.7.4 Gate Schottky Junction Built-In Potential

For direct band-gap semiconductors such as GaAs, the thermionic emission theory has been shown to best describe the junction behaviour. According to this theory, the built-in junction potential is given by [3.5]

$$\phi_B = \left( \frac{kT}{q} \right) \ln \left( \frac{A^* T^2}{J_S} \right) \quad (3.12)$$

where  $A^*$  is the modified Richardson constant ( $8.2 \text{ Acm}^{-2}\text{K}^{-2}$ ). The reverse saturation current density,  $J_S$ , is given by

$$J_S = \frac{I_S}{A_G} = \frac{I_S}{W_G L_G} \quad (3.13)$$

where  $A_G$  is the gate area. The gate periphery,  $W_G$  and the gate length,  $L_G$  are taken to be  $500 \mu\text{m}$  and  $0.3 \mu\text{m}$ , respectively for the AFT-10136 GaAs FET [3.6]. Therefore, the built-in potential for the titanium-tungsten/GaAs Schottky junction of the ATF-10136 is approximately 0.63 V.

## 3.8 GaAs FET Static Optical Parameters

To determine a value for the short-circuit gate photocurrent, the following optical parameters of the GaAs FET are required.

- Optically illuminated area,  $A_i$ .
- Optical power reflectivity,  $R$ .
- Photon flux density,  $\Phi_0$ .

These parameters were determined theoretically, as explained below.

### 3.8.1 Optically Illuminated GaAs FET Area

The area of the GaAs FET available for optical illumination is restricted to that defined by the gate periphery and the lateral extensions of the gate depletion region, as shown in Figure 3.12.

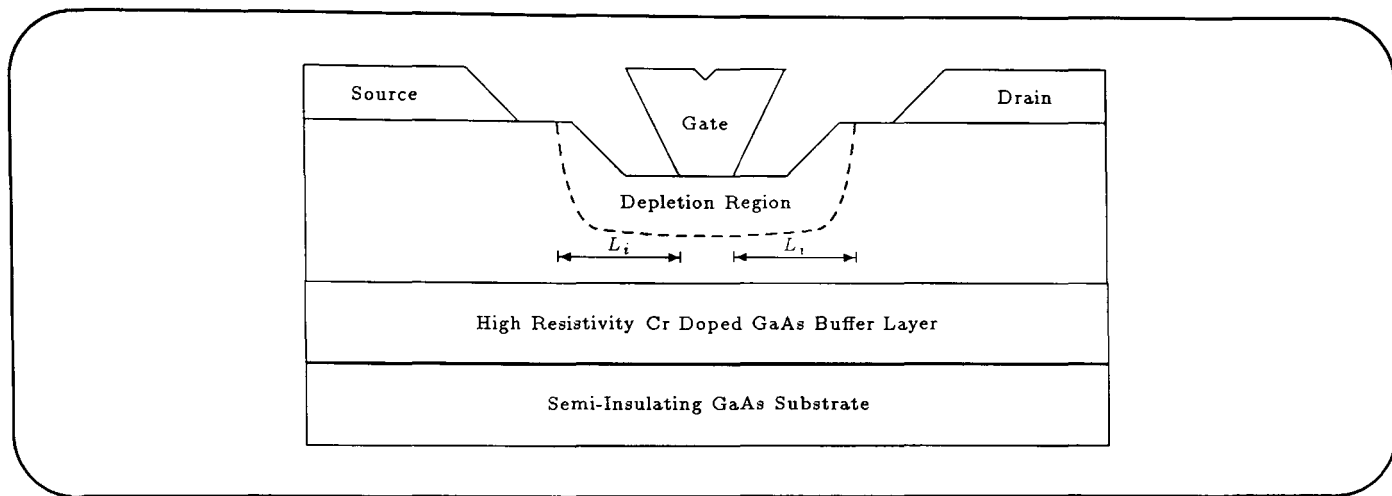


**Figure 3.12:** Cross-sectional view of a GaAs FET, indicating the areas of optical absorption created by the lateral extensions of the gate depletion region.

Since, for the optically controlled microwave switching device described in this thesis, the drain and source of the FET are both at DC earth potential, the lateral extensions on the drain and source side of the gate will be equal and will vary with distance towards the drain or source electrode. However, the illuminated lateral extension,  $L_i$ , can be approximated to the depletion region depth at the source or drain edge of the gate, as suggested by Madjar *et al.* [3.3]. For either side of the gate and a uniformly doped channel, this is expressed as [3.5]

$$L_i \simeq a \left( \frac{\phi_B - V_{GSi}}{|V_P| + \phi_B} \right)^{\frac{1}{2}} \quad (3.14)$$

where  $a$  is the thickness of the recessed GaAs epitaxial layer. From this the effective total optically illuminated area of the GaAs FET can be expressed as

$$A_i = 2L_i W_G = 2a W_G \left( \frac{\phi_B - V_{GSi}}{|V_P| + \phi_B} \right)^{\frac{1}{2}} \quad (3.15)$$

For the ATF-10136 FET with a recessed GaAs layer thickness of  $0.1 \mu\text{m}$ , the maximum optically illuminated area, achieved by biasing the GaAs FET at pinch-off, will be around  $10^{-10} \text{ m}^2$ .

### 3.8.2 Optical Power Reflectivity

The surfaces of most GaAs FET's are coated with some form of passivation to protect the device and maintain reliability. Silicon nitride ( $\text{Si}_3\text{N}_4$ ) is commonly used. The amount of optical power reflected from the device surface can be determined by considering the reflections of the optical signal due to the changing refractive indices of the air/ $\text{Si}_3\text{N}_4$ /GaAs interface and can be estimated from [3.3] as

$$R = \left| \frac{(1 - N_S)(N_S + N_G) + (1 + N_S)(N_S - N_G)e^{-j2\theta_S}}{(1 + N_S)(N_S + N_G) + (1 - N_S)(N_S - N_G)e^{-j2\theta_S}} \right|^2 \quad (3.16)$$

where  $\theta_S$  is the electrical length of the silicon nitride layer and  $N_S$  and  $N_G$  are the refractive indices of silicon nitride and GaAs, respectively. The electrical length of the  $\text{Si}_3\text{N}_4$  passivation layer is related to its physical thickness,  $l_{pas}$ , by

$$\theta_S = \frac{2\pi l_{pas} N_S}{\lambda} \quad (3.17)$$

where  $\lambda$  is the wavelength of the incident light. From the simple computer program given in Appendix A.4 and for refractive indices of 3.5 and 2.05 for GaAs and  $\text{Si}_3\text{N}_4$  [3.5], respectively and a passivation layer thickness of  $0.2 \mu\text{m}$ , this yields an optical power reflectivity of approximately 25%.

### 3.8.3 Photon Flux Density

The photon flux density at the surface of the device,  $\Phi_0$ , can be estimated as

$$\Phi_0 = \frac{P_{opt}}{E_{ph}} = \frac{\lambda P_{opt}}{hc} \quad (3.18)$$

where  $P_{opt}$  is the optical power density. Assuming the beam spot to be circular and for a focussed beam spot diameter of about  $100 \mu\text{m}$  the photon flux density is estimated to be approximately  $2 \times 10^{24} \text{ m}^{-2}\text{s}^{-1}$ .

# References

- [3.1] A. A. A. de Salles, *Optical control of microwave field effect transistors*. Ph.D. thesis, Univ. of London, 1982.
- [3.2] A. A. de Salles, "Optical control of GaAs MESFET's," *IEEE Trans. on Microwave Theory & Tech.*, vol. MTT-31, pp. 812–820, Oct. 1983.
- [3.3] A. Madjar, P. R. Herczfeld, and A. Paoletta, "Analytical model for optically generated currents in GaAs MESFETs," *IEEE Trans. Microwave Theory Tech.*, vol. 40, pp. 1681–1691, Aug. 1992.
- [3.4] P. H. Ladbrooke, *MMIC design: GaAs FETs and HEMTs*. Boston: Artech House, 1989.
- [3.5] S. M. Sze, *Physics of semiconductor devices*. New York: Wiley, second. ed., 1981.
- [3.6] Hewlett Packard, *Communications Components GaAs & Silicon Designer's Catalogue*, 1993.
- [3.7] H. Fukui, "Determination of the basic device parameters of a GaAs MESFET," *Bell Syst. Tech. J.*, vol. 58, pp. 771–797, Mar. 1979.

# Chapter 4

## Dynamic Photo-Effects in Microwave GaAs FET's

### Contents

---

<b>4.1</b>	<b>Introduction . . . . .</b>	<b>73</b>
<b>4.2</b>	<b>Dynamic Photovoltaic Effects . . . . .</b>	<b>74</b>
4.2.1	Barrier Interface Photovoltaic Effect . . . . .	74
4.2.2	Gate Depletion Photovoltaic Effect . . . . .	74
<b>4.3</b>	<b>GaAs FET Transient Response . . . . .</b>	<b>75</b>
4.3.1	Gate Junction Capacitance . . . . .	76

---

### 4.1 Introduction

**D**YNAMIC photo-effects in microwave GaAs FET's have not been investigated in the literature to the same extent as have static photo-effects, although some in-depth studies have appeared in the literature recently. Of particular significance are the works of Forrest *et al.* [4.1], Madjar *et al.* [4.2] and Paoletta *et al.* [4.3], who all developed comprehensive models for the GaAs FET subjected to pulsed or sinusoidal modulated optical illumination. The fundamental principles underlying the dynamic photo-effects can be examined by modifying the models developed for the static photo-effects in GaAs FET's. Since only optical switching applications are examined in this thesis, sinusoidal modulation will not be considered. Also the photoconductive current, will not be considered since it is extremely small. Furthermore, due to the significance of the gate photovoltaic effect, this particular photo-effect will be the main focus of the present discussion.

The modelling of the dynamic response is reviewed in Section 4.2, through an analysis of the barrier interface and gate depletion regions of a microwave GaAs FET.

The modelling of the transient response limitation, associated with the gate depletion region photovoltaic effect, is determined in Section 4.3 by consideration of the  $RC$  time constant of the gate depletion region capacitance and gate bias resistance combination.

The key points of this chapter are identified below.

- **Description and review of the following optically-induced mechanisms in microwave GaAs FET's under modulated optical control:**
  - barrier interface (internal) photovoltaic effect
  - gate depletion region (external) photovoltaic effect.
- **Modelling of the dynamic response of the GaAs FET under photovoltaic control.**
- **Determination of the GaAs FET gate depletion region capacitance.**

## 4.2 Dynamic Photovoltaic Effects

To predict the optically pulsed performance of a GaAs FET, the models for the barrier interface and gate depletion region photovoltaic effects under static conditions are considered and modified.

### 4.2.1 Barrier Interface Photovoltaic Effect

The model used in Section 3.4.1 (Figure 3.5) for the static photo-response of the GaAs FET due to the barrier interface photovoltage can be modified to include the barrier capacitance,  $C_{sub}$ , allowing the pulsed photo-response to be evaluated. From this model, shown in Figure 4.1, a nonlinear differential expression identifying the time constants associated with the barrier interface photovoltage can be developed and solved using numerical techniques (Runge-Kutta method) as proposed recently by Madjar *et al.* [4.2].

### 4.2.2 Gate Depletion Photovoltaic Effect

The use of a large gate bias resistance to induce a large photovoltaic effect has severe implications on the dynamic photoresponse at the gate of the FET. The model used in Section 3.5 (Figure 3.9) for the static photo-response of the GaAs FET due to the gate depletion photovoltage can be modified to include the gate Schottky junction capacitance,  $C_g$ , allowing the pulsed photo-response to be evaluated. From this model, shown in Figure 4.2, a nonlinear differential expression identifying the time constants associated with the gate photovoltage can be developed and solved, again using numerical techniques, as proposed recently by Madjar *et al.* [4.2].

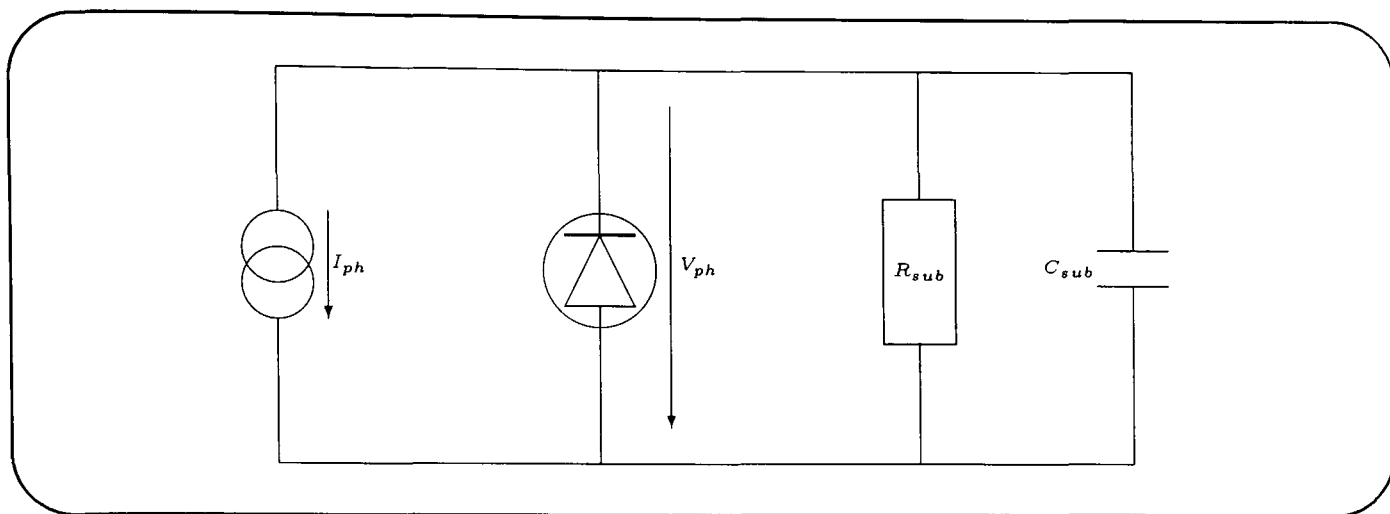


**Figure 4.1:** Dynamic equivalent circuit of the channel-to-substrate interface while under optical illumination.

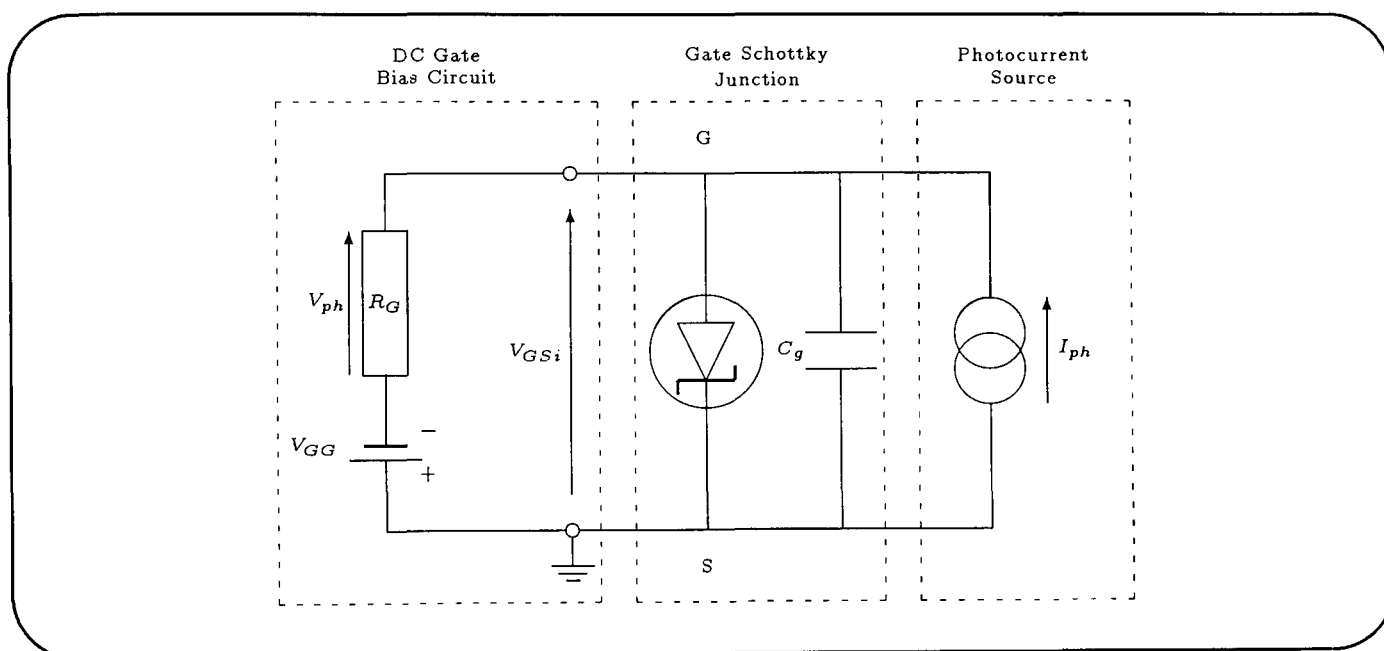


**Figure 4.2:** Dynamic equivalent circuit of the gate Schottky junction while under optical illumination.

### 4.3 GaAs FET Transient Response

The transient response (i.e. rise and fall times) associated with the preceding photovoltaic mechanisms has been evaluated theoretically and experimentally by Madjar *et al.* [4.2]. Their numerical solutions of the nonlinear differential equation for the barrier interface photovoltage indicated a rise time in the nano-second range and a fall time in the micro-second range. Their theoretical predictions are substantiated experimentally by the measurement of the transient response of the drain current, resulting from pulsed optical illumination. Their numerical solution of the nonlinear differential equation for the gate photovoltage indicated a rise and fall time in the nano-second range. However, their experimental transient response results associated with the gate photovoltaic effect were presented under gate loading and optical pulse conditions different from their simulated results, making a direct comparison difficult. Nevertheless, there

do appear to be discrepancies between their simulated and measured results. These are more evident for the fall time values. The discrepancies in the transient response associated with the gate photovoltaic effect are significant in the evaluation of the performance of the optically controlled switch described in this thesis. Consequently, accurate prediction of the gate transient response is a subject of further discussion in Chapter 7.

### 4.3.1 Gate Junction Capacitance

The transient response of the gate photovoltage is inevitably limited by the  $RC$  time constant associated with the large gate bias resistor,  $R_G$ , and the nonlinear gate capacitance,  $C_g$ . The nonlinear gate capacitance will depend upon the voltages at the gate and source terminals of the FET, and can be approximated simply by [4.2]

$$C_g = \frac{\epsilon_0 \epsilon_r A_G}{w} = \frac{\epsilon_0 \epsilon_r L_G W_G}{w} \quad (4.1)$$

where  $\epsilon_0$  is the permittivity in a vacuum and  $\epsilon_r$  the relative permittivity of the GaAs channel. The width of the depletion region  $w$  under illumination can be expressed as

$$w = a \left( \frac{\phi_B - V_{GSi}}{|V_P| + \phi_B} \right)^{\frac{1}{2}} \quad (4.2)$$

where  $a$  is the thickness of the recessed GaAs epitaxial layer,  $V_P$  the pinch-off voltage,  $\phi_B$  the built-in potential of the gate Schottky junction and  $V_{GSi}$  the gate-to-source voltage under illumination.

# References

- [4.1] J. R. Forrest, F. P. Richards, and A. Perichon, “The microwave MESFET optical detector,” in *Proc. IEEE IEDM Tech. Dig.*, (San Francisco), pp. 529–532, Nov. 1982.
- [4.2] A. Madjar, A. Paoletta, and P. R. Herczfeld, “Modeling the optical switching of MESFET’s considering the external and internal photovoltaic effects,” *IEEE Trans. Microwave Theory Tech.*, vol. 42, pp. 62–67, Jan. 1994.
- [4.3] A. Paoletta, A. Madjar, and P. R. Herczfeld, “Modeling the GaAs MESFET’s response to modulated light at radio and microwave frequencies,” *IEEE Trans. Microwave Theory Tech.*, vol. 42, pp. 1122–1130, July 1994.

# Chapter 5

## Microwave Switching With GaAs FET's

### Contents

---

<b>5.1</b>	<b>Introduction . . . . .</b>	<b>78</b>
<b>5.2</b>	<b>Hybrid <math>\Pi</math> GaAs FET Model . . . . .</b>	<b>80</b>
<b>5.3</b>	<b>'On' State GaAs FET Switch Model . . . . .</b>	<b>80</b>
5.3.1	Series Channel Resistance . . . . .	81
5.3.2	Drain and Source Resistances . . . . .	82
<b>5.4</b>	<b>'Off' State GaAs FET Switch Model . . . . .</b>	<b>83</b>
5.4.1	Electrode Capacitance . . . . .	83
5.4.2	Drain-to-Source Resistance . . . . .	85
5.4.3	Gate Depletion Region Capacitance . . . . .	85
5.4.4	Charging Resistances . . . . .	85
<b>5.5</b>	<b>Modelling of Hybrid GaAs FET Switches . . . . .</b>	<b>85</b>
5.5.1	Package Model . . . . .	86
5.5.2	Gate Resistance . . . . .	86

---

### 5.1 Introduction

IN the early 1980's, the difficulties of implementing *p-i-n* switching diodes in MMIC's were recognized and, due to the widespread application of GaAs FET's within MMIC's, this led to the establishment of MMIC switches based upon these FET devices. Ayasli [5.1], in 1982, developed an approximate lumped equivalent circuit model for the switching states of a reflective microwave GaAs FET switch, where 'on' and 'off' states of the switch were achieved by switching the gate of the FET between zero

bias and pinch-off, respectively. In these circumstances, the microwave signal can be applied to the drain or source of the FET, making the switch bi-directional, with the remaining terminal kept at RF ground. This represents a reflective switch configuration. A DC earth potential is maintained at the drain and source in both switching states, indicating a passive mode of operation. Taking a rather simplistic view of the switching process, the 'on' state occurs when the gate of the FET is at DC earth potential (i.e.  $V_{GS} = 0$  V). In this case the active channel region is undepleted, allowing a low impedance microwave path to exist between the drain and source. The 'off' state is established when the gate of the FET is biased beyond pinch-off (i.e.  $V_{GS} \geq V_P$ ) when the active channel region is fully depleted, presenting a high impedance microwave path between the drain and source. Therefore, provided the gate is isolated (i.e. represents a high RF impedance) from the microwave input signal in both switching states, the gate bias voltage can be used to switch the FET between approximately RF short- and open-circuit conditions in the 'on' and 'off' states, respectively. However, this must be regarded as a rather simplified approach, since in practice, the parasitic components associated with the intrinsic FET structure will significantly affect the microwave operation. The rather more elaborate models proposed by Ayasli [5.1] were used in the present investigation as the basis for developing a more comprehensive understanding of the GaAs FET switching behaviour. Since these models and the related intrinsic parameter evaluation techniques had not been tested rigorously in the literature, it was necessary to make a number of significant modifications to the approach proposed by Ayasli [5.1]. These changes yielded a simplified, yet more accurate and versatile, approach to modelling the switching performance of a GaAs FET.

In this chapter these modifications are examined and compared with conventional approaches to switch state modelling, although the experimental results pertaining to this aspect of the work are confined to Chapter 6, where the optically controlled GaAs FET switching performance is described.

The basic hybrid  $\Pi$  equivalent circuit for a GaAs FET is described briefly in Section 5.2, and forms the basis of a new modelling approach for GaAs FET switches. The approximate lumped equivalent circuit of an electrically controlled GaAs FET is developed for the 'on' and 'off' states in Sections 5.3 and 5.4, respectively. In addition, these sections describe present methods for determining the equivalent circuit element values and propose modifications to some of these approaches in order to enable more accurate and versatile modelling, applicable to optical as well as conventional electrical control of the switching state. In Section 5.5, some consideration is given to the modelling of some GaAs FET switches in hybrid form. These form part of the novel optically controlled prototype switches designed in Chapter 6.

The key points of this chapter are identified below.

- **Development of a more comprehensive and versatile model to represent**

the switching performance of a GaAs FET under direct optical, as well as conventional electrical control, of the switching states, through the following:

- development of a more accurate method for evaluating the ‘off’ state drain-to-source capacitance for the switch model, based upon 3-dimensional field simulations of the FET metallization layers
- use of a simplified approach to evaluating some of the intrinsic element values of the switch model, based upon the manufacturer’s standard hybrid  $\Pi$  FET model, which requires limited information on the specific device geometries and doping levels
- generation of a model which includes package parasitics
- accurate prediction of the occurrence of resonances which may hinder the switch performance in both states
- establishment of a novel technique for tuning out such resonances.

## 5.2 Hybrid $\Pi$ GaAs FET Model

Figure 5.1 shows the standard hybrid  $\Pi$  linear GaAs FET model often incorporated in microwave CAD packages and manufacturer’s literature. It is around this model that the simplified approach to switch state modelling proposed in this thesis was developed. The GaAs FET model is a simplified hybrid  $\Pi$  model, in which the intrinsic FET consists of a voltage controlled current source ( $g_m v_c$ ), the gate-to-source capacitance ( $C_{gs}$ ) across which the controlling voltage ( $v_c$ ) appears, and the channel or input resistance ( $R_c$ ). In addition, the transconductance ( $g_m$ ) has associated with it a phase delay ( $\tau_m$ ) to represent the delay in charging the capacitance associated with the gate depletion region. Terminal contact resistance ( $R_g$ ,  $R_s$ ,  $R_d$ ) and parasitic inductance ( $L_g$ ,  $L_s$ ,  $L_d$ ) at the gate, source and drain respectively are then added. The drain resistance is usually sufficiently low in value that it does not influence the  $S$ -parameters in the frequency range where the model is applicable ( $\sim 20$  GHz) and is therefore omitted from the model in Figure 5.1. The model is completed with the inclusion of the gate-to-drain coupling capacitance ( $C_{gd}$ ) which is predominant in determining the  $S_{12}$ -parameter and the drain-to-source resistance ( $R_{ds}$ ) and geometric capacitance ( $C_{ds}$ ).

## 5.3 ‘On’ State GaAs FET Switch Model

In the ‘on’ state the GaAs FET structure can be represented by the approximate lumped equivalent circuit of Figure 5.2 [5.1] which will have significance at microwave frequencies. The evaluation of these lumped elements is considered in this section.

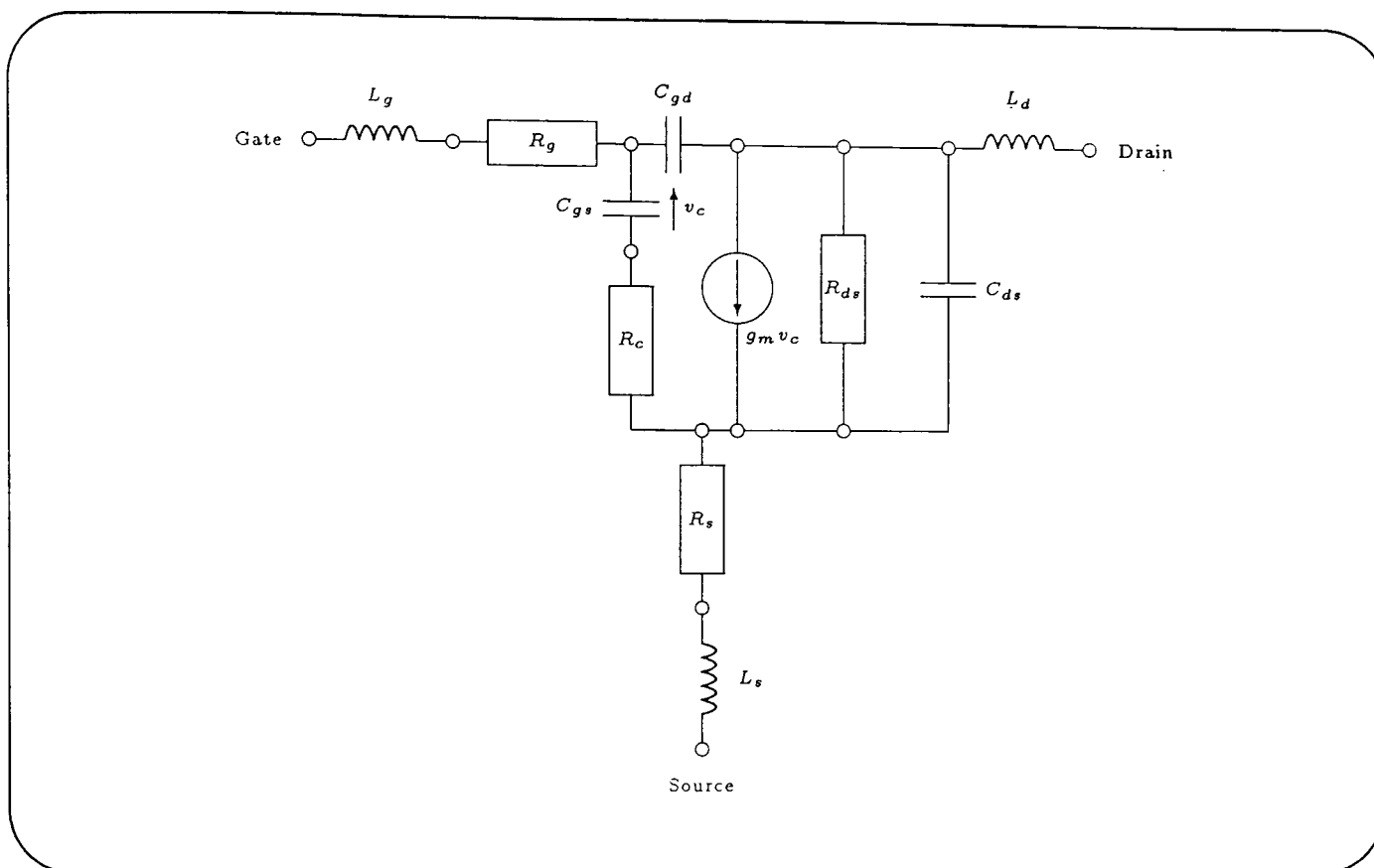


**Figure 5.1:** Basic hybrid II lumped equivalent circuit model of a GaAs FET (small-signal amplifier mode).

in relation to the methods suggested by Ayasli [5.1]. This contributes to a modified, simpler approach to switch state modelling.

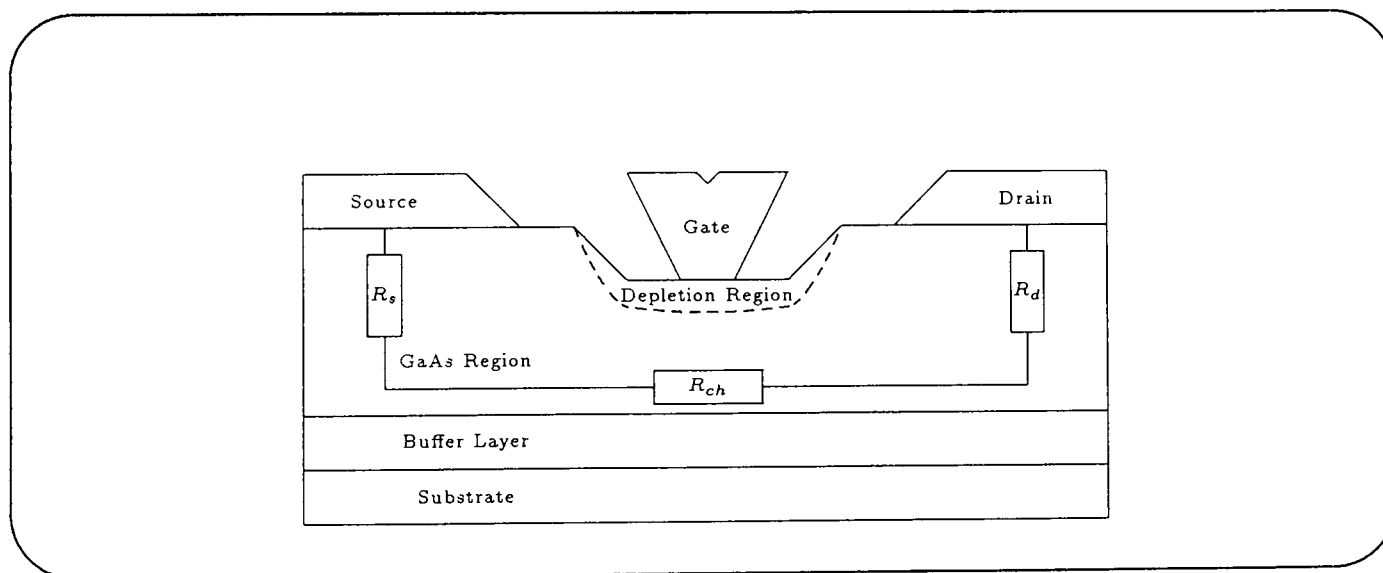


**Figure 5.2:** Approximate lumped equivalent circuit of a GaAs FET switch in the 'on' state, indicating the physical origins of the lumped circuit elements.

### 5.3.1 Series Channel Resistance

This accounts for the resistance of the open-channel in the 'on' state and was approximated by Ayasli [5.1] from the expression developed by Fukui [5.2]. The series channel

resistance can be expressed as

$$R_{ch} = \frac{L_G}{q\mu_0 N w_n W_G} \quad (5.1)$$

where  $N$  is the  $n$ -type channel carrier concentration,  $L_G$  the gate length,  $W_G$  the gate periphery,  $w_n$  the width of the undepleted active region,  $q$  the electronic charge and  $\mu_0$  the low-field drift mobility. In the 'on' state all the FET terminals are at earth potential, in which case the undepleted region width can be expressed as [5.3]

$$w_n = a \left[ 1 - \left( \frac{\phi_B}{|V_P| + \phi_B} \right)^{\frac{1}{2}} \right]. \quad (5.2)$$

These expressions were used initially in this investigation to establish the channel resistance. For the ATF-10136 FET, with an estimated channel doping level of  $2.5 \times 10^{17} \text{ cm}^{-3}$  and for a low-field mobility of  $2500 \text{ cm}^2\text{s}^{-1}\text{V}^{-1}$ , this gives a channel resistance of approximately  $1 \Omega$ . This method relies upon accurate values for the mobility and doping level under the gate of the FET which are difficult to define precisely. Consequently, to simplify the evaluation of the channel resistance and to avoid the uncertainty associated with the mobility and doping level, the input resistance parameter,  $R_c$ , from the standard hybrid  $\Pi$  FET model was used and this is considered in Chapter 6.

### 5.3.2 Drain and Source Resistances

The series drain and source resistances,  $R_d$  and  $R_s$ , consist of the resistance contributions from the ohmic contacts and from the access regions to the active channel.

#### Ohmic Contact Resistance

Ayasli [5.1] calculated the ohmic contact resistances from the expressions given by Fukui [5.2], which considered the drain and source contacts to an  $n^+$ -type layer. In the FET's used in this investigation, the drain and source made direct contact to the  $n$ -type GaAs layer and therefore the ohmic contact resistances were calculated initially from specific contact resistances as outlined by Ladbroke [5.4] and given by

$$R_{co} = \frac{\rho_c}{W_G} \quad (5.3)$$

where  $\rho_c$  is the specific contact resistance, which for Au-Ge-Ni contacts alloyed to  $n$ -GaAs doped to  $10^{17} \text{ cm}^{-3}$  or greater, is in the range  $0.1\text{--}0.5 \Omega\text{mm}$  [5.4]. For the ATF-10136 FET this gave a contact resistance of  $0.4 \Omega$ .

#### Access Region Resistance

Ayasli [5.1] calculated the resistance of the access regions based upon the approach of Fukui [5.2], which involved splitting this resistance into two components to account

for the unrecessed and recessed portions of the access region. For the FET's used in this investigation, the amount of recess depth was not known and therefore the access region resistance on the source side of the FET was approximated to the unrecessed value given by [5.4]

$$R_{gs} \simeq \frac{L_{GS}}{qN\mu_0aW_G} \quad (5.4)$$

where  $L_{GS}$  is the gate-to-source inter-electrode spacing. Since the drain and source are both at earth potential, a similar resistance expression is obtained for the drain side of the FET ( $R_{gd}$ ), with  $L_{GS}$  replaced by the drain-to-gate inter-electrode spacing ( $L_{GD}$ ). For the ATF-10136 FET, the inter-electrode spacings on either side of the gate are equal and from SEM pictures were established to be  $0.55 \mu\text{m}$ , which gave a access region resistance of  $1.1 \Omega$  on each side of the gate. The total drain and source resistances are given by

$$R_s = R_{co} + R_{gs} \quad (5.5)$$

$$R_d = R_{co} + R_{gd}. \quad (5.6)$$

This gives drain and source resistances of  $1.5 \Omega$  and these values were applied initially to the 'on' state switch model simulations. This evaluation method was later simplified by using the drain and source resistance values from the standard hybrid II FET model as considered in Chapter 6.

## 5.4 'Off' State GaAs FET Switch Model

In the 'off' state the GaAs FET structure can be represented by the approximate lumped equivalent circuit of Figure 5.3 [5.1], which also illustrates the position of the equivalent lumped elements. The evaluation of these lumped elements is considered in this section, and in relation to the methods suggested by Ayasli [5.1] and to the modified approach proposed in this investigation.

### 5.4.1 Electrode Capacitance

The inter-electrode capacitance,  $C_{ds}$ , represents the fringing capacitance between the drain and source electrodes in the 'off' state. The value of this parameter is of crucial importance to providing good switch isolation and was calculated by Ayasli [5.1] from the expression developed by Pucel *et al.* [5.5]. Since the inter-electrode spacings are small compared with the device thickness, Pucel *et al.* [5.5] estimated this capacitance by considering the electrostatic coupling between two parallel conductors on the surface of a semi-infinite dielectric medium representing the device. They modified the

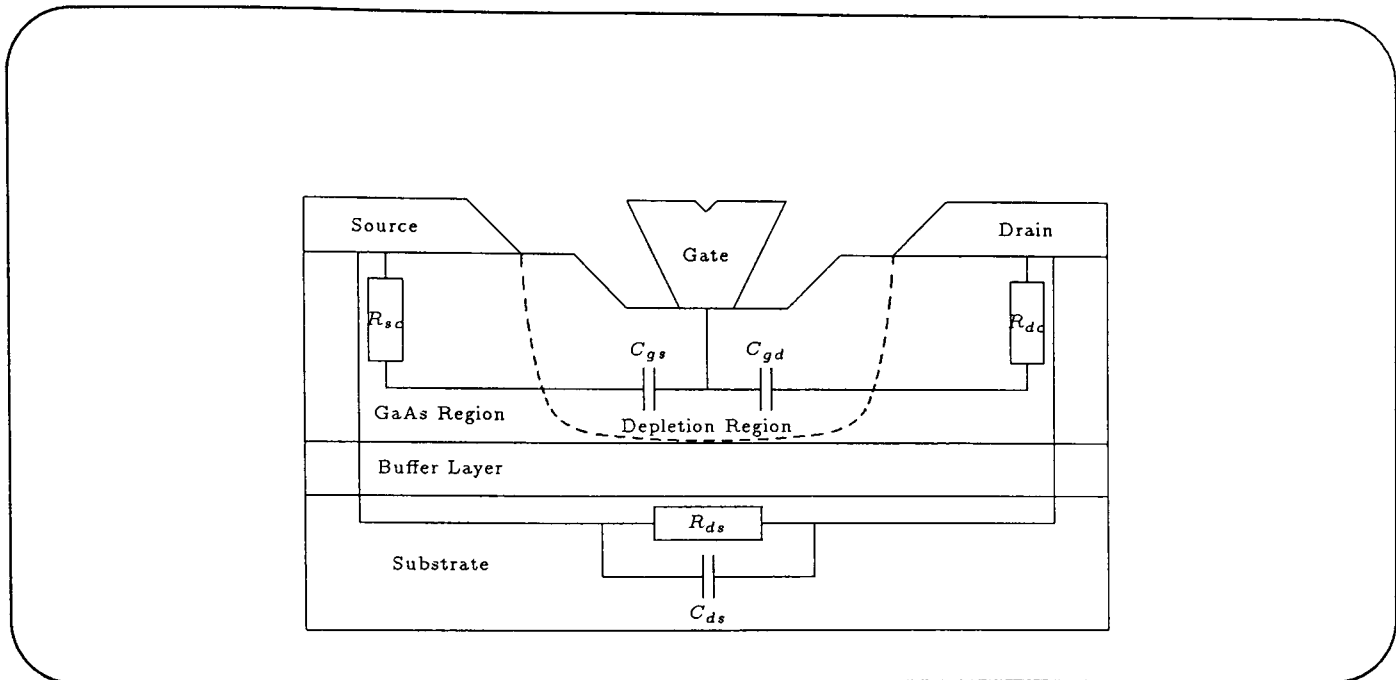


**Figure 5.3:** Approximate lumped equivalent circuit of a GaAs FET switch in the ‘off’ state, indicating the physical origins of the lumped circuit elements.

expression of Smythe [5.6] for inter-electrode capacitance between parallel strips immersed in an infinite dielectric medium, to account for the air above the drain and source electrodes. For an asymmetric FET this is given by [5.5]

$$C_{ds} = (\epsilon_r + 1)\epsilon_0 W_G \frac{K(1 - k_{ds}^2)^{\frac{1}{2}}}{K(k_{ds})} \quad (5.7)$$

where  $K$  is the complete elliptic integral of the first kind. The argument,  $k_{ds}$ , is related to the geometry of the electrodes by

$$k_{ds} = \left[ \frac{(2L_S + L_{DS})L_{DS}}{(L_S + L_{DS})^2} \right]^{\frac{1}{2}} \quad (5.8)$$

where  $L_{DS}$  is the drain-to-source inter-electrode spacing and  $L_S$  is the source electrode length. In this expression the following assumptions are made:

- equal drain and source electrode lengths (i.e.  $L_D = L_S$ )
- drain electrode length is much greater than the gate electrode length (i.e.  $L_D \gg L_G$ )
- source electrode length is much greater than the drain-to-source spacing (i.e.  $L_S \gg L_{DS}$ ).

These methods proposed by Ayasli [5.1] were found to give a large under-estimate of the actual drain-to-source capacitance, and could not be used in the ‘off’ state switch simulations. A novel and more accurate approach to evaluating this capacitance is proposed later in this thesis, using HFSS<sup>†</sup> to provide 3-D field simulations of the

<sup>†</sup>HP 85180A High-Frequency Structure Simulator.

FET structure. This method has yielded results which are in very good agreement with measurements performed on the FET switches. It is discussed in more detail in Chapter 10.

### 5.4.2 Drain-to-Source Resistance

The drain-to-source resistance,  $R_{ds}$ , shunts  $C_{ds}$  and represents the microwave losses associated with the GaAs FET switch structure. Ayasli [5.1] estimated a value for his FET switches which incorporated 1 mm gate periphery devices. In this investigation it has been found that the precise value of  $R_{ds}$  has little effect on the simulated switch performance. This is reasonable since its value would be expected to be in the kilo-ohm range. A value of 3.5 k $\Omega$  was used to simulate the switching performance of the FET's described in this thesis and is consistent with typical values from previously published data [5.1].

### 5.4.3 Gate Depletion Region Capacitance

This describes the capacitance of the gate depletion region with the channel fully depleted. Ayasli [5.1] separated this capacitance into two components,  $C_{gs}$  and  $C_{gd}$ , associated with the drain and source sides of the gate. Since the drain and source are both at earth potential and assuming the GaAs FET is symmetrical, this capacitance can be equated to one-half of that obtained for the overall gate depletion region capacitance at pinch-off to give [5.1]

$$C_{gs} = C_{gd} = \frac{C_g}{2} = \frac{\epsilon_0 \epsilon_r W_G L_G}{2a}. \quad (5.9)$$

For the ATF-10136 FET this corresponds to gate-to-source and gate-to-drain capacitances of approximately 0.088 pF.

### 5.4.4 Charging Resistances

The drain and source resistances,  $R_{dc}$  and  $R_{sc}$ , in the 'off' state represent the charging resistances of  $C_{gd}$  and  $C_{gs}$ , respectively. Based upon experiment, Ayasli [5.1] suggested that these resistances could be estimated from one-half of the total 'on' state resistance. This is consistent with the approach adopted for evaluating the gate capacitance. For the ATF-10136 this resulted in charging resistances of approximately 2  $\Omega$ .

## 5.5 Modelling of Hybrid GaAs FET Switches

The discussion thus far has been concerned with the modelling of the intrinsic elements of the GaAs FET when configured as a reflective microwave switch. It is appropriate

only for modelling monolithic forms of the GaAs FET switch. However, the investigation of this thesis concentrates on the hybrid implementation of the switch using packaged devices. To the author's knowledge, this is the first investigation of this kind and as such requires that a packaged model be included with the device model to predict fully the switching performance.

### 5.5.1 Package Model

The package model for the Hewlett Packard range of GaAs FET's is given in the manufacturer's data sheets [5.7] and is shown in Figure 5.4. This package model treats the leads and internal metallization as transmission lines  $T_g$ ,  $T_d$  and  $T_s$ . Coupling capacitances between the device terminals are included ( $C_{gsp}$ ,  $C_{gdp}$  and  $C_{dsp}$ ), as are the series inductances of the drain, source and gate bond wires ( $L_d$ ,  $L_s$ ,  $L_g$ ). This package model was used in conjunction with the intrinsic model for the GaAs FET switch described in the preceding sections.

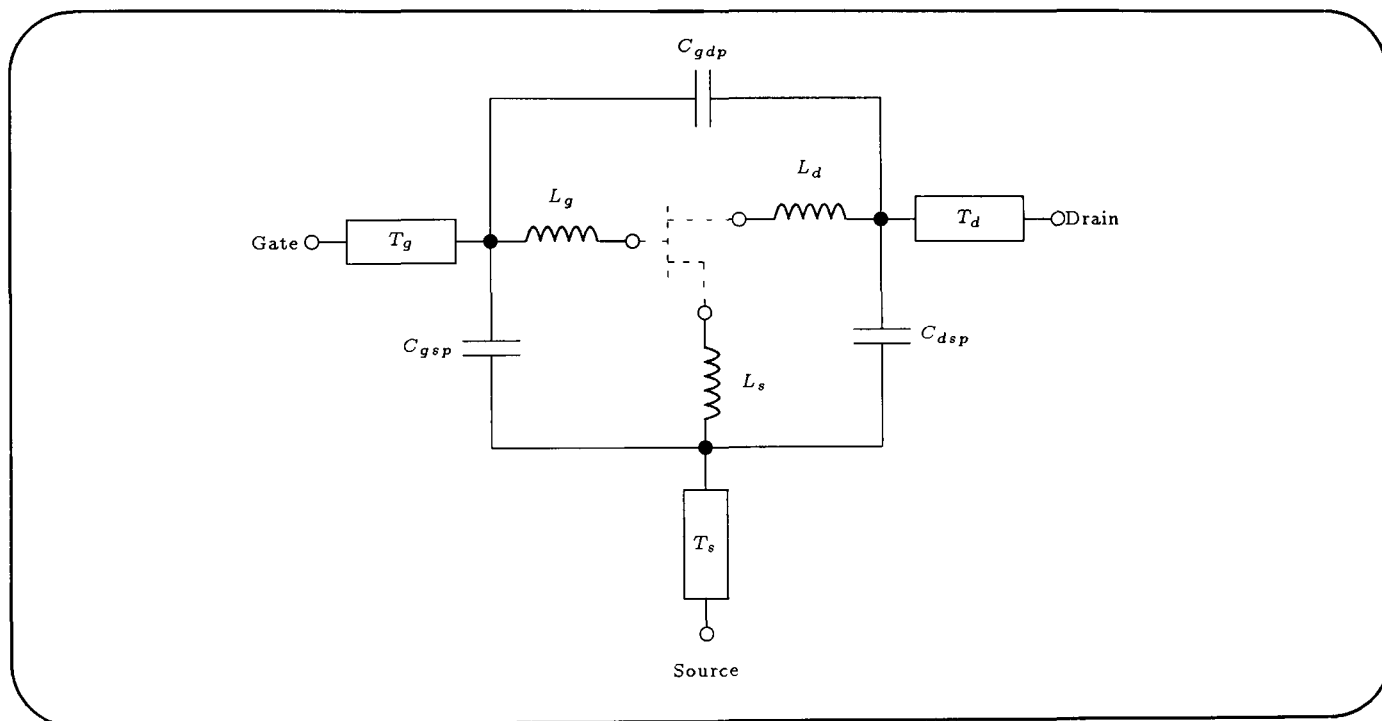


**Figure 5.4:** Approximate lumped equivalent circuit package model for the range of Hewlett Packard GaAs FET's [5.7].

### 5.5.2 Gate Resistance

The resistance at the gate of the FET,  $R_g$ , was not included in the model proposed by Ayasli [5.1] and therefore in this investigation the resistance at the gate of the FET was obtained from the manufacturer's data sheets and included in the models for the 'on' and 'off' states of the switch. The complete model, which includes the intrinsic elements of the FET switch equivalent circuit together with the device package model [5.7] and conventional representations of the microstrip elements of the switch circuit, was then

used in conjunction with MDS<sup>†</sup> to obtain simulations of the switch performance in both states. This is considered in more detail in the next chapter, in which direct optical control of the switching states of the GaAs FET is realized.

---

<sup>†</sup>HP 85150B Microwave and RF Design System.

# References

- [5.1] Y. Ayasli, “Microwave switching with GaAs FETs,” *Microwave J.*, vol. 25, pp. 61–74, Nov. 1982.
- [5.2] H. Fukui, “Determination of the basic device parameters of a GaAs MESFET.” *Bell Syst. Tech. J.*, vol. 58, pp. 771–797, Mar. 1979.
- [5.3] S. M. Sze, *Physics of semiconductor devices*. New York: Wiley, second. ed., 1981.
- [5.4] P. H. Ladbrooke, *MMIC design: GaAs FETs and HEMTs*. Boston: Artech House, 1989.
- [5.5] R. A. Pucel, H. A. Haus, and H. Statz, “Signal and noise properties of gallium arsenide microwave field-effect transistors,” *Advances in Electron. Electron Phys.*, vol. 38, pp. 195–265, 1975.
- [5.6] D. Smythe, *Static and dynamic electricity*, ch. 4, pp. 100–104. New York: McGraw-Hill, 1968.
- [5.7] Hewlett Packard, *Communications Components GaAs & Silicon Designer’s Catalogue*, 1993.

# Chapter 6

## Optical Switching of Microwave GaAs FET's

### Contents

---

<b>6.1</b>	<b>Introduction . . . . .</b>	<b>89</b>
<b>6.2</b>	<b>Hybrid GaAs FET Switch Design . . . . .</b>	<b>90</b>
6.2.1	Drain Circuit . . . . .	91
6.2.2	Source Circuit . . . . .	92
6.2.3	Gate Circuit . . . . .	93
6.2.4	Bias Circuit . . . . .	94
<b>6.3</b>	<b>Optically Controlled Switch State Modelling . . . . .</b>	<b>94</b>
6.3.1	Static Optical Control . . . . .	95
6.3.2	Switch State . . . . .	96
<b>6.4</b>	<b>GaAs FET Switch State Results . . . . .</b>	<b>98</b>
6.4.1	Optically 'On' State . . . . .	99
6.4.2	'Off' state . . . . .	101

---

### 6.1 Introduction

**D**ESPITE the concurrent development of electrically controlled GaAs FET switches and optical control in GaAs FET's, it was not until recently that interest has focussed upon combining these techniques to achieve direct optical control of microwave GaAs FET switches. However, the reported investigations such as those of Madjar *et al.* and Chakrabarti *et al.* [6.1–6.3] have examined only the switching speed of GaAs FET's under optical illumination and have not considered the microwave switch state performance under optical control. No publications to date have presented measured

switch state data for the GaAs FET under optical or electrical control, that verify the published models discussed in the previous chapter. In this chapter the direct optical control of a GaAs FET switch using the gate photovoltaic effect is addressed. The design methodology is established and measured and simulated results are presented for the switch state performance.

The design of a prototype GaAs FET switch which relies on direct optical control of the switching state is considered in Section 6.2, with the modelling of the switch described in Section 6.3. A direct comparison of the measured and simulated results for the switch state performance of two novel optically controlled GaAs FET switches is presented in Section 6.4, which verifies the newly proposed modelling approach for two very different GaAs FET gate structures.

The key points of this chapter are identified below.

- **Design approach for a novel direct optically controlled X-band GaAs FET switch.**
- **Modelling of the direct optically controlled GaAs FET switch.**
- **Consideration of package parasitics to model the hybrid switches.**
- **Experimental verification of the switch state performance through a direct comparison of measured and simulated results.**
- **Experimental validation of the novel approach to switch parameter evaluation for two very different FET gate structures.**

## 6.2 Hybrid GaAs FET Switch Design

The GaAs FET switch design described in this section can be used in optically or electrically controlled applications, noting that a large resistance ( $\gtrsim 100 \text{ k}\Omega$ ) must be incorporated into the gate bias network to achieve optical control of the switching state. The designs were implemented on RT/Duroid<sup>TM</sup> material which had a substrate thickness of  $635 \mu\text{m}$  and a relative permittivity of 10.5. Since the electrically controlled GaAs FET switches described in the literature have been developed only in monolithic form, a number of additional aspects of the switch circuit design had to be considered for a hybrid implementation of the switch. However, a design strategy was chosen for the hybrid circuits that would allow a straightforward extension to monolithic layouts if required. The switch circuits investigated employed the ATF-10136 and ATF-13136 packaged<sup>†</sup> GaAs FET's from Hewlett Packard [6.4]. These particular devices were selected due to their contrasting gate structures and this point is elaborated upon later

<sup>†</sup>Short leaded 36 micro-X package selected to minimize parasitic components.

in this chapter. The lids were removed and this enabled direct optical access to the sensitive regions of the FET. The switch circuits were designed to operate at X-band, although it is feasible to extend the design to give very broadband performance, as described in Chapter 10. The microstrip layout for the optically controlled GaAs FET switch is shown in Figure 6.1.

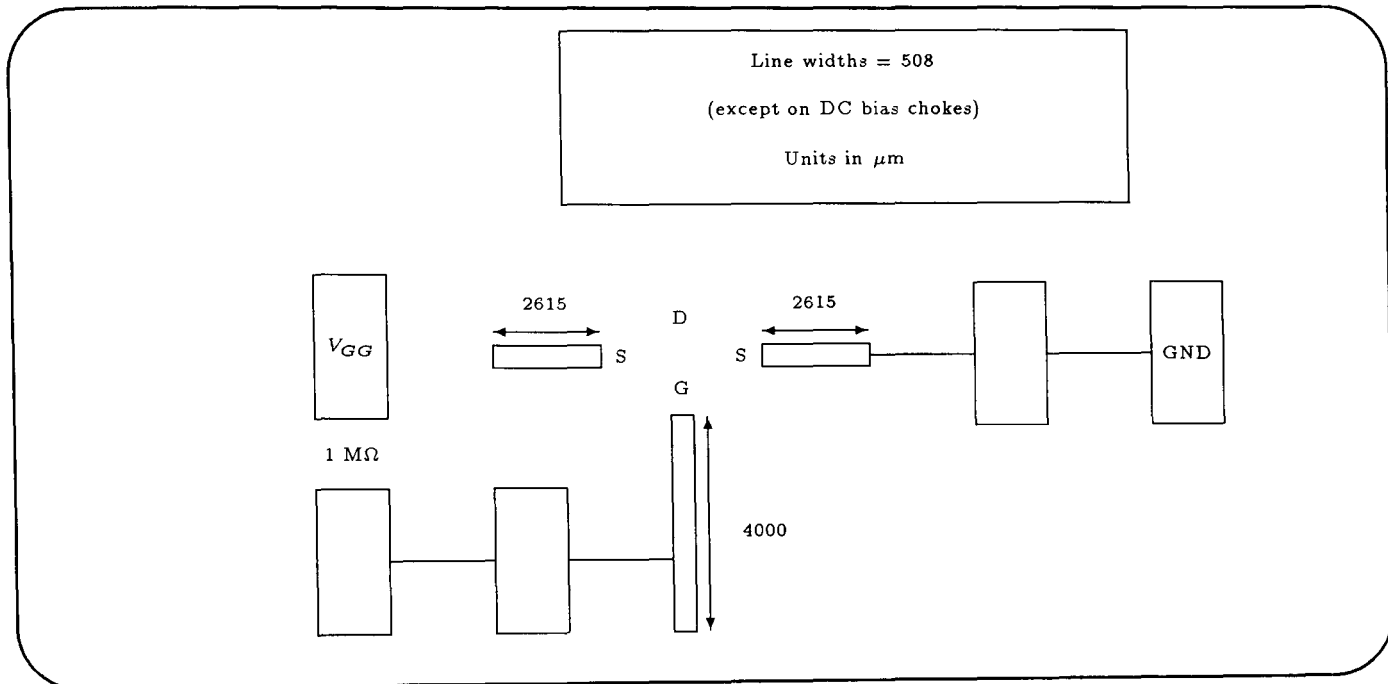


**Figure 6.1:** Microstrip circuit layout for direct optically controlled microwave switch.

All the microstrip dimensions for the switch circuit were extracted from the transmission line calculator available in MDS, and their effect on the switch circuit operation is discussed later in this chapter. The dimensional layout for the Hewlett Packard GaAs FET's is shown in Figure 6.2, which indicates that a 2.54 mm square gap in the microstrip layout allows the GaAs FET leads to be epoxy bonded to the microstrip lines. Furthermore, this gap ensures that the microstrip lines reach the edge of the main body of the package so as to reduce parasitic effects, particularly those associated with lead inductances.

### 6.2.1 Drain Circuit

The drain of the GaAs FET was used as the microwave reflective input port of the switch as shown schematically in Figure 6.3 and was therefore designed to have a characteristic impedance,  $Z_0$ , of 50 Ω, to match that of standard microwave measurement systems. In addition, the input line length was made three-quarters of a wavelength to avoid the possibility of resonances occurring between the launchers on the microstrip measurement jig and the device.

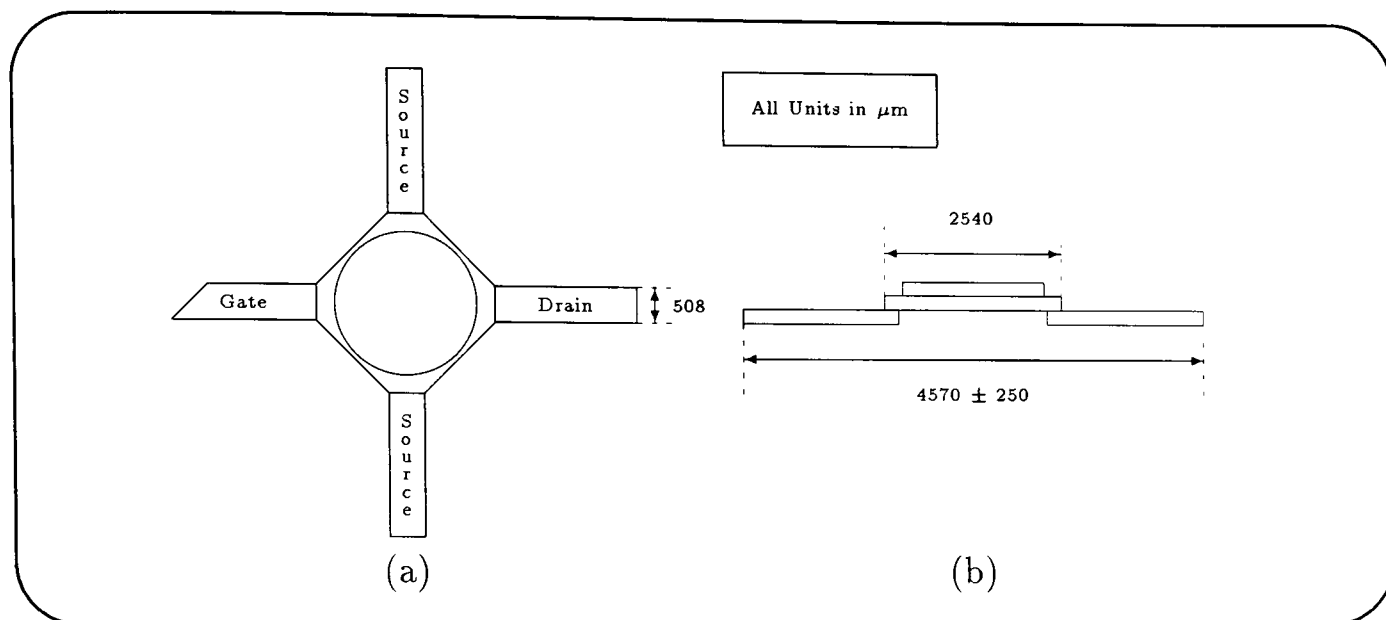


**Figure 6.2:** Micro-X package layout for the Hewlett Packard range of GaAs FET's. (a) Plan view. (b) Cross-sectional View.

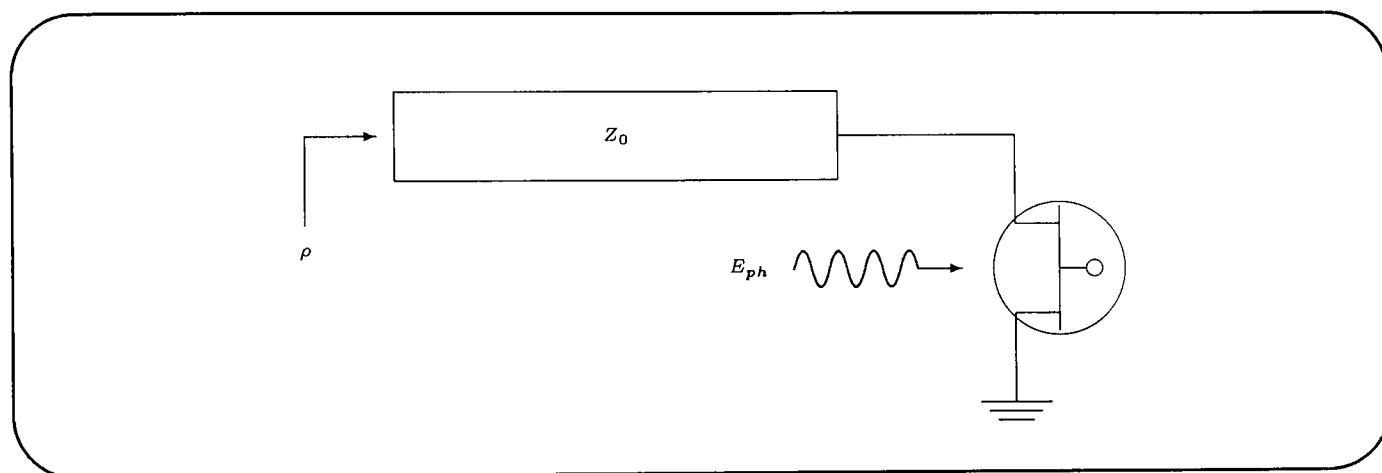


**Figure 6.3:** Schematic representation of the optically controlled reflective microwave GaAs FET switch.

Microstrip Drain Line Parameters				
Input Data:	$\epsilon_r = 10.5$	$h = 635 \mu\text{m}$	$t = 4 \mu\text{m}$	$Z_0 = 50 \Omega$
	$f = 10 \text{ GHz}$			
Output Data:	$w = 582 \mu\text{m}$	$\lambda_s = 11085 \mu\text{m}$	$\epsilon_{eff} = 7.31$	
Layout:	$w = 582 \mu\text{m}$	$l = \frac{3\lambda_s}{4} = 8314 \mu\text{m}$		

### 6.2.2 Source Circuit

To realize the switch operation, the source of the FET must appear as an RF ground connection. In monolithic versions of the switch this is achieved with a via hole from the source to the ground plane. Fabricating vias in microstrip can be achieved by using through-hole plating techniques, although the modelling of such a via can present difficulties. The use of open-circuit unfanned stubs, butterfly stubs and through-board

through-board connections were investigated as methods for providing an RF ground connection at the source of the FET. By experimental comparison of the stub reflection coefficients it was established that a quarter wavelength open-circuit stub, reflecting an effective RF short-circuit to the source of the FET, provided an adequate RF ground connection and could be modelled accurately. The width of the stub was made equal to that of the lead on the FET package, so as to avoid width change discontinuities. Since the FET has two source connections, an open-circuit stub was included at the end of each source lead. Finally, the open-circuit correction length,  $l_{oc}$ , due to capacitive fringing at the open end of the microstrip line was calculated from the expressions given by Kirschning *et al.* [6.5].

Microstrip Source Line Parameters				
Input Data:	$\epsilon_r = 10.5$	$h = 635 \mu\text{m}$	$t = 4 \mu\text{m}$	$w = 508 \mu\text{m}$
	$f = 10 \text{ GHz}$			
Output Data:	$Z_0 = 53.22 \Omega$	$\lambda_s = 11162 \mu\text{m}$	$\epsilon_{eff} = 7.21$	$l_{oc} = 176 \mu\text{m}$
Layout:	$w = 508 \mu\text{m}$	$l = \frac{\lambda_s}{4} - l_{oc}$	$= 2615 \mu\text{m}$	

### 6.2.3 Gate Circuit

Since the RF impedance of the gate network influences significantly the equivalent circuit of the FET in the 'off' state, the gate termination is usually configured to appear as an effective RF open-circuit, as suggested by Ayasli [6.6]. Ayasli achieved this effective RF open-circuit condition by incorporating a two-section low-pass filter at the gate terminal of the FET. In the FET switch design described here, this effective RF open-circuit condition at the gate terminal of the FET was achieved using a half-wavelength open-circuit stub.

Microstrip Gate Line Parameters				
Input Data:	$\epsilon_r = 10.5$	$h = 635 \mu\text{m}$	$t = 4 \mu\text{m}$	$w = 508 \mu\text{m}$
	$f = 10 \text{ GHz}$			
Output Data:	$Z_0 = 53.22 \Omega$	$\lambda_s = 11162 \mu\text{m}$	$\epsilon_{eff} = 7.21$	$l_{oc} = 176 \mu\text{m}$
Layout:	$w = 508 \mu\text{m}$	$l = \frac{\lambda_s}{2} - l_{oc}$	$= 5405 \mu\text{m}^\dagger$	

From the MDS simulations on the switch circuit described later in this chapter resonances were identified between the intrinsic FET elements and the package parasitics in both 'on' and 'off' states of the switch. Therefore, rather than maintaining the

<sup>†</sup>Reduced to 4000  $\mu\text{m}$  to avoid resonances (see Chapter 10).

gate stub line to present an effective RF open-circuit at the gate terminal of the FET, the stub length was altered so as to tune the resonances out of the operating band of the switch. The tuning stub operates by introducing at the gate of the GaAs FET a capacitive or inductive reactance which is determined by the stub length. The principle of operation of the gate tuning stub and the design methodology are described more fully in Chapter 10. The stub length was reduced to  $4000 \mu\text{m}$  in order to allow switch operation over the frequency range 8 to 12 GHz.

### 6.2.4 Bias Circuit

To realize the 'on' and 'off' states of the switch, a DC bias connection must be made to the gate terminal of the FET. As described in the Chapter 5, the drain and source must be maintained at DC earth potential in both switching states, while the gate is switched between zero bias and pinch-off representing the 'on' and 'off' states of the switch respectively. The DC connection at the drain of the FET was made using a coaxial bias-tee network incorporated into the measurement system. The bias connections at the source and gate of the FET were made on the actual microstrip circuit using a two-section bias-tee, as shown in Figure 6.4. Each section of the bias-tee incorporates a quarter wavelength low and high impedance microstrip line in order to present an effective RF open-circuit to the main line. Since the two source terminals of GaAs FET are electrically connected within their internal structure, only one of the source terminals needed to be biased.

Microstrip Bias Network Parameters				
Input Data:	$\epsilon_r = 10.5$	$h = 635 \mu\text{m}$	$t = 4 \mu\text{m}$	$w = 4000 \mu\text{m}$
	$f = 10 \text{ GHz}$			
Output Data:	$Z_0 = 14.53 \Omega$	$\lambda_s = 9835 \mu\text{m}$	$\epsilon_{eff} = 9.29$	$l_{oc} = 323 \mu\text{m}$
Layout:	$w = 4000 \mu\text{m}$	$l = \frac{\lambda_s}{4} - l_{oc}$	$= 2136 \mu\text{m}$	
Input Data:	$\epsilon_r = 10.5$	$h = 635 \mu\text{m}$	$t = 4 \mu\text{m}$	$w = 80 \mu\text{m}$
	$f = 10 \text{ GHz}$			
Output Data:	$Z_0 = 97.68 \Omega$	$\lambda_s = 11855 \mu\text{m}$	$\epsilon_{eff} = 6.40$	
Layout:	$w = 80 \mu\text{m}$	$l = \frac{\lambda_s}{4}$	$= 2964 \mu\text{m}$	

## 6.3 Optically Controlled Switch State Modelling

As has already been discussed, the gate photovoltaic effect can be exploited to give direct optical control of the GaAs FET switch. It has been noted that the optically-

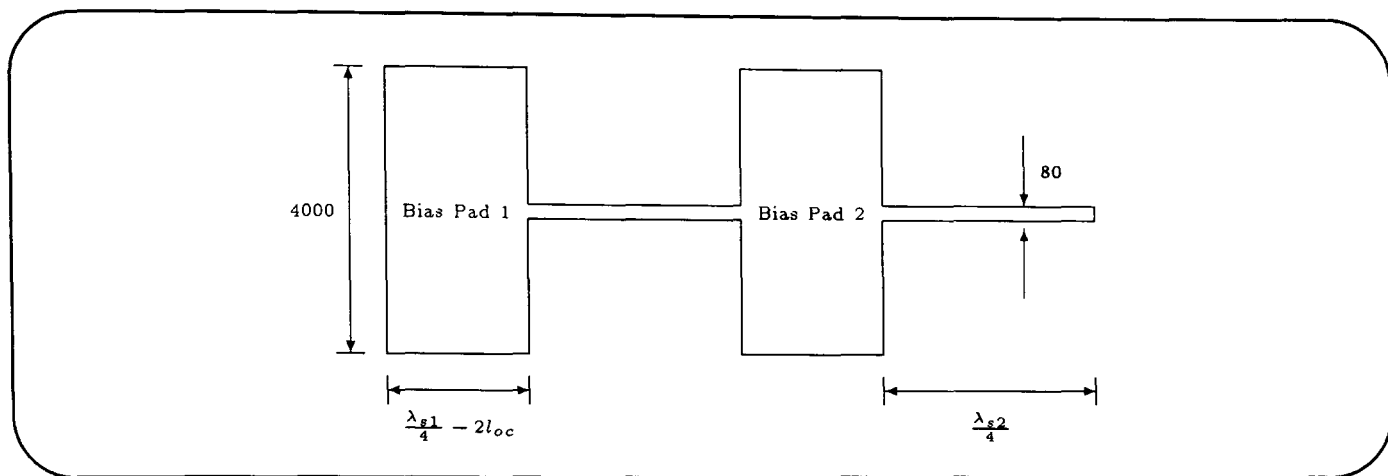


**Figure 6.4:** Two-section microstrip bias-tee arrangement (dimensions in  $\mu\text{m}$ ).

induced variations in the gate-to-source voltage are similar to those achieved with electrical control. This implies that the characteristics of the switch should be similar, whether optically or electrically controlled, and this forms the basis for the design methodology of the optically controlled switch.

### 6.3.1 Static Optical Control

The GaAs FET switch described in this thesis differs from any previously described in the literature as it relies on direct optical control of the switching state, in which the optically controlled FET interacts directly with the microwave signal. This is radically different from the indirect forms of optical control addressed so far in the literature [6.7], where there is no direct interaction between the optically illuminated FET and the microwave signal, and consequently a microwave GaAs FET is not required.

To achieve the direct optical control of a GaAs FET switch, the gate reverse bias (i.e.  $V_{GG}$ ) applied to the FET must be maintained at pinch-off in both states of the switch. With no optical signal present, the ‘off’ state of the switch is realized in an identical manner to that in the electrically controlled GaAs FET switch described in Chapter 5. When the optical signal is present, a photocurrent is generated in the gate circuit due to photon absorption in the gate depletion region of the FET. The presence of the large gate bias resistance,  $R_G$ , establishes a photovoltage which in turn counteracts the gate reverse bias,  $V_{GG}$ . When this photovoltage is sufficient to overcome the reverse bias present at the gate terminal, the optically ‘on’ state of the switch is established. The optical power required to switch the device from the ‘off’ state, where the gate-to-source voltage is at pinch-off, to the ‘on’ state, where the gate-to-source voltage,  $V_{GSi}$ , in the illuminated state is at zero bias, can be determined from the photovoltage developed across the large gate resistance. From the Schottky gate equivalent circuit under static optical illumination, shown in Figure 6.5,  $V_{GSi}$  can

be expressed as

$$V_{GSi} = V_{GG} + V_{ph} \quad (6.1)$$

$$= V_{GG} + I_{GS}R_G \quad (6.2)$$

where  $V_{ph}$  is the photovoltage developed across  $R_G$ .

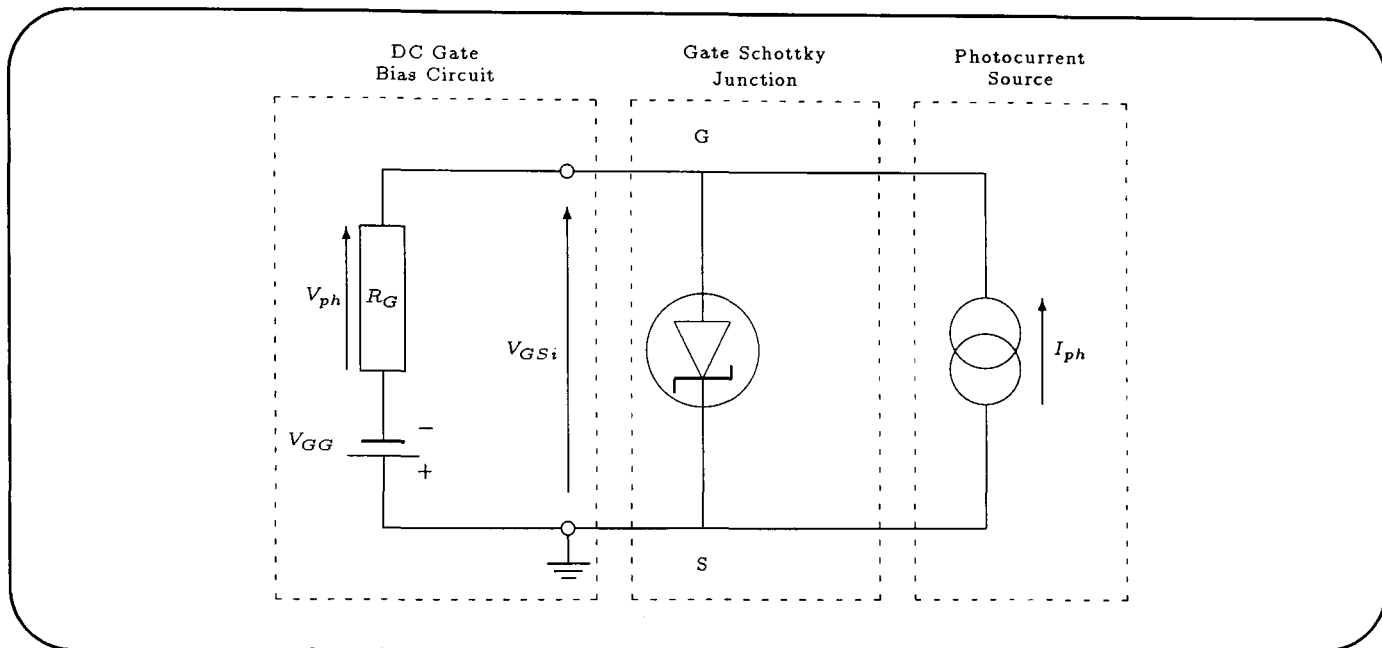


**Figure 6.5:** Gate Schottky junction equivalent circuit while under continuous optical illumination.

The gate-to-source current will consist of two components: the gate Schottky diode current,  $I_D$ , given by [6.8]

$$I_D = I_S \left\{ \exp \left( \frac{qV_{GSi}}{nkT} \right) - 1 \right\} \quad (6.3)$$

and the gate photocurrent,  $I_{ph}$ , given by equation (3.5). Therefore, from equation (6.2), the illuminated gate-to-source voltage can be expressed as

$$V_{GSi} = V_{GG} + R_G \left[ I_{ph} - I_S \left\{ \exp \left( \frac{qV_{GSi}}{nkT} \right) - 1 \right\} \right] \quad (6.4)$$

from which the gate photocurrent, and hence the optical power required to achieve the ‘on’ state, can be calculated. For the ATF-10136 GaAs FET biased at pinch-off and incorporating a 1 M $\Omega$  gate bias resistance, a gate photocurrent of approximately 1.6  $\mu$ A is required. This corresponds to an optical output power of about 3.3 mW from the laser source.

### 6.3.2 Switch State

The modelling of the switching states of an electrically controlled GaAs FET reflective microwave switch has been described in Chapter 5 and was based upon the methods proposed by Ayasli [6.6]. He used precise data relating to the physical structure

and doping levels of an FET fabricated ‘in-house’ to permit evaluation of the resistive component values associated with the intrinsic FET switch equivalent circuit in both states. This included the channel resistance,  $R_{ch}$ , and drain and source resistances,  $R_d$  and  $R_s$ , respectively. This method of component evaluation, together with approximate values for the device doping levels, was used initially in the work reported here to model the intrinsic GaAs FET switch configuration. In general, the microwave circuit designer, using commercially available or standard foundry FET's, is often limited by the information that is readily available from the manufacturer or foundry, concerning their device fabrication parameters. In the present work, rather than estimating device parameters, a simple approach for establishing these intrinsic FET parameters is proposed and is verified through comparisons of simulated and measured data for two very different FET gate structures.

In this approach, the intrinsic parameters are extracted directly from the standard hybrid  $\Pi$  model for the FET provided by the manufacturer, with the exception of the ‘off’ state drain-to-source resistance,  $R_{ds}$ . This element arises as a consequence of using the pinch-off bias of the FET in the ‘off’ state, rather than the gate voltage used for the common-source mode of operation. Its value, however, will be of the order of several kilo-ohms as suggested in [6.6]. Due to its position within the lumped equivalent circuit (i.e. shunting the drain-to-source capacitance), its precise value has been found in this work to have little effect on the modelling of the switch performance. The ‘off’ state gate-to-source and gate-to-drain capacitances,  $C_{gs}$  and  $C_{gd}$ , can be evaluated using the methods described in Section 5.4.3. A novel approach to evaluating the ‘off’ state drain-to-source capacitance,  $C_{ds}$ , is described in Chapter 10. The intrinsic FET parameters so evaluated for both FET's considered in this investigation are summarized in Table 6.1.

FET Type	‘On’ State			‘Off’ State				
	$R_{ch}$ $\Omega$	$R_d$ & $R_s$ $\Omega$	$R_g$ $\Omega$	$R_g$ $\Omega$	$R_{dc}$ & $R_{sc}$ $\Omega$	$R_{ds}$ k $\Omega$	$C_{gs}$ & $C_{gd}$ fF	$C_{ds}$ fF
ATF-10136	2.0	2.0	2.5	2.5	4.0	3.5	88	82
ATF-13136	2.0	1.5	3.0	3.0	3.5	3.5	44	45

**Table 6.1:** Values for intrinsic GaAs FET switch equivalent circuit elements.

The package parasitic elements (from the manufacturer) associated with Figure 5.4 are given in Table 6.2 [6.4].

The intrinsic elements of the FET switch equivalent circuit (Table 6.1), together with the device package model (Figure 5.4) and conventional representations of the microstrip elements of the switch circuit, were then used in conjunction with MDS

$L_g$ nH	$L_d$ nH	$L_s$ nH	$T_g$			$T_s$			$T_d$			$C_{gs}$ fF	$C_{ds}$ fF	$C_{gd}$ fF
			Z	l	$\epsilon_{eff}$	Z	l	$\epsilon_{eff}$	Z	l	$\epsilon_{eff}$			
			$\Omega$	$\mu\text{m}$		$\Omega$	$\mu\text{m}$		$\Omega$	$\mu\text{m}$				
0.9	0.6	0.15	65	889	7	30	381	7	65	889	7	50	50	5

**Table 6.2:** Circuit element values for FET package model [6.4].

to obtain simulations of the switch performance in both states. The MDS simulation schematics for the 'on' and 'off' states of the switch are shown in Figures 6.6 and 6.7, respectively, and were used to simulate the switching performance of both FET switches.

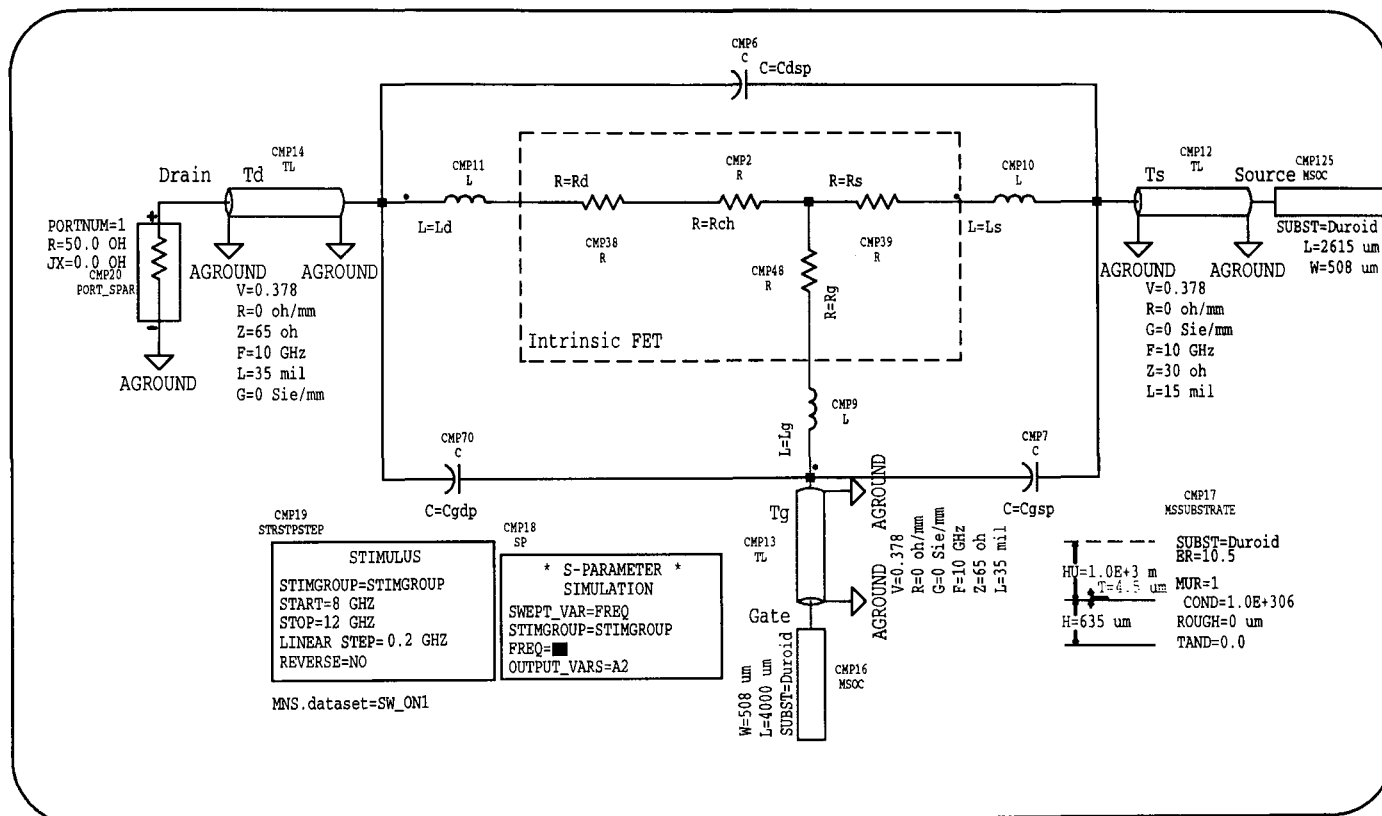


**Figure 6.6:** Simulation layout generated within MDS for determining the switch characteristics of both FET structures in the 'on' state.

## 6.4 GaAs FET Switch State Results

The switching circuits used in this investigation employed the ATF-10136 and ATF-13136 FET's from Hewlett-Packard. The ATF-10136 has an interdigitated gate structure which contrasts with the T-type structure of the ATF-13136. The differing gate structures for the FET's were selected deliberately to test the validity of the proposed methods for establishing the FET intrinsic elements of the switch model for significantly different gate structures. Both FET switch circuits used an identical microstrip layout, shown in Figure 6.1, to evaluate the switch characteristics. Packaged GaAs



### 6.4.1 Optically 'On' State

The measured and simulated magnitude and phase responses of the ATF-10136 and ATF-13136 FET switch circuits in the optically 'on' state are shown in Figures 6.8 and 6.9, respectively, and the agreement between measured and simulated results is generally good and within bounds of expected experimental error.

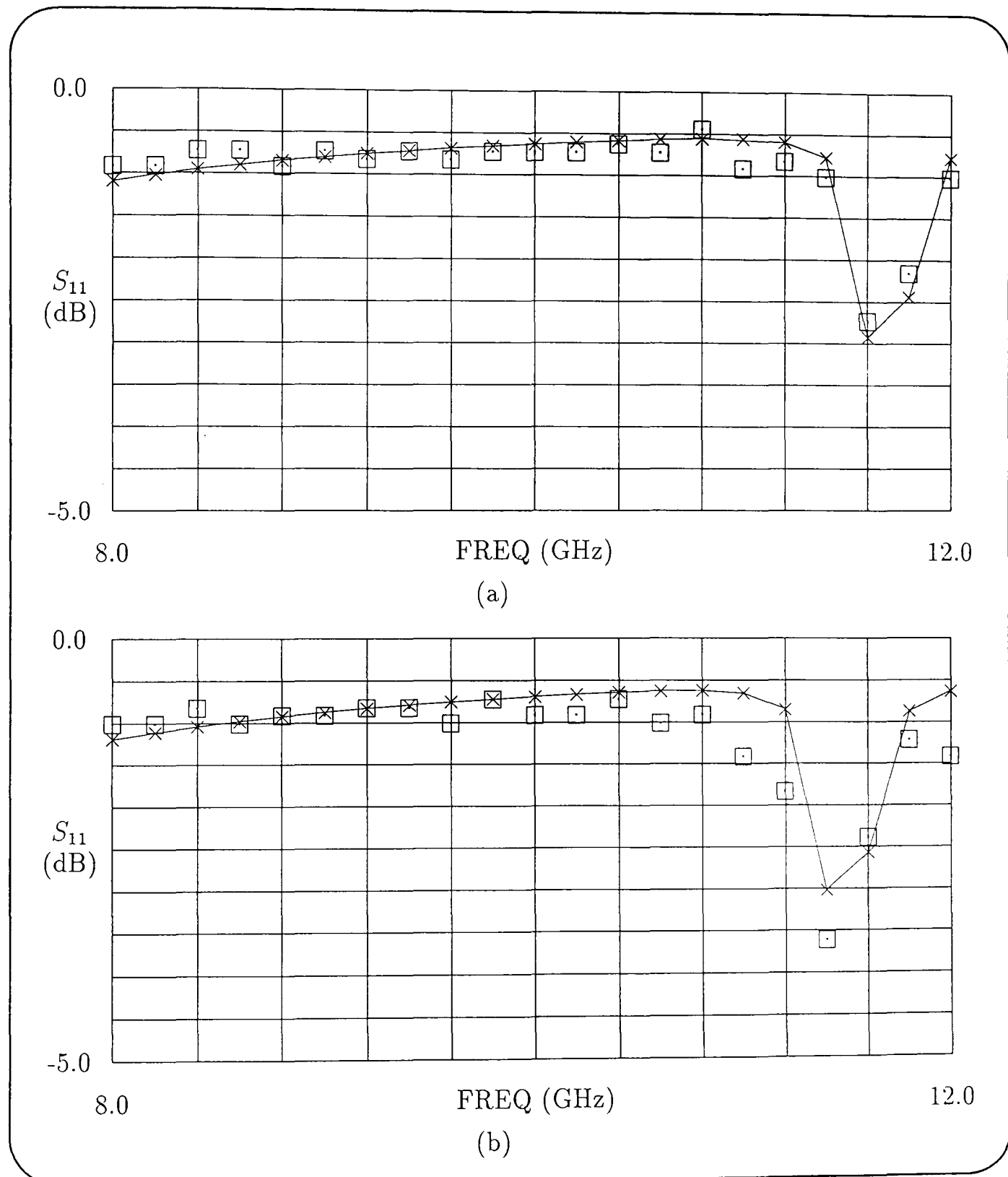
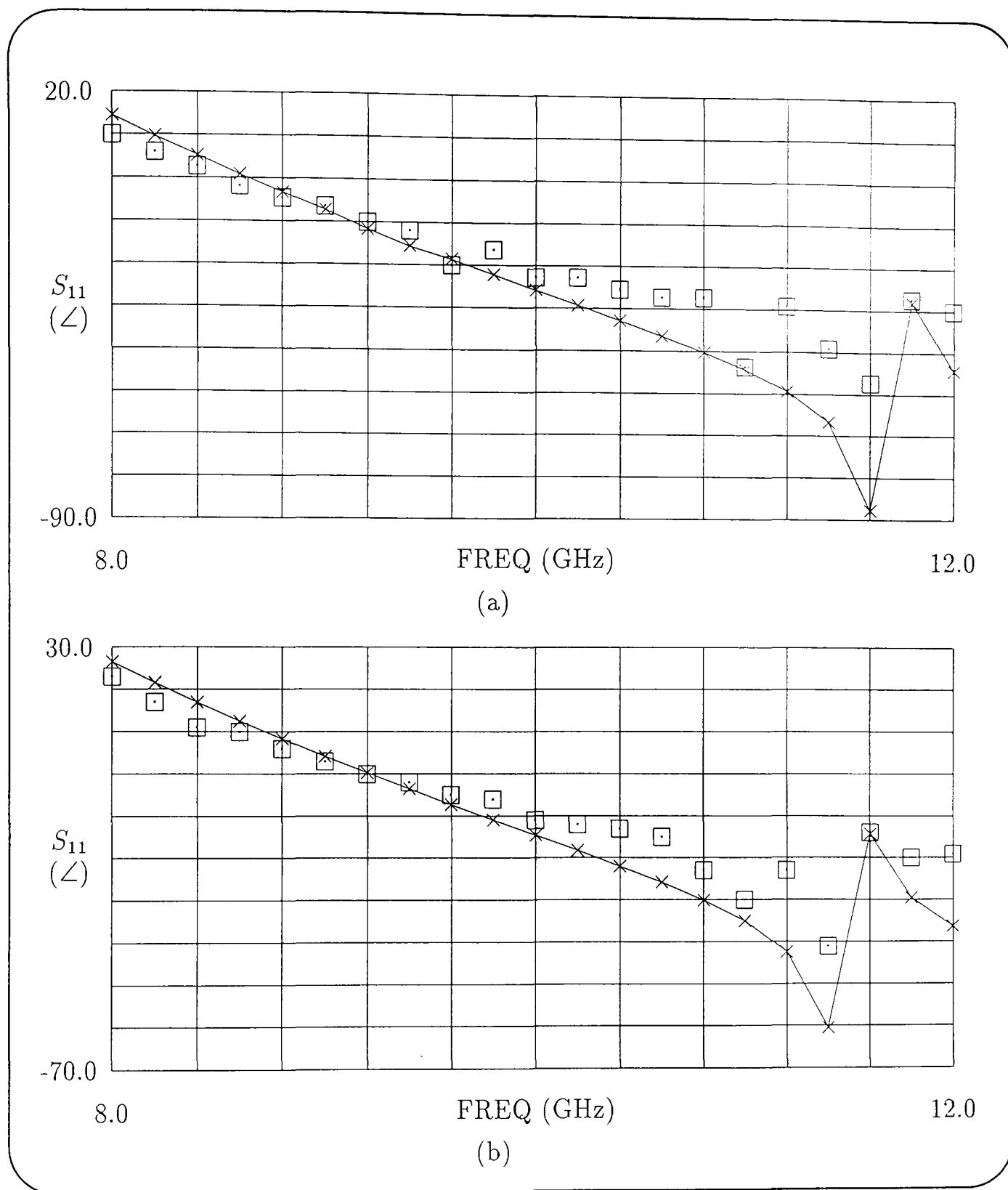


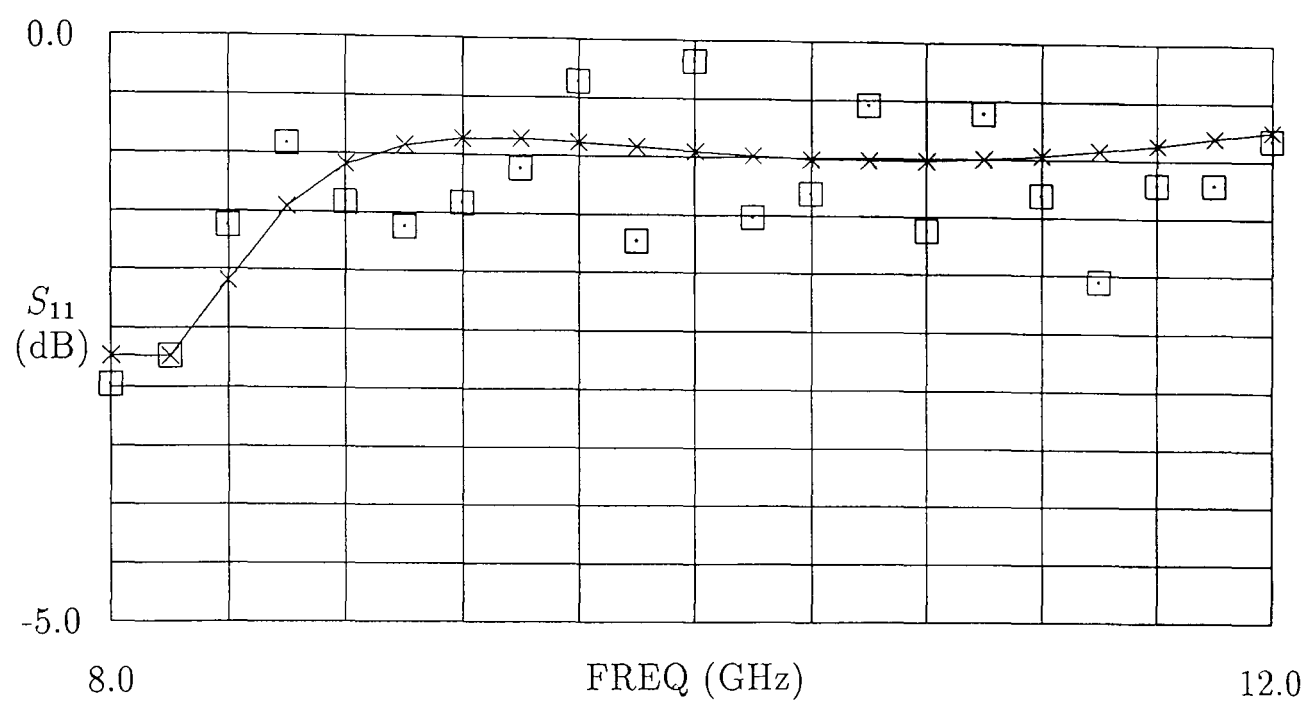
Figure 6.8: Measured ( $\square$ ) and simulated ( $\times$ ) return loss for the optically 'on' state of the GaAs FET switch. (a) ATF-10136. (b) ATF-13136.



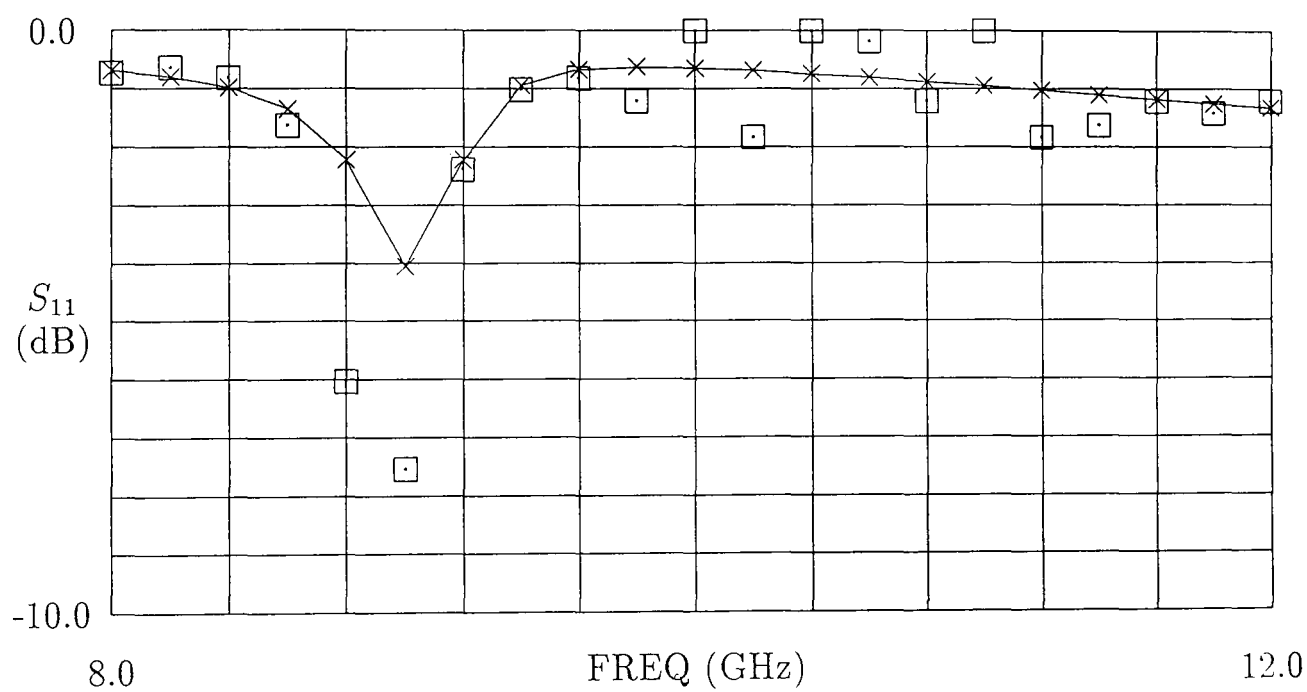
**Figure 6.9:** Measured ( $\square$ ) and simulated ( $\times$ ) phase for the optically 'on' state of the GaAs FET switch. (a) ATF-10136. (b) ATF-13136.

#### 6.4.2 'Off' state

The measured and simulated magnitude and phase responses of the ATF-10136 and ATF-13136 FET switch circuits in the 'off' state are shown in Figures 6.10 and 6.11, respectively, and the agreement between measured and simulated results is again generally good and within bounds of expected experimental error.



(a)



(b)

**Figure 6.10:** Measured ( $\square$ ) and simulated ( $\times$ ) return loss for the 'off' state of the GaAs FET switch. (a) ATF-10136. (b) ATF-13136.

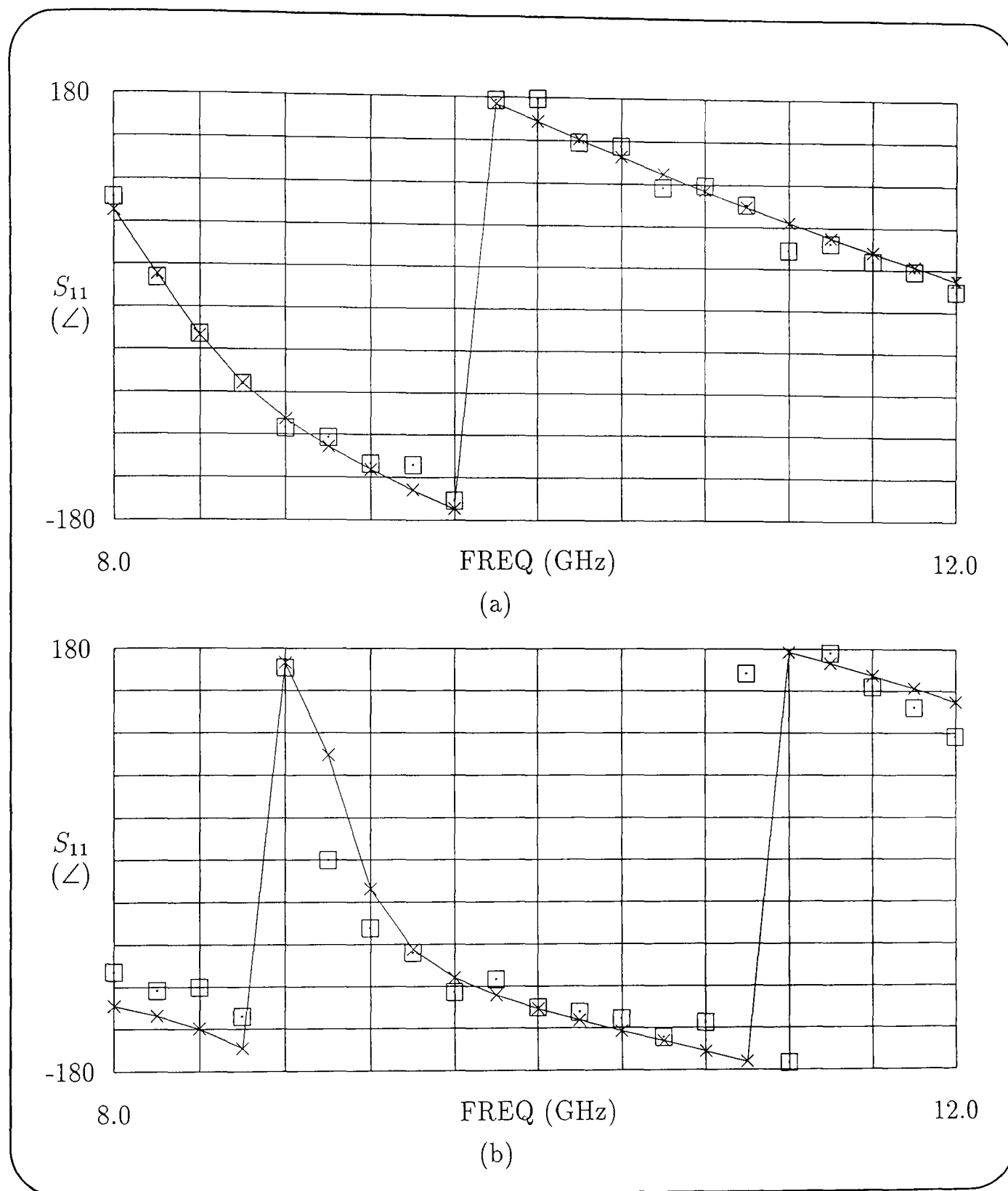


**Figure 6.11:** Measured ( $\square$ ) and simulated ( $\times$ ) phase for the 'off' state of the GaAs FET switch. (a) ATF-10136. (b) ATF-13136.

# References

- [6.1] A. Rosen and F. Zutavern, eds., *High-power optically activated solid-state switches*, ch. 9, pp. 187–217. Boston: Artech House, 1994.
- [6.2] A. Madjar, A. Paoletta, and P. R. Herczfeld, “Modeling the optical switching of MESFET’s considering the external and internal photovoltaic effects,” *IEEE Trans. Microwave Theory Tech.*, vol. 42, pp. 62–67, Jan. 1994.
- [6.3] P. Chakrabarti, S. K. Shrestha, A. Srivastava, and D. Saxena, “Switching characteristics of an optically controlled GaAs-MESFET,” *IEEE Trans. Microwave Theory Tech.*, vol. 42, pp. 365–375, Mar. 1994.
- [6.4] Hewlett Packard, *Communications Components GaAs & Silicon Designer’s Catalogue*, 1993.
- [6.5] M. Kirschning, R. H. Jansen, and N. H. L. Koster, “Accurate model for open end effect of microstrip lines,” *Electron. Lett.*, vol. 17, pp. 123–125, Feb. 1981.
- [6.6] Y. Ayasli, “Microwave switching with GaAs FETs,” *Microwave J.*, vol. 25, pp. 61–74, Nov. 1982.
- [6.7] A. Paoletta, A. Madjar, P. R. Herczfeld, and D. Sturzebecher, “Optically controlled GaAs MMIC switch using a MESFET as an optical detector,” in *Proc. IEEE MTT-S Int. Microwave Symp. Dig.*, pp. 941–944, 1990.
- [6.8] S. M. Sze, *Physics of semiconductor devices*. New York: Wiley, second. ed., 1981.

# Chapter 7

## Transient Response of Optically Controlled GaAs FET's

### Contents

---

<b>7.1</b>	<b>Introduction . . . . .</b>	<b>105</b>
<b>7.2</b>	<b>Transient Response Under Optical Control . . . . .</b>	<b>106</b>
7.2.1	Transient Response Measurement . . . . .	106
7.2.2	Transient Response Modelling . . . . .	107
<b>7.3</b>	<b>Optical Transient Response Results . . . . .</b>	<b>108</b>

---

### 7.1 Introduction

THE transient response of the optically controlled GaAs FET switch described in the previous chapter will determine the maximum rate at which the GaAs FET can be switched by the optical signal and therefore the maximum data rate that could be used if the device were incorporated in an optical sensor. Madjar *et al.* [7.1] have recently investigated the transient response of the GaAs FET by considering the photovoltaic effects in the gate depletion region and the barrier interface region. With regard to the gate photovoltaic effect, Madjar *et al.* [7.1] have developed a model for the transient response (i.e. rise and fall times) associated with the gate photovoltaic effect and this was considered in Chapter 4. While their experimental results identify the general transient behaviour associated with the photo-effect, a direct comparison between their measured and simulated results is difficult and to a large extent invalid due to the different gate loading and optical pulse conditions used for experiment and simulation. However, even given these limitations, there does appear to be a discrepancy between their simulated and measured results. This discrepancy is particularly evident for the fall times of the response which differ by up to a factor of ten between simulated and measured results.

Measurement and modelling techniques for the transient response of the gate depletion region photovoltaic effect are considered in detail in Section 7.2. The measured and simulated transient responses of the optically controlled GaAs FET switch are presented in Section 7.3, which for the first time verifies the transient response model. Furthermore, this section provides results which validate the transient response model for two very different GaAs FET gate structures.

The key points of this chapter are identified below.

- **Accurate modelling of the transient response associated with the gate depletion region photovoltaic effect.**
- **De-embedding of measurement probes.**
- **Experimental switch circuit design for transient response determination.**
- **Experimental verification of the transient response model through a direct comparison of measured and simulated rise and fall time results under identical gate loading and optical pulse conditions.**
- **Experimental validation of the transient response models for two very different FET gate structures.**

## 7.2 Transient Response Under Optical Control

In the following sections a model to characterize the transient response associated with the gate photovoltaic effect in a GaAs FET switch under pulsed optical control is developed and validated through practical measurement. In addition, the model has been verified for both types of FET switch.

### 7.2.1 Transient Response Measurement

The microstrip circuit used to evaluate the transient response for both FET switch circuits utilized a similar layout to that used to evaluate the switch state characteristics, with a  $1\text{ M}\Omega$  resistance incorporated in the gate bias circuit. To evaluate the transient response of the FET it became necessary to include an additional resistor ( $47\text{ k}\Omega$ ) in the gate bias circuit of the FET switch. The transient response was measured across this resistor rather than across the  $1\text{ M}\Omega$  gate resistor since this latter value would have imposed a severe frequency limitation when considered in conjunction with the measurement probe. The microstrip layout was modified to allow the additional resistor to be surface mounted, as shown in Figure 7.1.

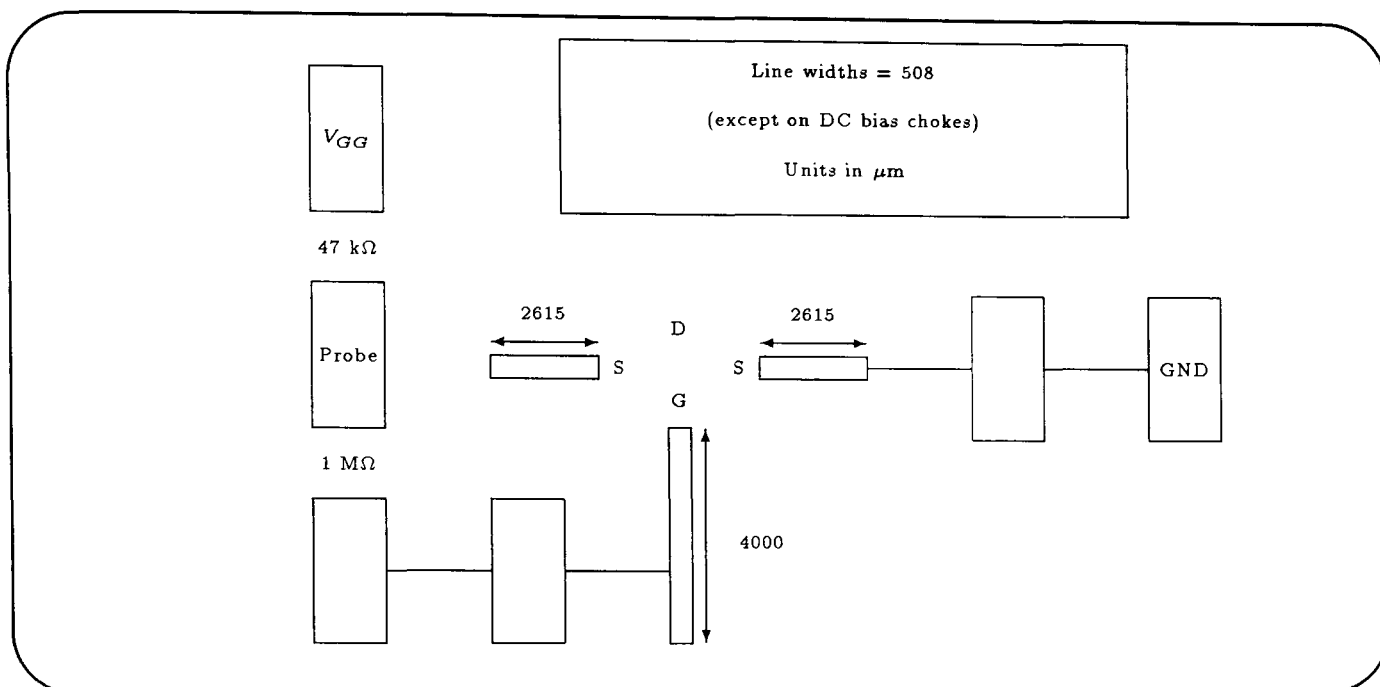


**Figure 7.1:** Microstrip circuit layout of the transient response measurement for the direct optically controlled microwave switch.

## 7.2.2 Transient Response Modelling

The optically controlled microwave switch, described in the previous chapter, relies on a photovoltage developed across the large gate bias resistance as the means of controlling the gate-to-source voltage, and therefore the switching state. The development of the optical transient response model for the gate photovoltaic effect (*external* photovoltaic effect) described in this thesis thus follows the initial approach of Madjar *et al.* [7.1]. The difference is that, since a reflective switch configuration is described here, the transient response of the switch will be determined by the rise and fall times associated with the gate-to-source voltage while under pulsed optical illumination (i.e.  $V_{GSi}$ ), rather than the drain current response considered in [7.1]. Also, rather than using numerical techniques to solve the nonlinear differential equation that results from the analysis of [7.1], the transient response was extracted from MDS. The MDS model incorporates the external DC gate bias circuit, which includes the large gate resistance, the internal elements of the gate junction, namely the gate Schottky junction, the nonlinear gate capacitance and the optically-induced gate short-circuit photocurrent (see Figure 4.2). The nonlinear gate capacitance expression used in the MDS simulations is obtained by combining equations (4.1) and (4.2) to give

$$C_g = \left( \frac{\epsilon_0 \epsilon_r L_G W_G}{a} \right) \left( \frac{|V_P| + \phi_B}{\phi_B - V_{GSi}} \right)^{\frac{1}{2}}. \quad (7.1)$$

The MDS simulation of the nonlinear gate capacitance requires an expression for the associated charge, which is obtained simply through the integration of equation (7.1)

to give

$$Q_g = \int C_g dV_{GSi} \quad (7.2)$$

$$= \frac{\epsilon_0 \epsilon_r L_G W_G \sqrt{|V_P| + \phi_B}}{a} \int \frac{1}{\sqrt{\phi_B - V_{GSi}}} dV_{GSi} \quad (7.3)$$

$$= -\frac{2\epsilon_0 \epsilon_r L_G W_G \sqrt{|V_P| + \phi_B}}{a} (\phi_B - V_{GSi})^{\frac{1}{2}} \quad (7.4)$$

where  $Q_g$  is the charge associated with the gate capacitance. The gate short-circuit photocurrent is modelled as an ideal impulse source which is generated by the pulsed optical illumination and whose numerical value at pinch-off can be determined by the methods described in Section 3.7. From this model the rise and fall times of the illuminated gate-to-source voltage can be evaluated while under pulsed optical control and hence the limitations on the optical switching speed of the FET switch can be established. Furthermore, to provide an accurate simulation of the transient response of the switch under pulsed optical control, a model to represent the effect of the measurement probe was included in MDS. The transient responses of both GaAs FET's were simulated with the same layout shown in Figure 7.2 to test the validity of the proposed methods for establishing the switching speed for significantly different gate structures.

### 7.3 Optical Transient Response Results

The measured and simulated transient response results for the ATF-10136 and ATF-13136 switch circuits under pulsed optical illumination are shown in Figures 7.3(a) and 7.3(b), respectively. These results represent, for the first time, a direct comparison between experimental and simulated results for the rise and fall times associated with the gate photovoltage transient response. Furthermore, it can be seen that, for the first time, very good agreement is obtained between the measured and simulated data for both types of optically controlled FET switch.

The simulated results include a model for the Hewlett Packard 10432A 10:1 oscilloscope probe used in the measurements to allow a direct comparison with the measured data. Initially, the probe was modelled as a 10 M $\Omega$  resistor shunted by a capacitance of 7.5 pF, based on the data given in [7.2]. However, due to the critical significance of the probe in the measurement of the transient response, the exact impedance of the probe was measured using a vector impedance meter. From the probe impedance,  $Z_p$ , this was measured to be 1.9 $\angle$ 92 $^\circ$  M $\Omega$  at 10 kHz<sup>†</sup>. Since the probe capacitance could be varied via a varicap it was assumed that the shunt resistance was correct at 10 M $\Omega$

<sup>†</sup>All transient response measurements made using this probe were performed over the kilo-Hertz range

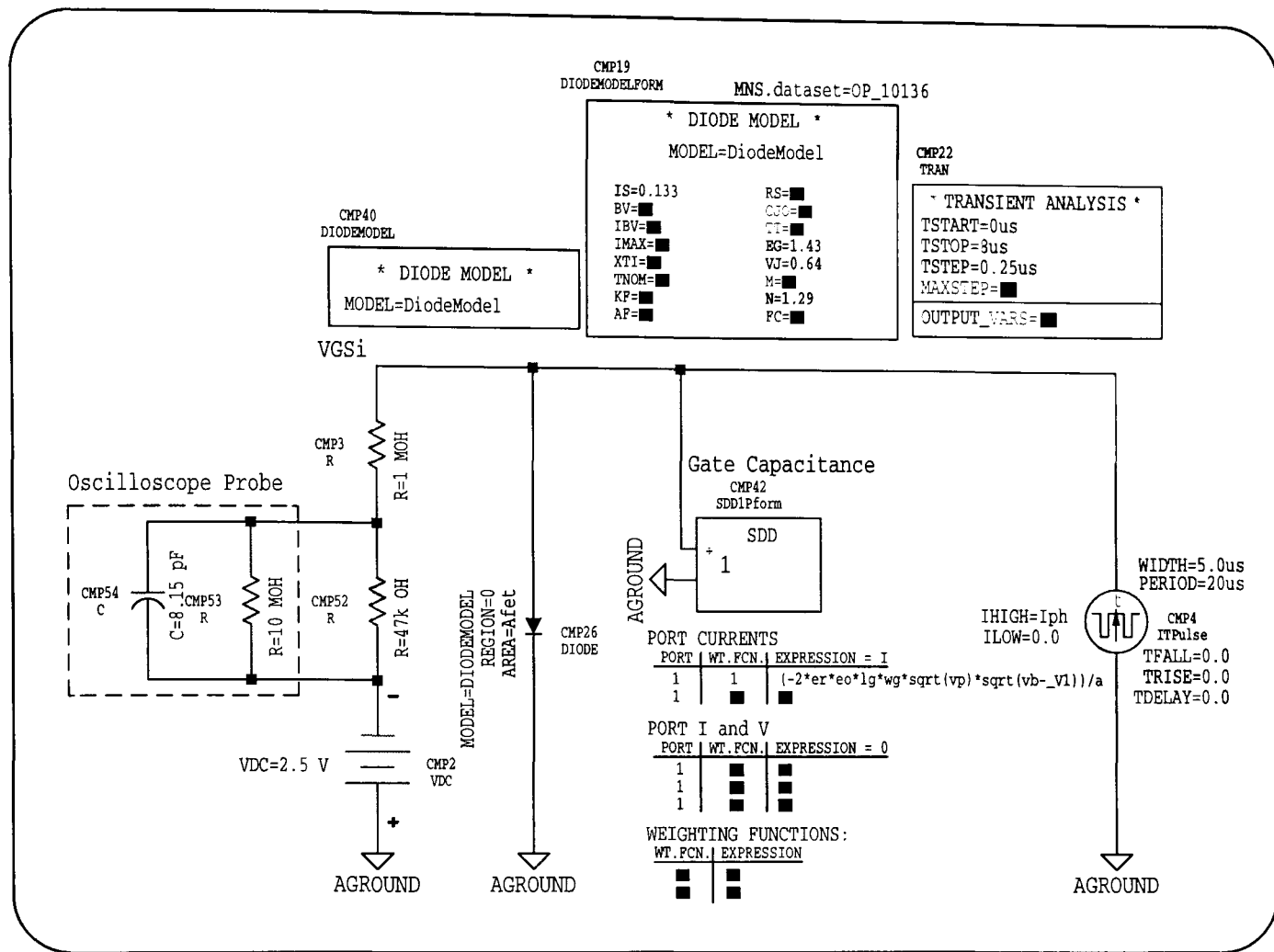


**Figure 7.2:** Simulation layout generated within MDS for determining the switch transient response of both FET structures.

and that the exact capacitance of the probe could be calculated from the measured impedance. For a parallel resistor and capacitor arrangement, the probe impedance is given by

$$Z_p = \frac{\frac{R_p}{j\omega C_p}}{R_p + \frac{1}{j\omega C_p}} \quad (7.5)$$

$$= \frac{R_p}{1 + (\omega R_p C_p)^2} - j \frac{\omega R_p^2 C_p}{1 + (\omega R_p C_p)^2} \quad (7.6)$$

where  $\omega$  is the angular frequency and  $R_p$  and  $C_p$  are the parallel resistance and capacitance values of the probe respectively. From the impedance measurement and equation (7.6) the shunt capacitance of the probe was established to be 8.15 pF. The 47 kΩ resistor incorporated in the gate bias circuit effectively shunts the 10 MΩ probe resistance, thus reducing the time constant associated with the probe. If the measurement were taken across the 1 MΩ gate resistor, the probe time constant would have been given by

$$t_p = R_G || R_p \times C_p \simeq 7.4 \mu s. \quad (7.7)$$

This time constant would mask the actual transient response of the FET switch, considering its expected response time was of the order of micro-seconds. With the mea-

surement taken across the 47 k $\Omega$  resistor, the time constant of the probe is reduced to approximately 380 ns, permitting the pulse response to be measured successfully. A lower resistance value would be preferable considering the expected response times of the FET, but, due to the voltage divider created by the two gate resistors, a lower value would cause the measured signal to fall below the voltage sensitivity of the oscilloscope being used. The probe was used in conjunction with the Hewlett Packard 54602A oscilloscope which allowed automatic determination of the rise and fall times associated with the FET transient response. The effect of the probe on the transient response of the FET was compensated theoretically by removing the model for the probe from the MDS simulation layout. In the transient response measurements, the FET switch circuit was illuminated by the focussed output of a 1 mW pulsed laser diode module having a maximum modulation frequency of 100 MHz and emitting at a wavelength of 670 nm. The optical pulse duration was set to 5  $\mu$ s. The measured and simulated rise and fall times for the ATF-10136 and ATF-13136 FET switching circuits while under pulsed optical control, with and without the effects of the oscilloscope probe, are summarized in Table 7.1. This confirms that the response times are less than 1  $\mu$ s for typical GaAs FET parameters.

FET Type	Simulated Response Without Probe		Measured/Simulated Response With Probe	
	Rise Time	Fall Time	Rise Time	Fall Time
	ns	ns	ns	ns
ATF-10136	555	400	1172	965
ATF-13136	276	200	972	872

**Table 7.1:** Rise and fall times associated with the gate photovoltaic effect in the FET switch.

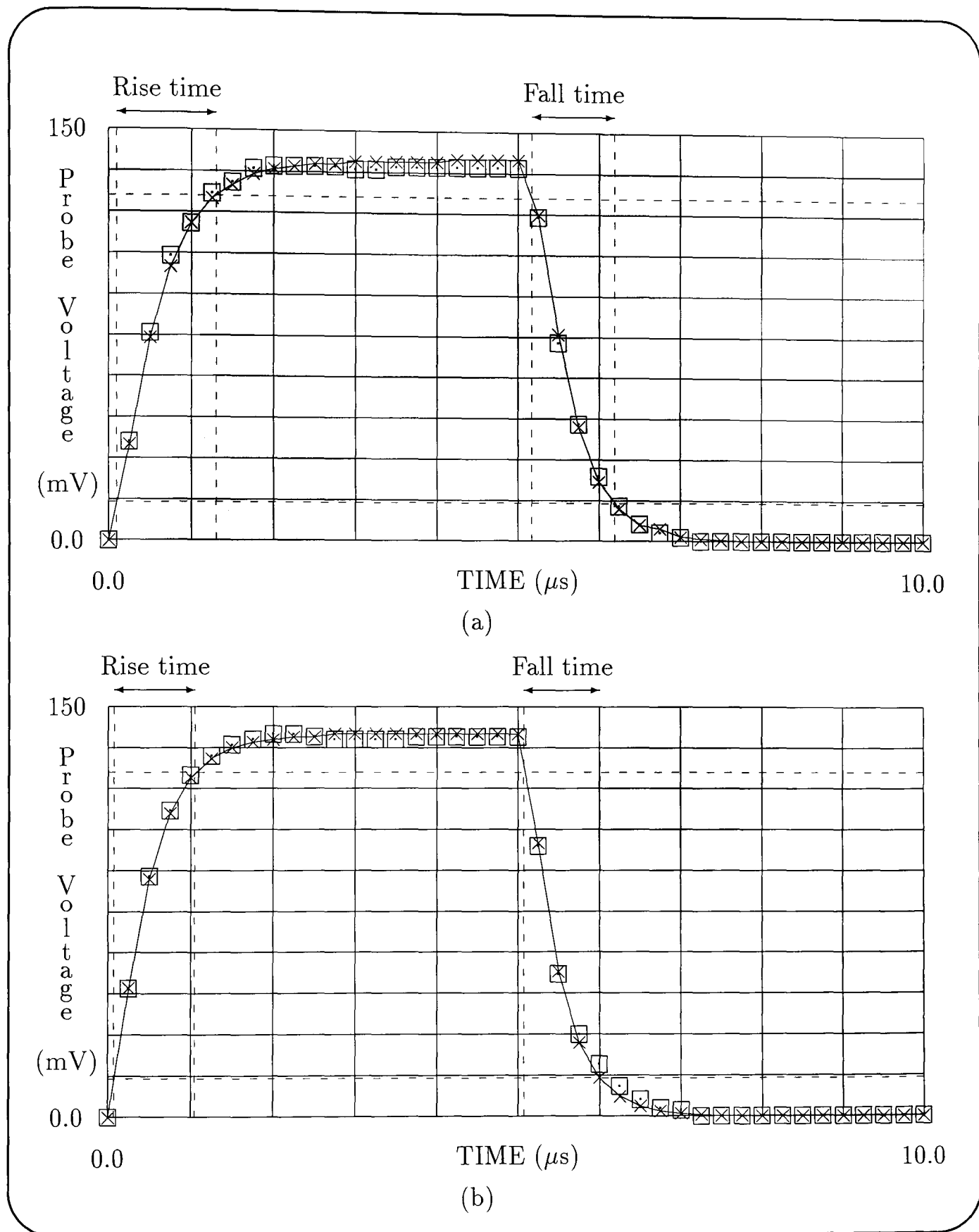


**Figure 7.3:** Measured ( $\square$ ) and simulated ( $\times$ ) transient response for optical FET switch circuit including oscilloscope probe. (a) ATF-10136. (b) ATF-13136.

# References

- [7.1] A. Madjar, A. Paoella, and P. R. Herczfeld, "Modeling the optical switching of MESFET's considering the external and internal photovoltaic effects," *IEEE Trans. Microwave Theory Tech.*, vol. 42, pp. 62–67, Jan. 1994.
- [7.2] Hewlett Packard, *Test and Measurement Catalogue*, 1994.

# Chapter 8

## Microwave GaAs FET Phase Shifters

### Contents

---

<b>8.1</b>	<b>Introduction . . . . .</b>	<b>113</b>
<b>8.2</b>	<b>Reflective Type Phase Shifters . . . . .</b>	<b>114</b>
8.2.1	Hybrid Coupled Phase Shifter . . . . .	115
8.2.2	Switched-Line Phase Shifter . . . . .	115
8.2.3	Loaded-Line Phase Shifter . . . . .	116
<b>8.3</b>	<b>Loaded-Line Phase Shifter Design . . . . .</b>	<b>117</b>
8.3.1	Analysis . . . . .	117
8.3.2	Shunt Loaded-Line Configurations . . . . .	117
<b>8.4</b>	<b>Large Phase Shifts In Loaded-Line Elements . . . . .</b>	<b>119</b>
8.4.1	Three-Stage Phase Shifter . . . . .	119
8.4.2	Four-Stage Phase Shifter . . . . .	120

---

### 8.1 Introduction

**I**N this chapter the theory and design of microwave phase shifters, in which the phase states are controlled by a digital (electrical) signal, are described with particular focus on monolithic circuit implementation. A conventional phase shifter design is used in Chapter 9, in the realization of a single-bit phase shifter, in which the phase states are controlled solely by an optical signal.

Whether the phase shifter employs optical or conventional electrical control, a particular phase state is set with a semiconductor switching device such as a microwave *p-i-n* diode or, more specific to this investigation, a microwave FET. These switching

devices are used to create a short- or open-circuit at the desired point in a microwave circuit. A variety of digitally controlled microwave phase shifters can be configured by appropriately mounting one or several of these switching devices in different types of transmission line circuit. In the subsequent sections of this chapter conventional electrically controlled phase shifter designs are reviewed, and in Chapter 9 the design is refined to incorporate the GaAs FET switches described in Chapter 5 to achieve optical control.

The fundamentals of the operation of digitally controlled reflection type phase shifters are described in Section 8.2, with the discussion focussing on the design of single-bit loaded-line phase shifters in Section 8.3. Some consideration of the design of multiple-bit loaded-line phase shifters is presented in Section 8.4.

The key points of this chapter are identified below.

- **Description of conventional reflection type, electrically controlled digital phase shifters.**
- **Design approaches for single and multiple bit loaded-line phase shifters.**

## 8.2 Reflective Type Phase Shifters

Phase shifters can be broadly classified as either the reflection type or transmission type, irrespective of the type of switching element being used. The ideal configurations are shown in Figure 8.1.

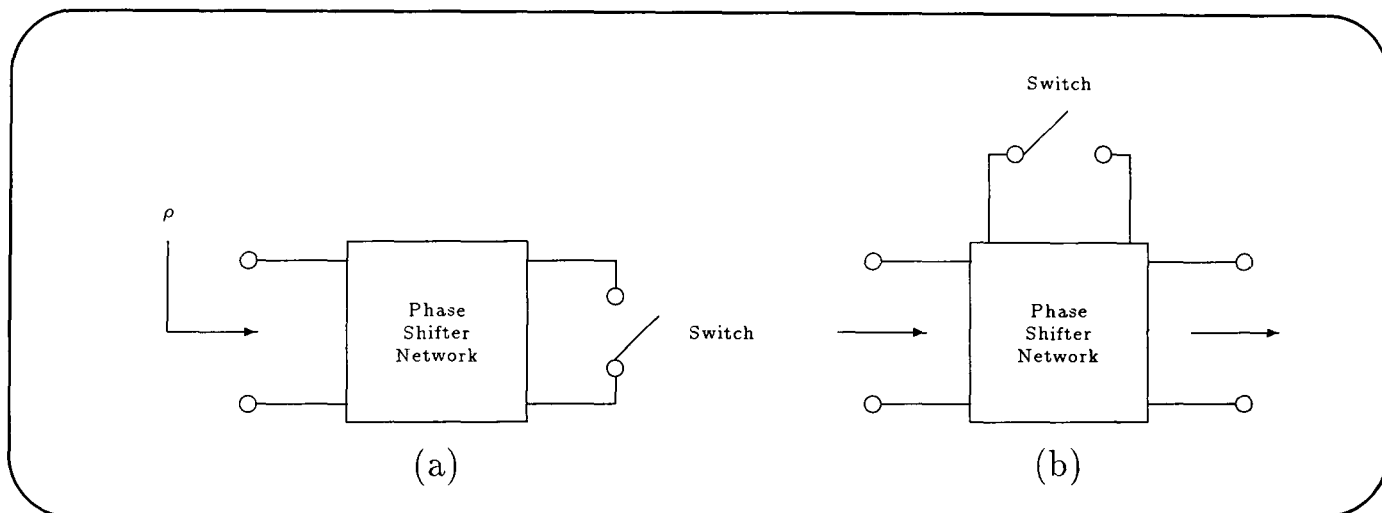


**Figure 8.1:** Schematic representation of two ideal phase shifter configurations. (a) Reflection type. (b) Transmission type.

The reflection type phase shifter is basically a one port device terminated by a switching element which reflects the microwave signal, ideally with zero loss (i.e. reflection coefficient of  $\pm 1$ ) and has a phase shift dependent upon the phase of the reflection coefficient in the two switching states. In contrast, the transmission type phase shifter is a two port device in which the phase of the transmission coefficient

through the device is altered by means of the switch. Ideally the magnitude remains the same in both states and the phase shift is given by the change in transmission phase between the two switching states. Since reflective switches have been adopted in this investigation, this chapter is concerned only with this configuration. A variety of reflection type phase shifters are described in the literature and although a specific type of phase shifter is implemented in this investigation, the general design methodology is applicable to any of the phase shifters described in this section.

Although hybrid phase shifter circuits commonly employ  $p-i-n$  diode switches, the incompatibility of  $p-i-n$  diodes with commercially offered monolithic processes necessitates the use of GaAs FET switches for MMIC phase shifter implementations. However this does not pose any problems of design validity, since in this instance the  $p-i-n$  diodes and GaAs FET's are performing identical functions.

### 8.2.1 Hybrid Coupled Phase Shifter

The hybrid coupled phase shifter makes use of a 3 dB,  $90^\circ$  hybrid coupler with two ports terminated in identical phase-controllable reflective switches. The hybrid coupler is used to provide isolation of the input and output ports. This style of phase shifter requires two reflective terminations (i.e. a minimum of two switch elements) per phase bit, as illustrated by Figure 8.2

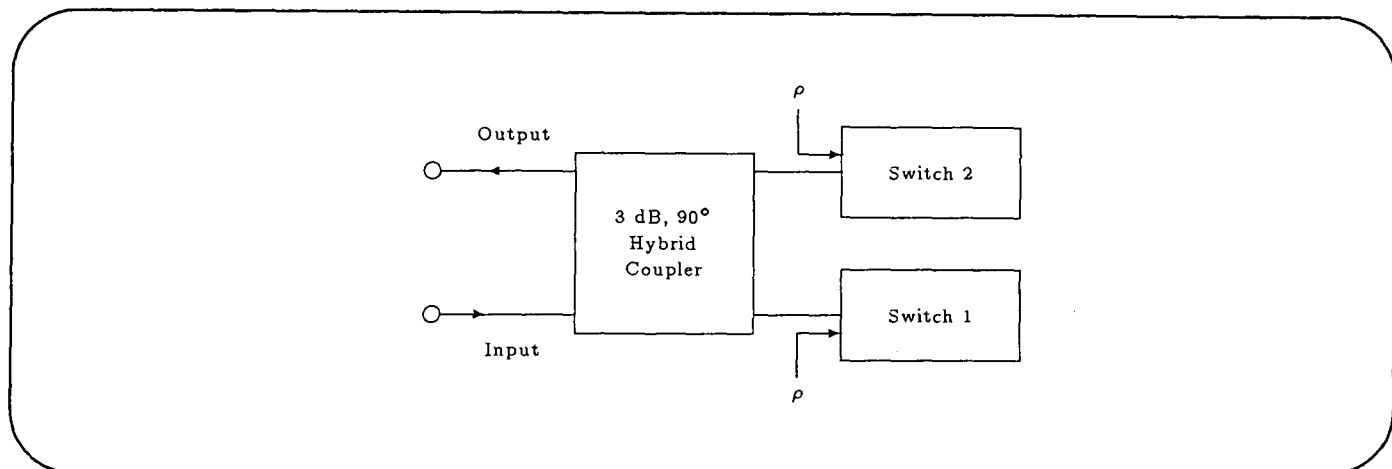


Figure 8.2: Schematic representation of a hybrid coupled phase shifter.

The hybrid coupled phase shifter is suitable for hybrid construction, where a branch-line, rat-race or backward wave coupler is commonly used. For MMIC versions of the hybrid coupled phase shifter, Lange couplers are used due to their small size, broadband performance and ease of implementation.

### 8.2.2 Switched-Line Phase Shifter

The switched-line phase shifter is a time delay circuit in which the phase shift is obtained by switching between two transmission line sections of different lengths, as shown in Figure 8.3.

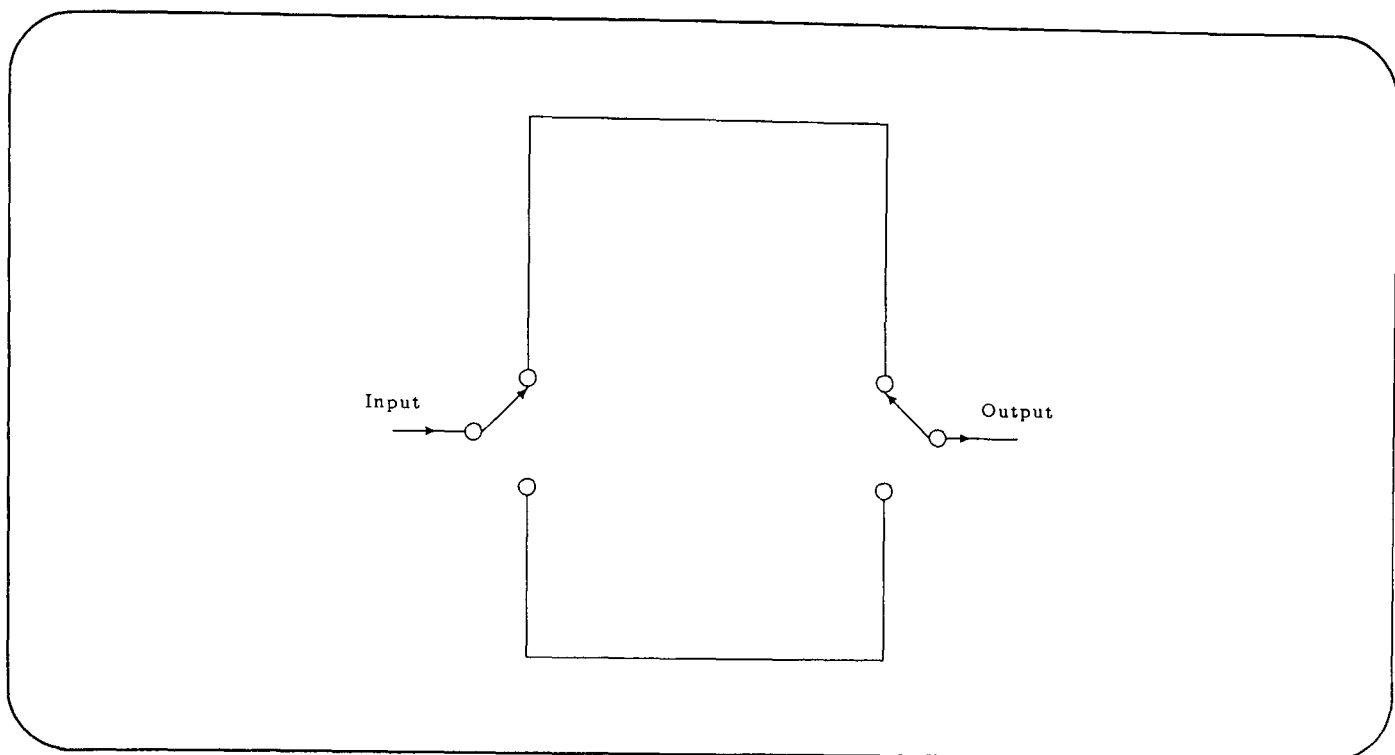


Figure 8.3: Schematic representation of a switched-line phase shifter.

This arrangement requires the maximum number of switches (i.e. three or four) per phase bit and can be implemented in hybrid or monolithic form.

### 8.2.3 Loaded-Line Phase Shifter

The loaded-line phase shifter makes use of a transmission line loaded with an identical pair of switchable reactive elements. The switchable reactive elements are most commonly connected in a shunt arrangement, as shown in Figure 8.4, since this arrangement involves a simpler biasing circuit.

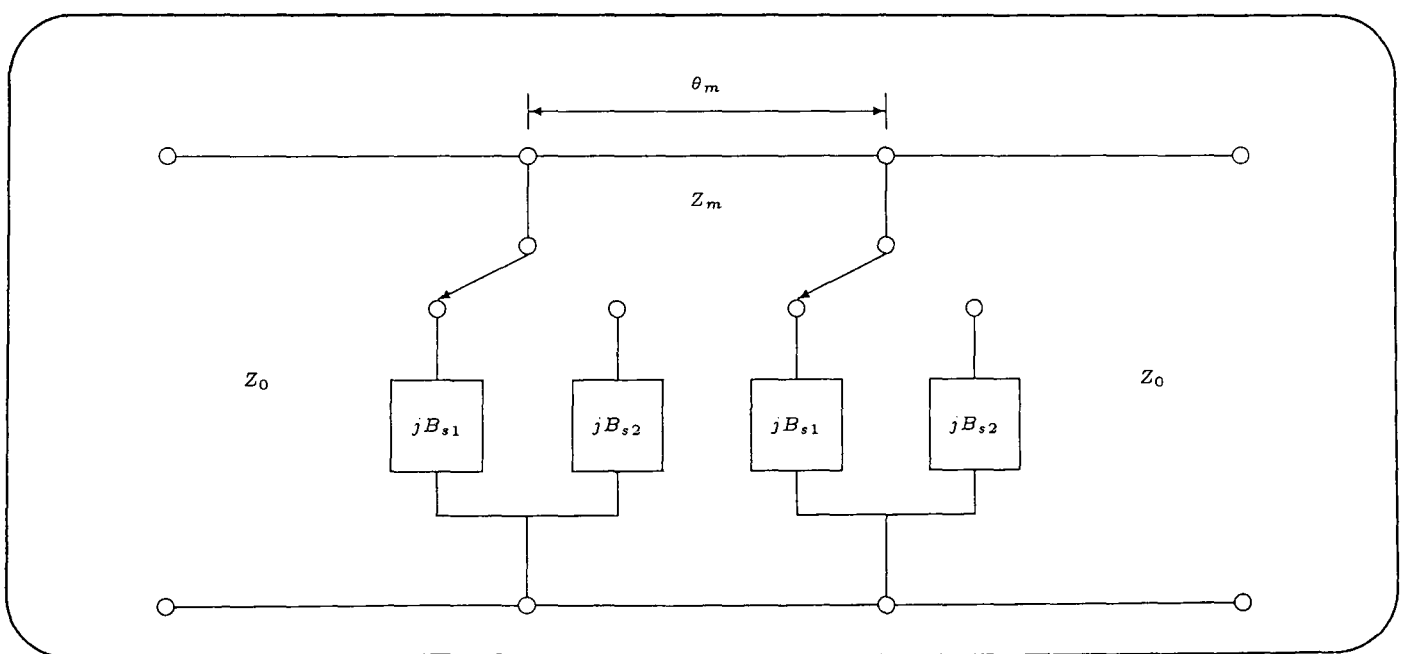


Figure 8.4: Schematic representation of a shunt loaded-line phase shifter.

The loaded-line arrangement is used primarily for achieving phase shifts up to  $45^\circ$ , since the susceptance magnitude of the loading element must be kept small for a good

input match over the desired frequency band.

## 8.3 Loaded-Line Phase Shifter Design

This type of phase shifter has been fabricated in hybrid and monolithic forms, and was used as the basis for the design of the optically controlled microwave phase shifter described in Chapter 9.

### 8.3.1 Analysis

The shunt loaded-line phase shifter can be analyzed very simply by considering cascaded ABCD matrices associated with the two shunt loading elements connected either side of the main transmission line element [8.1]. Based upon the initial work of Davies [8.2], Atwater [8.3] has shown that for a loss less loaded-line arrangement, the admittance of the main loaded transmission line,  $Y_m$ , of electrical length,  $\theta_m$ , is given by

$$Y_m = Y_0 \sin \theta_m \sec \left( \frac{\Delta\phi}{2} \right) \quad (8.1)$$

where  $Y_0$  is the characteristic admittance of the input and output port and  $\Delta\phi$  the required phase shift. The susceptance of the reactive load,  $B_{si}$ , required to yield a particular phase shift is given by [8.3]

$$B_{si} = Y_0 \left[ \cos \theta_m \sec \left( \frac{\Delta\phi}{2} \right) \pm \tan \left( \frac{\Delta\phi}{2} \right) \right] \quad (8.2)$$

where  $i = 1, 2$ , representing the two switching states, respectively. Opp *et al.* [8.4] have defined three classes of loading mode, with class III being defined as  $B_{s1} = -B_{s2}$ , allowing switching to be achieved between complex conjugate loads. In class III mode, the main loaded transmission line should have an electrical length of  $90^\circ$ , to achieve maximum bandwidth performance. When the susceptances are switched between  $B_{s1}$  and  $-B_{s1}$ , the phase changes by  $\pm\Delta\phi/2$ , about  $90^\circ$ . Therefore, with  $\theta_m$  set to  $90^\circ$ , equations (8.1) and (8.2) reduce to the following

$$Y_m = Y_0 \sec \left( \frac{\Delta\phi}{2} \right) \quad (8.3)$$

$$B_{si} = \pm Y_0 \tan \left( \frac{\Delta\phi}{2} \right). \quad (8.4)$$

### 8.3.2 Shunt Loaded-Line Configurations

Since the switching element rarely provides the susceptance requirements given by equation (8.4), it is necessary to incorporate impedance transformation networks such that

the correct load impedance is presented to the main line to achieve the required phase shift. This can be achieved using a shunt stub or tandem stub mounting arrangement, as shown in Figures 8.5(a) and 8.5(b), respectively.

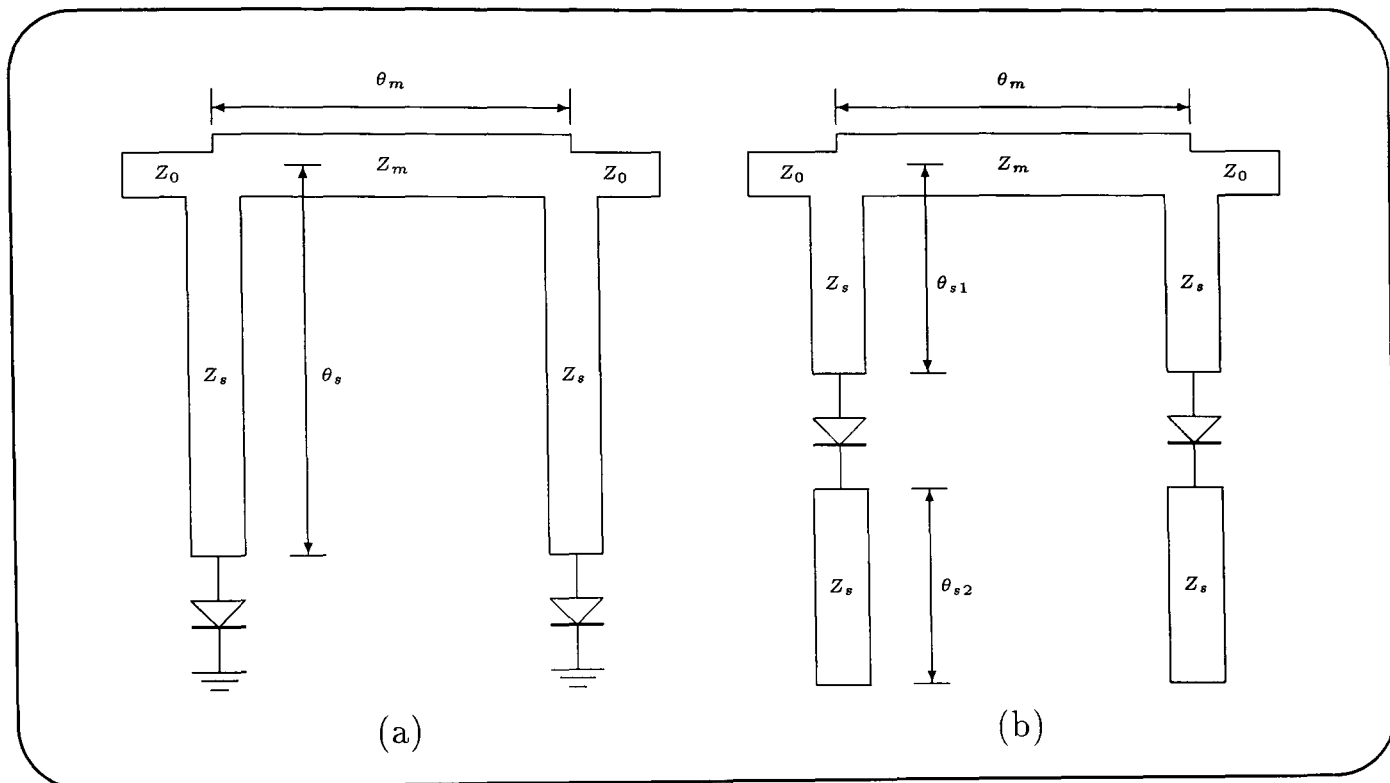


**Figure 8.5:** Impedance transformation in loaded-line phase shifters. (a) Shunt stub mounting. (b) Tandem stub mounting.

Considering the GaAs FET switch layout described in Chapter 5, in which the source terminal is held at RF ground potential, the shunt stub method was adopted for the phase shifter described in this work. For this arrangement the admittance across the loaded transmission line due to the impedance transformation stub and the switching element can be expressed as [8.5]

$$Y_{si} = \frac{(Z_s + jZ_{swi} \tan \theta_s)}{Z_s(Z_{swi} + jZ_s \tan \theta_s)} \quad (8.5)$$

where  $Z_{swi}$  is the switch state impedance and  $Z_s$  and  $\theta_s$  the transforming stub impedance and electrical length, respectively. For low-loss switching elements the resistive components of the switch state impedance can be ignored and therefore the susceptances presented to the main line due to the stub and the switch are given from [8.5] as

$$B_{si} = \frac{X_{swi} \tan \theta_s - Z_s}{Z_s(X_{swi} + Z_s \tan \theta_s)} \quad (8.6)$$

where  $X_{swi}$  is the reactance of the switch state. From the above, Bahl *et al.* [8.5] have shown that the required stub impedance and electrical length are given, respectively, by

$$Z_s = \left[ \frac{(X_{sw1} - X_{sw2} - X_{sw1}X_{sw2}(B_{s1} - B_{s2}))}{B_{s1} - B_{s2} - B_{s1}B_{s2}(X_{sw1} - X_{sw2})} \right]^{\frac{1}{2}} \quad (8.7)$$

and

$$\tan \theta_s = \frac{Z_s(1 + X_{sw1}B_{s1})}{(X_{sw1} - B_{s1}Z_s^2)} = \frac{Z_s(1 + X_{sw2}B_{s2})}{(X_{sw2} - B_{s2}Z_s^2)}. \quad (8.8)$$

These expressions, together with equations (8.3) and (8.4), form the basic design equations for the loaded-line phase shifter considered in Chapter 9. Quite often the switch state impedances yield a transforming stub impedance which cannot be realized physically, and as a result, additional impedance matching is required. This is considered further in Chapter 9.

## 8.4 Large Phase Shifts In Loaded-Line Elements

Although the loaded-line phase shifter arrangement can achieve only small phase shifts, large phase bits can be achieved by cascading a number of small phase bit sections. However, this approach requires a large number of switching elements. Nayagam *et al.* [8.6] have designed loaded-line elements with large phase shifts that use less switching elements than would be required by cascading individual phase bits.

### 8.4.1 Three-Stage Phase Shifter

By using three loading elements, separated by two  $90^\circ$  transmission line sections as shown in Figure 8.6, Nayagam *et al.* [8.6] have achieved phase shifts of  $90^\circ$  and  $180^\circ$ .

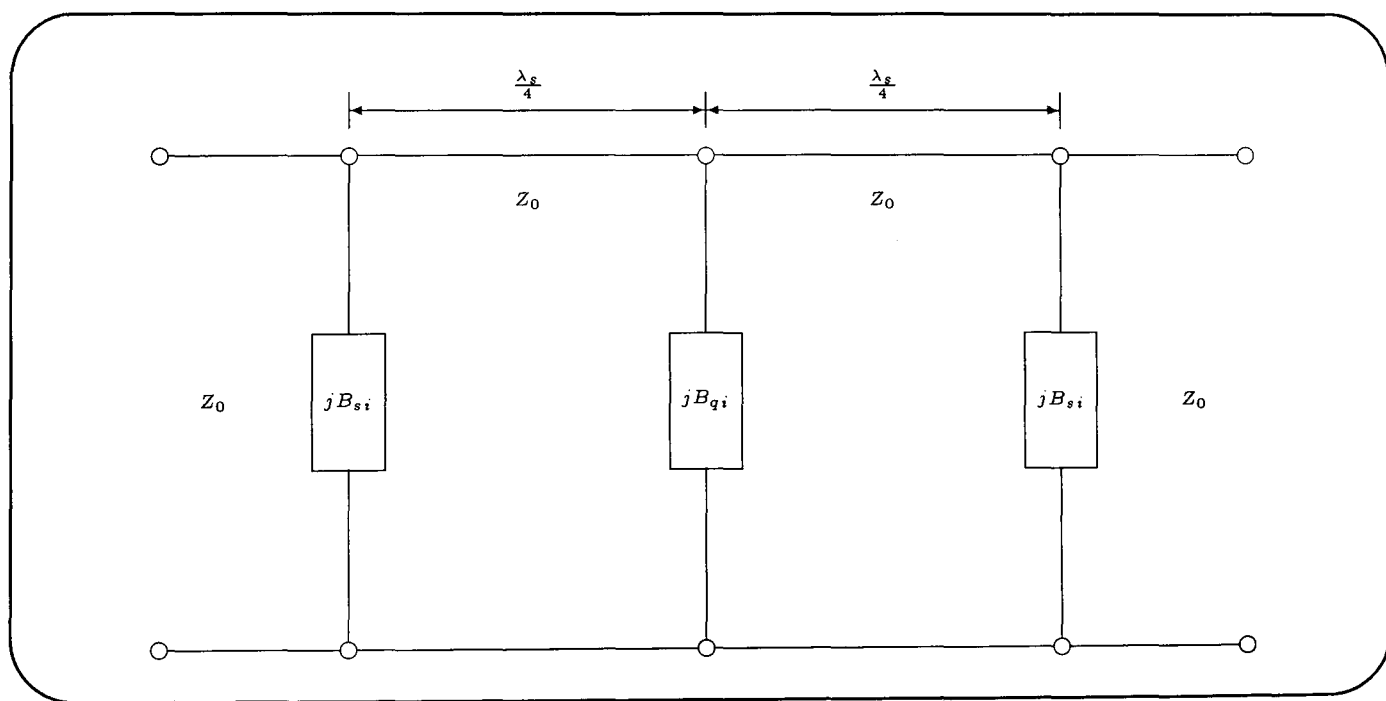


**Figure 8.6:** Schematic representation of a three stage loaded-line phase shifter.

Analyzing this arrangement using ABCD matrices, and assuming switching between complex conjugate loads, it can be shown [8.6] that the required phase shift is given by

$$\Delta\phi = 2 \tan^{-1} \left( \frac{2B_{s1}Z_0}{1 - B_{s1}^2Z_0^2} \right) \quad (8.9)$$

which is a transcendental function and can be solved to give one of the load susceptance values,  $B_{s1}$ . The remaining load susceptance value,  $B_{qi}$ , is obtained from [8.6]

$$B_{qi} = \frac{2B_{si}}{(B_{si}^2 Z_0^2 + 1)}. \quad (8.10)$$

This arrangement can achieve  $180^\circ$  phase shift with just three switching elements, rather than the eight switching elements required by cascading four  $45^\circ$  loaded-line sections.

### 8.4.2 Four-Stage Phase Shifter

The three-stage phase shifter suffers from narrow bandwidth. This has been overcome by using more stages, with four stages offering a compromise between the number of loading elements and the bandwidth performance. For this four-stage arrangement, shown in Figure 8.7, four switching elements are required with the phase shift given by [8.6] as

$$\Delta\phi = 2 \tan^{-1} \left| \frac{B_{q1}^2 Z_0^2 - 1}{Z_0 (B_{s1} + B_{q1} - B_{s1} B_{q1}^2 Z_0^2)} \right|. \quad (8.11)$$

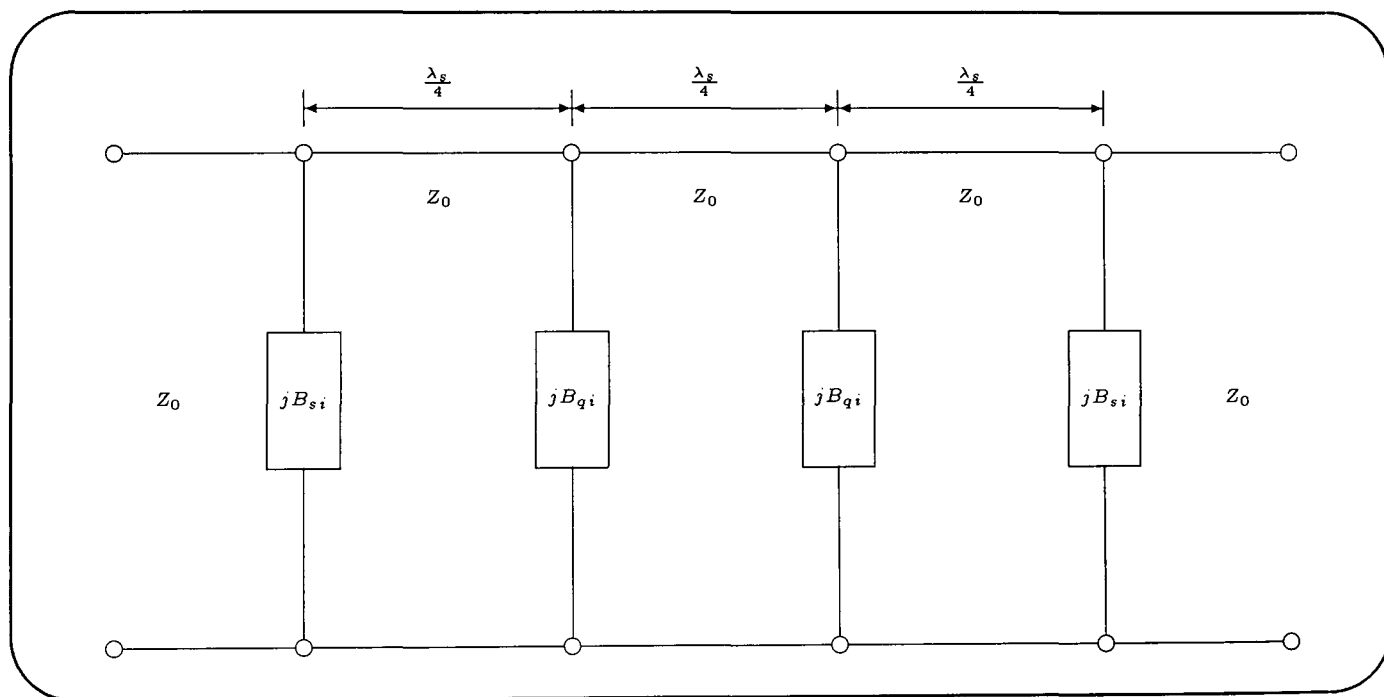


**Figure 8.7:** Schematic representation of a four-stage loaded-line phase shifter.

# References

- [8.1] J. F. White, *Microwave semiconductor engineering*. New Jersey: Van Nostrand, 1982.
- [8.2] W. A. Davies, "Design equations and bandwidth of loaded line phase shifters," *IEEE Trans. Microwave Theory Tech.*, vol. MTT-22, pp. 516–563, May 1974.
- [8.3] H. A. Atwater, "Circuit design of the loaded-line phase shifter," *IEEE Trans. Microwave Theory Tech.*, vol. MTT-33, pp. 626–634, July 1985.
- [8.4] F. L. Opp and W. F. Hoffman, "Design of digital loaded line phase shift networks for microwave thin film applications," *IEEE Trans. Microwave Theory Tech.*, vol. MTT-16, pp. 462–468, July 1968.
- [8.5] I. J. Bahl and K. C. Gupta, "Design of loaded-line p-i-n diode phase shifter circuits," *IEEE Trans. Microwave Theory Tech.*, vol. MTT-28, pp. 219–224, Mar. 1980.
- [8.6] S. Nayagam and S. Mahapatra, "On the design of high-power multiple-element loaded-line phase shifters," *Int. J. Electron.*, vol. 59, no. 2, pp. 175–186, 1985.

# Chapter 9

## Phase Shifting Using Optically Switched FET's

### Contents

---

<b>9.1</b>	<b>Introduction . . . . .</b>	<b>122</b>
<b>9.2</b>	<b>Optically Controlled Phase Shifter Design . . . . .</b>	<b>123</b>
9.2.1	GaAs FET Switch State Impedance . . . . .	124
9.2.2	Impedance Transformation Networks . . . . .	125
<b>9.3</b>	<b>Phase Shifter Modelling . . . . .</b>	<b>126</b>
<b>9.4</b>	<b>Optically Controlled Phase Shifter Results . . . . .</b>	<b>127</b>
9.4.1	Optically controlled 30° Phase Shifter . . . . .	129
9.4.2	Optically controlled 45° Phase Shifter . . . . .	129

---

### 9.1 Introduction

**O**PTICALLY controlled microwave phase shifting using indirect forms of optical control [9.1,9.2] has been described in the literature. In this form, the optical illumination does not interact directly with any of the microwave phase shifter elements. However, the terms of reference for the current work were to achieve a high level of integration and permit direct optical-to-microwave conversion for PSK transmission. This led to the requirement for a photo-detector that was not only MMIC compatible, but could also form part of a microwave PSK modulator. With these two prerequisites identified, a degree of commonality was established between the use of the GaAs as a microwave switch for MMIC phase shifting applications, and the use of the GaAs FET as an MMIC compatible photo-detector. The amalgamation of these circuit functions should lead to a highly integrated optical-to-microwave transducer, capable of providing PSK transmissions. In this arrangement the optically controlled GaAs FET switch

characterized in Chapters 6 and 7 is used as the switching element in the loaded-line phase shifter design, reviewed in Chapter 8.

A novel form of phase shifter which relies upon the direct optical control of a microwave GaAs FET switching element, is described in Section 9.2. The design of such a prototype phase shifter is further considered in Section 9.2. with the modelling of the phase shifter discussed in Section 9.3. A direct comparison of the measured and simulated responses of the optically controlled phase shifter is presented in Section 9.4, which validates the switch and phase shifter modelling approach for two different phase shifts.

The key points of this chapter are identified below.

- **Design of a novel direct optically controlled microwave phase shifter.**
- **Simulation and optimization of the performance of a prototype optically controlled hybrid phase shifter.**
- **Experimental verification of the phase shifter performance through a direct comparison of measured and simulated results.**

## 9.2 Optically Controlled Phase Shifter Design

The shunt loaded-line phase shifter described in Section 8.3.2 was used as the basis for the design of a direct optically controlled loaded-line digital phase shifter. Two such phase shifters were designed with different phase shifts and centre frequencies to test the validity of the design and simulation methods, although the design approach is identical for both. A  $45^\circ$  phase shifter, designed to operate at 10 GHz, is described in this chapter. For class III mode of operation and with port characteristic impedances of  $50 \Omega$  and  $\Delta\phi = 45^\circ$ , then from equations (8.3) and (8.4), the main line impedance,  $Z_m$  and loading susceptance,  $B_{si}$ , are calculated to be  $46.19 \Omega$  and  $\pm 8.28 \text{ mS}$ , respectively. From the MDS transmission line calculator, microstrip dimensions given in the table below were found.

Microstrip Main Line Parameters			
Input Data:	$\epsilon_r = 10.5$	$h = 635 \mu\text{m}$	$t = 4 \mu\text{m}$ $Z_0 = 46.19 \Omega$
	$f = 10 \text{ GHz}$		
Output Data:	$w = 685 \mu\text{m}$	$\lambda_s = 10988 \mu\text{m}$	$\epsilon_{eff} = 7.44$
Layout:	$w = 685 \mu\text{m}$ $l = \frac{\lambda_s}{4} = 2747 \mu\text{m}$		

### 9.2.1 GaAs FET Switch State Impedance

The ATF-10136 GaAs FET described in Chapter 6 was used as the optically activated switch, attached to the end of each loading stub of the phase shifter. The measured and simulated GaAs FET data previously obtained for the optically 'on' and 'off' states of the switch are plotted on the Smith charts of Figures 9.1 and 9.2, respectively. The relevant switch impedance data are summarized in Table 9.1 and were used as the basis for the design of the impedance transformation networks.

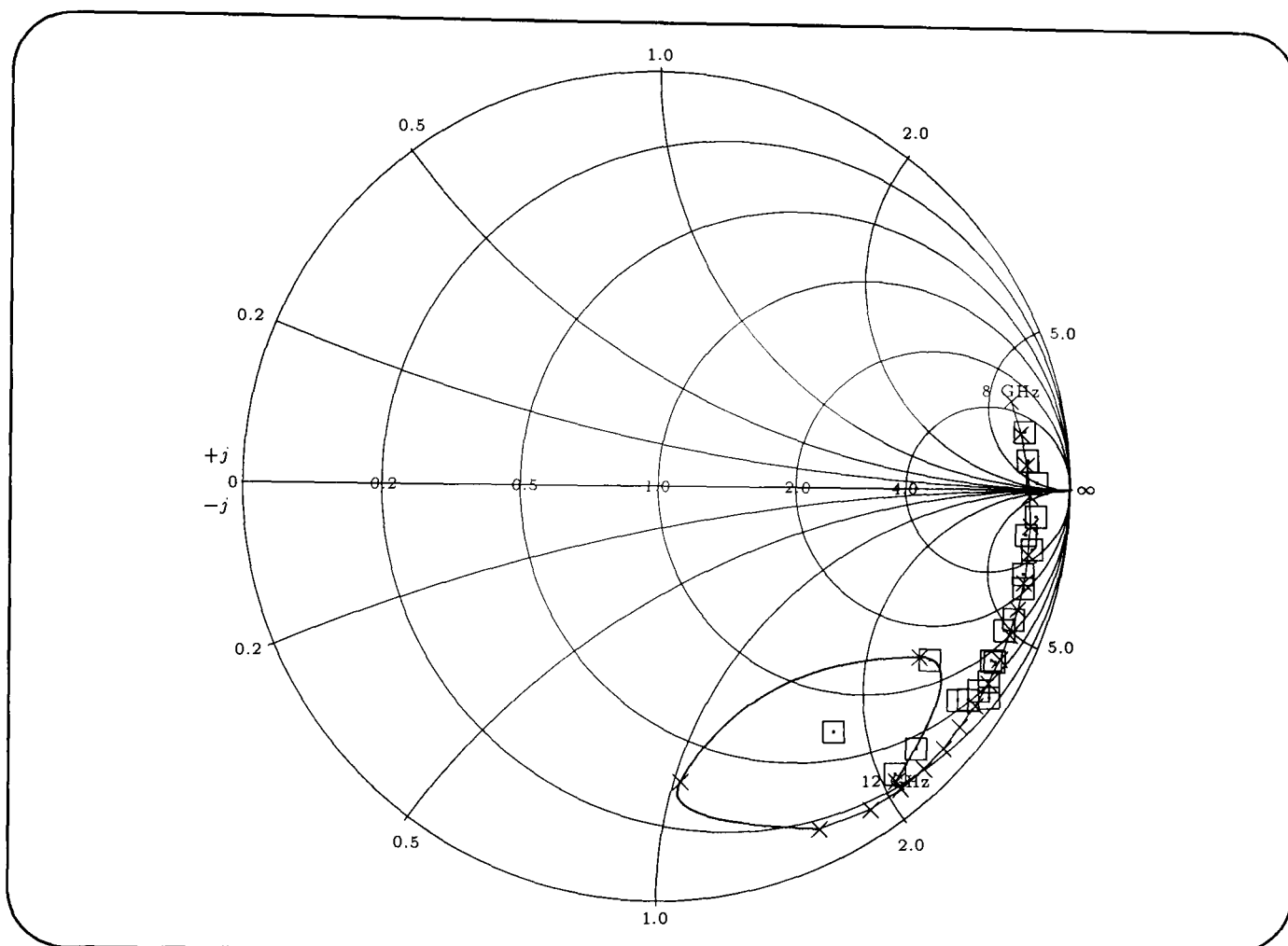


**Figure 9.1:** Measured ( $\square$ ) and simulated ( $\times$ ) Smith chart plots of ATF-10136 GaAs FET switch for optically 'on' state.

Frequency (GHz)	Optically 'On' State		'Off' State	
	Reflection	Impedance ( $\Omega$ )	Reflection	Impedance ( $\Omega$ )
10.0	$0.92 \angle -27^\circ$	$37.11 - j201.82$	$0.98 \angle 179^\circ$	$0.50 + j0.44$
10.2	$0.91 \angle -27^\circ$	$41.63 - j200.09$	$0.84 \angle 137^\circ$	$5.02 + j19.52$
10.4	$0.93 \angle -30^\circ$	$26.58 - j183.00$	$0.86 \angle 140^\circ$	$4.26 + j18.08$
10.6	$0.92 \angle -32^\circ$	$26.85 - j170.47$	$0.94 \angle 105^\circ$	$2.45 + j38.31$

**Table 9.1:** Experimentally obtained switch data for ATF-10136 GaAs FET.

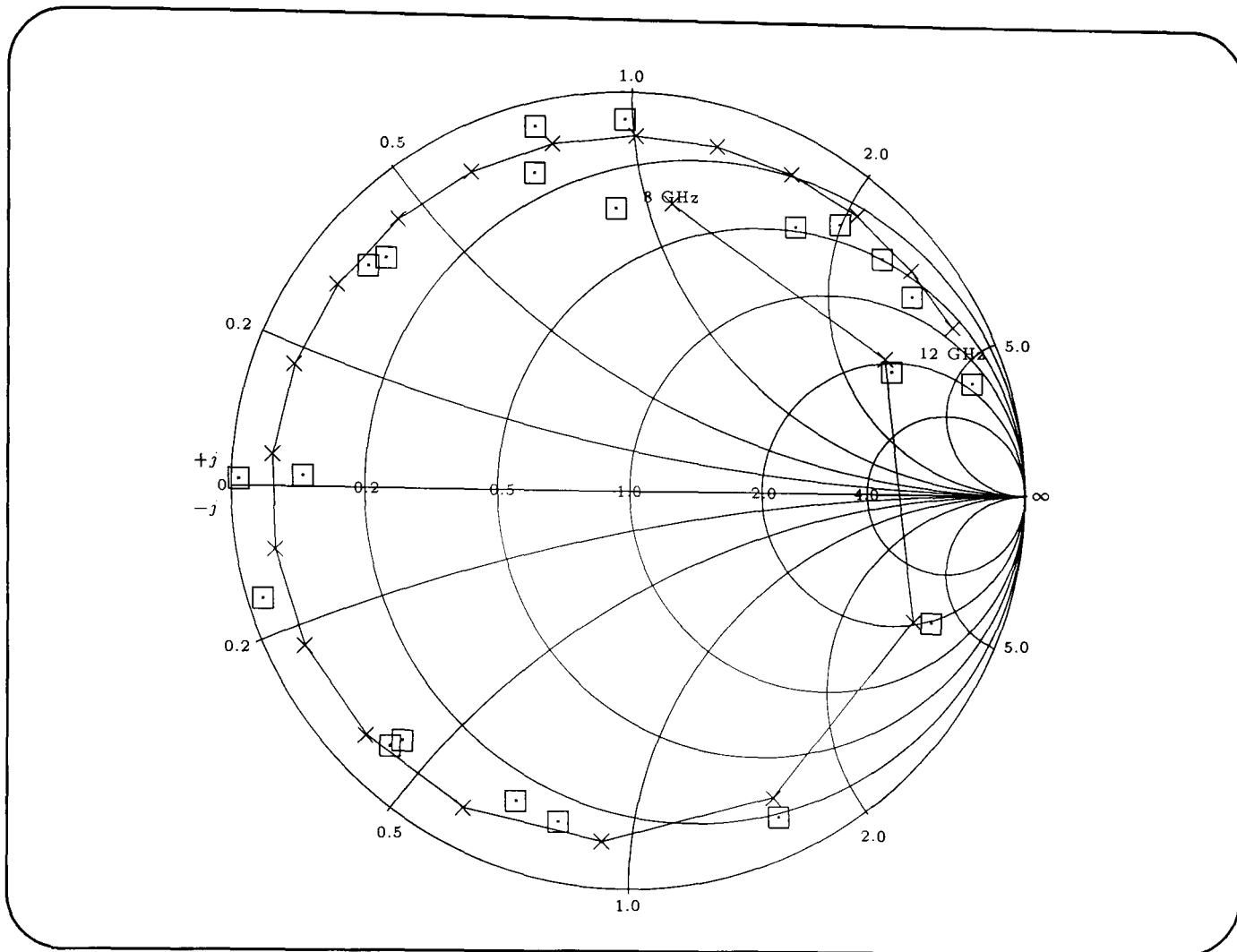


**Figure 9.2:** Measured (□) and simulated (×) Smith chart plots of ATF-10136 GaAs FET switch for 'Off' state.

### 9.2.2 Impedance Transformation Networks

To transform the switch impedances in the optically 'on' and 'off' states to give the correct loading susceptance as calculated in Section 9.2, the shunt loading stub approach described in Chapter 8 was used. The computer program given in Appendix A.6 was used to determine the required shunt loading stub impedance and electrical length. However, the GaAs FET impedances given in Table 9.1, could not be transformed to the loading susceptance required for both switch states using a single shunt loading since the transforming impedance was too large to be realized in microstrip. Subsequently, an additional matching stub of  $50 \Omega$  characteristic impedance was required to transform the switch state impedances to values that could be suitably matched to the required loading susceptance conditions. The computer program given in Appendix A.5 enabled the calculation of a suitable length for the additional  $50 \Omega$  section to give the desired shunt loading stub parameters. A schematic of the impedance transformation network is shown in Figure 9.3.

For the GaAs FET switch data given in Table 9.1, at 10 GHz a  $50 \Omega$  section of line with an electrical length of  $127^\circ$  transforms the optically 'on' and 'off' state impedances to  $(5.14 + j60.40)$  and  $(1.35 - j65.14) \Omega$  respectively. With these switch state

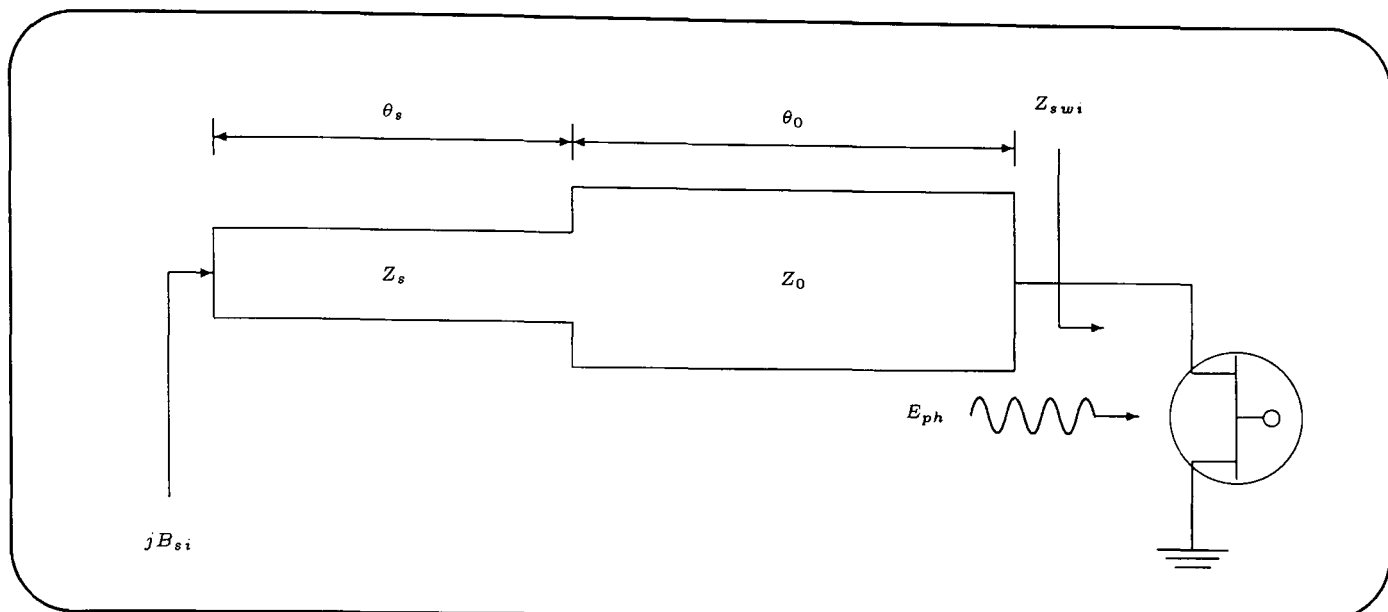


**Figure 9.3:** Schematic of impedance transformation network for optically controlled loaded-line phase shifter.

impedances, a shunt loading stub of  $87.02 \Omega$  characteristic impedance and electrical length of  $88.97^\circ$  will yield the required loading conditions at the main line in both states. From the MDS transmission line calculator, the following dimensions were obtained.

Microstrip Loaded-Line Parameters				
Input Data:	$\epsilon_r = 10.5$	$h = 635 \mu\text{m}$	$t = 4 \mu\text{m}$	$Z_0 = 50 \Omega$
	$f = 10 \text{ GHz}$			
Output Data:	$w = 582 \mu\text{m}$	$\lambda_s = 11085 \mu\text{m}$	$\epsilon_{eff} = 7.31$	
Layout:	$w = 582 \mu\text{m}$	$l = 127^\circ$	$= 3910 \mu\text{m}^\dagger$	
I/P Data:	$\epsilon_r = 10.5$	$h = 635 \mu\text{m}$	$t = 4 \mu\text{m}$	$Z_0 = 87.02 \Omega$
	$f = 10.5 \text{ GHz}$			
O/P Data:	$w = 120 \mu\text{m}$	$\lambda_s = 11681 \mu\text{m}$	$\epsilon_{eff} = 6.60$	
Layout:	$w = 120 \mu\text{m}$	$l = 88.97^\circ$	$= 2887 \mu\text{m}^\dagger$	

### 9.3 Phase Shifter Modelling

The design procedure described in the previous section was used to give an estimation of the phase shifter dimensions and took no account of discontinuities inherent in the loaded-line arrangement. These discontinuities are associated primarily with the tee-junctions created by the attachment of the shunt loading stubs, and with the step in

<sup>†</sup>Dimensions modified after simulation.

width (i.e. impedance) that occurs at the interface of the shunt loading stub and the  $50 \Omega$  transformation section. These discontinuities, together with conventional representations of the remaining microstrip elements of the phase shifter and the optically controlled GaAs FET switch models described in Chapter 6, were used in MDS to obtain computer simulations of the phase shifter performance. Furthermore, optimization routines in MDS were applied to the lengths of the shunt loading stub and the  $50 \Omega$  transformation section, to achieve the desired phase shifter response. The MDS simulation and optimization layout is shown in Figure 9.4. The microstrip layout of the optically controlled phase shifters is shown in Figure 9.5, with a GaAs FET switch mounted at the end of each shunt loading stub, which also includes the impedance transformation network such that the correct load impedance is presented to the main line to achieve the required phase shift. In addition a  $30^\circ$  loaded-line phase shifter was designed to operate at 10.5 GHz, to test the validity of the design and simulation approach.

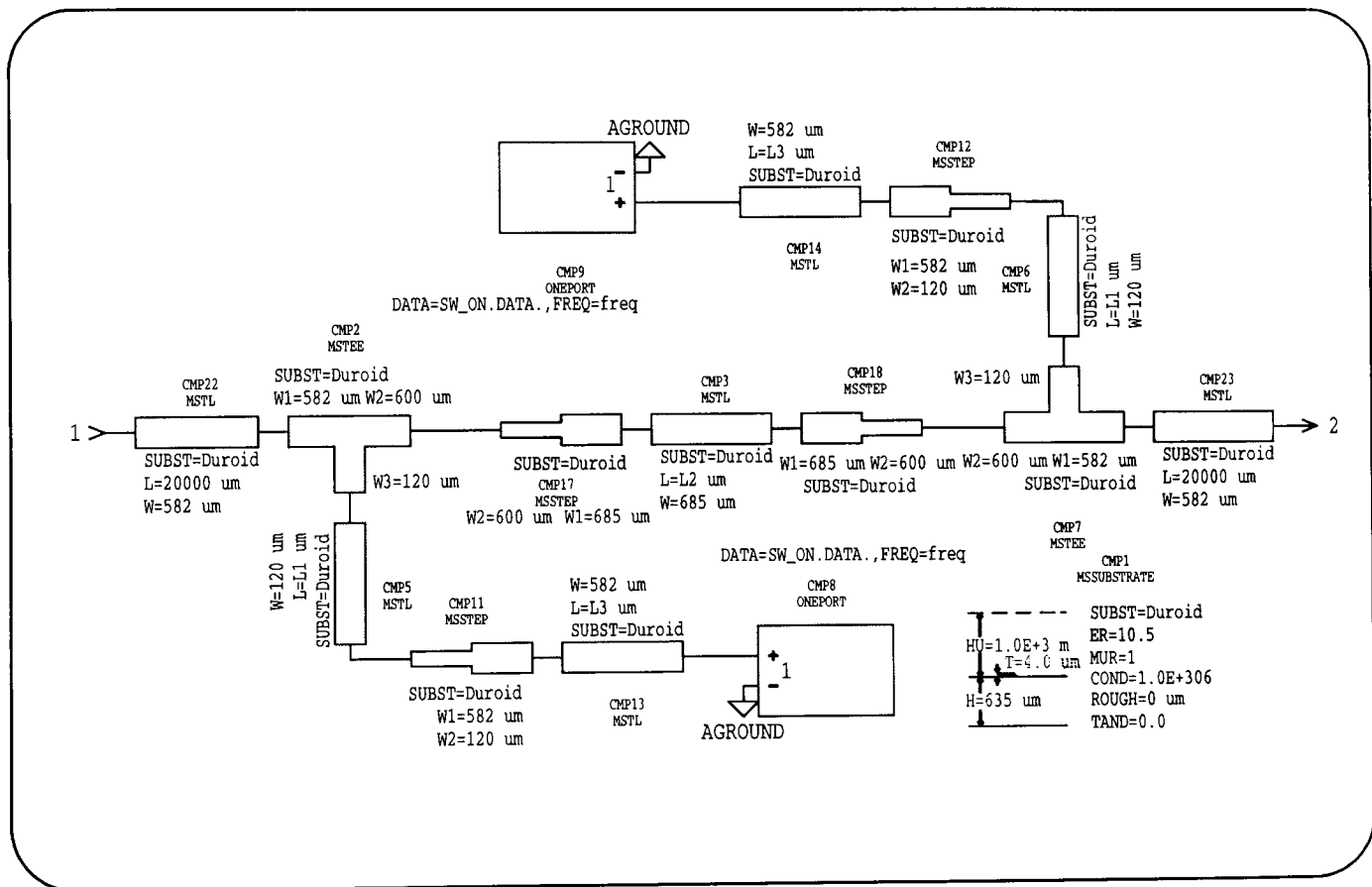
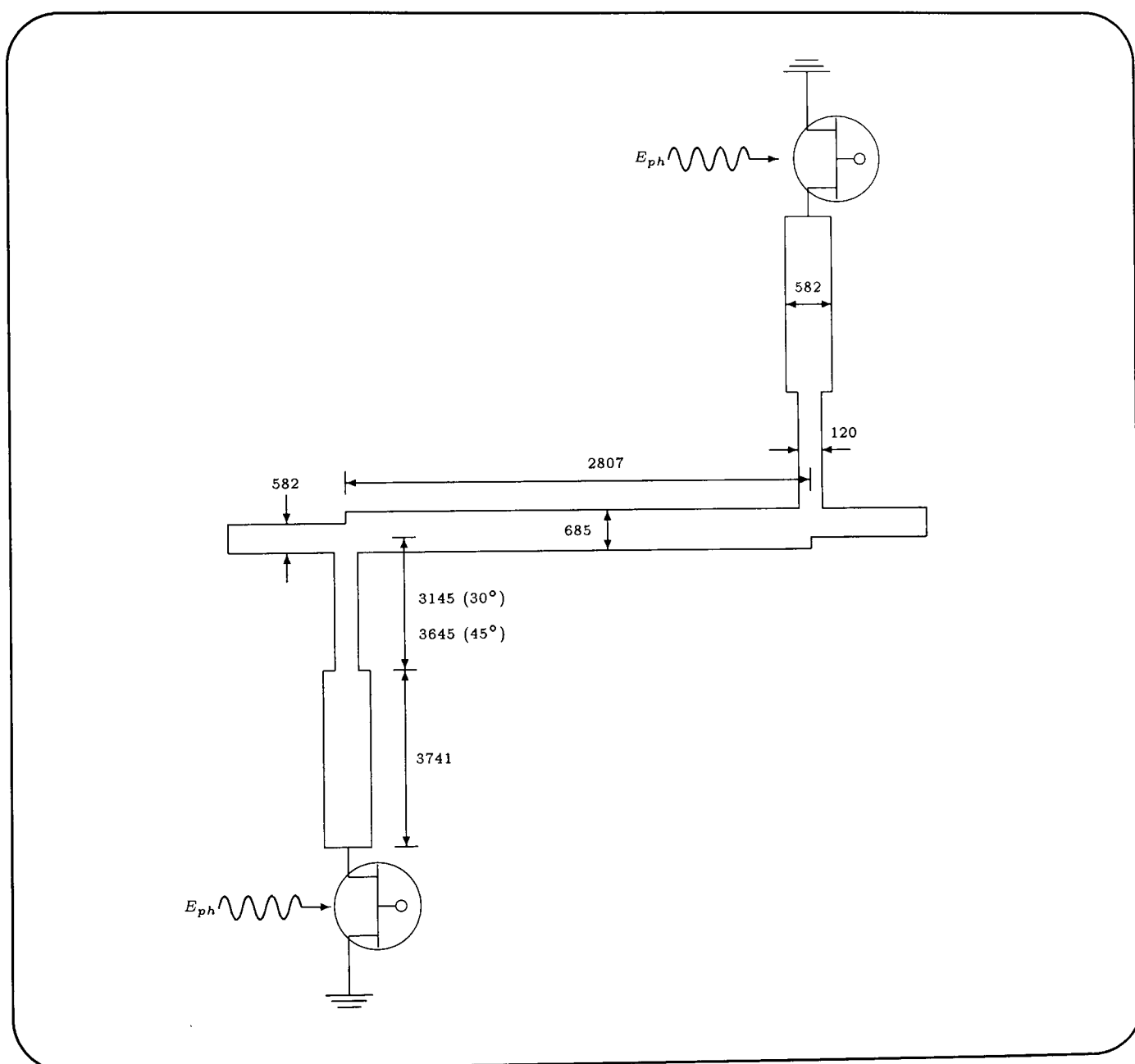


Figure 9.4: MDS simulation and optimization layout for direct optically controlled loaded-line phase shifter.

## 9.4 Optically Controlled Phase Shifter Results

Both optically controlled loaded-line phase shifters employed the ATF-10136 GaAs FET's, configured in the microstrip switch arrangement described in Chapter 6, and were fabricated on RT/Duroid<sup>TM</sup>. With a  $1 \text{ M}\Omega$  resistor in the gate bias circuit of the

GaAs FET, the focused output of a 5 mW InGaAlP laser diode module emitting light at a wavelength of 670 nm was used to optically switch each GaAs FET. It can be seen from the phase shifter microstrip layout of Figure 9.5 that the loaded-lines were connected either side of the main transmission line to enable suitable layout. Although conventionally the loaded lines are situated on the same side of the main line, this has no effect on the performance of the phase shifter. The measured and simulated differential insertion loss and phase shift for both phase shifters are compared in the next sections, with the switching states controlled optically. The hybrid implementation of GaAs FET switches in a phase shifter and the direct optical control of the phase shifter have, to the author's knowledge, not been addressed in the literature prior to the present work.



**Figure 9.5:** Microstrip circuit layout for direct optically controlled loaded-line phase shifters.

### 9.4.1 Optically controlled 30° Phase Shifter

The simulated and measured differential insertion loss and phase shift for the 30° optically controlled loaded-line phase shifter are shown in Figure 9.6.

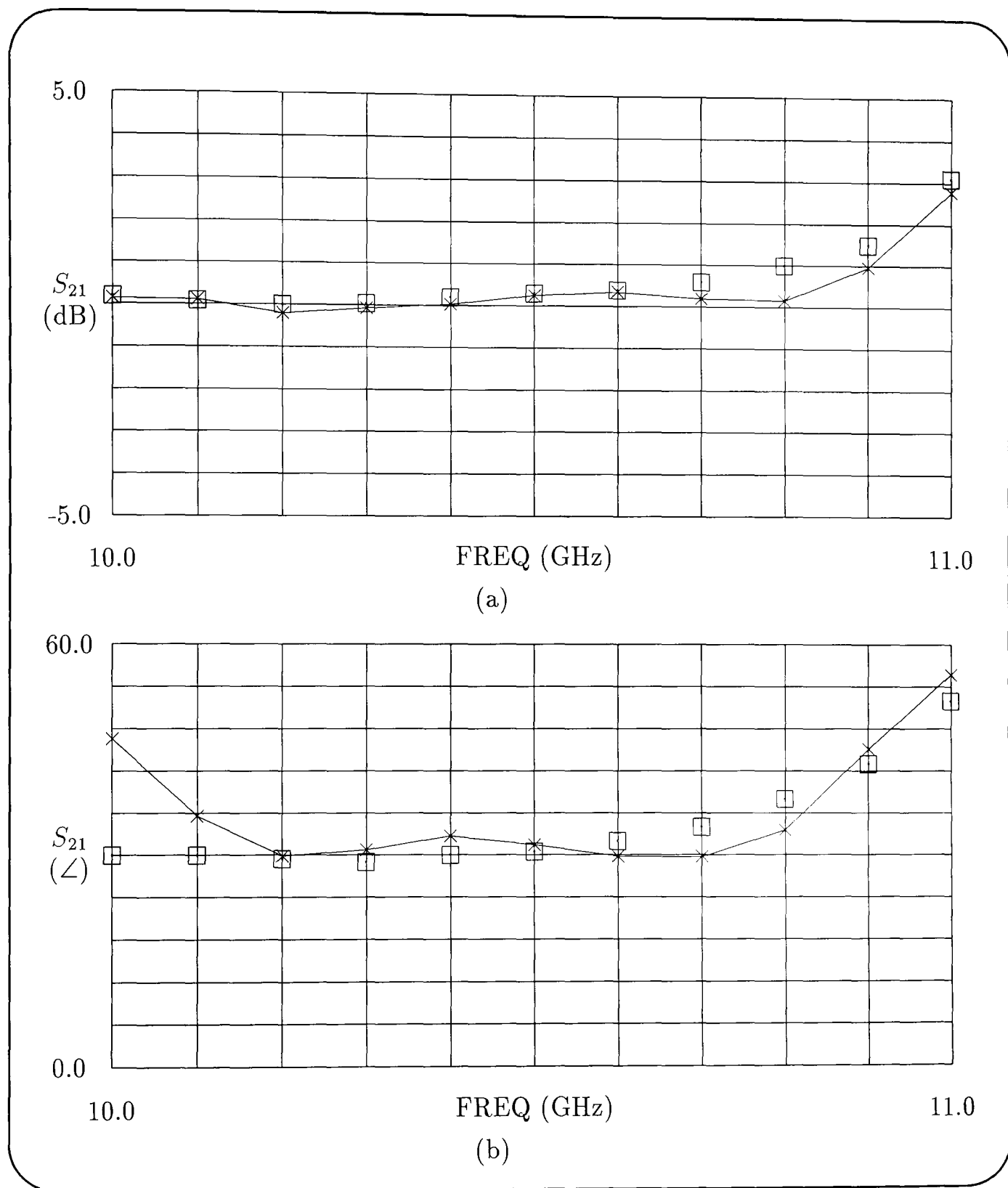


**Figure 9.6:** Measured ( $\square$ ) and simulated ( $\times$ ) response for the optically controlled 30° loaded-line phase shifter. (a) Differential insertion loss. (b) Differential phase shift.

### 9.4.2 Optically controlled 45° Phase Shifter

The simulated and measured differential insertion loss and phase shift for the 45° optically controlled loaded-line phase shifter are shown in Figure 9.7.

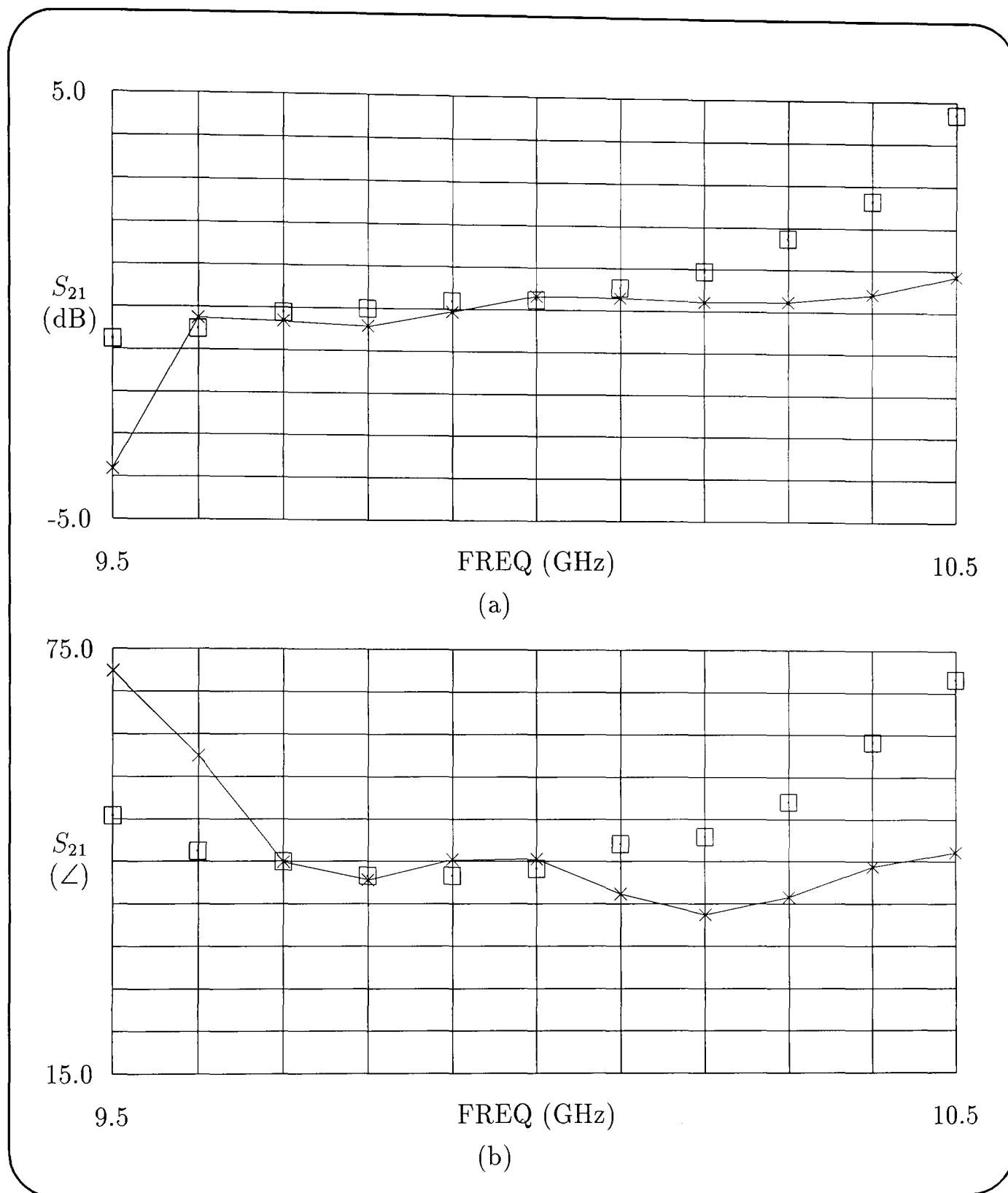


**Figure 9.7:** Measured (□) and simulated (×) response for the optically controlled 45° loaded-line phase shifter. (a) Differential insertion loss. (b) Differential phase shift.

# References

- [9.1] P. R. Herczfeld, A. Paoella, A. Daryoush, W. Jemison, and A. Rosen, “Optical phase and gain control of a GaAs MMIC transmit-receive module,” in *Proc. Eur. Microwave Conf.*, (Stockholm), pp. 831–836, Sept. 1988.
- [9.2] W. D. Jemison, T. Berceci, A. Paoella, P. R. Herczfeld, D. Kasemset, and A. W. Jacomb-Hood, “Optical control of a digital phase shifter,” in *Proc. IEEE MTT-S Int. Microwave Symp. Dig.*, pp. 233–236, 1990.

# Chapter 10

## Inter-Electrode Capacitance and Frequency Tuning in GaAs FET's

### Contents

---

<b>10.1 Introduction</b> . . . . .	<b>132</b>
<b>10.2 Inter-Electrode Capacitance Evaluation</b> . . . . .	<b>133</b>
10.2.1 Current Methods . . . . .	134
10.2.2 Coplanar Stripline Methods . . . . .	135
<b>10.3 Inter-Electrode Capacitance Simulation</b> . . . . .	<b>136</b>
10.3.1 3-D Field Simulation Methods . . . . .	136
10.3.2 Field Simulation Boundaries . . . . .	137
10.3.3 Parameter Evaluation . . . . .	139
10.3.4 Experimental GaAs FET Geometries . . . . .	139
<b>10.4 Inter-Electrode Capacitance Results</b> . . . . .	<b>140</b>
<b>10.5 Frequency Tuning in GaAs FET Switches</b> . . . . .	<b>140</b>
10.5.1 Simulation of GaAs FET Switch Resonances . . . . .	141
10.5.2 GaAs FET Switch Sensitivity Analysis . . . . .	142
10.5.3 Tuning Methods and Results . . . . .	142
<b>10.6 Broadband GaAs FET Switch Operation</b> . . . . .	<b>143</b>

---

### 10.1 Introduction

**I**NTER-ELECTRODE capacitance plays a significant role in determining the switching characteristics of GaAs FET's, in particular the isolation of the switch in the 'off' state. This chapter describes a novel approach to establishing the inter-electrode

capacitance in GaAs FET switches. This approach uses 3-dimensional field simulation software. It is proposed that this approach to evaluating inter-electrode capacitance yields a more precise value than the presently available methods described in the literature. Furthermore, an accurate approach to evaluating inter-electrode capacitance is crucial in the prediction of resonances in the switching performance of GaAs FET's in both switching states. Expressions are given for predicting resonances in the switch performance. These yield useful design information applicable to the frequency range 1 to 20 GHz. The work is extended to yield a novel and simple technique for shifting such resonances out of the intended frequency band for switch operation, resulting in a broadband design.

Various methods for determining inter-electrode capacitance in microwave GaAs FET's are compared in Section 10.2 and their inaccuracies identified. A novel method for evaluating this capacitance in GaAs FET switches is proposed in Section 10.3 and this approach is validated for two different GaAs FET gate structures in Section 10.4. A novel frequency tuning technique for GaAs FET switches is analyzed in Section 10.5 and useful data for the design of a broadband GaAs FET switch are presented in Section 10.6.

The key points of this chapter are identified below.

- **Novel and accurate method for evaluating inter-electrode capacitance in GaAs FET switches.**
- **Experimental validation of the capacitance model for two very different gate structures.**
- **Accurate approach to predicting the occurrence of resonances which may hinder the switch performance in both states.**
- **Novel technique for shifting such resonances out of the intended frequency band for switch operation.**
- **Development of a broadband optically controlled GaAs FET switch.**
- **Useful design data to predict resonances in the prototype switches.**

## 10.2 Inter-Electrode Capacitance Evaluation

Inter-electrode capacitance in GaAs FET's is often referred to as geometric in nature, because it is generally regarded as a function only of the planar geometry of the FET, and can be distinguished from the space-charge capacitance that arises in GaAs FET's. Ladbroke [10.1] has identified a number of geometric capacitances associated with typical GaAs FET structures by considering the fringing fields between the various

FET electrodes. Of these capacitive components, Ayasli [10.2] showed that the fringing capacitance between the drain and source electrodes,  $C_{ds}$ , was a predominant factor in modelling the characteristics of a GaAs FET switch in the ‘off’ state. This section discusses the inaccuracies associated with the present methods for determining inter-electrode capacitance<sup>†</sup>, with particular relevance to the GaAs FET structure, leading on to a description of the evaluation approach proposed in this thesis.

### 10.2.1 Current Methods

The methods described in the literature for evaluating inter-electrode capacitance in GaAs FET's are, in essence, based upon modifications to various capacitance expressions used in the determination of the characteristic impedance of coplanar striplines (CPS). In particular, the work of Ayasli [10.2] was related directly to the switching characteristics of GaAs FET's, and used the general GaAs FET inter-electrode capacitance expression developed by Pucel *et al.* [10.3] to evaluate the drain-to-source capacitance associated with the ‘off’ state GaAs FET switch model. The approach of Pucel *et al.* [10.3] estimated the inter-electrode capacitance by considering the electrostatic coupling between two parallel conductors, in this case the drain and source electrodes of a GaAs FET, as shown in Figure 10.1.

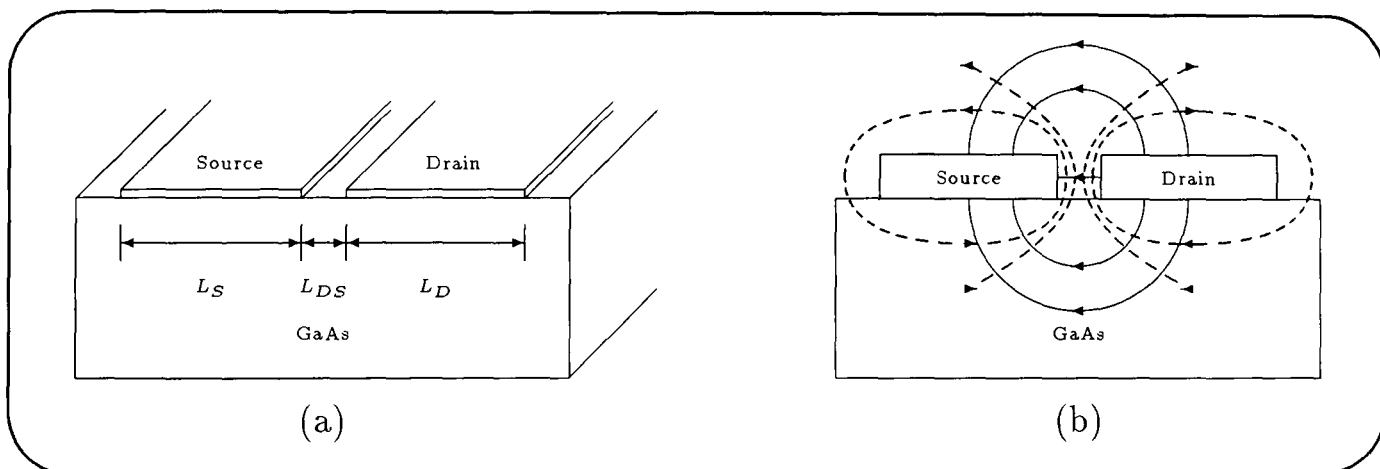


**Figure 10.1:** Geometric configuration used to determine the drain-to-source capacitance (a) CPS Geometry. (b) Electric (—) and magnetic(- -) field distribution.

In [10.3] the dielectric underneath the conductors was assumed to be semi-infinite, as a result of the inter-electrode spacing being small compared to the device (i.e. substrate) thickness. The inter-electrode capacitance was based upon modification of the capacitance expression for parallel strips immersed in an infinite dielectric medium, as developed by Smythe [10.4]. The modified expression took the sum of the capacitance contribution from the free space region above the electrodes and the capacitance contribution when the electric field was considered to be concentrated in the dielectric

<sup>†</sup>Throughout the remainder of this chapter, the term inter-electrode capacitance will be used to refer to the drain-to-source fringing capacitance.

region below the electrodes. As a result, the inter-electrode capacitance was expressed as [10.2, 10.3]

$$C_{ds} = (\epsilon_r + 1)\epsilon_0 W_G \frac{K(1 - k_{ds}^2)^{\frac{1}{2}}}{K(k_{ds})} \quad (10.1)$$

where  $K$  is the complete elliptic integral of the first kind. Although Pucel *et al.* [10.3] based their modifications on the capacitance expression given in [10.4], relevant to unsymmetrical (i.e. unequal drain and source electrode lengths) coplanar strips when evaluating the argument,  $k_{ds}$ , of the the complete elliptic integral they assumed the electrode lengths to be equal. Thus the argument was expressed as

$$k_{ds} = \left[ \frac{(2L_S + L_{DS})L_{DS}}{(L_S + L_{DS})^2} \right]^{\frac{1}{2}} \quad (10.2)$$

where  $L_{DS}$  is the drain-to-source inter-electrode spacing and  $L_S$  the source electrode length which is assumed to be equal to the drain electrode length,  $L_D$ . This condition will be true only for certain interdigitated GaAs FET gate geometries, and is therefore limited in its application. Furthermore, the general approach to evaluating the inter-electrode capacitance assumes that the drain and source electrode lengths are much greater than the drain-to-source spacing. In general, this condition is rarely satisfied in modern GaAs FET's, irrespective of the type of gate structure employed. As a result, the method proposed by Ayasli [10.2] for evaluating the 'off' state drain-to-source capacitance in GaAs FET switches has been found in this investigation to give an under-estimation of the actual capacitance.

### 10.2.2 Coplanar Stripline Methods

The inter-electrode capacitance evaluation method proposed by Ayasli [10.2] represents the only contribution in the literature relating directly to GaAs FET switches. The remaining methods considered in this investigation are derived from the various proposed techniques reported in the literature for evaluating capacitance in coplanar stripline structures. Gupta *et al.* [10.5] obtained an analytical expression for the capacitance of a CPS structure by following the conformal mapping approach used by Wen [10.6]. If this expression is translated to the GaAs FET structure under consideration here, the following relationship for inter-electrode capacitance is obtained

$$C_{ds} = \frac{1}{2}(\epsilon_r + 1)\epsilon_0 W_G \frac{K(1 - k_{ds}^2)^{\frac{1}{2}}}{K(k_{ds})} \quad (10.3)$$

where in this case the argument of the complete elliptic integral is given by

$$k_{ds} = \frac{L_{DS}}{2L_S + L_{DS}}. \quad (10.4)$$

Fouad Hanna [10.7] has modified the above expressions to account for the finite thickness of the dielectric. In this work, he assumed that the CPS capacitance was equal to the sum of the CPS capacitance in free space when the dielectric was replaced by air and the CPS capacitance obtained when assuming that the electric field was concentrated in a dielectric of thickness  $h$  and relative permittivity  $(\epsilon_r - 1)$ . When this approach is applied to the GaAs FET structure, the inter-electrode capacitance is given by

$$C_{ds} = \epsilon_0 W_G \frac{K(1 - k_{ds}^2)^{\frac{1}{2}}}{K(k_{ds})} + \frac{1}{2}(\epsilon_r - 1)\epsilon_0 W_G \frac{K(1 - k_{ds1}^2)^{\frac{1}{2}}}{K(k_{ds1})} \quad (10.5)$$

where  $k_{ds}$  is as in equation (10.4) and  $k_{ds1}$  is given by

$$k_{ds1} = \frac{\sinh\left(\frac{\pi L_{DS}}{4h}\right)}{\sinh\frac{\pi}{2h}\left(\frac{L_{DS}}{2} + L_S\right)}. \quad (10.6)$$

Although the above expressions may yield values for the inter-electrode capacitance that are in better agreement with experimental results than those obtained by the approach proposed by Ayasli [10.2], they assume again that the drain and source electrodes are equal in length, and more importantly that the electrodes remain uniform along the width of the GaAs FET. The later is sometimes true for interdigitated GaAs FET gate structures but is rarely the case for other styles of gate geometry. This implies that these expressions are inappropriate for the general case being considered in this work.

For reasons similar to those mentioned above, the methods more recently proposed by Ladbrooke [10.1], based upon graphical data related again to CPS structures, are inappropriate for accurate inter-electrode capacitance determination.

### 10.3 Inter-Electrode Capacitance Simulation

To model accurately the optically controlled switch in the ‘off’ state it is necessary to establish a precise value for the inter-electrode capacitance. Furthermore, since the method must be able to accommodate any form of GaAs FET gate geometry, a 3-dimensional solution to this problem is needed.

#### 10.3.1 3-D Field Simulation Methods

The novel approach proposed in this thesis uses a 3-D electro-magnetic (EM) simulator to provide a field solution based upon Maxwell’s equations for the various layers of the GaAs FET. The EM simulator uses a finite-element method, which subdivides the 3-D structure into a mesh and solves Maxwell’s equations according to the boundary conditions set by each finite element within the mesh. The contributions of each element

in the mesh are assembled such that a field distribution can be built up for the overall structure. The 3-D GaAs FET model included the drain and source metallization (i.e. electrode) layers, the GaAs channel, any buffer or substrate layers and the substrate ground plane metallization. The structure was modelled in HFSS, which determined the characteristic impedance,  $Z_0$ , and phase propagation constant,  $\beta$ , associated with the FET's drain and source structure. The capacitance per unit length,  $\bar{C}$ , is given by [10.1]

$$\bar{C} = \frac{1}{\nu_p Z_0} \quad (10.7)$$

where  $\nu_p$  is the phase velocity, which can be expressed as

$$\nu_p = \lambda_s f = \frac{2\pi f}{\beta} \quad (10.8)$$

where  $f$  is the frequency and  $\lambda_s$  the wavelength along the line. By substituting equation (10.8) into (10.7), the capacitance per unit length is expressed as

$$\bar{C} = \frac{\beta}{2\pi f Z_0} \quad (10.9)$$

from which the overall capacitance of the GaAs FET structure can be expressed as

$$C_{ds} = \frac{W_G \beta}{2\pi f Z_0}. \quad (10.10)$$

### 10.3.2 Field Simulation Boundaries

The version of HFSS used to perform the simulations imposed the condition that the structure under investigation should be enclosed within a 3-D bounding box. The bounding box, illustrated in Figure 10.2, consisted of perfect conductors to form an upper shielding, lower ground plane and all-round side walls with the GaAs FET layers positioned as shown.

The dimensions of the bounding structure had to be chosen judiciously, to ensure that they had no significant influence on the simulation results. This is particularly important for the GaAs FET structure considered here, since as mentioned earlier it resembles a CPS structure in which there are significant fringing fields, thereby increasing its sensitivity to environmental constraints.

The majority of foundry processes employ back surface metallization of their MMIC's to improve both the mechanical strength and the power-handling capabilities of the device, as well as providing a ground plane which can be connected to device electrodes using vias. The position of the ground plane metallization, which forms the conductive lower bounding region in the HFSS simulation, was fixed by the combined dimensions of the active channel, buffer and substrate layer thicknesses. Since this overall thickness is large (typically  $\sim 200$  to  $450 \mu\text{m}$  [10.1]) compared with the drain

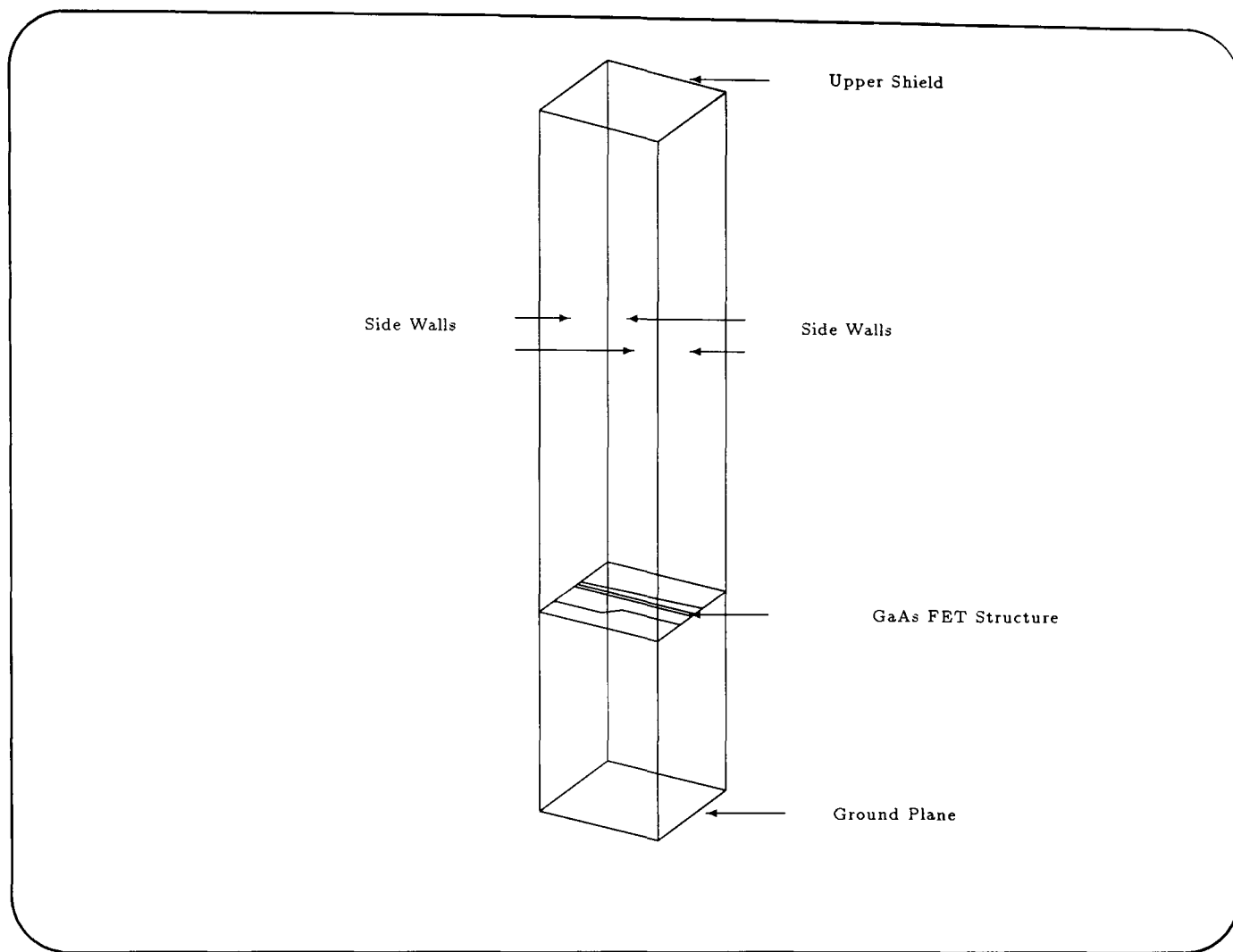


**Figure 10.2:** HFSS simulation layout for GaAs FET illustrating bounding box.

and source electrode spacing and length dimensions, the GaAs FET structure will *not* have prevailing microstrip behaviour. This is why the inter-electrode capacitance analysis reported previously in the literature [10.2, 10.3] was based upon CPS. In the absence of relevant data on the influences of all-round sidewall conducting planes and upper conducting shields on CPS structures, data for coplanar waveguide (CPW) were used, due to its similarities to CPS. Coplanar waveguide is commonly used in MMIC's to enable each device to be tested using on-wafer probing techniques and has therefore been considered in some detail in the literature. Ghione and Naldi [10.8] have shown that the upper shield height above the structure must be a factor of three greater than the strip spacing, and that the distance between the structure and sidewalls must be a factor of seven greater than the strip spacing, to eliminate parasitic effects. Using these findings as an approximate guide, it was possible to ensure that in the HFSS simulations, the sidewall and upper shielding spacings were sufficiently remote that parasitic effects were negligible.

### 10.3.3 Parameter Evaluation

When evaluating the characteristic impedance of the 3-D structure, HFSS uses three methods based upon the power and current, the power and voltage and the voltage and current distributions [10.9]. For transverse electro-magnetic (TEM) waves, these three sets of parameters will converge as the finite element mesh is refined. The CPS-like structure used to simulate the GaAs FET does not support a true TEM wave and as a result the impedance definition implemented by the simulator must be carefully selected. The power and voltage approach was used for the impedance definition, since the user is able to specify the path or impedance line over which the simulator integrates to determine the voltage used in the impedance calculation. For the GaAs FET structure, the impedance line was defined as the inter-electrode spacing and represents the points across which a maximum voltage difference is expected. If this method had not been specified, the simulator would have defined the impedance line as being between the electrodes and the ground plane (i.e. typical microstrip line definition of impedance) of the GaAs FET structure. Irrespective of the impedance definition selected, in evaluating the impedance and phase propagation constant at each port of the device the simulator assumes that the structure is connected to a transmission line with the same cross-section as the defined ports. It follows that, if a particular GaAs FET structure has a different geometric layout at each port, the simulator will, quite correctly, calculate a different impedance and phase propagation constant for each port. Considering the often complex geometric layout of the drain and source metallization layers of microwave GaAs FET's, this may present some problems in establishing a unique value for the impedance and phase propagation constant of the given structure and so undermine the proposed approach for inter-electrode capacitance evaluation. This situation can be avoided by prudent selection of the critical geometric regions of the GaAs FET metallization layers that are included in the simulation layout. For the inter-electrode capacitance evaluation, only the metallization region in close proximity to the drain-to-source spacing needs to be included, since this is where the field will be concentrated.

### 10.3.4 Experimental GaAs FET Geometries

The ATF-10136 and ATF-13136 GaAs FET structures were simulated in HFSS in order to establish a precise value for the inter-electrode capacitance, used to model the 'off' state of the optically controlled switches described in Chapter 6. The ATF-10136 has an interdigitated gate structure which contrasts with the T-type structure of the ATF-13136, as can be seen from the scanning electron microscope (SEM) pictures in Figures 10.3(a) and 10.3(b).

The very different gate structures for the two GaAs FET's were selected delib-

erately to test the validity of the proposed methods for evaluating the inter-electrode capacitance. The dimensions of the drains and sources of the two FET's were determined from the SEM pictures. The principal dimensions are summarized in Table 10.1. The HFSS structural layouts of the drain and source metallization layers for the ATF-10136 and ATF-13136 are shown in Figures 10.4(a) and 10.4(b) respectively, and clearly illustrate the distribution of the electric field over these regions.

FET Type	Gate Type	Device Dimensions ( $\mu\text{m}$ )			
		$L_S$	$L_D$	$L_{DS}$	$W_G$
ATF-10136	interdigitated	5.20	5.50	2.14	500
ATF-13136	Tee	8.60	8.60	2.80	250

**Table 10.1:** Principal device dimensions used to model the GaAs FET inter-electrode capacitance.

## 10.4 Inter-Electrode Capacitance Results

Table 10.2 gives a comparison of the inter-electrode capacitance values obtained by the method proposed in this investigation and from the approach suggested by Ayasli [10.2] (i.e. equation (10.1)). The field simulation data at 10 GHz obtained from HFSS and the complete elliptic integral data used in the evaluation of equation (10.1) were obtained from standard approximations, given by

$$\frac{K(k)}{K(k')} \simeq \begin{cases} \frac{1}{2\pi} \ln \left( 2 \frac{\sqrt{1+k} + \sqrt[4]{4k}}{\sqrt{1+k} - \sqrt[4]{4k}} \right) & \text{for } 1 \leq \frac{K(k)}{K(k')} \leq \infty \text{ and } \frac{1}{\sqrt{2}} \leq k \leq 1. \\ \frac{2\pi}{\ln \left( 2 \frac{\sqrt{1+k'} + \sqrt[4]{4k'}}{\sqrt{1+k'} - \sqrt[4]{4k'}} \right)} & \text{for } 0 \leq \frac{K(k)}{K(k')} \leq 1 \text{ and } 0 \leq k \leq \frac{1}{\sqrt{2}}. \end{cases} \quad (10.11)$$

where  $k' = \sqrt{1-k^2}$  and is the complementary elliptic function argument. The inter-electrode capacitance values obtained from the methods proposed in this work were substituted into the optically controlled switch model described in Chapter 6 and simulated using MDS. The measured and simulated responses for both FET switches have been compared in Chapter 6 and show good agreement over the frequency range 8 to 12 GHz.

## 10.5 Frequency Tuning in GaAs FET Switches

The electrically controlled GaAs FET switch designs presented by Ayasli [10.2] used a two-section low-pass filter to provide effective RF open-circuit and DC bias conditions at the gate terminal of the FET. Ayasli [10.2] explained that, since both the source

FET Type	Gate Type	Device Parameter			
		$\beta$ rad/cm	$Z_0$ $\Omega$	$C_{ds}$ pF	$C_{ds}$ [10.2] pF
ATF-10136	interdigitated	5.565	54.01	0.082	0.062
ATF-13136	Tee	5.567	48.79	0.045	0.033

**Table 10.2:** Principal parameters used to evaluate the GaAs FET inter-electrode capacitance.

and drain terminals were held at earth potential, the gate and drain terminals were not isolated in the ‘off’ state. This resulted in the gate bias circuit having a dominant influence on the equivalent drain-to-source impedance. He mentioned further the problem of the bandwidth performance of the switch that was hindered by resonances attributed to the ‘off’ state drain-to-source capacitance. The switch bandwidth was improved subsequently by tuning the drain-to-source capacitance with an inductive length of line connected across the drain and source electrodes. No method for determining the required inductance of the length of line was suggested by Ayasli [10.2], although a later analysis by Atwater [10.10] provided a theoretical approach to determining this line length. In the analyses of both Ayasli [10.2] and Atwater [10.10], only the intrinsic equivalent elements of the GaAs FET switch model were considered. No allowance was made for the influence of the parasitic components of the GaAs FET switch structure. However, this can influence significantly the switching performance of monolithic or packaged forms of the switch in both switching states. Furthermore, this inductive tuning method leads to a severe reduction in the switch bandwidth and a poorer ‘on’ state return loss performance. In this section, the influences of the parasitic and intrinsic elements of the switch model on the switching performance in both states are analyzed. A novel tuning method is proposed which enhances the switch bandwidth performance. This is based upon accurate prediction of resonances in both switching states and is used subsequently to establish the broadband operation of a GaAs FET switch under optical or conventional electrical control, of the switch state.

### 10.5.1 Simulation of GaAs FET Switch Resonances

The GaAs FET switch models used in the MDS simulations, described in Chapter 6, incorporated the intrinsic elements, a package (i.e. parasitic) model, and microstrip components associated with the switch design. They were used to predict accurately the switch performance in both states. When the gate stub line was used to present an effective RF open-circuit at the gate terminal of the FET, as suggested by Ayasli [10.2], resonances were identified by the computer simulations. These resonances occurred

between the intrinsic FET elements and package parasitics in both 'on' and 'off' states of the switch and as a result would limit the bandwidth performance of the switch.

### 10.5.2 GaAs FET Switch Sensitivity Analysis

To establish which aspects of the GaAs FET switch model had a dominant influence on the switch resonances, a sensitivity analysis was performed using MDS. In MDS, the sensitivity function is defined as the normalized derivative, given by [10.11]

$$\text{Sens}(c_r, c_p) = \lim_{\Delta c_p \rightarrow 0} \frac{\Delta c_r / c_r}{\Delta c_p / c_p} \quad (10.12)$$

where  $c_r$  is the circuit response and  $c_p$  is the circuit parameter. The sensitivity analysis was performed individually on each element within the 'on' and 'off' state switch models to establish its effect on the magnitude and phase of the switch reflection coefficient. From these analyses it was established that, in the 'on' state, the parasitic inductance at the gate of the FET had a dominant influence over the magnitude and phase of the reflection coefficient. In the 'off' state, the intrinsic gate-to-source and gate-to-drain capacitances were found to be the main influencing factors, as had previously been suggested by Ayasli [10.2]. These effects were followed closely in importance by the parasitic gate inductance. Since the gate-to-source and gate-to-drain capacitances are fixed by the switch bias in the 'off' state and the particular GaAs FET structure, external gate inductance was used as the basis for tuning resonances out of the switch operating band in both switching states.

### 10.5.3 Tuning Methods and Results

The impedance of an open-circuit stub can be expressed as

$$Z_{oc} = -jZ_0 \cot \theta_{oc} \quad (10.13)$$

where  $Z_0$  is the characteristic impedance of the stub and  $\theta_{oc}$  the electrical length of the stub. Thus from equation (10.13) it can be seen that, if the electrical length of the stub is chosen to be between  $\pi$  and  $\pi/2$  (i.e. a physical length between one-half and one-quarter of the line wavelength), then the stub will appear as an inductive reactance. This principle was used as the basis for the design of the GaAs FET switch tuning element. This involved the gate stub line length being altered so as to tune the resonances out of the operating band of the switch. The gate stub line length was varied so as effectively to shift the resonant points away from the frequency range of switch operation.

Using the MDS switch models described in Chapter 6, the resonance frequencies were obtained as a function of the gate stub length for both switching states of the

ATF-10136 GaAs FET switch. Two resonances occurred in each of the switching states, and these are shown in Figure 10.5.

By curve fitting this data using Chebyshev polynomials, expressions were obtained to predict the resonant frequencies,  $f_r$  (GHz) in both states. These expressions are

$$f_r \simeq \begin{cases} 15.6809 - y(3.2357 - 1.0072y) & \text{(i)} \\ 13.7048 - y(3.5760 - 1.0178y + 0.3752y^2) & \text{(ii)} \\ 9.5787 - x(3.4064 - 1.0586x) & \text{(iii)} \\ 4.5662 - x(1.7885 - 1.0892x + 0.6832x^2) & \text{(iv)} \end{cases} \quad (10.14)$$

with  $x$  and  $y$  being related to the open-circuit gate stub length,  $l_g$  in units of millimetres by

$$x = \frac{2l_g - 5.5}{4.5} \quad \text{for } (0.5 \leq l_g \leq 5.0) \quad (10.15)$$

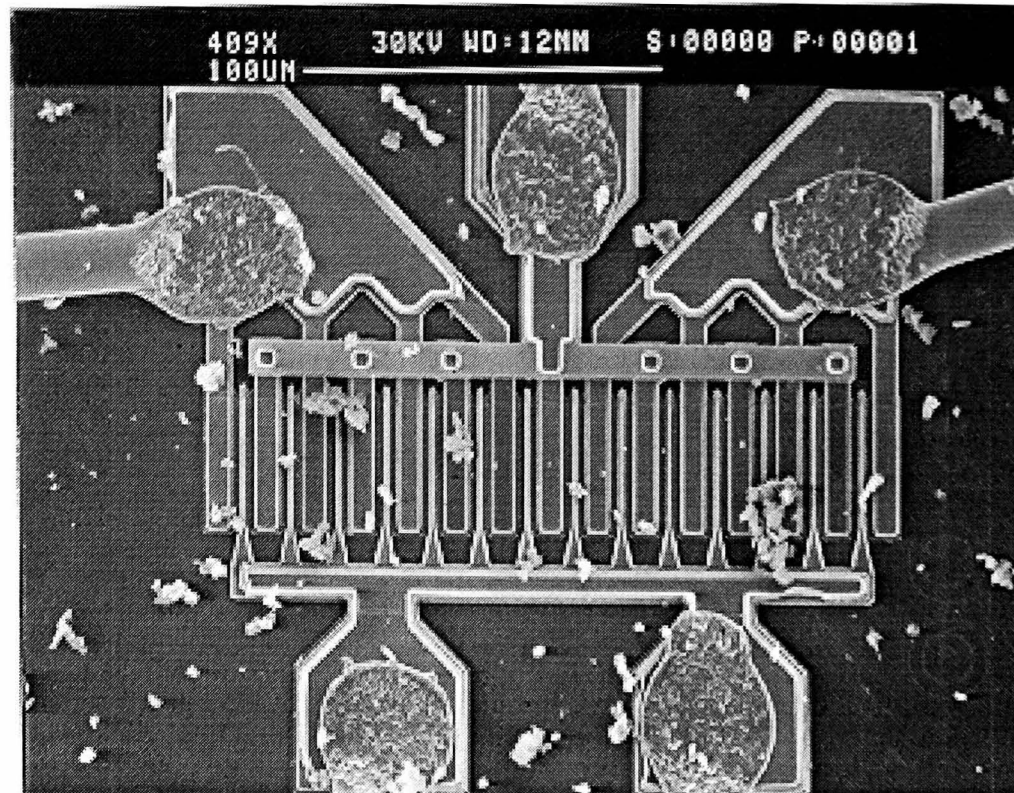
$$y = \frac{2l_g - 7.0}{3.0} \quad \text{for } (2.0 \leq l_g \leq 5.0) \quad (10.16)$$

## 10.6 Broadband GaAs FET Switch Operation

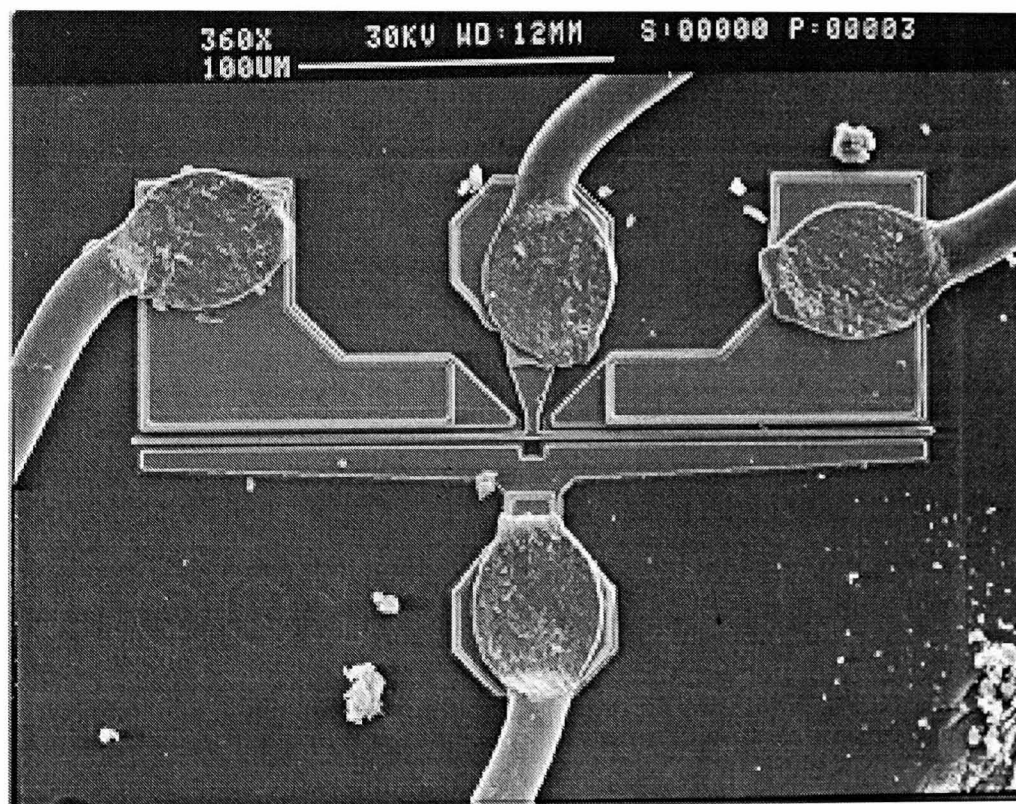
The simulated and measured results presented in Chapter 6 for the optically controlled ATF-10136 GaAs FET switch involved the tuning of the gate stub length to achieve a switch operating band from 8 to 12 GHz. From the data plotted in Figure 10.5 and equations (10.14 i-iv), it can be seen that particular lengths for the open-circuit stub line will allow the switch to be configured to operate over sections of the frequency range 1 to 20 GHz. The required open-circuit gate stub lengths and frequency bands of switch operation are summarized in Table 10.3.

Gate Stub Length mm	Operating Frequency GHz
0.5	1 $\rightarrow$ 8
4.0	8 $\rightarrow$ 12
1.5	12 $\rightarrow$ 20

**Table 10.3:** Open-circuit gate stub length required for determining switch frequency operation.



(a)



(b)

**Figure 10.3:** SEM photographs of the two different gate structures. (a) ATF-10136 interdigitated gate. (b) ATF-13136 T-type gate.

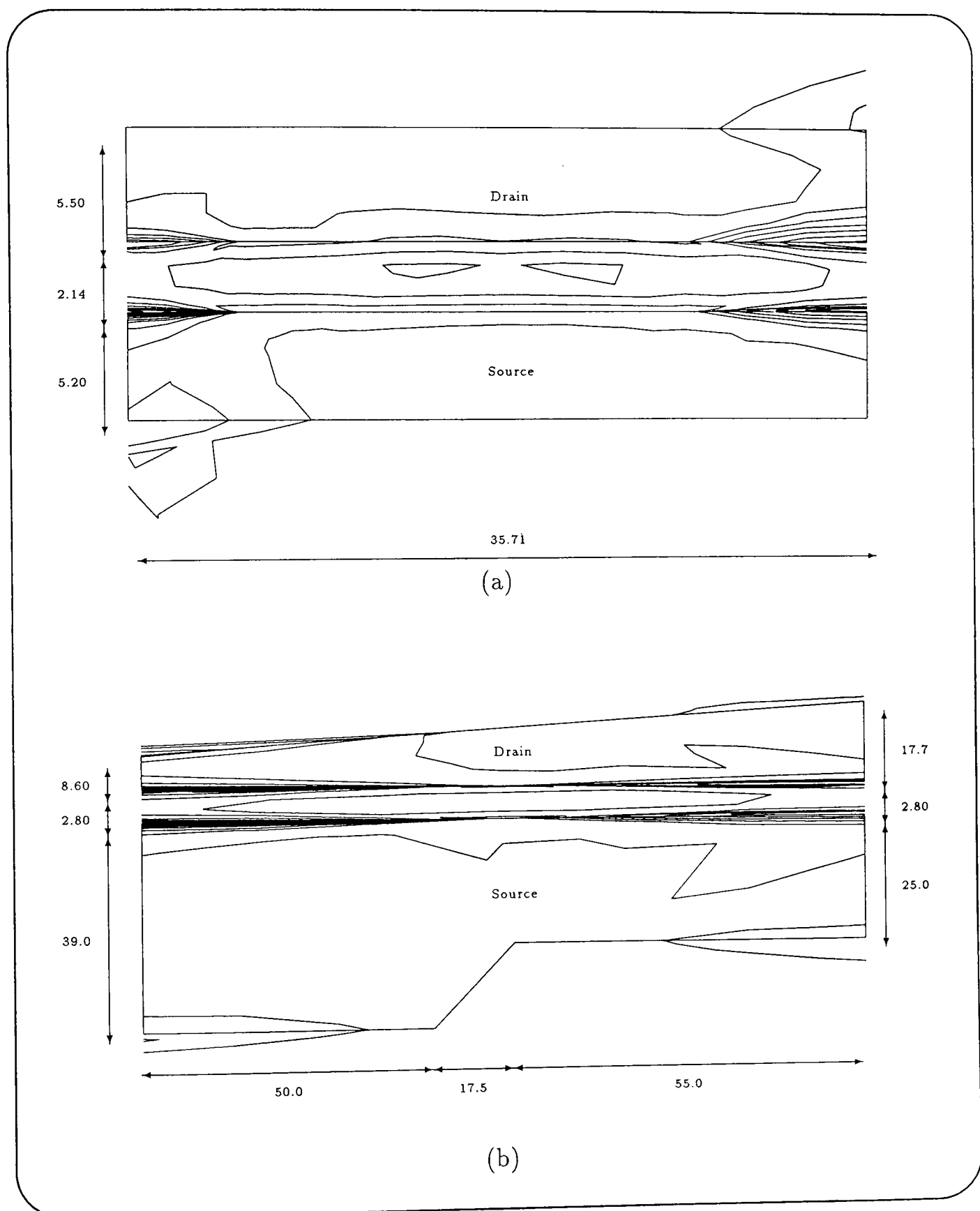


**Figure 10.4:** HFSS electric field contour plots for drain and source metallization layers per cell (all dimensions in  $\mu\text{m}$ ). (a) ATF-10136 GaAs FET. (b) ATF-13136 GaAs FET.

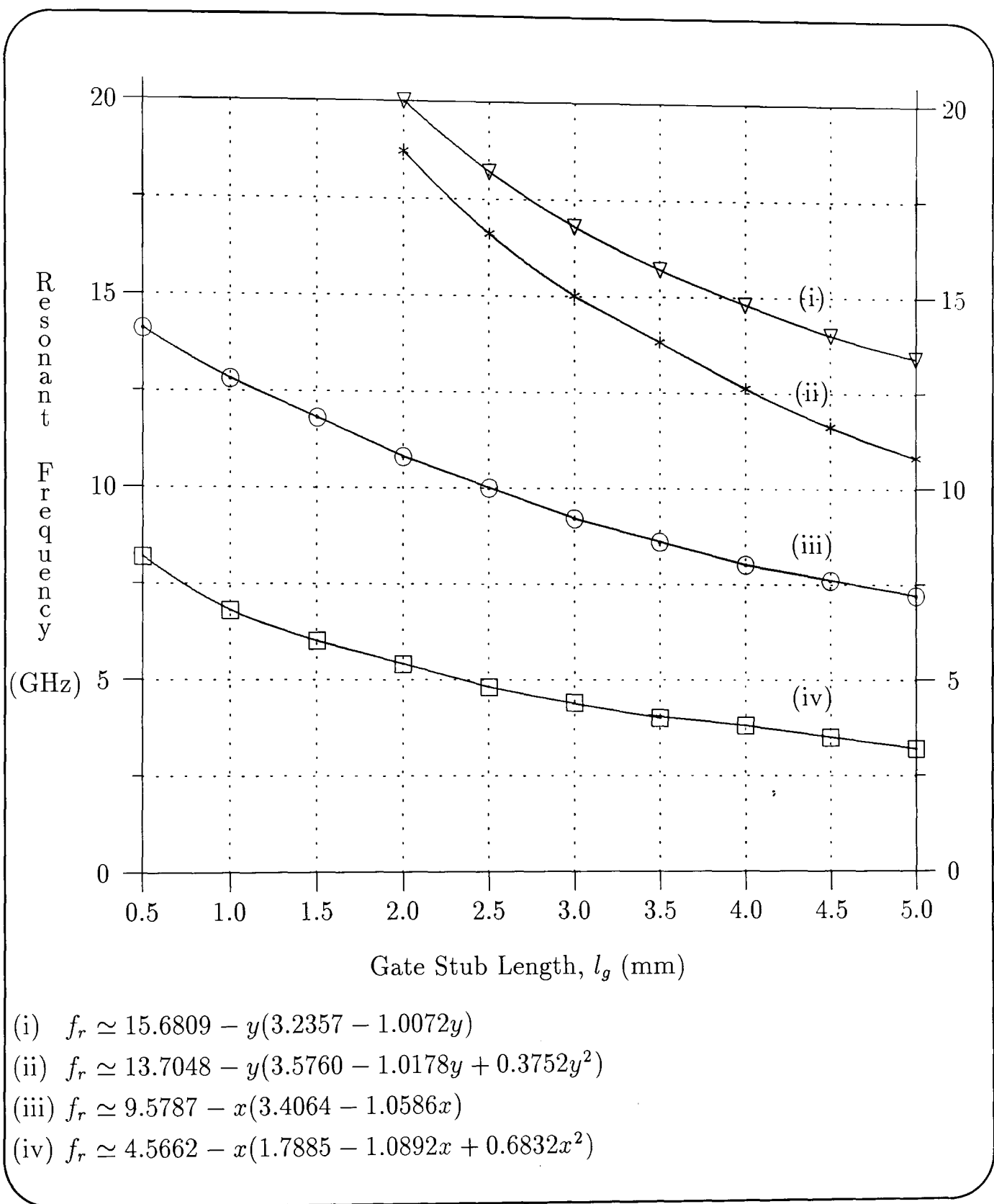


**Figure 10.5:** 'On' state ( $\square$ ,  $*$ ) and 'off' state ( $\odot$ ,  $\nabla$ ) resonance frequency variation with open-circuit gate stub length.

# References

- [10.1] P. H. Ladbrooke, *MMIC design: GaAs FETs and HEMTs*. Boston: Artech House, 1989.
- [10.2] Y. Ayasli, “Microwave switching with GaAs FETs,” *Microwave J.*, vol. 25, pp. 61–74, Nov. 1982.
- [10.3] R. A. Pucel, H. A. Haus, and H. Statz, “Signal and noise properties of gallium arsenide microwave field-effect transistors,” *Advances in Electron. Electron Phys.*, vol. 38, pp. 195–265, 1975.
- [10.4] D. Smythe, *Static and dynamic electricity*, ch. 4, pp. 100–104. New York: McGraw-Hill, 1968.
- [10.5] K. C. Gupta, R. Garg, and I. J. Bahl, *Microstrip lines and slotlines*, ch. 7, pp. 257–301. Dedham: Artech House, 1979.
- [10.6] C. P. Wen, “Coplanar waveguide: A surface strip transmission line suitable for non-reciprocal gyromagnetic device application,” *IEEE Trans. Microwave Theory Tech.*, vol. MTT-17, pp. 1087–1090, July 1969.
- [10.7] V. F. Hanna, “Finite boundary corrections to coplanar stripline analysis,” *Electron. Lett.*, vol. 16, pp. 604–606, July 1980.
- [10.8] G. Ghione and C. U. Naldi, “Coplanar waveguide for MMIC applications: Effect of upper shielding, conductor backing, finite-extent ground planes, and line-to-line coupling,” *IEEE Trans. Microwave Theory Tech.*, vol. MTT-35, pp. 260–267, Mar. 1987.
- [10.9] Hewlett Packard, *HP 85180A High-Frequency structure Simulator: User’s Reference*, May 1992.
- [10.10] H. A. Atwater, “Microstrip reactive circuit elements,” *IEEE Trans. Microwave Theory Tech.*, vol. MTT-31, pp. 488–491, June 1983.
- [10.11] Hewlett Packard, *HP 85150B Microwave and RF Design Systems: Designer’s Task Reference*, May 1994. Vol. 4—Simulating and Optimizing Circuit Performance.

# Chapter 11

## Monolithic Circuit Considerations

### Contents

---

<b>11.1 Introduction</b> . . . . .	<b>148</b>
<b>11.2 Inductive Tuning Element</b> . . . . .	<b>149</b>
11.2.1 Cascode Analysis With Resistive Feedback . . . . .	151
11.2.2 Cascode Analysis With GaAs FET Feedback . . . . .	153
<b>11.3 Monolithic Active Inductor Design</b> . . . . .	<b>155</b>
11.3.1 Monolithic Active Inductance . . . . .	155
11.3.2 Monolithic Active Inductance Variation . . . . .	155
<b>11.4 Active Inductor Performance</b> . . . . .	<b>156</b>
11.4.1 Improved Active Inductor Modelling . . . . .	157
11.4.2 Comparison of Active Inductance Results . . . . .	159

---

### 11.1 Introduction

**T**HE circuits described thus far establish the principle of direct optical control of a microwave GaAs FET switch and phase shifter using hybrid circuits. However, a design strategy was chosen so that there could be a straightforward extension to monolithic layouts if required and this is the main focus of this chapter.

In the optically controlled hybrid switch design, an open-circuit stub was used at each source terminal of the FET to achieve an effective RF short-circuit condition. In an MMIC design this would be replaced simply by via connections from the source electrode metallization to the ground plane metallization. In addition, the open-circuit tuning stub used at the gate terminal of the hybrid FET switch could be realized with a monolithic transmission line or a spiral inductor with an inductive reactance equivalent to that of the open-circuit stub. Therefore, the transfer from a hybrid to a monolithic

construction would be reasonably routine, provided the switch was to operate over a restricted frequency range. However, this transfer would not be so straightforward if the monolithic switch was to provide operation over sections of a broad frequency range, as was achieved for the hybrid version of the switch. In the hybrid designs, the switch could be configured to operate over sections of the frequency range 1 to 20 GHz by appropriate design of the gate tuning stub line in accordance with the data given in Table 10.3. In a monolithic design this would require a number of individual switches, each configured to operate over a pre-determined frequency range. Such an implementation is inefficient and would detract from the broadband capabilities of the hybrid switch design. Hence, this chapter proposes a monolithic approach to realizing the broadband capabilities achieved with the hybrid optically controlled GaAs FET switch. The approach uses additional DC electrical control of tuning at the gate of the FET.

The electrical control of a monolithic active inductor, based upon a cascode GaAs FET arrangement, is described and analyzed in Section 11.2. This analysis includes simplified modelling approaches for active inductors with resistive and common-gate (CG) GaAs FET feedback and presents modifications to previously published expressions that relate to the input impedance of the active inductor. The requirements of the active inductor for optically controlled GaAs FET switching applications are assessed in Section 11.3. A more comprehensive model for the active inductor is proposed in Section 11.4, and simulated results are compared with the models presently available in the literature. Furthermore, the simulated results are used to confirm the suitability of the active inductor as a tuning element for monolithic optically controlled GaAs FET switching applications.

The key points of this chapter are identified below.

- **Design for monolithic frequency tuning of GaAs FET switches using an active inductance tuning element.**
- **Corrections to the analysis of active inductance GaAs FET's, previously presented in the literature.**
- **More comprehensive model for the active inductor.**

## 11.2 Inductive Tuning Element

In order to reduce size and stray capacitance while achieving broadband operation, Hara *et al.* [11.1,11.2] proposed that spiral inductors could be replaced by a microwave active inductor comprising a cascode FET arrangement and a feedback resistor [11.1]. This common-source cascode FET active inductor arrangement, shown in Figure 11.1.

is limited in its application due to the loss associated with the equivalent series resistance. This has been shown to be approximately equal to the reciprocal of the GaAs FET transconductance. As a result, the original design was later modified by Hara *et al.* [11.2] to provide low loss characteristics by replacing the parallel feedback resistor by a common-gate GaAs FET, as depicted in Figure 11.2. These arrangements have been shown to provide a typical inductance of several nano-henries at X-band.

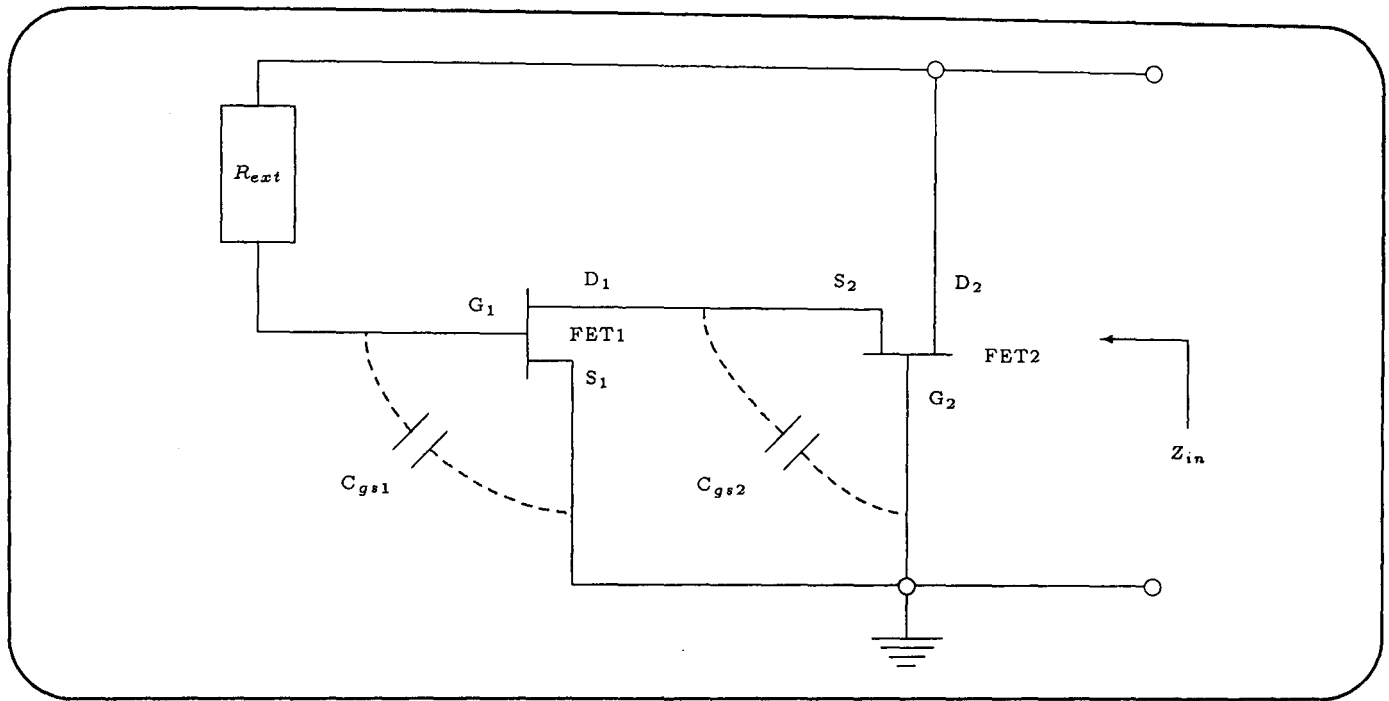


Figure 11.1: Circuit diagram of active inductor cascode GaAs FET arrangement with parallel feedback resistor.

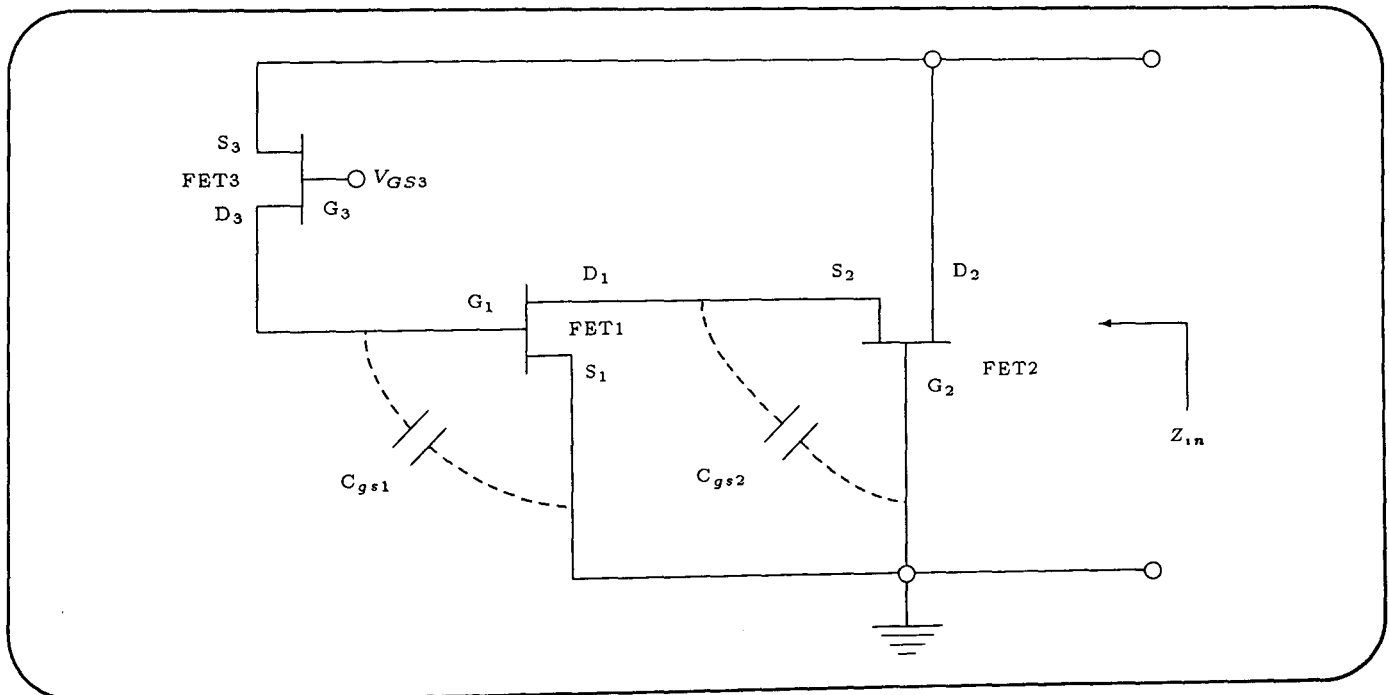


Figure 11.2: Circuit diagram of active inductor cascode GaAs FET arrangement with GaAs FET feedback element.

With the GaAs FET used as a feedback element, the inductance of the cascode arrangement can be controlled by changing the transconductance of the feedback FET

via the voltage at the gate terminal. This is the basis for an electrically controlled tuning element required for broadband operation of the monolithic implementation of the optically controlled GaAs FET switch.

### 11.2.1 Cascode Analysis With Resistive Feedback

The amount of inductive tuning required for the GaAs FET switch arrangement and the inductance change that can be achieved using the active inductor are established in this section. An analysis of the active inductor is also included, since there appears to be a discrepancy between the original active inductor impedance expression, equation(1) in [11.1], and that published later, equation (1) in [11.2]. Since no comparison is made between calculated and measured results in these publications it is not possible to ascertain the validity of the quoted expressions. The active inductor impedance derivation given here, is proposed as a modification to the original expressions presented in [11.1,11.2].

The analysis of the cascode active inductor arrangement presented here is consistent with that described originally by Hara *et al.* [11.1,11.2], wherein it is assumed that the FET is a combination of only the transconductance and the gate-to-source capacitance. With this assumption, the active inductor arrangement of Figure 11.1 can be represented by the AC equivalent circuit of Figure 11.3, from which an expression for the input impedance  $Z_{in}$  of the active inductor can be established.

From Figure 11.3, the input impedance of the active inductor arrangement can be expressed as

$$Z_{in} = \frac{v_{in}}{i_{in}} \quad (11.1)$$

where  $v_{in}$  and  $i_{in}$  are the voltage and current at the input terminals to the active inductor. The input voltage can be expressed in terms of the voltage and current associated with the feedback resistor,  $v_{ext}$  and  $i_{ext}$  respectively, as

$$v_{in} = v_{ext} + v_{gs1} = i_{ext}R_{ext} + v_{gs1} \quad (11.2)$$

where  $R_{ext}$  is the feedback resistance and  $v_{gs1}$  the gate-to-source voltage of the first FET. The current in the feedback resistor is given by

$$i_{ext} = j\omega C_{gs1}v_{gs1} \quad (11.3)$$

where  $C_{gs1}$  is the gate-to-source capacitance of the first FET and  $\omega$  the angular frequency. By substituting equation (11.3) into (11.2), the input voltage can be expressed as

$$v_{in} = v_{gs1}(1 + j\omega C_{gs1}R_{ext}). \quad (11.4)$$



Combining equations (11.4) and (11.8) and dividing through by  $g_{m2}^2$  gives the input impedance of the active inductor as

$$Z_{in} = \frac{\left[1 + \left(\frac{\omega C_{gs2}}{g_{m2}}\right)^2\right] (1 + j\omega C_{gs1} R_{ext})}{g_{m1} + j\omega \left[ C_{gs1} - C_{gs2} \left(\frac{g_{m1}}{g_{m2}}\right) + C_{gs1} \left(\frac{\omega C_{gs2}}{g_{m2}}\right)^2 \right]}. \quad (11.9)$$

This expression for the input impedance of the active inductor can be simplified by assuming the two GaAs FET's to have the same transconductance  $g_m$  and gate-to-source capacitance  $C_{gs}$ , as suggested in [11.1]. Therefore, equation (11.9) can be rewritten as

$$Z_{in} = \frac{\left[1 + \left(\frac{\omega C_{gs}}{g_m}\right)^2\right] (1 + j\omega C_{gs} R_{ext})}{g_m + j\omega C_{gs} \left(\frac{\omega C_{gs}}{g_m}\right)^2}. \quad (11.10)$$

Furthermore, as suggested by Hara *et al.* [11.1] for actual microwave FET's, it may be assumed that

$$g_m \gg \omega C_{gs} \left(\frac{\omega C_{gs}}{g_m}\right)^2 \quad (11.11)$$

so that equation (11.10) can be given approximately by

$$Z_{in} \simeq \frac{\left[1 + \left(\frac{\omega C_{gs}}{g_m}\right)^2\right] (1 + j\omega C_{gs} R_{ext})}{g_m} \quad (11.12)$$

which differs from the original expression presented previously in the literature [11.1, 11.2] in which the term  $\left[1 + \left(\frac{\omega C_{gs}}{g_m}\right)^2\right]$  is omitted. This part of the impedance expression is of particular significance at operating frequencies of 10 GHz and beyond.

### 11.2.2 Cascode Analysis With GaAs FET Feedback

If the feedback resistor is replaced by a common-gate GaAs FET, then the AC equivalent circuit can be modified as shown in Figure 11.4.

In this arrangement, the voltage and current at the input terminals can be expressed as

$$v_{in} = -v_{gs3} \quad (11.13)$$

$$i_{in} = g_{m2} v_{gs2} - g_{m3} v_{gs3} - j\omega C_{gs3} v_{gs3} \quad (11.14)$$

where  $C_{gs3}$ ,  $g_{m3}$  and  $v_{gs3}$  are respectively the gate-to-source capacitance, transconductance and gate-to-source voltage of the common-gate feedback GaAs FET. From Figure 11.4,  $v_{gs1}$  is given by

$$v_{gs1} = -\frac{g_{m3} v_{gs3}}{j\omega C_{gs1}} \quad (11.15)$$

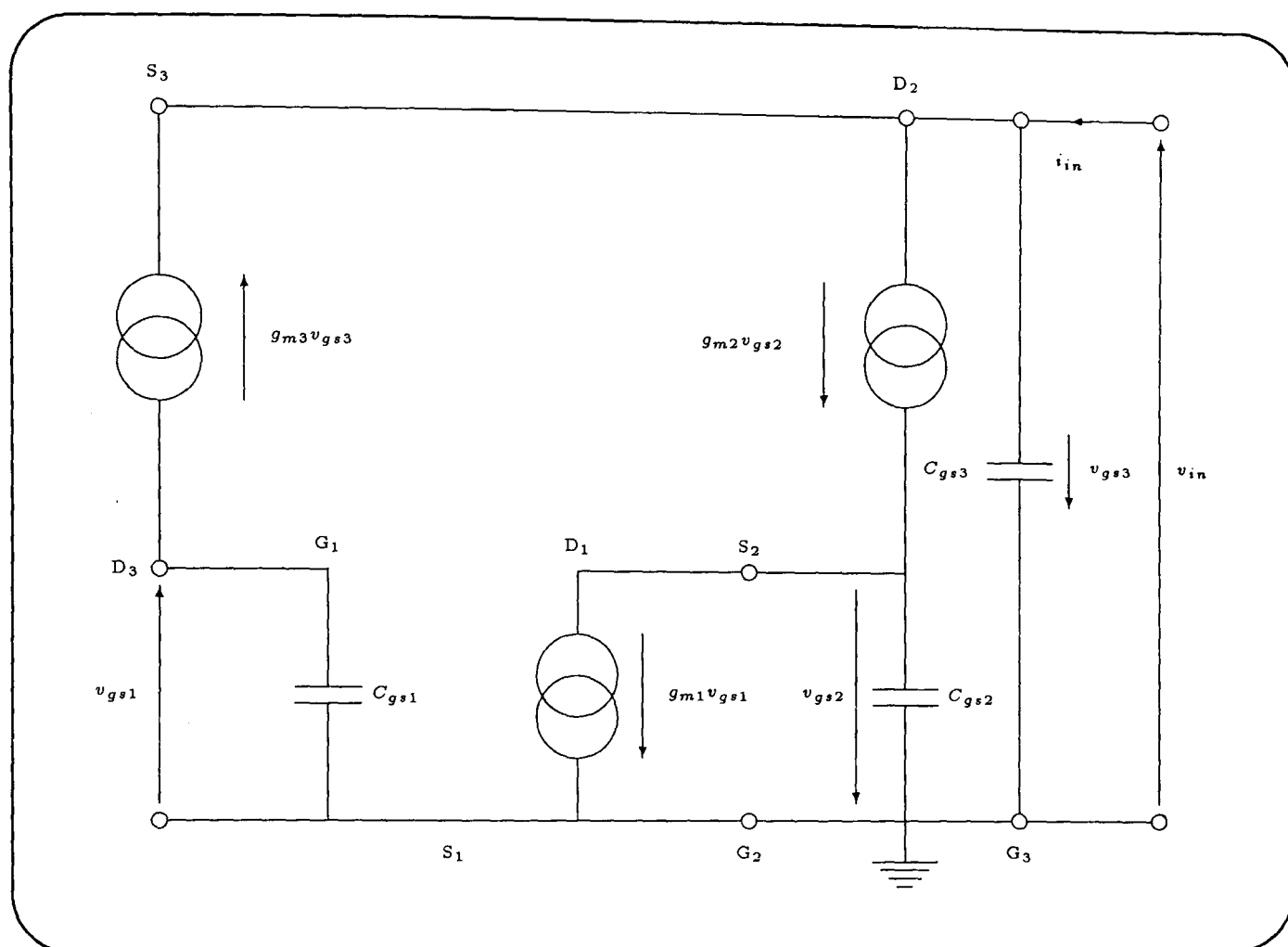


**Figure 11.4:** Simplified AC lumped equivalent circuit of the active inductor configuration with common-gate GaAs FET feedback.

which, when substituted into equation (11.7), gives

$$v_{gs2} = -\frac{g_{m1}g_{m3}v_{gs3}}{(g_{m2} + j\omega C_{gs2})(j\omega C_{gs1})}. \quad (11.16)$$

Substituting equation (11.16) into (11.14), yields

$$i_{in} = -v_{gs3} \left[ \frac{g_{m1}g_{m2}g_{m3}}{(g_{m2} + j\omega C_{gs2})(j\omega C_{gs1})} + g_{m3} + j\omega C_{gs3} \right] \quad (11.17)$$

to give an input admittance  $Y_{in}$  of

$$Y_{in} = \frac{g_{m1}g_{m2}g_{m3}}{(g_{m2} + j\omega C_{gs2})(j\omega C_{gs1})} + g_{m3} + j\omega C_{gs3} \quad (11.18)$$

which can be separated into real and imaginary components to give

$$Y_{in} = \frac{g_{m3} \left[ 1 - \frac{g_{m1}C_{gs2}}{g_{m2}C_{gs1}} + \left( \frac{\omega C_{gs2}}{g_{m2}} \right)^2 \right] + j\omega \left[ C_{gs3} + C_{gs3} \left( \frac{\omega C_{gs2}}{g_{m2}} \right)^2 - \frac{g_{m1}g_{m3}}{\omega^2 C_{gs1}} \right]}{1 + \left( \frac{\omega C_{gs2}}{g_{m2}} \right)^2}. \quad (11.19)$$

Once again, if the cascode GaAs FET's are assumed to have the same transconductance and gate-to-source capacitance, then equation (11.19) can be re-written as

$$Y_{in} = \frac{g_{m3}}{1 + \left( \frac{g_m}{\omega C_{gs}} \right)^2} + j \frac{\omega \left[ C_{gs3} + C_{gs3} \left( \frac{\omega C_{gs}}{g_m} \right)^2 - \frac{g_m g_{m3}}{\omega^2 C_{gs}} \right]}{1 + \left( \frac{\omega C_{gs}}{g_m} \right)^2} \quad (11.20)$$

in which case the input impedance can be expressed as

$$Z_{in} = \frac{1}{\frac{gm_3}{1 + \left(\frac{gm}{\omega C_{gs}}\right)^2} + j \frac{\omega \left[ C_{gs3} + C_{gs3} \left(\frac{\omega C_{gs}}{gm}\right)^2 - \frac{gm gm_3}{\omega^2 C_{gs}} \right]}{1 + \left(\frac{\omega C_{gs}}{gm}\right)^2}}. \quad (11.21)$$

## 11.3 Monolithic Active Inductor Design

In the design of an electrically controlled active inductor for GaAs FET switch tuning it is necessary to establish the required inductance and possible inductance variation available. These points are considered in relation to the hybrid GaAs FET switch design.

### 11.3.1 Monolithic Active Inductance

From the tuning arrangement used in the hybrid GaAs FET switch arrangement, the impedance of the open-circuit gate tuning stub was given in Chapter 10 as

$$Z_{oc} = -jZ_0 \cot \theta_{oc} \quad (11.22)$$

where  $Z_0$  is the characteristic impedance of the gate stub and  $\theta_{oc}$  the electrical length of the gate stub. The electrical length of the gate tuning stub can be determined from the data for the wavelength on the stub  $\lambda_s$  and the physical length of the stub  $l_g$ , as given in Chapter 6, using

$$\theta_{oc} = \beta l_g = \frac{2\pi l_g}{\lambda_s} \quad (11.23)$$

which, for a gate stub length of 4 mm and a wavelength of 11.162 mm, yields an electrical length of 129°. Then, for a stub characteristic impedance of 53  $\Omega$ , using equation (11.22) we obtain an inductive reactance of approximately 43  $\Omega$ , corresponding to an inductance of 0.686 nH at a frequency of 10 GHz. Therefore, the monolithic inductor must provide a nominal inductance of around 0.686 nH, with the actual amount of inductive tuning being determined by the transconductance and gate-to-source capacitance variation associated with the particular common-gate feedback FET being used.

### 11.3.2 Monolithic Active Inductance Variation

The variation in the inductance of the cascode active inductor will be determined by the feedback FET. It would be reasonable to assume that in monolithic form the same GaAs FET would be used for the cascode FET arrangement and for the common-gate feedback FET, since this simplifies circuit fabrication. Furthermore, using the same

GaAs FET for the complete active tuning element and for the optically controlled GaAs FET switch would be beneficial for similar reasons. Hence, it is assumed for the purposes of this analysis, that the monolithic version of the optically controlled switch is fabricated solely from a monolithic version of the GaAs FET used for the hybrid switch design (i.e. ATF-10136).

From the data sheets for the ATF-10136 GaAs FET [11.3], with the gate-to-source voltage held at zero (i.e.  $V_{GS} = 0$  V) and the drain biased at 2.0 V and 20 mA (i.e.  $V_{DS} = 2.0$  V,  $I_{DS} = 20$  mA) the transconductance is quoted to be typically 70 mS. The gate-to-source capacitance can be established from the expression used during earlier chapters and is given by

$$C_{gs} = \frac{\epsilon_0 \epsilon_r L_G W_G}{w} \quad (11.24)$$

where  $\epsilon_0$  is the permittivity in a vacuum,  $\epsilon_r$  the relative permittivity of the GaAs channel,  $L_G$  the gate length and  $W_G$  the gate periphery. The width of the depletion region  $w$  can be expressed as

$$w = a \left( \frac{\phi_B - V_{GS}}{|V_P| + \phi_B} \right)^{\frac{1}{2}} \quad (11.25)$$

where  $a$  is the recessed channel thickness,  $\phi_B$  the built-in potential of the gate Schottky junction,  $V_{GS}$  the gate-to-source bias voltage and  $V_P$  the pinch-off voltage. Since from data sheets we know the gate-to-source capacitance for  $V_{GS} = 0$  V, the above expressions can be used to evaluate the gate-to-source capacitance of the common-gate feedback GaAs FET, which will depend upon the bias applied at the gate terminal. The transconductance of the cascode GaAs FET's at  $V_{GS} = 0$  V can be obtained from the data sheets and provides a further basis for calculating the transconductance of the CG feedback GaAs FET. Ladbroke [11.4] has shown that the GaAs FET transconductance can be expressed as

$$g_m = \frac{\epsilon_0 \epsilon_r \nu_{sat} W_G}{w} \quad (11.26)$$

where  $\nu_{sat}$  is the saturation velocity. Since we know the GaAs FET transconductance when  $V_{GS} = 0$  V, we can calculate the saturation velocity and establish the transconductance variation of the CG feedback GaAs FET with applied gate bias<sup>†</sup>.

## 11.4 Active Inductor Performance

A Pascal computer program, given in Appendix A.7, was used to manipulate the simplified active inductor impedance expression and gate-to-source voltage dependent expressions. This enabled the input impedance of the active inductor to be determined for

<sup>†</sup>This assumes that current saturation is maintained in the CG GaAs FET mode.

various gate-to-source voltages applied to the CG feedback GaAs FET. Furthermore, to facilitate the determination of the frequency dependent characteristics of the active inductor, the simplified equivalent circuit for the active inductor (i.e. Figure 11.4) was simulated in MDS. The schematic model used in the MDS simulations is shown in Figure 11.5. This model enables also the transconductance delay associated with the voltage dependent current source to be incorporated. Although these simulations give an indication of the performance variation of the active inductor, the transconductance and gate-to-source capacitance model used is far too simplified to allow accurate prediction of the input impedance. The simplified model ignores a number of important intrinsic and parasitic parameters associated with the hybrid II model for the GaAs FET, described in Chapter 5. These additional elements must be accounted for fully if accurate tuning is to be achieved in the monolithic version of the optically controlled GaAs FET switch.

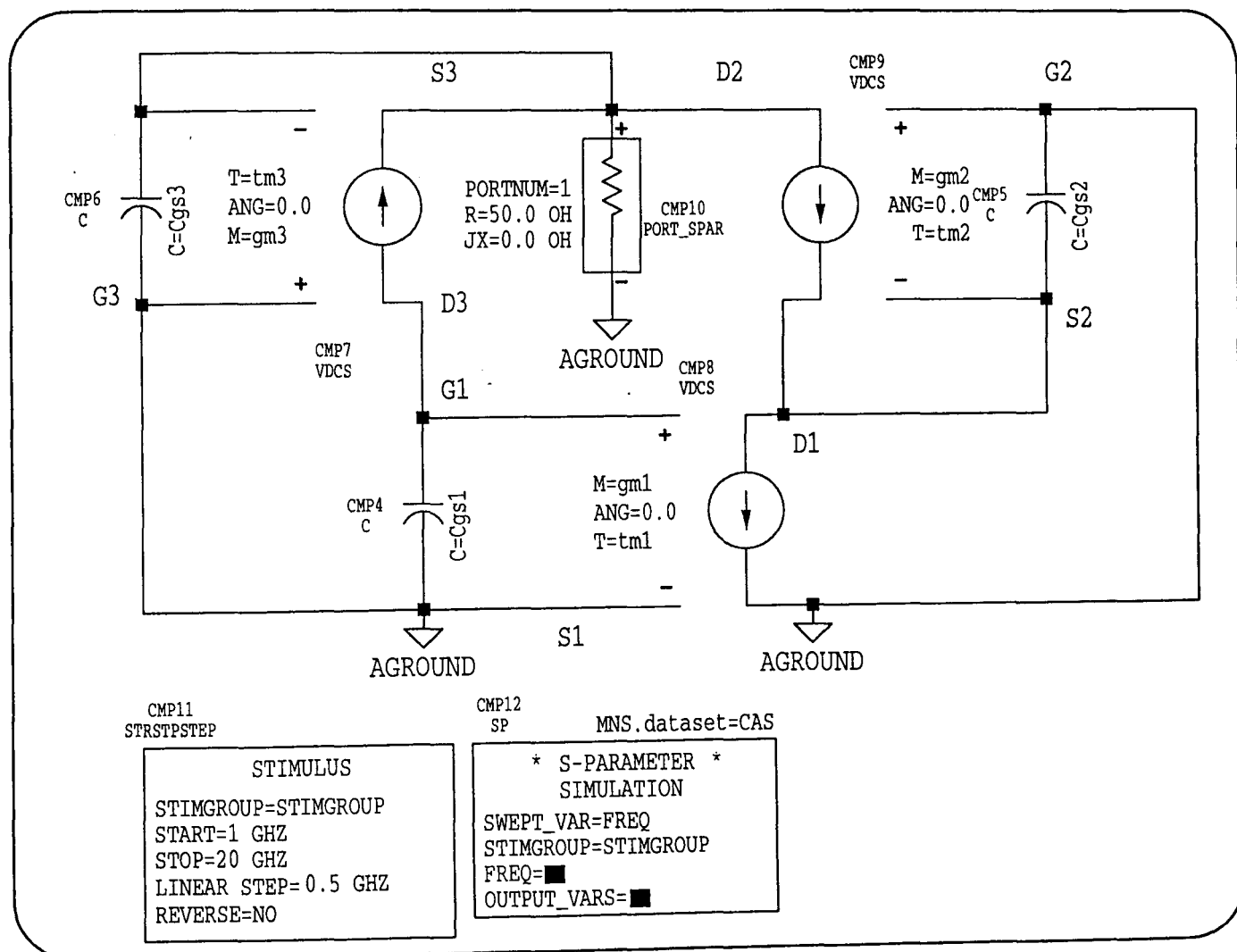


Figure 11.5: MDS simulation schematic of simplified active inductor.

### 11.4.1 Improved Active Inductor Modelling

A more accurate model for the active inductor is proposed which uses the standard hybrid II model for the GaAs FET described in Chapter 5, to simulate the performance of the cascode GaAs FET's and the CG feedback GaAs FET in the active inductor

configuration. The schematic models for each of the GaAs FET's and the overall active inductor configuration were simulated in MDS and are shown in Figures 11.6(a) and 11.6(b), respectively. The equivalent circuit element values for the cascode GaAs FET's are summarized in Table 11.1 and were extracted from the manufacturers' data sheets [11.3].

This enabled the frequency dependence of the active inductor input impedance to be evaluated. However, to allow the voltage dependence of the input impedance to be determined, the hybrid II model for the CG feedback GaAs FET was modified to include expressions for the gate-to-source voltage dependence of the equivalent circuit elements.

Equivalent Circuit Element Values for ATF-10136 GaAs FET [11.3]											
(V <sub>DS</sub> = 2.0 V, I <sub>DS</sub> = 20 mA)											
L <sub>g</sub>	L <sub>d</sub>	L <sub>s</sub>	R <sub>c</sub>	R <sub>g</sub>	R <sub>s</sub>	R <sub>ds</sub>	C <sub>gs</sub>	C <sub>gd</sub>	C <sub>ds</sub>	g <sub>m</sub>	τ <sub>m</sub>
nH	nH	nH	Ω	Ω	Ω	Ω	pF	pF	pF	mS	ps
0.9	0.6	0.15	2.0	2.5	2.0	200	0.25	0.10	0.10	70	0.001

**Table 11.1:** Equivalent circuit element values for ATF-10136 GaAs FET model [11.3].

The voltage dependent expressions used in the MDS simulations of the CG feedback GaAs FET are summarized below and were extracted from the analysis of Ladbrooke [11.4]. The superscript term in these expressions was used to represent the gate-to-source voltage condition and enables the element values given in Table 11.1, obtained at V<sub>GS</sub> = 0 V, to be used so as to simplify the evaluation of the parameters at particular gate-to-source voltages.

$$C_{gs}^{(V_{GS})} = \frac{\epsilon_0 \epsilon_r L_G W_G}{w} \quad (11.27) \quad g_m^{(V_{GS})} = \frac{\epsilon_0 \epsilon_r \nu_{sat} W_G}{w} \quad (11.31)$$

$$= C_{gs}^{(0)} \frac{w^{(0)}}{w^{(V_{GS})}} \quad (11.28) \quad = g_m^{(0)} \frac{w^{(0)}}{w^{(V_{GS})}} \quad (11.32)$$

$$C_{gd}^{(V_{GS})} = \frac{2\epsilon_0 \epsilon_r L_G W_G}{2L_{ex} + L_G} \quad (11.29) \quad R_c^{(V_{GS})} = \frac{L_G}{q\mu_0 N W_G (a - w)} \quad (11.33)$$

$$= C_{gd}^{(0)} \frac{2L_{ex}^{(0)} + L_G}{2L_{ex}^{(V_{GS})} + L_G} \quad (11.30) \quad = R_c^{(0)} \frac{a - w^{(0)}}{a - w^{(V_{GS})}} \quad (11.34)$$

where

$$w = a \left( \frac{\phi_B - V_{GS}}{|V_P| + \phi_B} \right)^{\frac{1}{2}} \quad (11.35)$$

and  $L_{ex}$  is the lateral extension of the gate depletion region towards the drain electrode,

given by [11.4]

$$L_{ex} = \frac{\omega(V_{DS} + \phi_B - V_{GS})}{\phi_B - V_{GS}}. \quad (11.36)$$

The above expressions form the basis of the MDS simulations, thus enabling the evaluation of the active inductor input impedance variation with the gate-to-voltage applied to the CG feedback GaAs FET.

### 11.4.2 Comparison of Active Inductance Results

The active inductor input impedance obtained from the simplified GaAs FET model and the complete GaAs FET model proposed in this thesis are compared in Figure 11.7 over the frequency range 1 to 20 GHz and for various gate-to-source voltages. The implications of these results are discussed in detail in Chapter 12.

From the MDS simulations of the modified active inductor model an inductance of approximately 0.686 nH, as required for the GaAs FET switch tuning element, can be achieved at 10 GHz with a gate-to-source voltage of -1.54 V applied to the CG feedback FET. The variation in the active inductor input impedance with frequency for  $V_{GS} = -1.54$  V is shown in Figures 11.8 and 11.9, and illustrates clearly the inductive and capacitive nature of the active inductor over the frequency range 1 to 20 GHz. The inductive and capacitive properties of the active inductor are consistent with the requirements of the GaAs FET switch tuning element, since from Chapter 10 it was established that for hybrid switch operation over certain bands of the frequency range, the length of the open-circuit gate stub was chosen to appear capacitive or inductive.

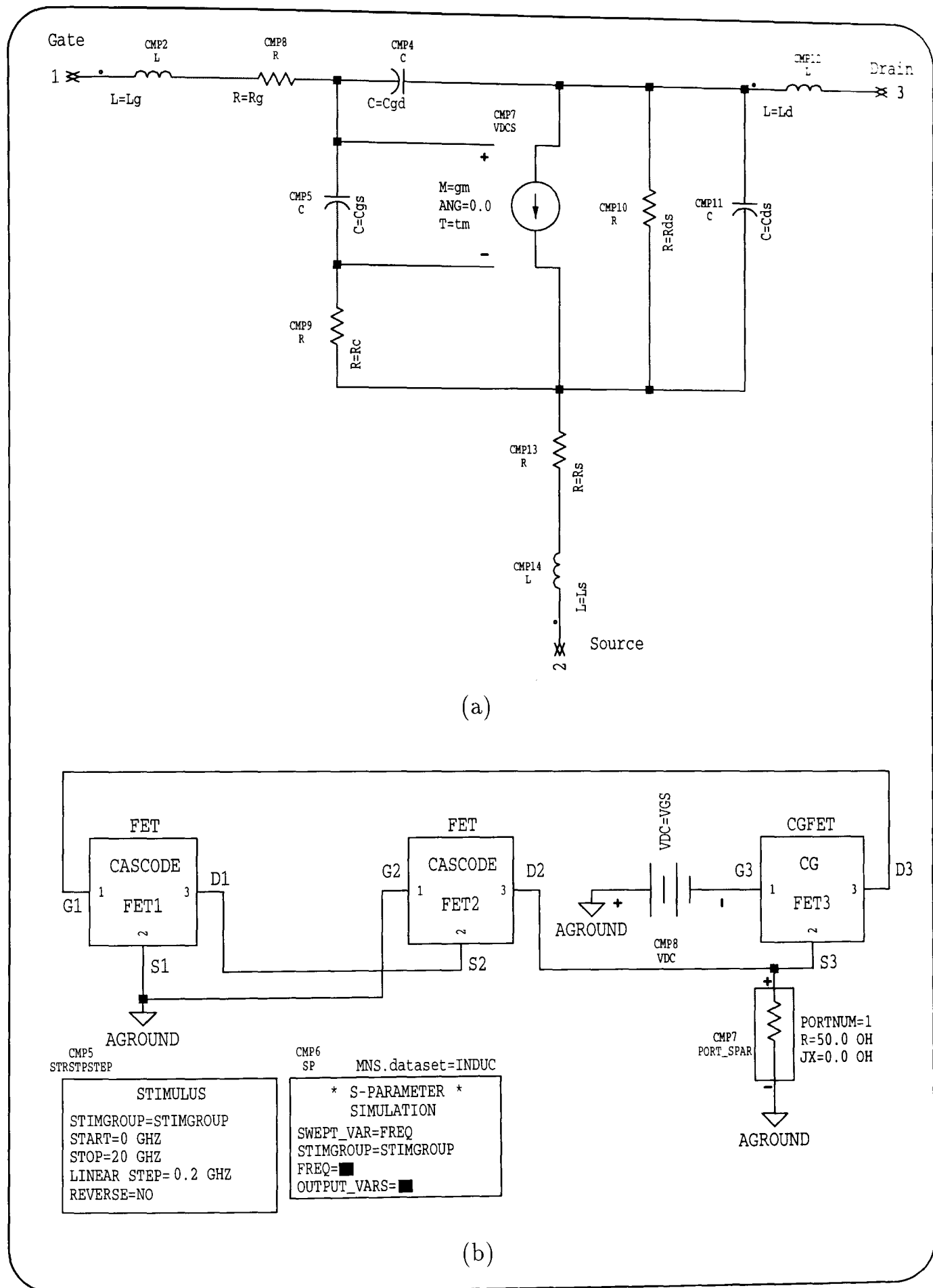
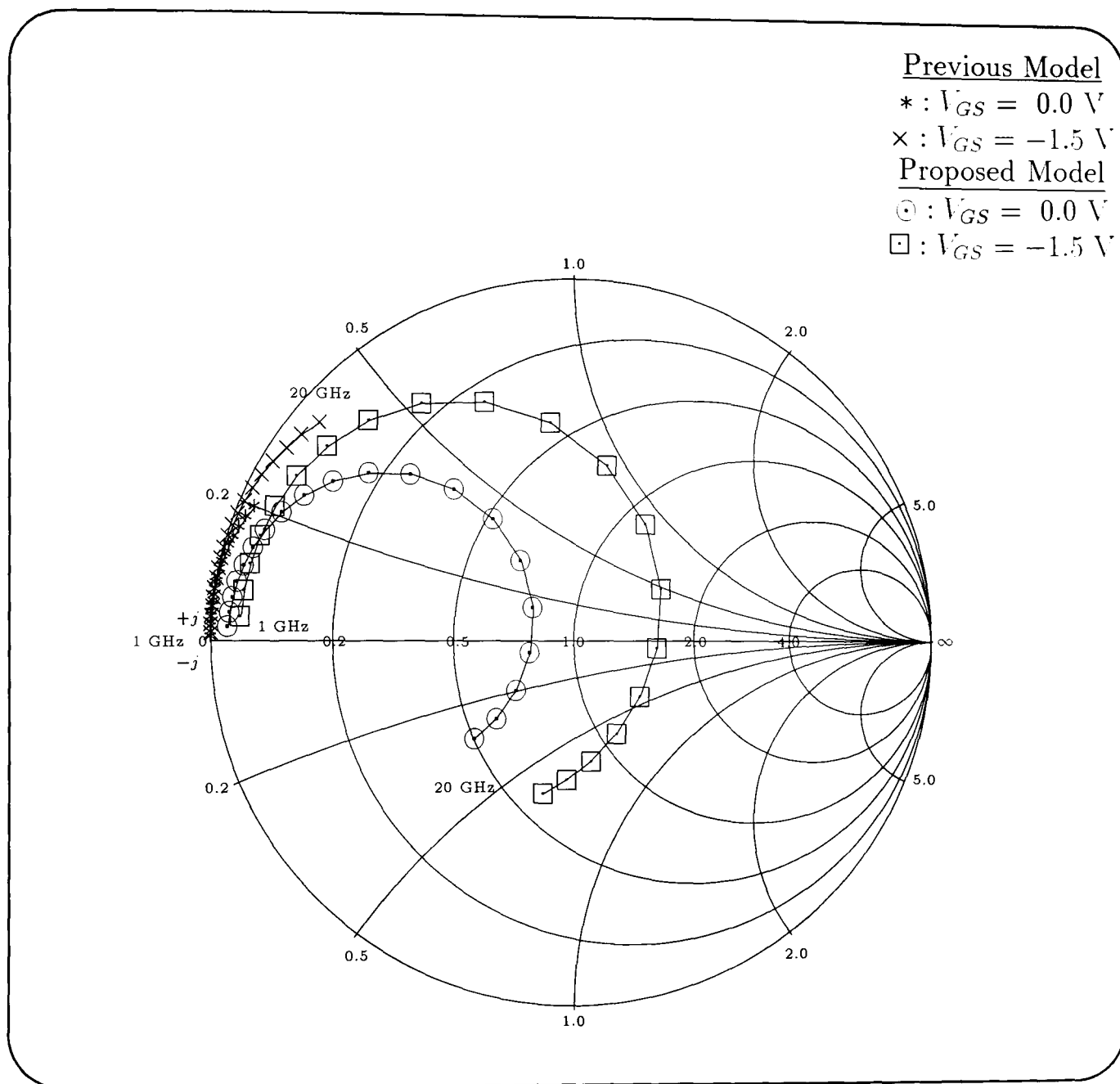


Figure 11.6: MDS simulation schematics for GaAs FET active inductor (a) GaAs FET model schematic. (b) Active inductor schematic.



**Figure 11.7:** Simulated Smith chart plot of ATF-10136 GaAs FET-based active inductor switch.

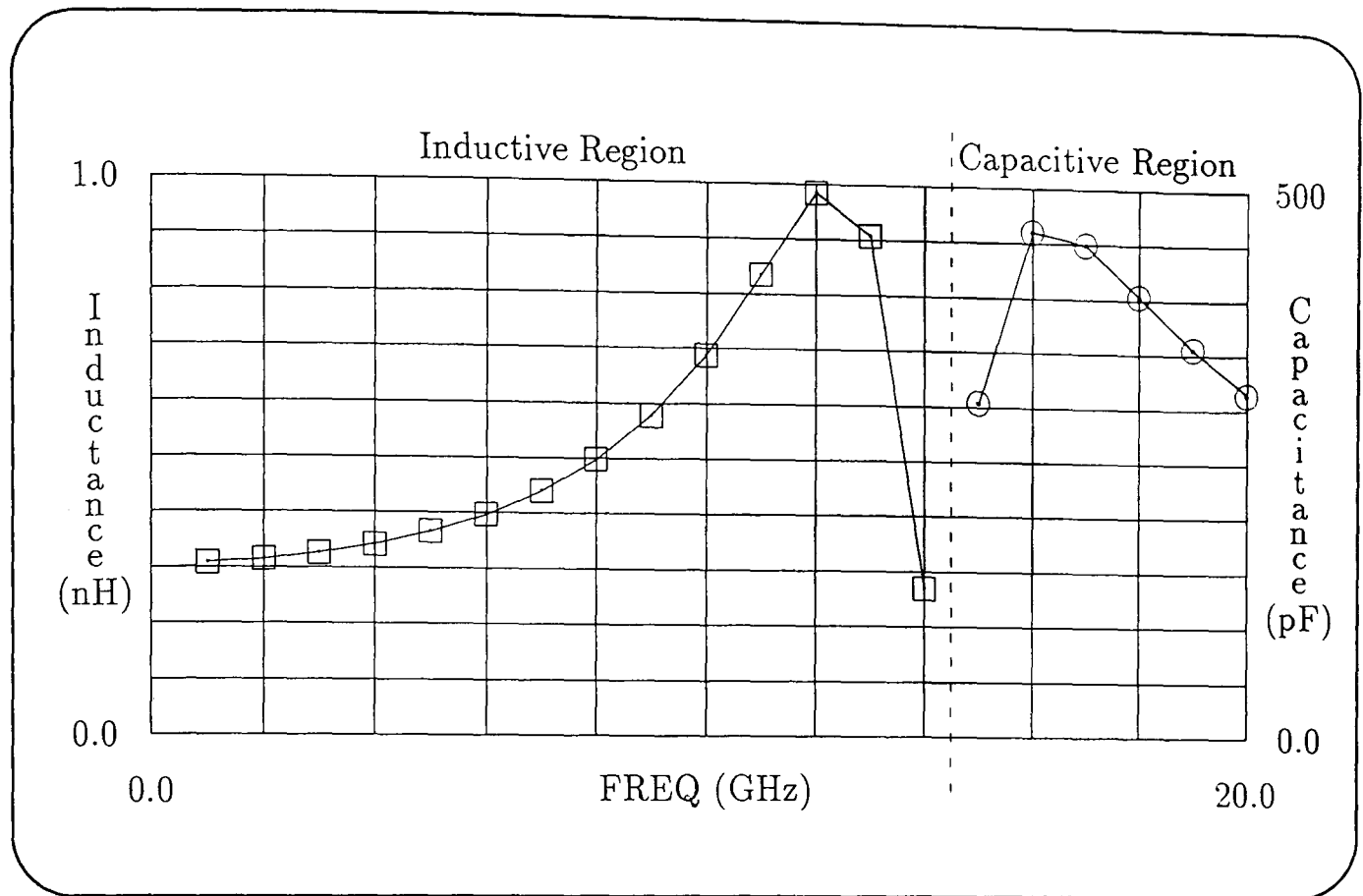


Figure 11.8: MDS simulation of inductive ( $\square$ ) and capacitive ( $\odot$ ) properties of the GaAs FET active tuning element.

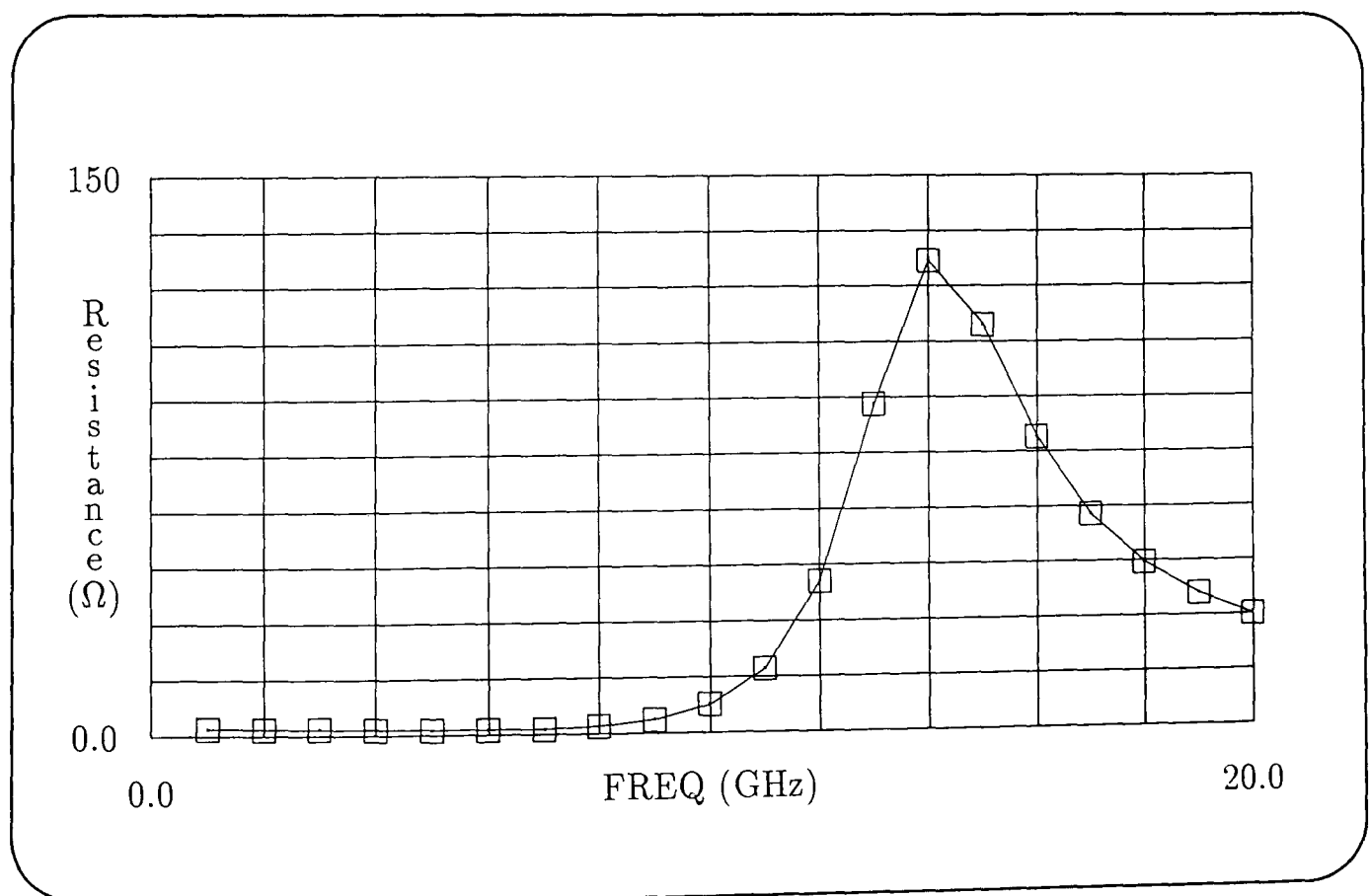


Figure 11.9: MDS simulation of resistive properties of the GaAs FET active tuning element.

# References

- [11.1] S. Hara, T. Tokumitsu, T. Tanaka, and M. Aikawa, “Broad-band monolithic microwave active inductor and its application to miniaturized wide-band amplifiers,” *IEEE Trans. Microwave Theory Tech.*, vol. 36, pp. 1920–1924. Dec. 1988.
- [11.2] S. Hara, T. Tokumitsu, and M. Aikawa, “Lossless broad-band monolithic microwave active inductors,” *IEEE Trans. Microwave Theory Tech.*, vol. 37, pp. 1979–1984, Dec. 1989.
- [11.3] Hewlett Packard, *Communications Components GaAs & Silicon Designer’s Catalogue*, 1993.
- [11.4] P. H. Ladbrooke, *MMIC design: GaAs FETs and HEMTs*. Boston: Artech House, 1989.

# Chapter 12

## Discussion of Results

### Contents

---

<b>12.1 Introduction</b> . . . . .	<b>164</b>
<b>12.2 Discussion of Results</b> . . . . .	<b>164</b>
12.2.1 Switch State Performance [12.1, 12.2] . . . . .	165
12.2.2 Switch Transient Response [12.2] . . . . .	166
12.2.3 GaAs FET Inter-electrode Capacitance [12.3] . . . . .	166
12.2.4 GaAs FET Resonances and Tuning [12.3] . . . . .	167
12.2.5 Phase Shifter Performance [12.1] . . . . .	167
12.2.6 Monolithic Active Inductor . . . . .	167

---

### 12.1 Introduction

**T**HIS chapter presents a summary of the work described in the thesis. Conclusions, recommendations for further research and potential applications are considered in subsequent Chapters.

In Section 12.2, the modelling approaches adopted in this thesis and the performance of the hybrid switch and phase shifter circuits under direct optical control, are assessed by examination of the simulation and experimental results of the earlier chapters.

### 12.2 Discussion of Results

The results presented in the earlier chapters of this thesis relate primarily to the design of a novel phase shifter using a novel GaAs FET switch configuration with control by direct optical illumination. Due to the complex structure of the microwave GaAs

FET, the switch and phase shifter designs necessitated the development of more accurate modelling approaches than exist at present in the literature. The methods can be used in conjunction with state-of-the-art simulation software. Validation of the various modelling approaches proposed in the earlier chapters is established, where possible, by the direct comparison of simulation and measurement results under identical microwave, DC and optical operating conditions.

### 12.2.1 Switch State Performance [12.1, 12.2]

In Chapter 6 measured results were presented for the frequency range 8 to 12 GHz for the switch state performance of the hybrid reflective microwave GaAs FET-based switch in which the switching state was controlled by direct optical illumination. For the first time in the literature these results were used to give a direct comparison of simulation and measurement results for the return loss and phase change upon reflection for the ‘off’ and optically ‘on’ states of the switch. The modelled results were obtained from circuit-based simulations performed using MDS. The agreement between measurement and simulation is generally very good and within the bounds of experimental error. It can be observed that the measured return loss exhibits a cyclic variation with frequency. This is attributed to multiple reflections which are often characteristic of low return loss measurements. However, the mean value of the measured data is in good agreement with the simulation result. The simulations and measurements for the phase responses show reasonable linearity over the frequency range of switch operation. As one might expect, the phase response becomes non-linear at the resonant points, as predicted. The good agreement between simulation and measurement has been achieved only through the development of more comprehensive and accurate approaches than those in the literature, for evaluating the equivalent circuit element values used to model the various regions of the GaAs FET switch in both states. These modelling improvements involved:

- a novel method for modelling the geometric capacitance of the GaAs FET in the ‘off’ state, based upon 3-dimensional field simulations of the GaAs FET metallization layers using the EM simulator HFSS.
- a simplified approach to evaluating some of the intrinsic element values of the switch model, based upon the manufacturers’ hybrid  $\Pi$  model, which requires limited information on the specific device geometries and doping levels.
- a model that included package parasitics.

These proposed approaches have been validated also for switch designs incorporating GaAs FET’s with very different gate structures. Moreover, these results show that the simulation gives an accurate prediction of the frequencies of the resonances

which were observed by measurement, and so validates the simple GaAs FET model which has been developed and proposed in this work. Furthermore, it was found that the response in the ‘on’ state while under electrical control, were almost identical to that under optical control, as predicted by the theory of Chapter 5.

### 12.2.2 Switch Transient Response [12.2]

In Chapter 7, simulation and measurement are compared directly for the transient response associated with the gate depletion region photovoltaic effect of the optically controlled GaAs FET switch. The simulated and measured responses are, for the first time, compared under identical gate loading and optical pulse conditions and show excellent agreement. This approach also establishes good agreement between the measured and simulated rise and fall times of this photovoltaic mechanism. For typical commercial GaAs FET parameters, the response times are shown to be less than 1  $\mu$ s. This degree of agreement was achieved through:

- accurate modelling of the optical response of the gate Schottky junction using the transient response facility in MDS.
- accurate allowance for the effects of measurement probes.

Moreover, the responses for the two different GaAs FET gate structures demonstrated that by reducing the gate periphery an approximately proportional reduction in the GaAs FET’s rise and fall times results, as predicted by the theory of Chapter 4.

The data currently available in the literature for the transient response of the gate photovoltaic effect in optically controlled GaAs FET’s [12.4] are inconclusive since measurement and simulation are done under differing optical and electrical conditions, making a direct comparison difficult. However, even given these limitations, discrepancies exist between their simulated and measured results. This discrepancy is particularly evident for the fall times of the response which differ by up to a factor of ten.

### 12.2.3 GaAs FET Inter-electrode Capacitance [12.3]

In chapter 10 a new method for evaluating inter-electrode capacitance was described and data presented from 3-dimensional field simulations of the GaAs FET structure using HFSS. This novel approach was one of the main factors responsible for the precise definition of the switching performance of the GaAs FET switches and the accurate prediction of switch state resonances. The proposed method was used to model an interdigitated and T-type gate FET structure, with confirmation of the proposed approach being evident in the close agreement achieved between simulation and measurement for the switch state responses of both GaAs FET’s. Moreover, this method

provides a more comprehensive and versatile approach to the determination of the GaAs FET inter-electrode capacitance than is presently available in the literature. It should be noted that this method for predicting accurately inter-electrode capacitance in GaAs FET's is not limited to GaAs FET switching applications, but can be used for  $S$ -parameter modelling of GaAs FET's.

#### 12.2.4 GaAs FET Resonances and Tuning [12.3]

The problem with resonances in the switch state performance was considered in Chapter 10 and results for the frequency range of switch operation were presented. Sensitivity analyses of the GaAs FET switch were performed in MDS and showed that the resonant frequencies predicted in the simulations, and verified in the experimental work were determined by the bond wire and terminal contact inductance at the gate of the GaAs FET switch. In addition, these results showed that these resonances could be tuned out of the frequency range of switch operation so as to have no significance. This was achieved by using an open-circuit stub attached to the gate terminal of the GaAs FET switch. For particular lengths of gate tuning stub, the switch could be configured to operate over sections of the frequency range 1 to 20 GHz, yielding, for the first time, useful design information for broadband switch operation. For the GaAs FET switches investigated, the frequency ranges 1 to 8 GHz, 8 to 12 GHz and 12 to 20 GHz were identified by curve fitting data for predicting the occurrence of resonances.

#### 12.2.5 Phase Shifter Performance [12.1]

The accurate modelling of the optically controlled GaAs FET switch led to the design of a novel digital loaded-line phase shifter, controlled by direct optical illumination, the results for which are presented in Chapter 9. The measured and simulated differential insertion loss and phase shift were compared directly for 10 GHz, 45° and 10.5 GHz, 30° phase shifter designs and showed good agreement over the phase shifters' frequency range of operation. The 30° optically controlled phase shifter has a 3 dB bandwidth of 15% and an absolute mid-band insertion loss of 0.15 dB. The 45° phase shifter has a 3 dB bandwidth of 12% and an absolute mid-band insertion loss of 0.25 dB. The performances of the optically controlled phase shifters are comparable with those presented in the literature for electrically controlled phase shifters.

#### 12.2.6 Monolithic Active Inductor

Since part of the terms of reference of the work was to establish a design compatible with monolithic implementation, Chapter 11 considered the monolithic transformation of the hybrid optically controlled GaAs FET switch design. In particular, the gate tuning stub was substituted by an electrically controlled MMIC active inductor. A new,

more comprehensive modelling approach was also proposed for the active inductor. The direct comparison of the presently available models with that proposed in Chapter 11 suggests that the present models described in the literature are far too simplified. In particular, the model proposed here confirms the inductive properties of the device but also highlights the effects of non-lossless behaviour which are usually omitted from the simplified models. Since the simplified model omits the resistive and parasitic components associated with the GaAs FET's incorporated in the active inductor, it is not surprising that these models do not predict accurately the impedance behaviour of the active inductor. The proposed model verifies the use of the active inductor as a suitable tuning element for the MMIC GaAs FET switch by demonstrating inductive and capacitive characteristics over the frequency range 1 to 20 GHz. This result is consistent with the reactive impedance properties of the gate stub tuning element used in the hybrid switch designs. Furthermore, by applying a suitable bias to the active inductor arrangement, simulations show that the correct inductance values can be achieved in order to obtain the required amount of frequency tuning.

# References

- [12.1] S. J. Rossek and C. E. Free, "Optically controlled microwave switching and phase shifting using GaAs FET's," *IEEE Microwave Guided Wave Lett.*, vol. 5, pp. 81–83, Mar. 1995.
- [12.2] S. J. Rossek and C. E. Free, "The transient response and switching performance of direct optically controlled microwave GaAs FET's." Submitted for Publication to *IEEE Trans. on MTT*.
- [12.3] S. J. Rossek and C. E. Free, "Methods for accurately evaluating interelectrode capacitance and frequency tuning range in microwave GaAs FET switches." *Electron. Lett.*, vol. 31, pp. 764–765, Apr. 1995.
- [12.4] A. Madjar, A. Paoletta, and P. R. Herczfeld, "Modeling the optical switching of MESFET's considering the external and internal photovoltaic effects," *IEEE Trans. Microwave Theory Tech.*, vol. 42, pp. 62–67, Jan. 1994.

# Chapter 13

## Conclusions

THE design of a novel reflective microwave GaAs FET switch in which the switching state is controlled by direct optical illumination has been presented and validated through measurement.

The validity of a model to characterize the switching performance and transient response associated with the gate photovoltaic effect in such a GaAs FET switch under continuous and pulsed optical conditions has been established through practical measurement. The measurements were performed on hybrid microstrip circuits incorporating commercially available packaged GaAs FET's.

The switch state model has the capability to predict accurately the occurrence of resonances which may hinder the switch operation in either or both switching states, and has followed from a more precise evaluation of the GaAs FET inter-electrode capacitance than hitherto available in the literature. A novel tuning element has been developed to shift such resonances out of the frequency band of switch operation and expressions for predicting resonances in the switch performance have yielded useful design data for switch operation over the frequency range 1 to 20 GHz. In addition, the model has been shown to be valid for FET's with significantly different gate structures. Interdigitated and T-type gate structures were investigated which both showed very close agreement between measured and simulated results. Moreover, this has led to the design of a phase shifter in which the phase state is controlled by direct optical illumination.

The monolithic implementation of the switch design has been considered, by using an active inductive tuning element to achieve broadband switch operation. Accurate models to predict the impedance properties of the active inductor have been developed and simulations have shown that the frequency range of operation for the monolithic switch can be controlled adequately by altering the electrical bias on the active inductor.

The transient measurements have established values for the response times of optically controlled commercial microwave GaAs FET's, using the gate photovoltaic

effect as the means of optical control. These response times are less than  $1 \mu\text{s}$ . The performance of the optically controlled switch and phase shifter have been used to establish a proof-of-concept for the design of a highly integrated electro-optic microwave sensor.

# Chapter 14

## Recommendations for Further Research

### Contents

---

<b>14.1 Recommendations for Further Research . . . . .</b>	<b>172</b>
14.1.1 Experimental Work . . . . .	172
14.1.2 Theoretical/Simulation Work . . . . .	174
<b>14.2 Phase shifter Applications . . . . .</b>	<b>175</b>
14.2.1 Electro-Optic Microwave Sensor . . . . .	175
14.2.2 Phased-Array Radar . . . . .	177

---

### 14.1 Recommendations for Further Research

**T**HIS study has provided a basis for the realization of a phase shifter controlled by direct optical illumination, through the design of hybrid switching and phase shifting circuits. In particular, models which predict accurately the performance of these circuits and are applicable to hybrid or monolithic constructions have been proposed and verified.

#### 14.1.1 Experimental Work

Although some consideration of the realization of the circuits in a monolithic form was the subject of Chapter 11, these results were obtained through simulation and have not been verified experimentally. The next logical step in this research would be to transfer the switch designs to a monolithic form, according to the suggestions given in Chapter 11. This could best be achieved in three stages.

1. Design of an MMIC switch with an open-circuit tuning stub connected to the gate of the GaAs FET in order to validate the switch performance over a pre-determined and fixed frequency range.
2. Design of the MMIC active inductor circuit to validate the modelling approaches of Chapter 11.
3. Re-design of the MMIC switch with the active inductor connected to the gate of the GaAs FET.

It is expected that the parasitic gate inductance value for the monolithic switch design will be similar to that experienced in the packaged devices, since in both cases a wire bond is required at the gate of the GaAs FET in order to permit biasing of the switch. In the re-design of the MMIC switch it is likely that the principal modifications will be associated with the active tuning element. Since simulations have established a non-lossless characteristic for the active inductor, modifications may be required to avoid absorption in the tuning element. It is anticipated that this could be achieved through careful selection of the properties of the GaAs FET's used in the active inductor and through the use of simulations using the modelling approach proposed in Chapter 11.

In a practical situation the MMIC version of the optically controlled switches and phase shifters are likely to be combined with various other microwave circuits (e.g. oscillators, amplifiers) on the same chip, in order to fulfil a practical function. Although GaAs FET's have widespread use in MMIC's, if higher frequency operation and/or lower noise performance are a requirement, it may become necessary to implement these additional circuit functions using HEMT devices. In this case, the MMIC fabrication process could be simplified by using HEMT devices also for the optically controlled circuit functions, thereby obtaining all circuit functions with one type of transistor. Since the GaAs FET and HEMT have been shown in the literature to exhibit similar photo-mechanisms, the characterization of HEMT's for optical switching operation at the higher microwave frequencies will be a future, if not immediate, area of further research. Consequently, some preliminary investigations have already been conducted by the author on the switch state performance of a HEMT-based switch over the frequency range 8 to 12 GHz. These are presented in Figure 14.1.

This switch circuit incorporated the ATF-35576 pseudomorphic HEMT from Hewlett Packard. The PHEMT was mounted in a microstrip circuit similar to that described in Chapter 6, with the exception that the microstrip source to ground connections had to be modified to account for a difference in the device packaging. The measured responses for the optically controlled HEMT-based switch reveal the following behaviour:

- a larger return loss in the optically 'on' state of the switch which, despite the lower source resistance characteristic of HEMT devices, is reflected in a larger

drain resistance of  $5 \Omega$  compared with a typical value of  $2 \Omega$  in the GaAs FET devices [14.1].

- changes in the frequencies at which resonances occur, which are expected to be a net result of the change in packaging style used for the HEMT and the differing gate, drain and source geometries for this device.

It is expected also that some modification to the switch model used for GaAs FET's will be required to account for the structural and operational differences between the HEMT and FET devices. This is considered further in the next section.

### 14.1.2 Theoretical/Simulation Work

The models for the GaAs FET switch proposed in this thesis involved the extraction of some of the lumped equivalent circuit element values from the standard hybrid  $\Pi$  model for the GaAs FET. This hybrid  $\Pi$  model is usually limited to a maximum frequency of 20 GHz [14.1], and as a result, the switch performance beyond this frequency has not been investigated. Further research is required in order to determine the modifications to the switch models proposed in this thesis necessary to predict the switch state performance at higher microwave frequencies. It is anticipated that at these higher frequencies the modifications will, primarily, be associated with the geometric properties of the GaAs FET. In addition, the use of HEMT-based switches will involve further modifications to the presently proposed switch state model. It is anticipated that these modifications will be related principally to the different gate-to-source and gate-to-drain capacitances, which result from the slightly different depletion mechanisms associated with HEMT and FET devices.

Although the basis of modelling the response times of the GaAs FET was presented and verified through experiment, the trade-offs between the optical signal parameters, DC bias conditions and GaAs FET parameters have not been investigated rigorously. This is suggested as an area for further investigation. In particular, the following areas could be considered initially:

- using a lower value for the gate bias resistance, in which case a higher optical flux density may be required to achieve the photovoltage necessary to realize the switch states.
- using a FET with a smaller gate periphery to reduce the gate capacitance, in which case the optical coupling efficiency may be reduced.

This work could then be extended to model the transient response of optically switched HEMT's, through appropriate modification of the gate capacitance expression, in order to account for the slight differences between the gate depletion mechanisms in HEMT and FET devices.

Although optically controlled GaAs FET's configured as reflective switches have been the subject of this work, a transmissive switch configuration is sometimes preferred for phase shifting applications (e.g. switched-line phase shifters). Therefore, appropriate modifications to the switch design and modelling approaches proposed in this thesis are necessary to realize a transmissive optically controlled switch.

## 14.2 Phase shifter Applications

In this work, a direct optically controlled GaAs FET-based switch was developed, with a view primarily to the development of a novel electro-optic microwave sensor. In this proposed arrangement, the GaAs FET provides a monolithic interface between a digital optical sensor and a microwave transceiver, with such a combination effectively acting as a radio sensor. The GaAs FET switch developed herein has formed part of an optically controlled digital phase shifting arrangement in order to provide phase modulated microwave transmissions controlled directly by the optical data. Such a phase shifter has the ability to permit 'precise' phase selection (i.e. phase steps) over a range of frequencies. Since both the optical and microwave aspects of this sensor can be made compatible through the use of the GaAs FET as an MMIC-compatible photo-detector, it is expected that such a sensor could be realized in a highly integrated form.

The optically controlled switch state performance of the GaAs FET was modelled accurately and verified experimentally to permit accurate design of the optically controlled phase shifter. In addition, the performance of the GaAs FET under optically pulsed conditions was evaluated to determine the suitability of this device for the sensor application. Since most sensor applications involve a relatively slow change with time, the response times of the GaAs FET switch will be more than adequate for this application. Although the work described here has shown theoretically and experimentally a proof-of-concept for the sensor design, further development is required to provide a complete interface. Some of these further developments are considered below.

### 14.2.1 Electro-Optic Microwave Sensor

Digital fibre optic sensors in which the optically-sensed data are digitally encoded at the sensor head offer not only the benefits associated with optical sensing techniques but provide also the detection and processing advantages of digital methods. Digitally encoding the optical measurand provides several significant advantages over analogue techniques; i.e.

- the digital nature of the sensor eliminates the need for periodic re-calibration.

- there is good immunity from source intensity fluctuations, variable connector and fibre losses, and changing measurand characteristics.

Such digital fibre optic sensors have been developed to measure a number of parameters. Particular examples include Dakin [14.2], in which the digital encoding of the optical data is described, and Morris and Pollock [14.3], who developed a liquid level sensor based upon the digital encoding technique. For the purpose of this discussion, the sensor developed by Morris and Pollock [14.3] is taken as a typical example to illustrate the concept underlying the electro-optic microwave sensor design. In this liquid level sensor, a single source fibre is used to inject light into a sensor head incorporating several output fibres and a digital encoding mask. The sensor operates by virtue of light from the source fibre being coupled to the output fibres according to the level of the liquid and the pattern on the encoding mask. Such an arrangement produces a digital optical signal on each of the output fibres which corresponds to one bit in a binary word. It is intended that the output from each of these fibres be used to control an individual phase shifting arrangement. For the optically controlled loaded-line phase shifter developed in this work, two optical fibres, each carrying the same information, are required for each phase shifter, since the spacing between each GaAs FET switch will not permit the use of a single fibre to illuminate both switching GaAs FET's. Thus each twin set of fibres will illuminate the two GaAs FET's that control the phase state of the phase shifter. By cascading a number of such phase shifters in an MMIC design, discrete phase shifts controlled by the fibre optic sensor data can be realized in a similar manner to that achieved using electrical control of multiple bit MMIC phase shifters [14.4]. A suitable arrangement for interfacing the MMIC with the optical fibre outputs from the sensor head might consist of an array of optical fibres in a ribbon cable, as shown in Figure 14.2 [14.5].

Such an arrangement has been proven commercially for both multimode and single-mode fibres, and permits mass splicing with low optical loss [14.6]. The spacing between individual fibres in the ribbon cable will be determined by the distance between the GaAs FET switches in each phase shifter. This will be governed by the phase shifter design or possibly by the limitations imposed by the layout rules specified by the MMIC foundry, on the minimum distance between components. As an example, for the optically controlled loaded-line phase shifter, a quarter-wavelength spacing between each loaded-line is required for maximum bandwidth performance. For an MMIC design on GaAs at a frequency of 10 GHz, this corresponds to a loaded-line separation of approximately 2500  $\mu\text{m}$ . At 40 GHz this is reduced to approximately 620  $\mu\text{m}$ . For the GEC-Marconi MMIC process, the minimum distance between components is determined, in this example, by the allowable spacing between the centres of the

ground via connections used on the source of each GaAs FET switch<sup>†</sup>. A minimum separation of 250  $\mu\text{m}$  is specified for this particular foundry process [14.7]. Therefore the separation will be dictated by the phase shifter design and not by the MMIC process constraints. For practical purposes it would be advantageous to keep the fibre separation fixed so that a standard interface is required, irrespective of the frequency of operation of the MMIC phase shifter. Although this fixes the spacing between the switching GaAs FET's, the loaded lines in the MMIC design can easily be modified to give the correct point of attachment on the main line. The exact position of each optical fibre is not critical, since, as was established during earlier chapters, the optical beam spot that might emerge from a typical optical fibre will be much greater than the optically sensitive regions of the GaAs FET. If focusing of the optical beam spot is required, possibly due to optical power constraints, then it is envisaged that this could be achieved by using a microlens. Such a lens could be made in monolithic form by appropriately grading the refractive index of surface layers used to coat the MMIC. Such an arrangement is similar to the GRIN-rod lens presently employed in optical fibre sources and couplers [14.5]. A possible configuration for the electro-optic microwave sensor interface is shown in Figure 14.3 and indicates some typical dimensions for the device.

### 14.2.2 Phased-Array Radar

Although the optically controlled phase shifter described in this thesis was primarily aimed at a sensor application, the phase shifter operation offers the flexibility to be applied in other optically controlled microwave applications. Of particular interest is the use of optically controlled phase shifters for future advanced phased-array radar systems. In such systems it is intended that the distribution of microwave reference signals and digital command data can be achieved effectively by using optical fibres as discussed in Chapter 1. In addition, MMIC variable phase shifters and amplifiers are required to permit the creation of the correct phase and amplitude distribution that are appropriate to the desired radiated beam configuration. The GaAs FET switch described in this thesis could provide the direct (monolithic) interface between the optical command data and the MMIC circuit functions.

---

<sup>†</sup>This results from constraints imposed by the foundry which specify that the gate terminals for all GaAs FET's must run parallel throughout the circuit.

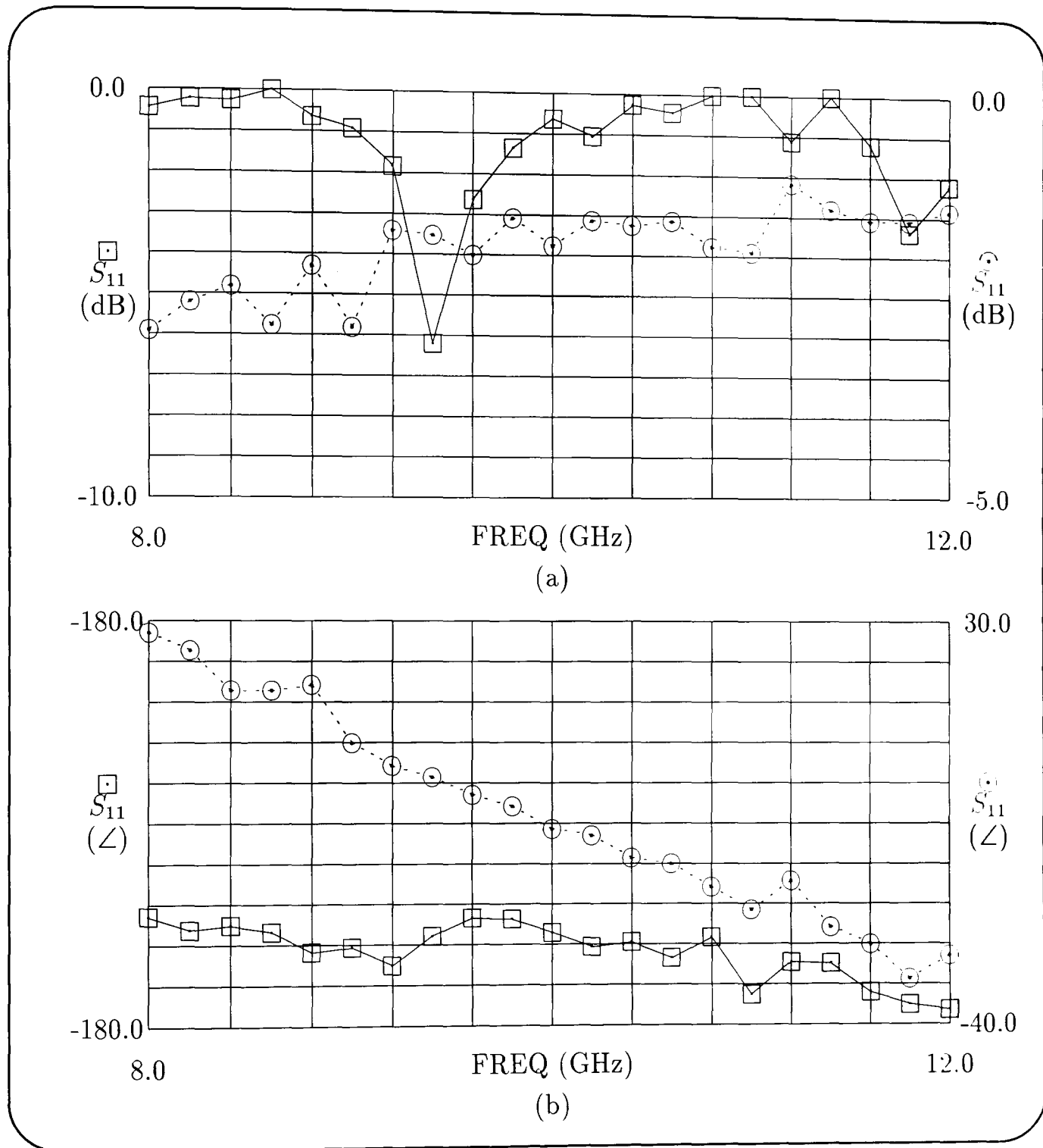


**Figure 14.1:** Measured performance of ATF-35576 pseudomorphic HEMT switch in 'off' state (□) and optically 'on' state (⊙). (a) Return loss. (b) Phase change upon reflection.

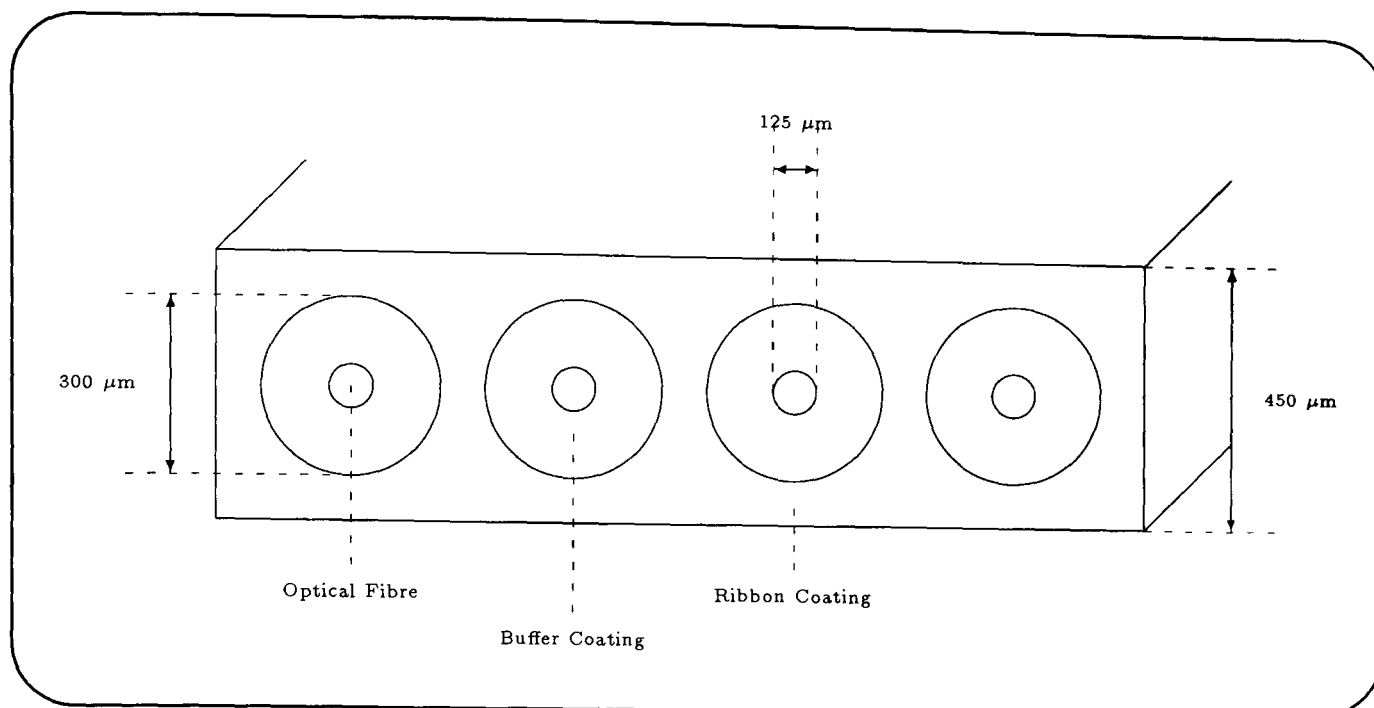


**Figure 14.2:** Schematic cross-section of ribbon cable structure, showing typical dimensions for optical fibre communication applications.

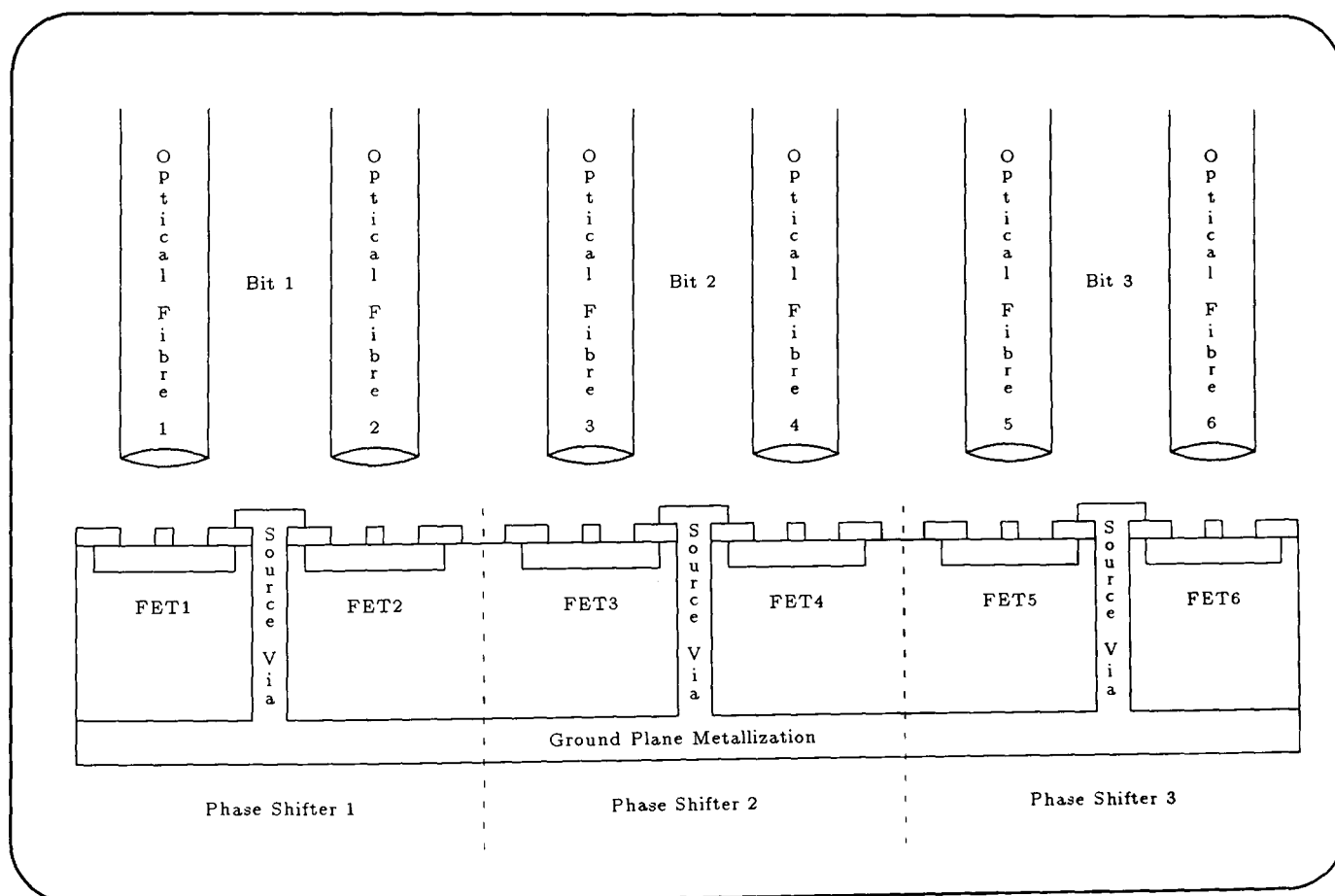


**Figure 14.3:** Schematic cross-section of the typical layout of a MMIC-based electro-optic microwave sensor interface.

# References

- [14.1] Hewlett Packard, *Communications Components GaAs & Silicon Designer's Catalogue*, 1993.
- [14.2] J. P. Dakin, "A liquid level sensor based on O-H or C-H absorption monitoring," *Plessey Technical J. Systems Technology*, vol. 28, pp. 91-95, May 1984.
- [14.3] J. A. Morris and C. R. Pollock, "A digital fiber-optic liquid level sensor," *IEEE J. Lightwave Technol.*, vol. LT-5, pp. 920-925, July 1987.
- [14.4] C. Andricos, I. J. Bahl, and E. L. Griffin, "C-Band 6-bit GaAs monolithic phase shifter," *IEEE Trans. Microwave Theory Tech.*, vol. MTT-33, pp. 1591-1596, Dec. 1985.
- [14.5] J. M. Senior, *Optical fiber communications: principles and practice*, ch. 5, pp. 235-249. New York: Prentice Hall, second. ed., 1992.
- [14.6] Y. Katsuyama, S. Hatano, K. Hogari, T. Matsumoto, and T. Kokubun, "Single-mode optical-fibre ribbon cable," *Electron. Lett.*, vol. 21, pp. 134-135, Feb. 1985.
- [14.7] GEC-Marconi Materials Technology, *GEC-Marconi F20 Design Manual*, July 1995. Ch. 8-Layout Rules.

# Appendix A

## Pascal Computer Programs

### Contents

---

A.1	Microstrip Open-End Correction . . . . .	181
A.2	Asymmetric Tee-Junction Compensation . . . . .	182
A.3	Impedance Step Compensation . . . . .	183
A.4	Optical Reflectivity . . . . .	184
A.5	Switch Impedance Transformation . . . . .	185
A.6	Phase Shifter Design . . . . .	187
A.7	GaAs FET Active Inductor . . . . .	191

---

THIS appendix give the listings of various Pascal computer programs used in the design of the optically controlled switch and phase shifter circuits described in this thesis.

### A.1 Microstrip Open-End Correction

This program calculates the reduction in length, required to compensate for the fringing effect at the end of an open-circuit microstrip stub, and is based upon the expressions given by Kirschning *et al.* [A.1].

```
program open(input,output);
    {M. Kirschning, A. H. Jansen, N. H. L. Koster}
    {Accurate model for open end effect of microstrip lines}
    {Electronics Letters, vol. 17, no. 3, pp. 77-86, Feb. 1981}
const pi=3.141592654;
var   er,eff,h,w,a,b,c,d,e,g,i,j,k,l,m,n,o:real;
begin
    writeln('Enter the relative permittivity');
```

```

readln(er);
writeln('Enter the effective relative permittivity');
readln(ef);
writeln('Enter the substrate height in mm');
readln(h);
writeln('Enter the track width in mm');
readln(w);
a:=w/h;
b:=exp(0.8544*ln(a));
c:=exp(0.81*ln(ef));
d:=(0.434907)*((c-0.26)/(c-0.189))*((b+0.236)/(b+0.87));
e:=1+((exp(0.371*ln(a)))/((2.358*er)+1));
f:=1.9413/e;
g:=0.084*(exp(f*ln(a)));
if g<=1 then i:=g-((g*g*g)/3)+((g*g*g*g*g)/5)+((g*g*g*g*g*g*g)/7)
else i:=(pi/2)-(1/g)+(1/(3*g*g*g))-1/(5*g*g*g*g*g);
j:=1+((0.5247*i)/(exp(0.9236*ln(ef))));
k:=(0.067*(exp(1.456*ln(a))))*(6-(5*(exp(0.036*(1-er)))));
if k<=1 then l:=k-((k*k*k)/3)+((k*k*k*k*k)/5)+((k*k*k*k*k*k*k)/7)
else l:=(pi/2)-(1/k)+(1/(3*k*k*k))-1/(5*k*k*k*k*k);
m:=1+(0.0377*l);
n:=1-(0.218*(exp(-7.5*a)));
o:=(h*d*j*n)/m;
writeln('The open-end correction length in mm =',o)
end.

```

## A.2 Asymmetric Tee-Junction Compensation

This program calculates the reference plane shifts, required to compensate for discontinuities in microstrip asymmetric tee-junctions, and is based upon the expressions given by Hammerstad [A.2].

```

program astj(input,output);
  {E. Hammerstad}
  {Computer-aided design of microstrip couplers with accurate discontinuity
  models}
  {IEEE MTT-S International Microwave Symposium Digest, pp. 54-56, 1981}
const pi=3.141592654;
var eef1,eef2,w1,w2,h,z1a,z1b,z2,a,b,f,f1,d1a,d1b,d2:real;
begin

```

```

writeln('Enter the substrate height in mm');
readln(h);
writeln('Enter the impedance of the input line');
readln(z1a);
writeln('Enter the relative permittivity of the input line');
readln(eef1);
writeln('Enter the impedance of the output line');
readln(z1b);
writeln('Enter the impedance of the shunt line');
readln(z2);
writeln('Enter the relative permittivity of the shunt line');
readln(eef2);
writeln('Enter the frequency in GHz');
readln(f);
a:=(sqrt(z1a*z1b))/z2;
f1:=0.4*z1a/h;
b:=sqr(f/f1);
w1:=(120*pi*h)/(z1a*(sqrt(eef1)));
w2:=(120*pi*h)/(z2*(sqrt(eef2)));
d1a:=(0.055*w2*z1a/z2)*(1-((z1a/z2)*b));
d1b:=(0.055*w2*z1b/z2)*(1-((z1b/z2)*b));
d2:=(w1*a)*((0.5)-((0.05)+(0.7*exp(-1.6*a)))+(0.25*a*b)-
(0.17*(ln(a))));
writeln('Shunt line reference plane shifted down by',d2);
writeln('Input line reference plane shifted left by',d1a);
writeln('Output line reference plane shifted right by',d1b)
end.

```

### A.3 Impedance Step Compensation

This program calculates the reference plane shifts, required to compensate for impedance step discontinuities in microstrip, and is based upon the expressions given by Garg *et al.* [A.3].

```

program step(input,output);
  {R. Garg and I. J. Bahl}
  {Microstrip discontinuities}
  {International Journal of Electronics, vol. 45, no. 1, pp. 81-87, Jan. 1978}
var  w1,w2,h,er,a,b,c,d,z1,z2,eef1,eef2,s1,l1,lc:real;

```

```

begin
  writeln('Enter the larger width in mm');
  readln(w2);
  writeln('Enter the impedance of the wider line');
  readln(z2);
  writeln('Enter the effective permittivity of the wider line');
  readln(eef2);
  writeln('Enter the smaller width in mm');
  readln(w1);
  writeln('Enter the impedance of the narrower line');
  readln(z1);
  writeln('Enter the effective permittivity of the narrower line');
  readln(eef1);
  writeln('Enter the relative permittivity');
  readln(er);
  writeln('Enter the substrate height in mm');
  readln(h);
  s1:=300000000;
  a:=(ln(er))/(ln(10));
  b:=w2/w1;
  d:=(sqrt(w1*w2))*0.001;
  if (b>=1.5)and(b<=3.5) then c:=((((10.1*a)+2.33)*b)-(12.6*a)
  -(3.17))*d;
  if (b>3.5) and (b<=10) then c:=((130*((ln(b))/(ln(10))))-44)*d;
  l:=((40.5*(b-1))-(75*((ln(b))/(ln(10))))+(0.2*(sqr(b-1))))*h*0.001;
  lc:=((s1*z2*c)/(sqrt(eef2)))*(exp(-12*ln(10)));
  ll:=((l*s1)/(z1*(sqrt(eef1)))*(exp(-9*ln(10))));
  writeln('The wider line is shortened by the length (mm)', lc);
  writeln('The narrow line is shortened by the length (mm)', ll)
end.

```

## A.4 Optical Reflectivity

This program calculates the theoretical optical reflectivity,  $R$ , of the GaAs FET surface due to a  $\text{Si}_3\text{N}_4$  passivation layer, and is based upon the expressions given by Madjar *et al.* [A.4].

```

program passivation(input,output,pasfle);
  {A. Madjar, P. R. Herczfeld, and A. Paoletta}
  {Analytical model for optically generated currents in GaAs MESFETs}

```

```

    {IEEE Trans. Microwave Theory Tech., vol. 40, no. 8, pp. 1681-1691, Aug.
    1992}
const pi=3.141592654;
      ng=3.5;
      ns=2.05;
var   a,b,c,d,e,f,g,h,i,l,t,w,w1,w2:real;
      pasfle:text;
begin
  rewrite(pasfle);
  writeln('Enter silicon-nitride passivation layer thickness in um');
  readln(l);
  writeln('Enter the start wavelength of incident light in nm');
  readln(w);
  writeln('Enter the stop wavelength of incident light in nm');
  readln(w1);
  writeln('Enter the increment wavelength of incident light in nm');
  readln(w2);
  while w<=w1 do
  begin
    a:=(ns-ng)/(ns+ng);
    b:=2*pi*ns*l*1000/w;
    c:=((1+ns)*a*(cos(2*b)))+(1-ns);
    d:=(1+ns)*(-a)*(sin(2*b));
    e:=((1-ns)*a*(cos(2*b)))+(1+ns);
    f:=(1-ns)*(-a)*(sin(2*b));
    g:=(sqr(e))+sqr(f);
    h:=((c*e)+(d*f))/g;
    i:=((d*e)-(c*f))/g;
    t:=1-((sqr(h))+sqr(i));
    writeln(pasfle,w,t);
    w:=w+w2
  end
end.

```

## A.5 Switch Impedance Transformation

This program calculates the switch impedance transformation through a  $50\ \Omega$  length of line and was used in the impedance matching networks for the loaded-line phase shifter design.

```
program transform(input,output);
const pi=3.141592654;
var   z,r,x,th,th1,aux,a,b,c,d,e,f,g,h,i,j:real;
      x1,r1,a1,b1,c1,d1,e1,f1,g1,h1,i1,j1:real;
begin
  z:=50;
  writeln('Enter the on-state switch impedance in Ohms');
  writeln('The real part');
  readln(r);
  writeln('The imaginary part');
  readln(x);
  writeln('Enter the off-state switch impedance in Ohms');
  writeln('The real part');
  readln(r1);
  writeln('The imaginary part');
  readln(x1);
  writeln('Enter electrical length of the matching line in deg. ');
  readln(th);
  th1:=pi*th/180;
  aux:=(sin(th1))/(cos(th1));
  a:=z-(x*aux);
  b:=r*aux;
  c:=z*r;
  d:=(z*z*aux)+(z*x);
  g:=(c*c)+(d*d);
  e:=((a*c)+(b*d))/g;
  f:=((b*c)-(a*d))/g;
  h:=(e*e)+(f*f);
  i:=e/h;
  j:=-f/h;
  writeln('Transformed on-state impedance');
  writeln('The real part is', i);
  writeln('The imaginary part is', j);
  a1:=z-(x1*aux);
  b1:=r1*aux;
  c1:=z*r1;
  d1:=(z*z*aux)+(z*x1);
  g1:=(c1*c1)+(d1*d1);
  e1:=((a1*c1)+(b1*d1))/g1;
```

```

f1:=((b1*c1)-(a1*d1))/g1;
h1:=(e1*e1)+(f1*f1);
i1:=e1/h1;
j1:=-f1/h1;
writeln('Transformed off-state impedance');
writeln('The real part is', i1);
writeln('The imaginary part is', j1)
end.

```

## A.6 Phase Shifter Design

This program calculates the matching stub impedance and electrical length required to achieve a particular phase shift and was used in the loaded-line phase shifter design. The program is based upon the design expressions given in Chapter 8 and the transformed switch impedance data obtained from the program given in Appendix A.5.

```

program phase(input,output);
const pi=3.141592654;
var  dbon,angon1,angon,dbof,angof1,angof,polon,polof:real;
     reon,imon,reof,imof,rf,xf,rr,xr,a,b,c,d,e,f,th,th1,zc:real;
     bs1,bs2,bq1,bq2,z1,z2,ph,ph1,ph2,c1,d1,e1,f1,aux,aux1:real;
begin
  writeln('Enter mag.  of on-state reflection coeff.  in dB. ');
  readln(dbon);
  writeln('Enter phase of on-state reflection coeff.  in deg. ');
  readln(angon1);
  writeln('Enter mag.  of off-state reflection coeff.  in dB. ');
  readln(dbof);
  writeln('Enter phase of off-state reflection coeff.  in deg. ');
  readln(angof1);
  angon:=(angon1*pi)/180;
  angof:=(angof1*pi)/180;
  polon:=exp((dbon/20)*ln(10));
  polf:=exp((dbof/20)*ln(10));
  reon:=(polon)*(cos(angon));
  imon:=(polon)*(sin(angon));
  reof:=(polf)*(cos(angof));
  imof:=(polf)*(sin(angof));
  if (angon<0) and (angon<=-90) then imon:=- (imon);
  if (angon>90) and (angon<=180) then reon:=- (reon);

```

```

if (angon>-90) and (angon<-180) then
begin
    reon:=-reon;
    imon:=-imon;
end;
if (angof<0) and (angof<=-90) then imof:=-imof;
if (angof>90) and (angof<=180) then reof:=-reof;
if (angof>-90) and (angof<-180) then
begin
    reof:=-reof;
    imof:=-imof;
end;
a:=(sqr(1-reon))+sqr(imon);
rf:=50*(((1+reon)*(1-reon))-sqr(imon))/a;
xf:=50*(((1-reon)*imon)+((1+reon)*imon))/a;
b:=(sqr(1-reof))+sqr(imof);
rr:=50*(((1+reof)*(1-reof))-sqr(imof))/b;
xr:=50*(((1-reof)*imof)+((1+reof)*imof))/b;
writeln('Enter the required phase shift in deg. ');
readln(th1);
if th1<90 then
begin
    th:=(th1*pi)/180;
    zc:=50*cos(th/2);
    bs1:=((sin(th/2))/(cos(th/2)))/50;
    bs2:=-bs1;
    z1:=sqrt(((xf-xr)-(2*xf*xr*bs1))/((2*bs1)+(bs1*bs1*
    (xf-xr))));
    c:=z1*(1+(xf*bs1));
    d:=xf-(bs1*z1*z1);
    e:=c/d;
    aux:=sqrt(e*e);
    if aux<=1 then f:=e-((e*e*e)/3)+((e*e*e*e*e)/5)-
    ((e*e*e*e*e*e*e)/7)
    else f:=(pi/2)-(1/e)+(1/(3*e*e*e))-1/(5*e*e*e*e*e);
    ph:=(f*180)/pi;
    if e<0 then
    begin
        if c<0 then ph:=-ph

```

```

        else ph:=180-ph
    end
    else
    begin
        if c<0 then ph:=180+ph
    end;
    writeln('Impedance of quarter-wavelength through
line=',zc);
    writeln('Impedance of shunt-stub line=',z1);
    writeln('Electrical length of shunt-stub line=',ph)
end;
if (th1>=90) and (th1<180) then
begin
    bs1:=((sqrt(2))-1)/50;
    bs2:=-bs1;
    bq1:=(2*bs1)/(((bs1*bs1)*(50*50))+1);
    bq2:=-bq1;
    z1:=sqrt(((xf-xr)-((xf*xr)*(bs1-bs2)))/(bs1-bs2-((bs1*bs2)
*(xf-xr))));
    c:=z1*(1+(xf*bs1));
    d:=xf-(bs1*z1*z1);
    e:=c/d;
    aux:=sqrt(e*e);
    if aux<=1 then f:=e-((e*e*e)/3)+((e*e*e*e*e)/5)-
((e*e*e*e*e*e*e)/7)
    else f:=(pi/2)-(1/e)+(1/(3*e*e*e))-1/(5*e*e*e*e*e);
    ph1:=(f*180)/pi;
    if e<0 then
    begin
        if c<0 then ph1:=-ph1
        else ph1:=180-ph1
    end
    else
    begin
        if c<0 then ph1:=180+ph1
    end;
    z2:=sqrt(((xf-xr)-((xf*xr)*(bq1-bq2)))/(bq1-bq2-((bq1*bq2)
*(xf-xr))));
    c1:=z2*(1+(xf*bq1));

```

```

d1:=xf-(bq1*z2*z2);
e1:=c1/d1;
aux1:=sqrt(e1*e1);
if aux1<=1 then f1:=e1-((e1*e1*e1)/3)+((e1*e1*e1*e1*e1)/5)-
((e1*e1*e1*e1*e1*e1*e1)/7)
else f1:=(pi/2)-(1/e1)+(1/(3*e1*e1*e1))-
(1/(5*e1*e1*e1*e1*e1));
ph2:=(f1*180)/pi;
if e1<0 then
begin
    if c1<0 then ph2:=-ph2
    else ph2:=180-ph2
end
else
begin
    if c1<0 then ph2:=180+ph2
end;
writeln('Impedance of quarter-wavelength through lines=50');
writeln('Impedance of first and third stub line=',z1);
writeln('Electrical length of first and third stub line=',
ph1);
writeln('Impedance of second stub line=',z2);
writeln('Electrical length of second stub line=',ph2)
end;
if (th1>=180) and (th1<270) then
begin
    bs1:=1/50;
    bs2:=-bs1;
    z1:=sqrt(((xf-xr)-((xf*xr)*(bs1-bs2)))/(bs1-bs2-((bs1*bs2)
*(xf-xr))));
    c:=z1*(1+(xf*bs1));
    d:=xf-(bs1*z1*z1);
    e:=c/d;
    aux:=sqrt(e*e);
    if aux<=1 then f:=e-((e*e*e)/3)+((e*e*e*e*e)/5)-
((e*e*e*e*e*e*e)/7)
    else f:=(pi/2)-(1/e)+(1/(3*e*e*e))-1/(5*e*e*e*e*e);
    ph1:=(f*180)/pi;
    if e<0 then

```

```

        begin
            if c<0 then ph1:=-ph1
            else ph1:=180-ph1
        end
    else
        begin
            if c<0 then ph1:=180+ph1
        end;
        writeln('Impedance of quarter-wavelength through lines=50');
        writeln('Impedance of all three stub lines=',z1);
        writeln('Electrical length of all three stub lines=',ph1);
        writeln('4-section 180 = 3-section 90')
    end;
    writeln(c,d,e,f)
end.

```

## A.7 GaAs FET Active Inductor

This program calculates the input impedance of the cascode GaAs FET active inductor, incorporating a CG feedback GaAs FET, and was used as a monolithic tuner in the GaAs FET switch design. The program is based upon the design expressions and analysis given in Chapter 11

```

program inductor(input,output,infile);
const pi=3.141592654;
var  f1,gm,gf,cg,f,cf,aux,r,i,i1,l,vb,vs,vgs,vgss,vgsi:real;
     a,a1,e,er,vp,w,wg1,lg1,a0,c,d,wg,lg,rref,iref:real;
     infile:text;
begin
    rewrite(infile);
    writeln('Enter the frequency in gigahertz');
    readln(f1);
    writeln('Enter the GaAs FET transconductance at VGS=0V');
    readln(gm);
    writeln('Enter the GaAs FET gate length in micrometers');
    readln(lg1);
    writeln('Enter the GaAs FET gate periphery in micrometers');
    readln(wg1);
    writeln('Enter the magnitude of the GaAs FET pinch-off voltage');
    readln(vp);

```

```
writeln('Enter the built-in potential of the gate junction');
readln(vb);
writeln('Enter the recessed GaAs channel thickness in micrometers');
readln(a1);
writeln('Enter the gate-to-source voltage start value');
readln(vgs);
writeln('Enter the gate-to-source voltage stop value');
readln(vgss);
writeln('Enter the gate-to-source volatge increment');
readln(vgsi);
f:=f1*(exp(9*ln(10)));
a:=a1*(exp(-6*ln(10)));
e:=8.85*(exp(-12*ln(10)));
lg:=lg1*(exp(-6*ln(10)));
wg:=wg1*(exp(-6*ln(10)));
er:=13.1;
a0:=a*(sqrt((vb)/(vp+vb)));
cg:=(e*er*lg*wg)/a0;
vs:=(gm*a0)/(e*er*wg);
while vgs>=vgss do
begin
    w:=a*(sqrt((vb-vgs)/(vp+vb)));
    cf:=(e*er*lg*wg)/w;
    gf:=(e*er*vs*wg)/w;
    aux:=sqr(((2*pi*f*cg)/(gm)));
    r:=(1+aux)/aux;
    i1:=(2*pi*f)*(cf+(cf*aux)-((gm*gf)/(4*pi*pi*f*f*cg)));
    i:=(1+aux)/(-i1);
    l:=i/(2*pi*f);
    c:=r-50;
    d:=r+50;
    rref:=((c*d)+(i*i))/((d*d)+(i*i));
    iref:=((-c*i)+(i*d))/((d*d)+(i*i));
    writeln(infile,vgs,r,i,l,rref,iref);
    vgs:=vgs+vgsi
end
end.
```

# References

- [A.1] M. Kirschning, R. H. Jansen, and N. H. L. Koster, “Accurate model for open end effect of microstrip lines,” *Electron. Lett.*, vol. 17, pp. 123–125, Feb. 1981.
- [A.2] E. Hammerstad, “Computer-aided design of microstrip couplers with accurate discontinuity models,” in *Proc. IEEE MTT-S Int. Microwave Symp. Dig.*, pp. 54–56, 1981.
- [A.3] R. Garg and I. J. Bahl, “Microstrip discontinuities,” *Int. J. Electron.*, vol. 45, pp. 81–87, Jan. 1978.
- [A.4] A. Madjar, P. R. Herczfeld, and A. Paoella, “Analytical model for optically generated currents in GaAs MESFETs,” *IEEE Trans. Microwave Theory Tech.*, vol. 40, pp. 1681–1691, Aug. 1992.

# Appendix B

## Design Expressions

### Contents

---

<b>B.1 Gate Depletion Region Photocurrent</b> . . . . .	<b>194</b>
<b>B.2 Optical Reflectivity</b> . . . . .	<b>196</b>
<b>B.3 Gate Depletion Region Lateral Extension</b> . . . . .	<b>198</b>
<b>B.4 Phase Shifter Matching Stub</b> . . . . .	<b>199</b>

---

**T**HIS appendix outlines the origins of some of the important design expressions used during this investigation, and in particular includes derivations not easily accessible in the literature.

### B.1 Gate Depletion Region Photocurrent

The optically controlled GaAs FET switch described in this thesis relies on a photovoltaic effect at the gate of the FET to control the switching state. The gate photovoltaic effect is generated by the combination of a small optically-induced gate current and a large resistance placed in the gate bias network. An expression for the short-circuit gate photocurrent was derived originally by de Salles [B.1], and included the combined effects of the photo-generated carriers from within the gate depletion region and those created in the GaAs region which were able to diffuse into the depletion region. The derivation of the short-circuit gate photocurrent presented here follows the approach of de Salles with the exception that the diffusion component of the gate photocurrent is ignored, in accordance with the suggestions by Madjar *et al.* [B.2].

Referring to Figure B.1, the photocurrent density due to optically-induced carriers generated in the gate depletion region is determined by integrating the rate of optically generated electron-hole pairs over the depth of the gate depletion region, extending from  $y = 0$  to  $y = w$ . Since optical absorption can take place only between the gate-to-source and gate-to-drain inter-electrode spacing, Madjar *et al.* [B.2] evaluated the

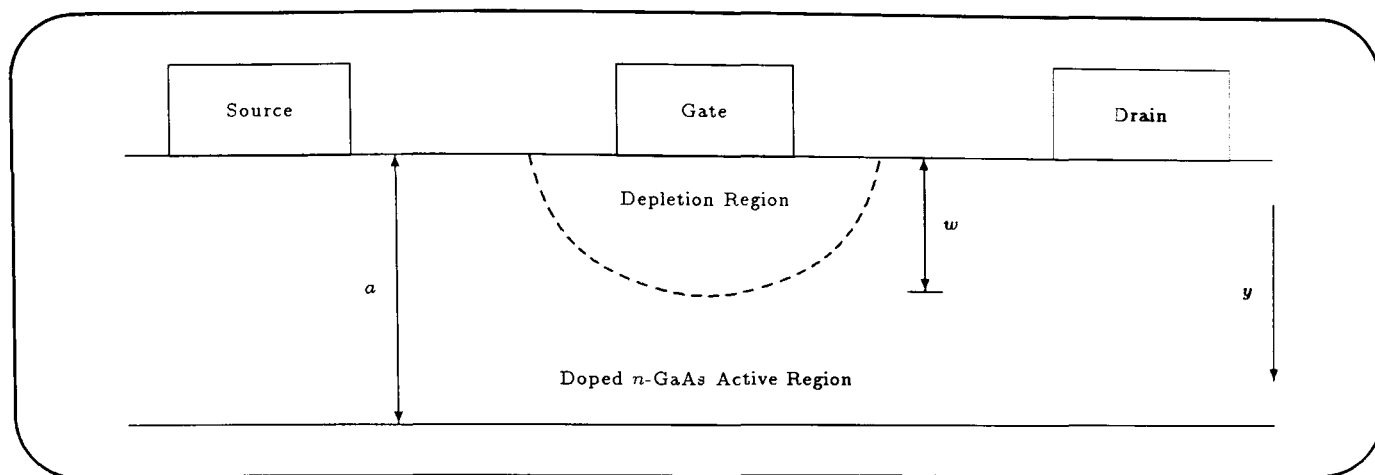


**Figure B.1:** Simplified schematic cross-section of a microwave GaAs MESFET.

contribution from each side of the gate separately, on the basis that the differing bias conditions at the source and drain meant that the vertical extension of the depletion region would be different on either side of the gate. Since the GaAs FET switch described in this investigation has an identical bias at the drain and source terminals, the depletion region depth will be uniform, in which case the gate depletion region photocurrent density can be expressed as<sup>†</sup>

$$J_{depi} = q \int_0^w g_p(y) dy \quad (\text{B.1})$$

where  $g_p(y)$  is the electron-hole pair generation rate,  $q$  the electronic charge and  $w$  the gate depletion region depth.

The optical absorption coefficient,  $\alpha$ , is defined as the rate of decrease in the photon flux per unit distance and, from Lambert's law, the photon flux at a distance  $y$  can be expressed as [B.3]

$$\Phi(y) = \Phi_0 e^{-\alpha y} \quad (\text{B.2})$$

where  $\Phi_0$  is the photon flux density at the surface (i.e. at  $y = 0$ ). The number of photons per unit volume is given by

$$N_{ph} = \frac{\Phi(y)}{\nu_{ph}} \quad (\text{B.3})$$

where  $\nu_{ph}$  is the photon energy propagation velocity, given by

$$\nu_{ph} = \frac{dy}{dt} \quad (\text{B.4})$$

where  $t$  is time. Therefore, the rate of loss of photons per unit volume is given by

$$\frac{dN_{ph}}{dt} = \left( \frac{dN_{ph}}{dy} \right) \left( \frac{dy}{dt} \right) \quad (\text{B.5})$$

$$= - \left( \frac{\alpha \Phi_0 e^{-\alpha y}}{\nu_{ph}} \right) \left( \frac{dy}{dt} \right) \quad (\text{B.6})$$

$$= -\alpha \Phi_0 e^{-\alpha y}. \quad (\text{B.7})$$

<sup>†</sup>It is assumed that positive current is for holes flowing in the direction of  $y$  decreasing.

If it is assumed that for each photon absorbed, one electron-hole pair (i.e. a quantum efficiency of unity) is generated. Then the pair generation rate is given by

$$g_p(y) = \alpha\Phi_0 e^{-\alpha y}. \quad (\text{B.8})$$

If some of the light is reflected at the device surface, then equation (B.8) becomes

$$g_p(y) = \alpha\Phi_0(1 - R)e^{-\alpha y} \quad (\text{B.9})$$

where  $R$  is the optical power reflectivity at the device surface. Substituting equation (B.9) into (B.1) and integrating, yields the following expression

$$J_{depi} = q(1 - R)\Phi_0 (1 - e^{-\alpha w}). \quad (\text{B.10})$$

Since in the off-state the GaAs FET switch is biased at pinch-off, the GaAs channel region will be fully depleted and equation (B.10) can be re-written as

$$J_{depi} = q(1 - R)\Phi_0 (1 - e^{-\alpha a}) \quad (\text{B.11})$$

where  $a$  is the unrecessed GaAs epitaxial layer thickness.

## B.2 Optical Reflectivity

The surface of most FET's is coated with some form of passivation to protect the device and maintain reliability, with silicon nitride ( $\text{Si}_3\text{N}_4$ ) being commonly used. The amount of light that actually penetrates this passivation layer to be subsequently absorbed in the GaAs active region of the FET was used to determine the optical power required to activate the GaAs FET switches described in this thesis. This can be evaluated by considering the optical reflectivity,  $R$ , due to the changing refractive indices of the air/ $\text{Si}_3\text{N}_4$ /GaAs interface, as shown in Figure B.2. The derivation presented here follows the approach of Madjar *et al.* [B.2] and uses the theory of small reflections commonly encountered in optical and microwave circuit analysis [B.4].

In Figure B.2, light is considered in the form of a plane electromagnetic wave that is incident normally on the flat interface between the air and  $\text{Si}_3\text{N}_4$ . For an incident wave of unit amplitude, the total reflected wave has an amplitude of  $\Gamma$ , equal to the net optical reflection coefficient. There will be partial reflection and transmission at the air/ $\text{Si}_3\text{N}_4$  and  $\text{Si}_3\text{N}_4$ /GaAs interfaces. If  $\theta_s$  is the electrical length of the  $\text{Si}_3\text{N}_4$  passivation layer, then the total reflected wave is the sum of the partially reflected waves i.e.

$$\Gamma = \Gamma_1 + T_{12}T_{21}\Gamma_3 e^{-2j\theta_s} + T_{12}T_{21}\Gamma_3^2\Gamma_2 e^{-4j\theta_s} + \dots \quad (\text{B.12})$$

$$= \Gamma_1 + T_{12}T_{21}\Gamma_3 e^{-2j\theta_s} \sum_{n=0}^{\infty} \Gamma_2^n \Gamma_3^n e^{-2jn\theta_s}. \quad (\text{B.13})$$

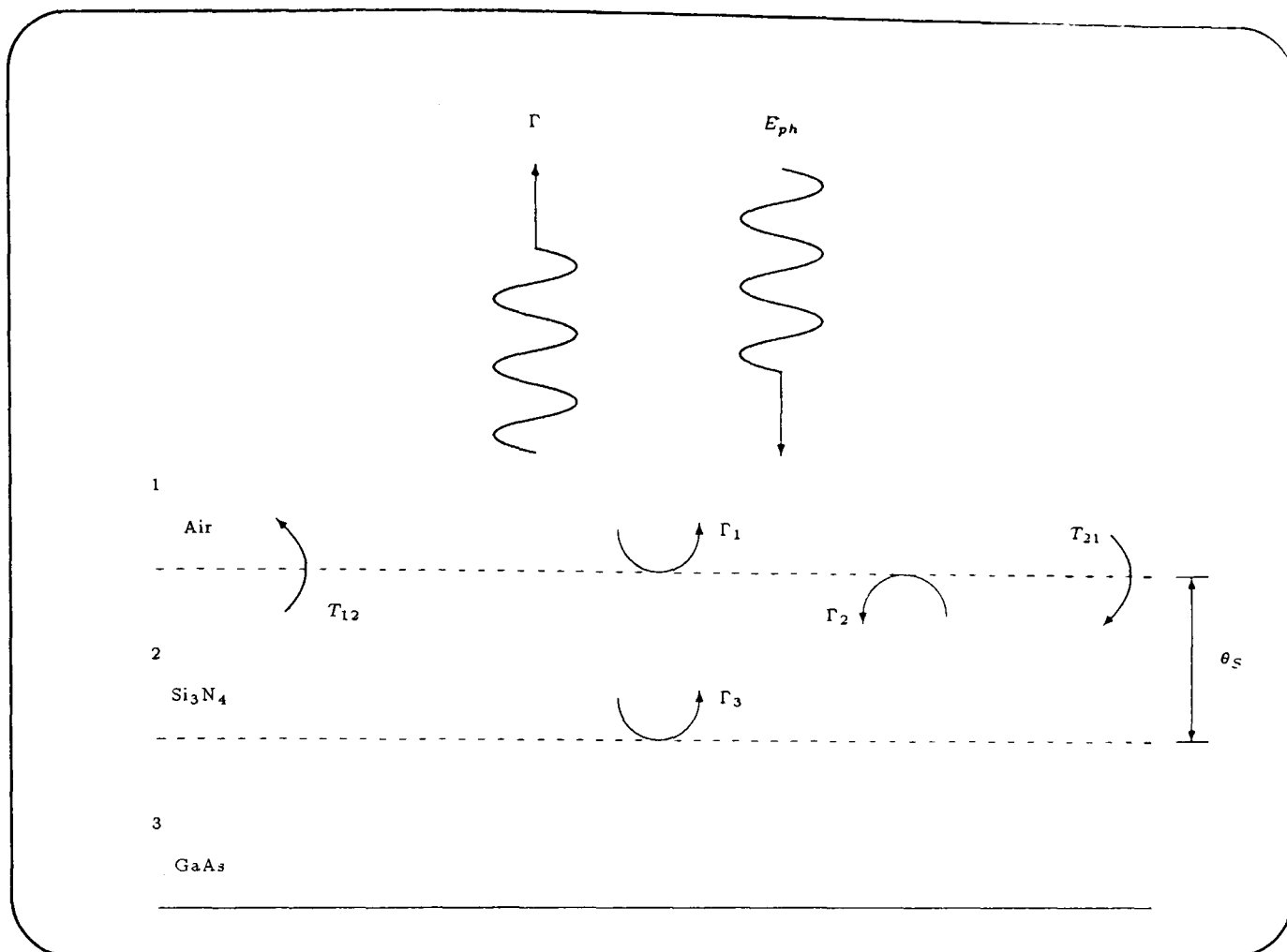


Figure B.2: Optical reflection from the surface passivation layer of a GaAs FET.

The second term in equation (B.13) is a convergent series of the general form

$$\sum_{n=0}^{\infty} x^n = \frac{1}{1-x} \quad (\text{B.14})$$

which, when applied to equation (B.13), gives

$$\Gamma = \Gamma_1 + \frac{T_{12}T_{21}\Gamma_3e^{-2j\theta_S}}{1 - \Gamma_2\Gamma_3e^{-2j\theta_S}}. \quad (\text{B.15})$$

Replacing  $T_{12}$  by  $1 + \Gamma_2 = 1 - \Gamma_1$  and  $T_{21}$  by  $1 + \Gamma_1$  gives

$$\Gamma = \frac{\Gamma_1 + \Gamma_3e^{-2j\theta_S}}{1 + \Gamma_1\Gamma_3e^{-2j\theta_S}}. \quad (\text{B.16})$$

From the theory of optics it can be shown that the amplitude reflection coefficient,  $r$ , of a light wave at the interface between two media of refractive indices  $n_1$  and  $n_2$  is given by [B.5]

$$r = \frac{n_1 - n_2}{n_1 + n_2}. \quad (\text{B.17})$$

from which the reflection coefficients at the Si<sub>3</sub>N<sub>4</sub>/GaAs and air/Si<sub>3</sub>N<sub>4</sub> interfaces can be expressed respectively as

$$\Gamma_1 = \frac{1 - N_S}{1 + N_S} \quad (\text{B.18})$$

$$\Gamma_3 = \frac{N_S - N_G}{N_S + N_G} \quad (\text{B.19})$$

where  $N_S$  and  $N_G$  are the refractive indices of silicon nitride and gallium arsenide respectively. Hence the optical power reflectivity,  $R$ , can be expressed as

$$R = |\Gamma|^2 \quad (\text{B.20})$$

$$= \left| \frac{(1 - N_S)(N_S + N_G) + (1 + N_S)(N_S - N_G)e^{-j2\theta_S}}{(1 + N_S)(N_S + N_G) + (1 - N_S)(N_S - N_G)e^{-j2\theta_S}} \right|^2. \quad (\text{B.21})$$

The electrical length of the  $\text{Si}_3\text{N}_4$  passivation layer can be related to its physical thickness,  $l_{pas}$ , by

$$\theta_S = \beta l_{pas} \quad (\text{B.22})$$

$$= \frac{2\pi\sqrt{\epsilon_r}l_{pas}}{\lambda} \quad (\text{B.23})$$

$$= \frac{2\pi l_{pas}N_S}{\lambda} \quad (\text{B.24})$$

where  $\lambda$  is the optical wavelength,  $\epsilon_r$  is the relative permittivity and  $\beta$  the phase propagation constant.

### B.3 Gate Depletion Region Lateral Extension

For the GaAs FET switch, the lateral extension of the gate depletion region determines the volume over which optical absorption occurs on either side of the FET gate electrode, as shown in Figure B.3. The lateral extension forms part of the optically illuminated area of the FET, which, when considered in conjunction with the gate photocurrent density expression, yields the short-circuit gate photocurrent.

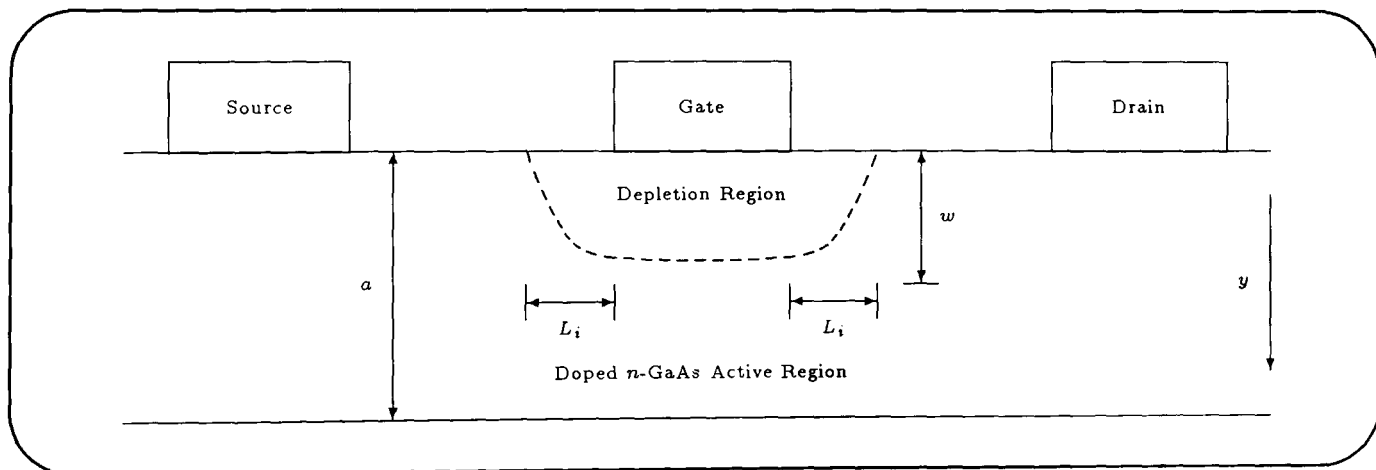


**Figure B.3:** Simplified schematic cross-section of a microwave GaAs MESFET.

The lateral extension of the depletion region on either side of the gate will be identical since the drain and source terminals are at the same potential in both switching states. Therefore the lateral extension on both sides was approximated to the gate depletion region depth which is determined by solving the Poisson equation under the abrupt junction approximation, as given by [B.6]

$$\frac{\partial^2 V}{\partial y^2} = -\frac{qN}{\epsilon_r \epsilon_0} \quad (\text{B.25})$$

where  $V$  is the voltage,  $N$  the doping density and  $\epsilon_r$  and  $\epsilon_0$  the relative and free-space permittivity respectively. Integrating Poisson's equation twice gives the voltage across the depletion region as

$$V_{dep} = \frac{qNw^2}{2\epsilon_r\epsilon_0} \quad (\text{B.26})$$

where  $w$  is the depletion region depth. Since the drain and source are held at DC earth potential during both switching states, the voltage across the depletion region will consist of the voltage applied to the gate terminal plus the built-in potential of the gate Schottky junction. Thus, from equation (B.26) it follows that

$$\phi_B - V_{GS} = \frac{qNw^2}{2\epsilon_r\epsilon_0} \quad (\text{B.27})$$

where  $V_{GS}$  is the gate-to-source voltage and  $\phi_B$  the built-in potential of the Schottky barrier. At pinch-off, the channel is fully depleted and the depletion region depth is equal to the unrecessed GaAs epitaxial thickness (i.e.  $w = a$ ). In which case

$$\phi_B - V_P = \frac{qNa^2}{2\epsilon_r\epsilon_0} \quad (\text{B.28})$$

where  $V_P$  is the external voltage applied at the gate to bring about pinch-off. Rearranging equations (B.28) and (B.27) gives

$$\frac{qN}{2\epsilon_r\epsilon_0} = \frac{V_P + \phi_B}{a^2} \quad (\text{B.29})$$

$$w = \left\{ \frac{2\epsilon_r\epsilon_0(\phi_B - V_{GS})}{qN} \right\}^{\frac{1}{2}} \quad (\text{B.30})$$

By substituting equation (B.29) into (B.30), the depletion region depth can be expressed as

$$w = a \left( \frac{\phi_B - V_{GS}}{|V_P| + \phi_B} \right)^{\frac{1}{2}}. \quad (\text{B.31})$$

Therefore the lateral extension of the gate depletion region on both the drain and source sides of the gate can be approximated by

$$L_i \simeq a \left( \frac{\phi_B - V_{GS}}{|V_P| + \phi_B} \right)^{\frac{1}{2}}. \quad (\text{B.32})$$

## B.4 Phase Shifter Matching Stub

A matching stub was used in the design of the optically controlled loaded-line phase shifter in order to transform the switch state impedances to give the required loading susceptances. The derivation of the stub design equations presented here follows the approach of Bahl and Gupta [B.7].

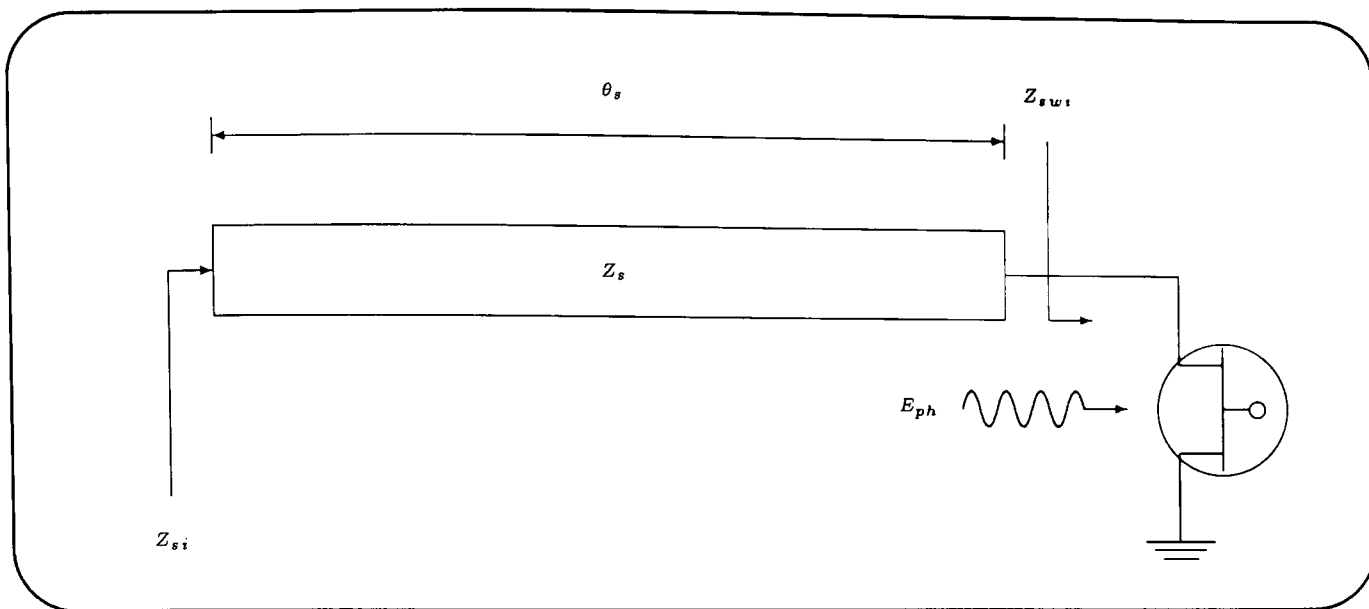


**Figure B.4:** Schematic of stub impedance matching network for optically controlled loaded-line phase shifter.

For a matching stub of characteristic impedance  $Z_s$  and electrical length  $\theta_s$ , terminated in a GaAs FET switch, as shown in Figure B.4, the input impedance can be obtained from standard transmission line theory as

$$Z_{si} = \frac{Z_s(Z_{swi} + jZ_s \tan \theta_s)}{(Z_s + jZ_{swi} \tan \theta_s)} \quad (\text{B.33})$$

where  $Z_{swi}$  is the switch state impedance and  $i = 1, 2$  represents the two switching states. This can be re-written in terms of input admittance as

$$Y_{si} = \frac{(Z_s + jZ_{swi} \tan \theta_s)}{Z_s(Z_{swi} + jZ_s \tan \theta_s)}. \quad (\text{B.34})$$

For a low-loss switch and low-loss line, we can neglect the real components of the switch state impedance to give  $Z_{swi} = jX_{swi}$ , where  $X_{swi}$  is the switch state reactance. With this approximation the input susceptance to the stub (i.e. the reactive component of the input admittance) can be expressed, from equation (B.34), as

$$B_{si} = \frac{(X_{swi} \tan \theta_s - Z_s)}{Z_s(X_{swi} + Z_s \tan \theta_s)}. \quad (\text{B.35})$$

By solving for  $Z_s$  and  $\theta_s$ , for the two switch states, we obtain

$$Z_s = \left[ \frac{(X_{sw1} - X_{sw2} - X_{sw1}X_{sw2}(B_{s1} - B_{s2}))}{B_{s1} - B_{s2} - B_{s1}B_{s2}(X_{sw1} - X_{sw2})} \right]^{\frac{1}{2}} \quad (\text{B.36})$$

$$\tan \theta_s = \frac{Z_s(1 + X_{sw1}B_{s1})}{(X_{sw1} - B_{s1}Z_s^2)} = \frac{Z_s(1 + X_{sw2}B_{s2})}{(X_{sw2} - B_{s2}Z_s^2)} \quad (\text{B.37})$$

where it is assumed that the phase shifter is operated under class III mode, in which case  $B_{s1} = -B_{s2}$ .

# References

- [B.1] A. A. A. de Salles, *Optical control of microwave field effect transistors*. Ph.D. thesis, Univ. of London, 1982.
- [B.2] A. Madjar, P. R. Herczfeld, and A. Paoletta, "Analytical model for optically generated currents in GaAs MESFETs," *IEEE Trans. Microwave Theory Tech.*, vol. 40, pp. 1681–1691, Aug. 1992.
- [B.3] J. Wilson and J. F. B. Hawkes, *Optoelectronics: An introduction*, ch. 5, pp. 159–161. New York: Prentice Hall, second. ed., 1989.
- [B.4] R. E. Collin, *Foundations for microwave engineering*, ch. 5, pp. 347–348. New York: McGraw-Hill, second. ed., 1992.
- [B.5] J. B. Marion and W. F. Hornyak, *Physics for science and engineering*, ch. 40, pp. 1079–1081. New York: Holt-Saunders, 1982.
- [B.6] S. M. Sze, *Physics of semiconductor devices*. New York: Wiley, second. ed., 1981.
- [B.7] I. J. Bahl and K. C. Gupta, "Design of loaded-line p-i-n diode phase shifter circuits," *IEEE Trans. Microwave Theory Tech.*, vol. MTT-28, pp. 219–224, Mar. 1980.